University of Strathclyde

Department of Mechanical & Aerospace Engineering

Deterministic Numerical Simulation of the Boltzmann and Kinetic Model Equations for Classical and Quantum Dilute Gases

Lei Wu

A thesis presented in fulfilment of the requirements

for the degree of Doctor of Philosophy

2013

Declaration of author's rights

This thesis is the result of the author's original research. It has been composed by the author and has not been previously submitted for examination which has led to the award of a degree.

Lei Wu

July 2013

Abstract

In the areas of low-density aerodynamics, vacuum industry, and micro-electromechanical systems, the Navier-Stokes-Fourier equations fail to describe the gas dynamics when the molecular mean free path is not negligible compared to the characteristic flow length. Instead, the Boltzmann equation is used to account for the non-continuum nature of the rarefied gas. Although many efforts have been made to derive the macroscopic equations from the Boltzmann equation, the numerical simulation of the Boltzmann equation is indispensable in the study of moderately and highly rarefied gas.

We aim to develop an accurate and efficient deterministic numerical method to solve the Boltzmann equation. The fast spectral method [1], originally developed by Mouhot and Pareschi for the numerical approximation of the collision operator, is extended to deal with other collision kernels, such as those corresponding to the soft, Lennard-Jones, and rigid attracting potentials. The accuracy of the fast spectral method is checked by comparing our numerical results with the exact Bobylev-Krook-Wu solutions of the space-homogeneous Boltzmann equation for a gas of Maxwell molecules. It is found that the accuracy is improved by replacing the trapezoidal rule with Gauss-Legendre quadrature in the calculation of the kernel mode, and the conservation of momentum and energy are ensured by the Lagrangian multiplier method without loss of spectral accuracy. The relax-to-equilibrium processes of different collision kernels with the same value of shear viscosity are then compared and the use of special collision kernels is justified. An iteration scheme, where the numerical errors decay exponentially, is employed to obtain stationary solutions of the space-inhomogeneous Boltzmann equation. Sever classical benchmarking problems (the normal shock wave, and the planar Fourier/Couette/force-driven Poiseuille flows) are investigated. For normal shock waves, our numerical results are compared with the finite-difference solution of the

Boltzmann equation for hard sphere molecules, the experimental data, and the molecular dynamics simulation of argon using the realistic Lennard-Jones potential. For the planar Fourier/Couette/force-driven Poiseuille flows, our results are compared with the Direct Simulation Monte Carlo method. Excellent agreements are observed in all test cases.

The fast spectral method is then applied to the linearised Boltzmann equation. With appropriate velocity discretization, the classical Poiseuille and thermal creep flows are solved up to $Kn \sim 10^6$, where the accuracy in the mass and heat flow rates is comparable to those from the finite-difference method and the efficiency is much better than the low-noise Direct Simulation Monte Carlo method. The fast spectral method is also extended to solve the Boltzmann equation for binary gas mixtures, both in the framework of classical and quantum mechanics.

With the accurate numerical solution provided by the fast spectral method, we check the accuracy of kinetic model equations to find out at what flow regime can the complicated Boltzmann collision kernel be replaced by the simple kinetic ones. We also solve the collective oscillation of quantum gas confined in external trap and compare the numerical solutions with the experimental data, indicating the applicability of quantum kinetic model.

Acknowledgements

Firstly I thank my supervisors Dr. Yonghao Zhang and Prof. Jason M. Reese for their constant guidance, advice, and support throughout the past 3 years.

I would also like to thank other researchers in the James Weir Fluids Laboratory for many useful and enlightening discussions. The academic freedom and research environment of the group is always a huge source of inspiration. In particular, I am grateful to Dr. Craig White for patient discussion on DSMC. Without him, the paper "Deterministic numerical solutions of the Boltzmann equation using the fast spectral method" published in Journal of Computational Physics would not have been possible. I also thank Dr. Jianping Meng for many hours of discussions.

I am grateful to the financial support from the University of Strathclyde and Scottish Overseas Research Students Awards Scheme.

Finally, I would like to thank my family and friends for their love, support and words of encouragement.

Contents

List of Figures

List of Tables

Nomenclature

A	aspect ratio of rectangular tube
$\mathbf{a}$	acceleration
a_s	s-wave scattering length
B	collision kernel
b_a	aiming distance
D	parameter used to calculate the shear viscosity, Eq. (1.17)
$\mathcal{D}$	difference between Boltzmann and kinetic collision operators
D_m	coefficient of mass diffusion
d	molecular diameter
$\mathbf{e}$	unit vector in a sphere
e	specific energy
f, h	velocity distribution function
$\hat{f}, \hat{h}$	spectrum of velocity distribution function
K	effective temperature
k_B	Boltzmann constant
Kn	Knudsen number
Kn'	normalised Knudsen number, Eq. (2.17)
K_t	thermal conductivity
L	maximum discrete molecular velocity
$\mathcal{L}_g$	linearised gain term of the Boltzmann collision operator
ℓ	characteristic length of flow structure
$\mathbf{l}, \mathbf{m}, \mathbf{j}$	frequency index
M	number of discrete angle
Ma	Mach number

m	molecular mass
m_r	reduced mass
N	number of discrete velocities in one direction
n	number density
Pr	Prandtl number
$\mathbf{P}$	pressure tensor
p	scaler pressure
Q	binary collision kernel
$\hat{Q}$	spectrum of binary collision kernel
Q^+, Q^-	gain, loss term of the collision kernel
$\mathbf{q}$	heat flux
R	truncated radius of collision operator
r	intermolecular distance
S	support of velocity distribution function
T	temperature
T_B	binding temperature of the dimer state
t	time
U	effective potential
$\mathbf{u}$	relative molecular velocity in a collision
$\mathbf{v}$	molecular velocity
v_m	most probable velocity
$\mathbf{v}_r$	peculiar velocity
$\mathbf{V}$	bulk velocity
W	width of Gaussian potential
x	spatial Cartesian co-ordinates
Z	fugacity

Greek

α, γ	parameters used in the collision kernel, Eq. (2.9)
β	kernel mode
δ	Dirac's delta function
η, κ	parameters define power-law potentials
$\phi(r)$	intermolecular potential
Γ	gamma function
λ	mean free path
$\lambda_n, \lambda_v, \lambda_e$	Lagrangian multipliers
μ	shear viscosity
ν	collision frequency
Ω	solid angle
ω	viscosity index
ω_x, ω_y	frequency of external harmonic potential
ρ	mass density
σ	differential cross-section
σ_μ	viscosity cross-section
σ_M	momentum transfer cross-section
τ	local relaxation time
ξ	frequency components

Superscripts

$\prime$	post-collision molecular velocity
$\imath, \jmath$	species index
k	iteration step

Subscripts

0	reference quantities
$*$	velocity of the second molecular
$coll$	collision properties
d	down stream
eq	equilibrium
g	gas properties
j	spatial direction
r	relative/reference
w	wall properties

Acronyms

BE	Boltzmann Equation
BGK	Bhatnagar-Gross-Krook
DSMC	Direct Simulation Monte Carlo
ES	Ellipsoidal-Statistical
FSM	Fast Spectral Method
LJ	Lennard-Jones
MD	Molecular Dynamics
NSF	Navier-Stokes-Fourier
S	Shakhov
VDF	Velocity Distribution Function
VHS	Variable Hard Sphere
VSS	Variable Soft Sphere

Chapter 1

Introduction

1.1 Background

A macroscopic volume of gas is a system of a very large number of molecules moving constantly in a rather irregular way. This huge number of degrees of freedom makes the trace of motion of each molecular impossible. The fundamental and practical task in the study of gas dynamics is hence to obtain the evolution of macroscopic quantities such as the mass density ρ, bulk velocity $\mathbf{V}$, temperature T, pressure tensor $\mathbf{P}$, and the heat flux $\mathbf{q}$. The evolution of these macroscopic quantities may be modelled at either the macroscopic or the microscopic level.

1.1.1 Analytical treatments

Traditionally, when the molecular mean free path λ (average distance between two subsequent collisions of a molecular) is negligible in comparison with a typical length of the flow structure ℓ, the gas is treated as a continuous medium and the famous Navier-Stokes-Fourier (NSF) equations are established in terms of the mass, momentum, and energy conservation

$$\frac{\partial \rho}{\partial t} + \frac{\partial (\rho V_j)}{\partial x_j} = 0, \tag{1.1}$$

$$\frac{\partial (\rho V_i)}{\partial t} + \frac{\partial (\rho V_i V_j + P_{ij})}{\partial x_j} = \rho a_i, \tag{1.2}$$

$$\frac{\partial \left[\rho \left(\frac{3k_B T}{2m} + \frac{V_i^2}{2}\right)\right]}{\partial t} + \frac{\partial \left[\rho V_j \left(\frac{3k_B T}{2m} + \frac{V_i^2}{2}\right) + V_i P_{ij} + q_j\right]}{\partial x_j} = \rho V_j a_j, \tag{1.3}$$

together with the Newton's law for the shear stress

$$P_{ij} = \frac{\rho k_B T}{m}\delta_{ij} - \mu\left(\frac{\partial V_i}{\partial x_j} + \frac{\partial V_j}{\partial x_i} - \frac{2}{3}\frac{\partial V_k}{\partial x_k}\delta_{ij}\right), \tag{1.4}$$

and the Fourier's law for the thermal conduction

$$q_i = -K_t\frac{\partial T}{\partial x_i}, \tag{1.5}$$

where t is the time, $\mathbf{x}$ is the spatial coordinate, $\mathbf{a}$ is the external acceleration, k_B is the Boltzmann constant, m is the molecular mass, δ is Dirac's delta function, μ is the shear viscosity, and K_t is the thermal conductivity. Note that the Einstein's summation rule is used throughout the thesis.

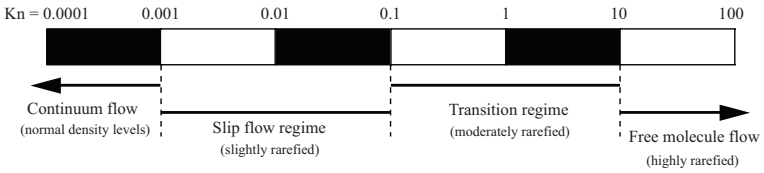

Figure 1.1: Flow regimes in terms of the Knudsen number. The figure is adapted from Ref. [2].

An important parameter in the study of gas dynamics is the Knudsen number:

$$\mathrm{Kn} = \frac{\lambda}{\ell}, \tag{1.6}$$

which is defined as the ratio of the molecular mean free path to the characteristic flow length. Different flow regimes in terms of the Knudsen number are shown in Figure 1.1. Usually, the NSF equations can be used to describe the gas dynamics[1], up to $\mathrm{Kn} < 0.001$. When the Knudsen number becomes large, the continuum hypothesis breaks down and the NSF equations fail to capture the non-conventional behaviour of rarefied gas flows. This situation is frequently encountered in the areas of low-density aerodynamics and vacuum industry (where the mean free path is large) and micro/nano-electromechanical systems (where the characteristic flow length is small). At $0.001 < Kn < 0.1$, however, the non-intuitive rarefied effects (such as velocity slip

[1] There are some exceptions, where the NSF equations do not describe the gas dynamic accurately even when $\mathrm{Kn} \to 0$. For example, the ghost effect induced by the periodical variation of the wall temperature [3].

and temperature jump) only exist in a small region close to the wall. With appropriate velocity and temperature wall boundary conditions, the NSF equations may still produce accurate velocity profiles for flows in a micro-channel [2].

To describe the non-continuous nature of the rarefied gas, a fundamental theory at the microscopic level is needed. In statistical physics, the velocity distribution function (VDF) $f(t, \mathbf{x}, \mathbf{v})$ is introduced to describe the system state, where $\mathbf{v}$ is the molecular velocity. The VDF is defined in such a way that the quantity $f(t, \mathbf{x}, \mathbf{v})d\mathbf{x}d\mathbf{v}$ is the particle number in the phase-space volume $d\mathbf{x}d\mathbf{v}$. All macroscopic quantities can be calculated via the moments of the VDF: the molecular number density n, bulk velocity, temperature, pressure tensor, and heat flux are given by

$$
\begin{aligned}
n(t, \mathbf{x}) &= \int_{\mathbb{R}^3} f(t, \mathbf{x}, \mathbf{v}) d\mathbf{v}, && (1.7)\\
\mathbf{V}(t, \mathbf{x}) &= \frac{1}{n(t, x)} \int_{\mathbb{R}^3} \mathbf{v} f(t, \mathbf{x}, \mathbf{v}) d\mathbf{v}, && (1.8)\\
T(t, \mathbf{x}) &= \frac{m}{3k_B n(t, x)} \int_{\mathbb{R}^3} |\mathbf{v} - \mathbf{V}|^2 f(t, \mathbf{x}, \mathbf{v}) d\mathbf{v}, && (1.9)\\
P_{ij}(t, \mathbf{x}) &= m \int_{\mathbb{R}^3} (v_i - V_i)(v_j - V_j) f(t, \mathbf{x}, \mathbf{v}) d\mathbf{v}, && (1.10)\\
q_i(t, \mathbf{x}) &= \frac{m}{2} \int_{\mathbb{R}^3} |\mathbf{v} - \mathbf{V}|^2 (v_i - V_i) f(t, \mathbf{x}, \mathbf{v}) d\mathbf{v}. && (1.11)
\end{aligned}
$$

The governing equation for the evolution of VDF is derived by Ludwig Boltzmann. In his description, all molecules move in straight lines with fixed velocities until they encounter elastic collisions with other molecules. Under the assumptions of molecular chaos and binary collisions (dilute gas), a nonlinear collision operator is proposed to model the collision, where the intermolecular interaction is incorporated into the collision kernel. The celebrated Boltzmann equation (BE) takes the form of [4]:

$$
\frac{\partial f}{\partial t} + \mathbf{v} \cdot \frac{\partial f}{\partial \mathbf{x}} + \mathbf{a} \cdot \frac{\partial f}{\partial \mathbf{v}} = Q(f, f_*), \tag{1.12}
$$

where the first term on the left hand side describes the change of f with time, the second term is the convective change of f, the third term represents the change of f induced by the external acceleration (assume it is independent of the molecular velocity). Finally, the term on the right hand side is the quadratic collision operator $Q(f, f_*)$, which

consists of the gain term Q^+ and the loss term Q^-. The collision operator is local in time and space. For simplicity t and $\mathbf{x}$ will be omitted in writing the collision operator[2]:

$$Q(f, f_*) = \underbrace{\int_{\mathbb{R}^3}\int_{\mathbb{S}^2} B(\cos\theta, |\mathbf{v}-\mathbf{v}_*|) f(\mathbf{v}'_*) f(\mathbf{v}') d\Omega d\mathbf{v}_*}_{Q^+} - \underbrace{\nu(\mathbf{v}) f(\mathbf{v})}_{Q^-}, \tag{1.13}$$

$$\nu(\mathbf{v}) = \int_{\mathbb{R}^3}\int_{\mathbb{S}^2} B(\cos\theta, |\mathbf{v}-\mathbf{v}_*|) f(\mathbf{v}_*) d\Omega d\mathbf{v}_*, \tag{1.14}$$

where $\nu(\mathbf{v})$ is the collision frequency, $\mathbf{v}, \mathbf{v}_*$ are the pre-collision particle velocities, while $\mathbf{v}', \mathbf{v}'_*$ are the corresponding post-collision velocities. Conservation of momentum and energy yield the following relations

$$\begin{aligned} \mathbf{v}' &= \frac{\mathbf{v}+\mathbf{v}_*}{2} + \frac{|\mathbf{v}-\mathbf{v}_*|}{2}\Omega = \mathbf{v} + \frac{|\mathbf{u}|\Omega - \mathbf{u}}{2}, \\ \mathbf{v}'_* &= \frac{\mathbf{v}+\mathbf{v}_*}{2} - \frac{|\mathbf{v}-\mathbf{v}_*|}{2}\Omega = \mathbf{v}_* - \frac{|\mathbf{u}|\Omega - \mathbf{u}}{2}, \end{aligned} \tag{1.15}$$

where $\mathbf{u} = \mathbf{v} - \mathbf{v}_*$ is the relative pre-collision velocity and Ω is a vector in the unit sphere $\mathbb{S}^2$ along the relative post-collision velocity $\mathbf{v}' - \mathbf{v}'_*$. The deflection angle θ between the pre- and post-collision relative velocities satisfies $\cos\theta = \Omega \cdot \mathbf{u}/|\mathbf{u}|$, $0 \le \theta \le \pi$. Finally, the collision kernel B can be calculated when the intermolecular potential is known, see details in §2.1.

The BE is more complicated than the NSF equations, not only because the VDF is defined in six-dimensional phase-space (three dimensional spatial space and three dimensional velocity space), but also because of its high dimensional collision operator (fivefold integral with three dimensions in velocity space and two dimensions in a unit sphere). Therefore, it is highly desirable to have macroscopic equations like the NSF ones. To eliminate the microscopic velocity variables, moment equations from the BE should be considered. Multiplying Eq. (1.12) by 1, $\mathbf{v}$, and $|\mathbf{v}|^2$, and integrating the resulting equations with respect to the molecular velocity $\mathbf{v}$, one gets Eqs. (1.1)–(1.3). However, these equations are not closed because expressions for shear stress and heat flux are not known.

[2] The quantum statistics is not considered. The classical mechanics works when the mean distance between molecules is much larger than the thermal de Broglie wavelength $\lambda_B = \hbar/\sqrt{mk_BT/2\pi}$, i.e., $n\lambda_B^3 \ll 1$, with $\hbar$ being the Planck constant divided by 2π. For molecules, the thermal de Broglie wavelength is very small at room temperature. The quantum BE will be presented and solved in Chapter 6.

A traditional way to obtain expressions for the shear stress and heat flux is the Chapman-Enskog (CE) method [5], where the VDF is obtained by successive approximation, i.e., $f = f^{(0)} + f^{(1)} + f^{(2)} + \cdots$. The VDF obtained from the zeroth order expansion is the equilibrium (Maxwellian) distribution function f_{eq},

$$f = f_{eq} \equiv n \left(\frac{m}{2\pi k_B T} \right)^{3/2} \exp \left[-\frac{m(\mathbf{v} - \mathbf{V})^2}{2k_B T} \right], \tag{1.16}$$

and the corresponding set of macroscopic equations are the Euler equations (Eqs. (1.1)–(1.3) with $P_{ij} = nk_B T\delta_{ij}$ and $\mathbf{q} = 0$). The VDF from the first order expansion is

$$f = f_{eq} \left[1 - \frac{2mK_t}{5nk_B^2 T} \left(\frac{mv_r^2}{2k_B T} - \frac{5}{2} \right) v_{ri} \frac{\partial \ln T}{\partial x_i} - \frac{m\mu}{nk_B^2 T^2} \frac{\partial V_i}{\partial x_j} \left(v_{ri} v_{rj} - \frac{v_r^2}{3} \right) \delta_{ij} \right],$$

where $\mathbf{v}_r = \mathbf{v} - \mathbf{V}$ is the peculiar velocity. The corresponding macroscopic equations are the NSF equations Eqs. (1.1)–(1.5), where the shear viscosity is given by[3]

$$\mu = \frac{5\sqrt{\pi m k_B T}}{8D}, \quad D = \left(\frac{m}{4k_B T} \right)^4 \int_0^\infty u^7 \sigma_\mu \exp \left(-\frac{mu^2}{4k_B T} \right) du, \tag{1.17}$$

with $\sigma_\mu = 2\pi \int_0^\pi B \sin^3 \theta d\theta / |u|$ being the viscosity cross-section, and the thermal conductivity is given by

$$K_t = \frac{15}{4} \frac{k_B}{m} \mu. \tag{1.18}$$

The key success of the CE expansion is the recovery of the NSF equations from the first principle. The second and third expansions lead to the Burnett and super-Burnett equations [5, 6], respectively. In the slip flow regime, the Burnett equations are more accurate than the NSF equations [7, 8]. However, due to its intrinsic instability at large Knudsen numbers [9], it seems that the Burnett and super-Burnett equations are not widely used nowadays.

Another way to obtain the closed macroscopic equations is proposed by Grad [10]. In his method, the state of a gas is described by a set of moments (for instance, ρ, $\mathbf{V}$, T, $\mathbf{P}$, and $\mathbf{q}$ are used in Grad 13 method) and the corresponding moment equations are closed by expanding f in Hermite polynomials and assuming this VDF only depends

[3] Only the first-order term of the Sonine-polynomials is used to calculate the shear viscosity [5], as the rest of the terms are negligible. For example, they make zero contribution to the shear viscosity for Maxwell molecules, and only make a 2% contribution for hard sphere molecules.

on these moments. Generally speaking, when the rarefied effects becomes significant, the number of moments should be increased. For example, for normal shock waves with Mach number up to 1.65 and 1.887, at least 13 and 21 moments are needed to capture the shock profiles [11]. Contrary to the Burnett and super-Burnett equations, research into the Grad moment equations remains active and significant progress has been made. For instance, the regularised 13 moment equations have been successfully applied to the lid-driven flow up to $Kn \sim 0.7$ [12] and the regularised 26 moment equations are applied to micro-channel flows in the transition regime [13].

1.1.2 Numerical methods for the Boltzmann equation

For moderately or highly rarefied gases, a numerical solution of the BE is necessary. However, the multidimensional structure of the collision operator poses a real challenge to solve the BE numerically. From a historical point of view, realistic numerical computations are based on probabilistic methods. Well-known examples are the direct simulation Monte Carlo (DSMC) methods developed by Bird and Nanbu [14, 15]. Despite their stochastic nature, DSMC solutions converge to those of the BE for monatomic gases in the limit of vanishing discretization and stochastic errors [16]. The main advantages of the DSMC method are: (i) the simulated particles in DSMC represent a large number of real molecules so that the number of operations is greatly reduced; (ii) it does not need artificial boundaries in the velocity space; (iii) particles concentrate in regions where the VDF is not small so that computer memory is not wasted. These properties make the DSMC very efficient for high-speed rarefied gas flows. However, DSMC becomes time-consuming if the flow is in the continuum-fluid regime, especially when the Mach number is small. Note that recently developed information-preservation (IP) DSMC method [17–19], hybrid continuum/particle approaches [20–22], and the low-noise DSMC method [23–25] have partly eased these difficulties.

Contrasting with DSMC, there are numerical methods that solve the Boltzmann collision operator deterministically, including the discrete velocity model (DVM), the finite-difference method, and the Fourier spectral method. A brief introduction to these methods is given below.

In 1989, Goldstein, Sturtevant, and Broadwell developed the first version of DVM [26].

They used a fixed set of discrete velocities to approximate the continuous velocity space, and constructed a discrete collision mechanics on the velocity nodes in order to preserve the main physical properties of the collision operator. However, a large amount of computational resources are wasted since the post-collision velocities must lie on the velocity nodes. Bobylev, Palczewski, and Schneider considered the direct approximation of the collision operator and demonstrated that the computational cost is of the order $O(N^7)$, while the formal accuracy is less than first order in velocity, where N is the number of grid points in each velocity direction [27]. The high computational cost drove researchers to consider mixed deterministic and stochastic methods [28–30]. Recently, Morris, Varghese, and Goldstein used an interpolation shceme to map the post-collision velocities back onto the velocity nodes and adopted the Monte-Carlo scheme to pick up the collision pairs; they found that the performance of DVM is comparable to (or even faster than) DSMC in normal shock wave simulations [31]. To improve the accuracy, Tcheremissine [32–34] replaced the Monte-Carlo scheme by the integration method from the number theory, where 8-dimensional integrating grids were generated on the basis of Korobov sequence. Also note that Mouhot, Pareschi, and Rey constructed a DVM for hard sphere molecules with computational cost $O(\overline{N}^3 N^3 \log N)$, $\overline{N} \ll N$ [35].

The kinetic theory group in Kyoto University has developed a family of finite difference methods for the BE. In 1989, Sone, Ohwada, and Aoki proposed an accurate numerical kernel method for computing the linearized collision operator for hard sphere molecules [36]. Four years later, Ohwada extended the numerical kernel method to calculate the full nonlinear collision operator for hard sphere molecules [37, 38]. In 2001, the numerical kernel method was applied by Kosuge, Aoki, and Takata to the BE for a binary gas mixture of hard sphere molecules [39]. This method seems to be restricted to the hard sphere molecules, and usually only one-dimensional problems such as normal shock flow and Fourier heat flow between two parallel plates where the VDF has a cylindrical symmetry are considered. In this way, the VDF is a function of the longitudinal and transversal velocities and the number of velocity nodes and the computational cost are dramatically reduced. Recently, this method has been applied to the Poiseuille and thermal creep flows in two-dimensional spatial space [40].

In 1996, inspired by the pioneering work of Bobylev using Fourier transform tech-

niques in the analysis of the BE for Maxwell molecules [41], Pareschi and Perthame proposed a spectral method to approximate the collision operator for a class of collision kernels, where the computational cost is of the order $O(N^6)$ [42]. One year later, Bobylev and Rjasanow developed a numerical method to solve the collision operator for Maxwell molecules with computational cost of the order $O(N^4)$ [43]. This is in general the fastest algorithm to date. However, its formal accuracy is only of the order $O(N^{-1/2})$. For one-dimensional problems such as Fourier heat flow and normal shock flow, Watchararuangwita, Grigoriev, and Meleshko observed that cylindrical symmetry allows a reduction of the computational cost to the order $O(N^2 \log N)$ by employing the fast Fourier transform (FFT) in the longitudinal velocity direction and Hankel transform in the transverse direction [44]. In 1999, based on the Carleman-like representation, Bobylev and Rjasanow were able to solve the collision operator for hard sphere molecules with a computational cost $O(N^6 \log N)$ and formal accuracy $O(N^{-2})$, using generalized Radon and X-ray transforms [45]. A faster numerical method with a computational cost $O(N^6)$ and formal accuracy $O(N^{-2})$ has also been proposed for the variable hard sphere (VHS) model by Ibragimov and Rjasanow [46]. Based on these Fourier spectral methods, Gamba and Tharkabhushanam developed a spectral-Lagrangian method both for elastic and inelastic collision operators and investigated space-inhomogeneous problems, i.e., one-dimensional Fourier heat flow and shock flow [47, 48].

In 2000, Pareschi and Russo developed an algorithm to solve the collision operator for the VHS model with a computational cost of $O(N^6)$ [49]. The approximation of the collision operator is spectrally accurate for smooth VDFs, where the error decay rate is faster than any polynomial, i.e., faster than $\mathrm{O}(N^{-r})$ for any $r > 0$. The method has been applied to space-inhomogeneous problems in two-dimensional velocity space [50]. Six years later, by means of the Carleman-like representation, Mouhot and Pareschi developed a faster spectral method (FSM) with a computational cost $O(M^2 N^3 \log N)$ and spectral accuracy, where M is the number of grid points in the discretizations of polar and azimuthal angles [1]. In practical calculations, $M \ll N$, say, $M = 4 \sim 6$ [1, 51]. The FSM has been applied to space-inhomogeneous problems in two-dimensional (2D) velocity space as well as quantum collision operators [51–54].

1.2 Objectives

The direct numerical simulation of the BE is indispensable in the study of rarefied gas dynamics. In this thesis, we aim to develop an accurate and efficient deterministic numerical scheme to solve the BE. Specifically, we focus on the fast algorithm to calculate the Boltzmann collision operator. From the introduction in the previous section, it seems that the FSM is the best one among all the deterministic numerical methods, in terms of the accuracy and computational cost. Compared to the VHS model where the collision kernel is isotropic (independent of the deflection angle), this method works only for hard sphere molecules. Therefore, one of the key objective here is to design new collision kernels which will extend the applicability of the FSM.

Since the FSM has only been applied to BE with single-species molecules, we try to extend it to a binary mixture of monoatomic gases. We will also extend the FSM to solve the quantum BE, which has applications in ultra-cold dilute quantum gases.

Even with FSM, the computational cost of the BE is high. Therefore, we will check the accuracy of kinetic models by comparing their solutions with the BE, aiming to identifying the flow regimes where the kinetic collision operators can be used to replace the complicated Boltzmann collision operator.

1.3 Thesis Outline and Key Developments

In Chapter 2, we solve the BE for single-species monoatomic gas by the FSM. The algorithm for the implementation of FSM is presented in details, and the accuracy of the FSM is evaluated by comparing numerical solutions with analytical results for Maxwell molecules. Good agreements with the experiment and other numerical schemes are also observed in space-inhomogeneous problems such as the shock waves, planar Couette, Fourier, and force-driven Poiseuille flows. The key developments are:

- Novel anisotropic collision kernels are designed, extending the applicability of the FSM to all inverse power-law potentials except the Coulomb potential. Also, special collision kernels are designed for molecules interacting through the Lennard-Jones (LJ) and rigid attracting potentials, by observing that the corresponding cross-sections can be well approximated by superpositions of several single-term

cross-sections. Nevertheless, the numerical simulations are as fast as that for a single-term collision kernel.

- In the calculation of the kernel mode, the integration in a unit sphere is approximated by the Gauss-Legendre quadrature, instead of the trapezoidal rule. Better accuracy is achieved for the same number of discrete polar and azimuthal angles.

- Since the FSM conserves mass and approximates momentum and energy with spectral accuracy, we use the method of Lagrangian multipliers to correct the momentum and energy. While it ensures conservation, the Lagrangian multiplier method does not affect accuracy of the FSM.

In Chapter 3, we apply the FSM to the linearised BE and solves the Poiseuille and thermal creep flows in both one- and two-dimensional space with the Knudsen number up to 10^6. At large Kn, the singular behaviour in the VDF poses a big challenge for the numerical solution of the BE. This problem is solved by introducing special forms of velocity discretisation and multi-resolution scheme in the frequency space, which makes the accuracy of FSM comparable to those from the Kyoto Kinetic Group and the efficiency much better than the low-noise DSMC (which is the fastest DSMC method for flows with small velocities).

As the application of FSM, various interesting problems are solved in Chapter 4. A new kinetic model, which has the ability to reduce its difference to the Boltzmann collision operator, is introduced. The accuracy of the kinetic model equations is checked by comparing their solutions with those from the BE.

The FSM is extended to solve the BE for two-species monoatomic gases in Chapter 5 and the quantum BE for Fermi gases in Chapter 6.

In Chapter 7, we consider the collective oscillation of quantum gases confined by external harmonic and Gaussian potentials. We compare the numerical results with the experiments, demonstrating the applicability of quantum BE in describing the collective behaviour of quantum Fermi gas.

The key findings of this research presented in this thesis and discussion of future work based on it, is summerised in Chapter 8.

1.4 Published papers

The work from this thesis has contributed to the following peer-reviewed papers:

1. Lei Wu, Craig White, Thomas J. Scanlon, Jason M. Reese, and Yonghao Zhang, Deterministic numerical solutions of the space-inhomogeneous Boltzmann equation using the fast spectral method, *Journal of Computational Physics*, 250:27-52, 2013.

2. Lei Wu and Yonghao Zhang. Applicability of the Boltzmann equation for a two-dimensional Fermi gas, *Physical Review A*, 85:045601, 2012.

3. Lei Wu and Yonghao Zhang. Numerical investigation of the radial quadrupole and scissors modes in trapped gases, *Europhysics Letters*, 97:16003, 2012.

4. Lei Wu, Jianping Meng, and Yonghao Zhang. Kinetic modelling of the quantum gases in the normal phase, *Proceedings of the Royal Society A-Mathematical Physics and Engineering Sciences*, 468:1799-1823, 2012.

5. Jianping Meng, Lei Wu, Jason M. Reese, and Yonghao Zhang, Assessment of the ellipsoidal-statistical Bhatnagar-Gross-Krook model for force-driven Poiseuille flows, *Journal of Computational Physics*, 251:383-395, 2013.

Chapter 2

Fast spectral method for monoatomic gas

In this Chapter, we first show how to recover the shear viscosity when special forms of collision kernels are used. Second, we present the detailed calculation of the spectral approximation of the collision operator and check the accuracy of the FSM by comparing the numerical results with analytical solutions for Maxwell molecules. Third, the relax-to-equilibrium process of different collision kernels with the same value of shear viscosity is compared and the use of special collision kernels is justified. Fourth, an iteration scheme is used to find steady solutions of the space-inhomogeneous problems.

2.1 Collision kernel suitable for the fast spectral method

The collision kernel $B(\cos\theta, |\mathbf{u}|)$ in Eq. (1.13) is at the heart of the collision operator. It is always non-negative, and depends on the modulus of the relative velocity and the deflection angle. For hard sphere molecules, the deflection angle is determined through $b_a = d\cos(\theta/2)$, where b_a is the aiming distance and d is the molecular diameter. Hence the differential cross-section, defined as

$$\sigma = \frac{b_a |db_a|}{\sin\theta |d\theta|}, \tag{2.1}$$

is $d^2/4$. The collision kernel, which is a product of the relative collision velocity and the differential cross-section, is $B = |\mathbf{u}|\sigma = |\mathbf{u}|d^2/4$. For a general spherically symmetrical intermolecular potential $\phi(r)$, the deflection angle is ([5], p.170; [14], p.37)

$$\theta(b, |\mathbf{u}|) = \pi - 2\int_0^{W_1} \left[1 - W^2 - \frac{4\phi(r)}{m|\mathbf{u}|^2}\right]^{-1/2} dW, \tag{2.2}$$

where $W = b_a/r$ and W_1 is the positive root of the term in the brackets.

2.1.1 Power-law potentials

The inverse power-law potential is $\phi(r) = \kappa/(\eta - 1)r^{\eta-1}$, which is called hard and soft potentials when $\eta > 5$ and $\eta < 5$, respectively. Maxwell molecules have the potential with $\eta = 5$ and the Coulomb potential has $\eta = 2$. The collision kernel is a power-law function of the relative velocity:

$$B = \frac{b_a|db_a|}{\sin\theta|d\theta|}|\mathbf{u}| \equiv c_\alpha(\theta)|\mathbf{u}|^\alpha, \quad \alpha = \frac{\eta - 5}{\eta - 1}. \tag{2.3}$$

It can be shown that $c_\alpha(\theta)$ approaches to $\theta^{(\alpha-5)/2}$ at the grazing collision limit $\theta \to 0$. This indicates that the total cross-section $\int \sigma d\Omega$ is infinite. Although the global existence and rapid relax-to-equilibrium of the classical solutions has been proven [55], a finite cutoff is introduced in numerical simulations using particle methods. One way to eliminate the infinity is to cut off $c_\alpha(\theta)$, i.e., set $c_\alpha(\theta) = 0$ when θ is smaller than a fixed value of angle, or equivalently, when b_a is larger than a fixed value of distance. This is justified by the fact that grazing collisions only lead to small changes of the system state. Another prevalent way to simplify the collision kernel is to replace $c_\alpha(\theta)$ with the constant C_α, yielding the well-known VHS model in DSMC [14]:

$$B = C_\alpha|\mathbf{u}|^\alpha, \tag{2.4}$$

where the constant C_α is empirically determined by equating the shear viscosities of the BE when the collision kernels are given by Eq. (2.3) and Eq. (2.4), respectively. Accordingly, we have

$$C_\alpha = \frac{3}{4}\left(\frac{2\kappa}{m}\right)^{2/(\eta-1)} A_2(\eta), \tag{2.5}$$

with the numerical factor $A_2(\eta) = \int_0^\infty \sin^2\theta W_0 dW_0$ and $W_0 = b_a(m|u|^2/2\kappa)^{1/(\eta-1)}$ [14]. Note that in the VHS model, the shear viscosity and temperature have the following relation:

$$\mu \propto T^\omega, \quad \omega = \frac{\eta+3}{2(\eta-1)}. \tag{2.6}$$

In the VHS model, the differential cross-section $\sigma = C_\alpha|\mathbf{u}|^{\alpha-1}$ is independent of the deflection angle. This model is widely used in DSMC, and the isotropic cross-section makes DSMC easy and effective to implement when $\alpha \geq 0$. For other numerical methods to solve the collision operator efficiently, it may be easier to include the θ-dependent collision kernel and the total cross-section does not have to be finite.

To achieve the maximum efficiency in the numerical approximation of the Boltzmann collision operator, special forms of the collision kernel are needed. For example, Mouhot and Pareschi [1] suggested the following anisotropic collision kernel:

$$B = C'_\alpha \sin^{\alpha-1}\left(\frac{\theta}{2}\right)|\mathbf{u}|^\alpha, \tag{2.7}$$

where C'_α is a constant. This special θ-dependent collision kernel not only enables the development of the FSM for computing the collision operator deterministically, but also mimics the growth trend of the collision kernel when decreasing the deflection angle. Like the VHS model in DSMC, the constant C'_α should be determined by equating the shear viscosities of the BE when the collision kernels are given by Eq. (2.3) and Eq. (2.7), respectively, yielding

$$C'_\alpha = \frac{(\alpha+3)(\alpha+5)}{24}C_\alpha. \tag{2.8}$$

Note that for hard sphere molecules ($\alpha = 1$), the VHS collision kernel and the collision kernel (2.7) are exactly the same.

We find that the collision kernel (2.7) can be extended to the following general form:

$$\begin{aligned} B &= C''_{\alpha,\gamma} \sin^{\alpha+\gamma-1}\left(\frac{\theta}{2}\right)\cos^{-\gamma}\left(\frac{\theta}{2}\right)|\mathbf{u}|^\alpha, \\ C''_{\alpha,\gamma} &= \frac{\Gamma[(7+\alpha)/2]}{6\Gamma[(3+\alpha+\gamma)/2]\Gamma(2-\gamma/2)}C_\alpha, \end{aligned} \tag{2.9}$$

where Γ is the gamma function. The additional parameter γ introduces plenty of

flexibility, not only to extend the applicability of the FSM to all inverse power-law potentials except the Coulomb potential, but also to recover the correct ratio between coefficients of shear viscosity and diffusion.

It will be interesting to compare our collision kernel with that of the VSS model. For the VSS model in DSMC, the aiming distance b_a and the molecular diameter d have the relation $b_a = d\cos^{\gamma'}(\theta/2)$ (when $\gamma' = 1$ it turns to the VHS model), so that the VSS collision kernel is related to the deflection angle as $\cos^{2\gamma'-2}(\theta/2)$, i.e., it is B a function of the deflection angle. Therefore, one may call the collision kernels (2.7) and (2.9) as the generalized VSS collision kernel.

2.1.2 Lennard-Jones potential

The power-law intermolecular potential is a phenomenological model. In reality, the potential between monatomic gas molecules is better described by the LJ potential. Here we consider argon, where the LJ potential is

$$\phi(r) = 4\epsilon\left[\left(\frac{d_{LJ}}{r}\right)^{12} - \left(\frac{d_{LJ}}{r}\right)^{6}\right], \tag{2.10}$$

with a potential depth $\epsilon = 119.18k_B$, $d_{LJ} = 3.42 \times 10^{-10}m$, and r being the distance between two molecules. For other molecules, the values of ϵ and d_{LJ} may be different. However, the following analysis applies to all LJ potentials of the form in Eq. (2.10).

When the potential is known, the shear viscosity can be calculated by Eq. (1.17) with the help of Eqs. (2.1) and (2.2). The numerical results for the parameter D are shown in Figure 2.1. A more accurate calculation may be found in Ref. [56].

Unlike the power-law potential, the shear viscosity is not a single power-law function of the temperature over the whole temperature range [5]. Only when the temperature does not vary too much could D be a single power-law function of T. For instance, when k_BT/ϵ is large (or small), the repulsive (or attractive) part of the force is dominant, and $D \propto T^{-1/6}$ (or $D \propto T^{-1/3}$). Also, when $2 < k_BT/\epsilon < 3$, we have $D \propto T^{-0.31}$, see Figure 2.1. In these regions, the VHS model can be successfully implemented in DSMC, producing satisfactory results. However, a single power-law fit is not adequate over a wider temperature range. To tackle this problem, the generalized VHS model of Hassan

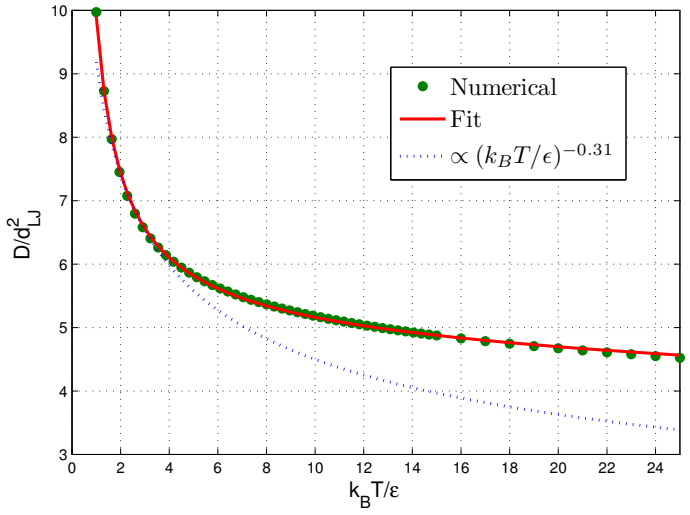

Figure 2.1: D/d_{LJ}^2 vs k_BT/ϵ for the LJ potential, see Eq. (1.17). The solid line is a nonlinear least squares fit (with 95% confidence bounds) of D/d_{LJ}^2 as a function of k_BT/ϵ by the sum of three power-law functions: $D/d_{LJ}^2 = b_1(k_BT/\epsilon)^{-0.4} + b_2(k_BT/\epsilon)^{-0.45} + b_3(k_BT/\epsilon)^{-0.5}$, with $b_1 = 407.4, b_2 = -811.9$, and $b_3 = 414.4$.

and Hash [57], the variable sphere model of Matsumoto [58], and the generalized soft sphere model of Fan [59], have been proposed and tested in DSMC.

Here we employ the concept of the generalized VHS model to construct the collision kernel that is suitable for the FSM to solve the collision operator. According to Eq. (1.17), we observe that the special form of D given by the fit function in Figure 2.1 can be recovered if the collision kernel takes the form of

$$B = \frac{d_{LJ}^2}{32\pi} \sum_{j=1}^{3} \frac{(m/4\epsilon)^{(\alpha_j-1)/2} b_j}{\Gamma(\frac{3+\alpha_j}{2})} \sin^{\alpha_j-1}\left(\frac{\theta}{2}\right) |\mathbf{u}|^{\alpha_j}, \tag{2.11}$$

where $\alpha_1 = 0.2, \alpha_2 = 0.1$, $\alpha_3 = 0$, and the values of b_j are shown in Figure 2.1.

For argon with $\epsilon = 119.18k_B$, the fit in Figure 2.1 covers the temperature range from 120K to 3000K, while the VHS model with $\mu \propto T^{0.81}$ (dotted line) works only when 240K$< T <$360K. For wider temperature range, more terms with different values of α_j and b_j may be needed. We note that, no matter how many terms are added (as long as $\alpha_j > -1$), the computational time of the corresponding collision operator will not increase. The reason for this will be discussed at the end of §2.3.2. In the following, if the LJ potential is not specified, the shear viscosity of argon is proportional to $T^{0.81}$, that is, the collision kernel is given by Eq. (2.7) or Eq. (2.9) with $\alpha = 0.38$.

2.1.3 Sutherland's molecular model

For a gas whose molecules are rigid attracting spheres, its shear viscosity is given by the Sutherland formula:

$$\mu = \frac{5\sqrt{\pi m k_B T}}{16\sigma_{T,\infty}} \frac{T}{T + T_r}, \tag{2.12}$$

where T_r is a reference temperature and $\sigma_{T,\infty}$ is the total cross-section in the limiting case of infinite relative velocity $|u|$. This formula reproduces the experimental data for many real gases over a considerable range of temperature [5, 14].

The Sutherland formula for shear viscosity can be recovered if we use the following superposition of the modified collision kernels

$$B = C''_{1,\gamma_1} \sin^{\gamma_1}\left(\frac{\theta}{2}\right) \cos^{-\gamma_1}\left(\frac{\theta}{2}\right) |u| + C''_{-1,\gamma_2} \sin^{\gamma_2 - 2}\left(\frac{\theta}{2}\right) \cos^{-\gamma_2}\left(\frac{\theta}{2}\right) |u|^{-1}, \tag{2.13}$$

with

$$\begin{aligned} 8\pi C''_{1,\gamma_1} \Gamma\left(2 - \frac{\gamma_1}{2}\right) \Gamma\left(2 + \frac{\gamma_1}{2}\right) &= 2\sigma_{T,\infty}, \\ 8\pi C''_{-1,\gamma_1} \Gamma\left(2 - \frac{\gamma_2}{2}\right) \Gamma\left(1 + \frac{\gamma_2}{2}\right) &= 2\sigma_{T,\infty} T_r \frac{4k_B}{m}, \end{aligned} \tag{2.14}$$

where special values of γ_1 and γ_2, i.e., $2 > \gamma_1 = \gamma_2 > 0$, can make the FSM as fast as that for the single-term collision kernel (2.7) or (2.9). Detailed discussions will be given at the end of §2.3.2.

2.2 Normalization

For practical calculations, it is convenient and useful to introduce dimensionless variables. The following dimensionless variables are introduced:

$$\begin{aligned} &\widetilde{f} = \frac{v_m^3}{n_0} f, \quad \widetilde{\mathbf{x}} = \frac{\mathbf{x}}{\ell}, \quad (\widetilde{\mathbf{v}}, \widetilde{\mathbf{V}}) = \frac{(\mathbf{v}, \mathbf{V})}{v_m}, \quad \widetilde{t} = \frac{v_m}{\ell} t, \quad \widetilde{\mathbf{a}} = \frac{\ell}{v_m^2} \mathbf{a}, \\ &\widetilde{n} = \frac{n}{n_0}, \quad \widetilde{T} = \frac{T}{T_0}, \quad \widetilde{\mathbf{P}} = \frac{\mathbf{P}}{n_0 k_B T_0}, \quad \widetilde{\mathbf{q}} = \frac{\mathbf{q}}{n_0 k_B T_0 v_m}, \end{aligned} \tag{2.15}$$

where n_0 is the average molecular number density, ℓ is the characteristic length, $v_m = \sqrt{2k_B T_0/m}$ is the most probable molecular speed with T_0 being the reference temperature.

Under these normalizations, the BE with the collision kernel (2.9) takes the following form

$$\frac{\partial \widetilde{f}}{\partial \widetilde{t}} + \widetilde{\mathbf{v}} \cdot \frac{\partial \widetilde{f}}{\partial \widetilde{\mathbf{x}}} + \widetilde{\mathbf{a}} \cdot \frac{\partial \widetilde{f}}{\partial \widetilde{\mathbf{v}}} = \frac{1}{Kn'} \int \int \sin^{\alpha+\gamma-1}\left(\frac{\theta}{2}\right) \cos^{-\gamma}\left(\frac{\theta}{2}\right) |\widetilde{\mathbf{u}}|^{\alpha} \times [\widetilde{f}(\widetilde{\mathbf{v}}'_*)\widetilde{f}(\widetilde{\mathbf{v}}') - \widetilde{f}(\widetilde{\mathbf{v}}_*)\widetilde{f}(\widetilde{\mathbf{v}})] d\Omega d\widetilde{\mathbf{v}}_*, \tag{2.16}$$

where the normalized Knudsen number is

$$Kn' = \frac{64\sqrt{2}^{\alpha}}{5} \Gamma\left(\frac{\alpha+\gamma+3}{2}\right) \Gamma\left(2-\frac{\gamma}{2}\right) Kn, \tag{2.17}$$

with

$$Kn = \frac{\mu}{n_0 \ell} \sqrt{\frac{\pi}{2mk_BT_0}} \tag{2.18}$$

being the unconfined Knudsen number. Here, $(\mu/n_0)\sqrt{\pi/2mk_BT_0}$ is the unconfined mean free path at the reference temperature T_0 and molecular number density n_0, which is $15\pi/2(7-2\omega)(5-2\omega)$ times larger than the equilibrium mean free path defined in Eq. (4.52) in Ref. [14].

For the LJ potential, when the collision kernel takes the form of Eq. (2.11), the term $\sin^{\alpha+\gamma-1}(\theta/2)\cos^{-\gamma}(\theta/2)|\widetilde{\mathbf{u}}|^{\alpha}/Kn'$ in Eq. (2.16) should be replaced by

$$\frac{5\sum_{j=1}^{3} b_j (k_BT_0/2\epsilon)^{(\alpha_j-1)/2} \sin^{\alpha_j-1}(\theta/2)|\widetilde{\mathbf{u}}|^{\alpha_j}/\Gamma(\frac{\alpha_j+3}{2})}{64\sqrt{2}Kn\sum_{j=1}^{3} b_j (k_BT_0/\epsilon)^{(\alpha_j-1)/2}}. \tag{2.19}$$

A similar expression can be given for the rigid attracting potential.

Considering the above normalization scheme, the normalized macroscopic quantities are related to the normalized VDF as follows:

$$\begin{aligned} \widetilde{n} &= \int \widetilde{f} d\widetilde{\mathbf{v}}, \quad \widetilde{\mathbf{V}} = \frac{1}{\widetilde{n}} \int \widetilde{\mathbf{v}} \widetilde{f} d\widetilde{\mathbf{v}}, \quad \widetilde{T} = \frac{2}{3\widetilde{n}} \int |\widetilde{\mathbf{v}} - \widetilde{\mathbf{V}}|^2 \widetilde{f} d\widetilde{\mathbf{v}}, \\ \widetilde{P}_{ij} &= 2\int (\widetilde{v}_i - \widetilde{V}_i)(\widetilde{v}_j - \widetilde{V}_j) \widetilde{f} d\widetilde{\mathbf{v}}, \quad \widetilde{q}_i = \int |\widetilde{\mathbf{v}} - \widetilde{\mathbf{V}}|^2 (\widetilde{v}_i - \widetilde{V}_i) \widetilde{f} d\widetilde{\mathbf{v}}. \end{aligned} \tag{2.20}$$

2.3 Fast spectral method for the collision operator

The numerical approximation of the Boltzmann collision operator by the FSM is now introduced and discussed. For its main properties we refer to the original paper [1].

Some detailed calculations are presented below because different sources in the literature give different results for the kernel mode [1, 51, 54]. For simplicity, the tildes on normalized quantities will be omitted hereafter. We first consider the simple case where the collision kernel is given by Eq. (2.9).

2.3.1 Carleman-like representation

We rewrite the collision operator using the Carleman-like representation. With the basic identity $2\int_{\mathbb{R}^3}\delta(2\mathbf{y}\cdot\mathbf{u}+|\mathbf{y}|^2)f(\mathbf{y})d\mathbf{y} = |\mathbf{u}|\int_{\mathbb{S}^2} f(|\mathbf{u}|\Omega-\mathbf{u})d\Omega$, the collision operator on the right hand side of Eq. (2.16) can be rewritten as

$$\begin{aligned}
Q(f,f_*) =& \frac{1}{Kn'}\int_{\mathbb{R}^3}\int_{\mathbb{S}^2}\Theta|\mathbf{u}|[f(\mathbf{v}'_*)f(\mathbf{v}')-f(\mathbf{v}_*)f(\mathbf{v})]d\Omega d\mathbf{v}_* \\
=& \frac{1}{Kn'}\int_{\mathbb{R}^3}\int_{\mathbb{S}^2}\Theta|\mathbf{u}|\left[f\left(\mathbf{v}_*-\frac{|\mathbf{u}|\Omega-\mathbf{u}}{2}\right)f\left(\mathbf{v}+\frac{|\mathbf{u}|\Omega-\mathbf{u}}{2}\right)-f(\mathbf{v}_*)f(\mathbf{v})\right]d\Omega d\mathbf{v}_* \\
=& \frac{2}{Kn'}\int_{\mathbb{R}^3}\int_{\mathbb{R}^3}\Theta\delta(2\mathbf{y}\cdot\mathbf{u}\ +|\mathbf{y}|^2)\left[f\left(\mathbf{v}_*-\frac{\mathbf{y}}{2}\right)f\left(\mathbf{v}+\frac{\mathbf{y}}{2}\right)-f(\mathbf{v}_*)f(\mathbf{v})\right]d\mathbf{y}d\mathbf{v}_* \\
=& \frac{4}{Kn'}\int_{\mathbb{R}^3}\int_{\mathbb{R}^3}\Theta\delta(\mathbf{y}\cdot\mathbf{u}+|\mathbf{y}|^2)[f(\mathbf{v}_*-\mathbf{y})f(\mathbf{v}+\mathbf{y})-f(\mathbf{v}_*)f(\mathbf{v})]d\mathbf{y}d\mathbf{v}_* \\
=& \frac{4}{Kn'}\int_{\mathbb{R}^3}\int_{\mathbb{R}^3}\Theta\delta(\mathbf{y}\cdot\mathbf{z}\ )[f(\mathbf{v}+\mathbf{z})f(\mathbf{v}+\mathbf{y})-f(\mathbf{v}+\mathbf{y}+\mathbf{z})f(\mathbf{v})]d\mathbf{y}d\mathbf{z},
\end{aligned}$$

where $\Theta = \sin^{\alpha+\gamma-1}(\theta/2)\cos^{-\gamma}(\theta/2)\,|\mathbf{u}|^{\alpha-1}$.

Notice that in the above calculations we have used the transformations $\mathbf{y} = (|\mathbf{u}|\Omega-\mathbf{u})/2$ and $\mathbf{z} = \mathbf{v}_*-\mathbf{v}-\mathbf{y} = -\mathbf{u}-\mathbf{y}$. Therefore, the deflection angle θ satisfies

$$\cos\theta = \frac{\Omega\cdot\mathbf{u}}{|\mathbf{u}|} = \frac{-(\mathbf{y}-\mathbf{z})\cdot(\mathbf{y}+\mathbf{z})}{|\mathbf{y}+\mathbf{z}|^2} \overset{\mathbf{y}\perp\mathbf{z}}{=} \frac{|\mathbf{z}|^2-|\mathbf{y}|^2}{|\mathbf{y}|^2+|\mathbf{z}|^2},$$

which results in

$$\sin\left(\frac{\theta}{2}\right) = \frac{|\mathbf{y}|}{\sqrt{|\mathbf{y}|^2+|\mathbf{z}|^2}}, \quad \cos\left(\frac{\theta}{2}\right) = \frac{|\mathbf{z}|}{\sqrt{|\mathbf{y}|^2+|\mathbf{z}|^2}}. \tag{2.21}$$

Hence $\Theta = |\mathbf{y}|^{\alpha+\gamma-1}|\mathbf{z}|^{-\gamma}$ and the collision operator is simplified to

$$\begin{aligned}
Q(f,f_*) = \frac{4}{Kn'}\int_{\mathbb{R}^3}\int_{\mathbb{R}^3}&\delta(\mathbf{y}\cdot\mathbf{z})|\mathbf{y}|^{\alpha+\gamma-1}|\mathbf{z}|^{-\gamma} \\
&\times[f(\mathbf{v}+\mathbf{z})f(\mathbf{v}+\mathbf{y})-f(\mathbf{v}+\mathbf{y}+\mathbf{z})f(\mathbf{v})]d\mathbf{y}d\mathbf{z}.
\end{aligned} \tag{2.22}$$

2.3.2 Fourier-Galerkin spectral method

In the FSM, the VDF is periodised on the domain $\mathcal{D}_L = [-L, L]^3$. We adopt uniform grid points in the velocity space: $v_k(j_k) = 2j_kL/N_k$ with $k = 1, 2, 3$, where $j_k \in [-N_k/2, -N_k/2+1, \cdots, N_k/2-1]$ and N_k is the number of velocity grid points in the k-th velocity direction[1]. Suppose $\mathcal{B}_S$, a sphere of radius S centered at the origin, is the support of the VDF. Usually the minimum value $L = (3+\sqrt{2})S/2$ is chosen to avoid the aliasing error caused by the periodicity of the velocity VDF [49]. The VDF is then approximated by a truncated Fourier series,

$$f(\mathbf{v}) = \sum_{\mathbf{j}=-(N_1,N_2,N_3)/2}^{(N_1,N_2,N_3)/2-1} \hat{f}_{\mathbf{j}} \exp(i\xi_{\mathbf{j}} \cdot \mathbf{v}), \tag{2.23}$$

$$\hat{f}_{\mathbf{j}} = \frac{1}{(2L)^3} \int_{\mathcal{D}_L} f(\mathbf{v}) \exp(-i\xi_{\mathbf{j}} \cdot \mathbf{v}) d\mathbf{v}, \tag{2.24}$$

where $\mathbf{j} = (j_1, j_2, j_3)$, i is the imaginary unit, and $\xi_{\mathbf{j}} = \mathbf{j}\pi/L$ are the frequency components.

The collision operator (2.22) is also truncated, with the infinite region $\mathbb{R}^3$ replaced by the finite one $\mathcal{B}_R$, where the truncation radius R satisfies $R \geq \sqrt{2}S$ [1, 51]. Numerical analysis in Figure 2.4 reveals that, however, R cannot be larger than L.

Expanding the truncated collision operator in the truncated Fourier series, we find that the **j**-th mode of the truncated collision operator is related to the Fourier coefficient $\hat{f}$ of the VDF:

$$\widehat{Q}_{\mathbf{j}} = \sum_{\substack{\mathbf{l}+\mathbf{m}=\mathbf{j} \\ \mathbf{l},\mathbf{m}=-(N_1,N_2,N_3)/2}}^{(N_1,N_2,N_3)/2-1} \hat{f}_{\mathbf{l}} \hat{f}_{\mathbf{m}} [\beta(\mathbf{l}, \mathbf{m}) - \beta(\mathbf{m}, \mathbf{m})], \tag{2.25}$$

[1] For space-inhomogeneous problems, however, we use symmetrical velocity grids which does not pass zero, since this kind of velocity grids generally have better accuracy than the velocity girds passing zero when the grid numbers are the same, for example see [60].

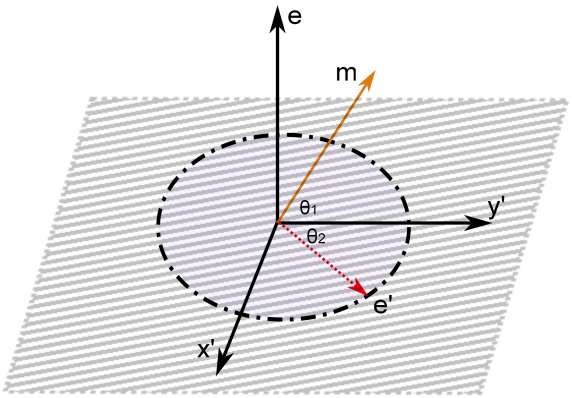

Figure 2.2: Demonstration of the integral with respect to $\mathbf{e}'$ used in the calculation of the kernel mode (2.26). When the vector $\mathbf{e}$ is fixed, $\mathbf{e}'$ is in the $x'y'$ plane perpendicular to $\mathbf{e}$. That is, it degenerates to a two-dimensional vector characterized by the polar angle θ_2 varying from 0 to 2π. Because of symmetry, we only consider the region $0 \le \theta_2 \le \pi$.

where $\mathbf{l} = (l_1, l_2, l_3)$, $\mathbf{m} = (m_1, m_2, m_3)$, and the kernel mode $\beta(\mathbf{l}, \mathbf{m})$ is simplified to

$$\begin{aligned}
\beta(\mathbf{l},\mathbf{m}) =& \frac{4}{Kn'} \int_{\mathcal{B}_R} \int_{\mathcal{B}_R} \delta(\mathbf{y}\cdot\mathbf{z}) |\mathbf{y}|^{\alpha+\gamma-1} |\mathbf{z}|^{-\gamma} \exp(i\xi_{\mathbf{l}}\cdot\mathbf{y} + i\xi_{\mathbf{m}}\cdot\mathbf{z}) d\mathbf{y} d\mathbf{z} \\
=& \frac{1}{Kn'} \int\int \delta(\mathbf{e}\cdot\mathbf{e}') \left[\int_{-R}^{R} |\rho|^{\alpha+\gamma} \exp(i\rho\xi_{\mathbf{l}}\cdot\mathbf{e}) d\rho \right] \\
& \qquad \times \left[\int_{-R}^{R} |\rho'|^{1-\gamma} \exp(i\rho'\xi_{\mathbf{m}}\cdot\mathbf{e}') d\rho' \right] d\mathbf{e}' d\mathbf{e} \\
=& \frac{1}{Kn'} \int_{\mathbb{S}^2} \phi_{\alpha+\gamma}(\xi_{\mathbf{l}}\cdot\mathbf{e}) \left[\int_{\mathbb{S}^2} \delta(\mathbf{e}\cdot\mathbf{e}') \phi_{1-\gamma}(\xi_{\mathbf{m}}\cdot\mathbf{e}') d\mathbf{e}' \right] d\mathbf{e}, \qquad (2.26)
\end{aligned}$$

with $\mathbf{e}, \mathbf{e}'$ being the unit vectors in the sphere $\mathbb{S}^2$, and

$$\phi_\delta(s) = 2 \int_0^R \rho^\delta \cos(\rho s)\, d\rho. \qquad (2.27)$$

Equation (2.26) can be simplified further. We construct a new Cartesian coordinate system, where the z' axis is parallel to $\mathbf{e}$, the y' axis is just the projection of vector $\mathbf{m}$ into the plane $e_\perp$ perpendicular to the z' axis, and the x' axis is in the plane $e_\perp$ and perpendicular to the y' axis, see Figure 2.2. Suppose the polar and azimuthal angles of $\mathbf{e}'$ in the new coordinate system are θ and $\pi/2 - \theta_2$, respectively, and the angle between the vector $\mathbf{m}$ and y'-axis is θ_1. Then, we have $\delta(\mathbf{e}\cdot\mathbf{e}') = \delta(\cos\theta)$ so that $\int_0^\pi g(\theta)\delta(\cos\theta)d\theta = g(\pi/2)$ for arbitrary function $g(\theta)$, $\xi_{\mathbf{m}}\cdot\mathbf{e}' = |\xi_{\mathbf{m}}|\cos\theta_1\cos\theta_2$, and

the kernel mode becomes

$$\begin{aligned}\beta(\mathbf{l},\mathbf{m}) &= \frac{1}{Kn'}\int_{\mathcal{S}^2}\phi_{\alpha+\gamma}(\xi_{\mathbf{l}}\cdot\mathbf{e})\left[\int_0^{2\pi}\int_0^{\pi}\delta(\cos\theta)\phi_{1-\gamma}(|\xi_{\mathbf{m}}|\cos\theta_1\cos\theta_2)d\theta d\theta_2\right]d\mathbf{e}\\ &= \frac{1}{Kn'}\int_{\mathcal{S}^2}\phi_{\alpha+\gamma}(\xi_{\mathbf{l}}\cdot\mathbf{e})\left[\int_0^{2\pi}\phi_{1-\gamma}(|\xi_{\mathbf{m}}|\cos\theta_1\cos\theta_2)d\theta_2\right]d\mathbf{e}\\ &= \frac{2}{Kn'}\int_{\mathcal{S}^2}\phi_{\alpha+\gamma}(\xi_{\mathbf{l}}\cdot\mathbf{e})\cdot\psi_{\gamma}(|\xi_{\mathbf{m}}|\cos\theta_1)d\mathbf{e},\end{aligned} \tag{2.28}$$

where

$$\psi_{\gamma}(s) = \int_0^{\pi}\phi_{1-\gamma}(s\cos\theta_2)d\theta_2 = 2\pi\int_0^{R}\rho^{1-\gamma}J_0(\rho s)d\rho, \tag{2.29}$$

with J_0 being the zeroth-order Bessel function.

Note that $\xi_{\mathbf{l}}(=\mathbf{l}\pi/L)$ and $\xi_{\mathbf{m}}(=\mathbf{m}\pi/L)$ in the integration (2.28) appear in two functions. If they also appear in two different functions in the final form of $\beta(\mathbf{l},\mathbf{m})$, Eq. (2.25) can be calculated effectively by the FFT-based convolution. The separation of $\mathbf{l}$ and $\mathbf{m}$ can be realised by calculating (2.28) approximately using the numerical quadrature method. Two different methods will be employed and compared:

- in the first method, $\beta(\mathbf{l},\mathbf{m})$ is calculated numerically in spherical coordinates by the trapezoidal rule. Suppose the polar and azimuthal angles of the unit vector $\mathbf{e}$ are θ and φ, respectively. We divide each region $0\le\theta\le\pi$ and $0\le\varphi\le\pi$ (for symmetry) into M sections, i.e., $\theta_p = p\pi/M$ and $\varphi_q = q\pi/M$ with $p,q = 1,2,\cdots,M$. Then the kernel mode (2.28) is approximated by

$$\beta(\mathbf{l},\mathbf{m}) \simeq \frac{4\pi^2}{Kn'M^2}\sum_{p,q=1}^{M-1,M}\phi_{\alpha+\gamma}(\xi_{\mathbf{l}}\cdot\mathbf{e}_{\theta_p,\varphi_q})\cdot\psi_{\gamma}\left\{\sqrt{|\xi_{\mathbf{m}}|^2-(\xi_{\mathbf{m}}\cdot\mathbf{e}_{\theta_p,\varphi_q})^2}\right\}\cdot\sin\theta_p. \tag{2.30}$$

- in the second method, $\beta(\mathbf{l},\mathbf{m})$ is approximated by a Gauss-Legendre quadrature of order M:

$$\beta(\mathbf{l},\mathbf{m}) \simeq \frac{4}{Kn'}\sum_{p,q=1}^{M}\omega_p\omega_q\phi_{\alpha+\gamma}(\xi_{\mathbf{l}}\cdot\mathbf{e}_{\theta_p,\varphi_q})\cdot\psi_{\gamma}\left\{\sqrt{|\xi_{\mathbf{m}}|^2-(\xi_{\mathbf{m}}\cdot\mathbf{e}_{\theta_p,\varphi_q})^2}\right\}\cdot\sin\theta_p, \tag{2.31}$$

  where θ_p (φ_q) and ω_p (ω_q) are the p (q)-th point and weight in the Gauss-Legendre quadrature with $\theta,\varphi\in[0,\pi]$, and $\mathbf{e}_{\theta_p,\varphi_q} = (\sin\theta_p\cos\varphi_q, \sin\theta_p\sin\varphi_q, \cos\theta_p)$.

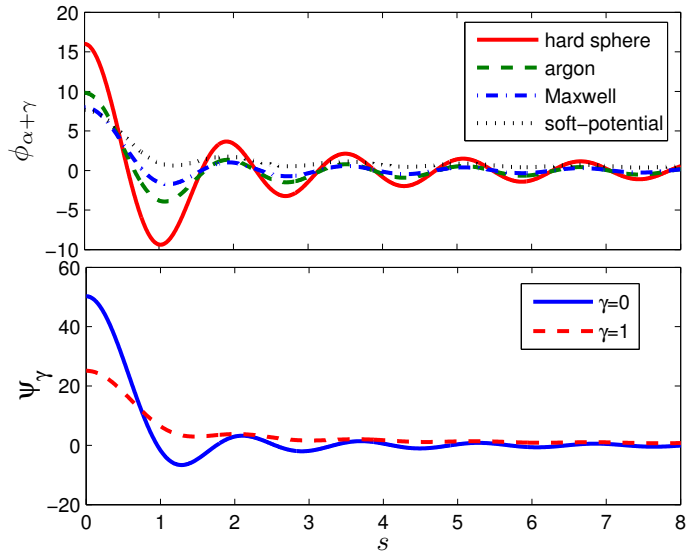

Figure 2.3: Profiles of $\phi_{\alpha+\gamma}$ when $\gamma = 0$ and ψ_γ according to Eqs. (2.27) and (2.29) when $R = 4$. Because of symmetry, the region $s < 0$ is not plotted. For the soft potential, we use $\alpha = -0.4$ and the shear viscosity is proportional to $T^{1.2}$.

For the LJ potential, when the normalised collision kernel is given by Eq. (2.19), γ in the function ψ_γ is zero. Meanwhile, one needs to replace the term $\phi_{\alpha+\gamma}(\xi_{\mathbf{l}} \cdot \mathbf{e}_{\theta_p,\varphi_q})/Kn'$ in Eq. (2.30) or Eq. (2.31) by

$$\frac{5\sum_{j=1}^{3} b_j (k_B T_0/2\epsilon)^{(\alpha_j-1)/2} \phi_{\alpha_j}(\xi_{\mathbf{l}} \cdot \mathbf{e}_{\theta_p,\varphi_q})/\Gamma(\frac{\alpha_j+3}{2})}{64\sqrt{2}Kn\sum_{j=1}^{3} a_j (k_B T_0/\epsilon)^{(\alpha_j-1)/2}}. \tag{2.32}$$

The analytical form of $\phi_{\alpha+\gamma}(s)$ can be obtained when $\alpha + \gamma$ is an integer. For instance, when $\gamma = 0$, for Maxwell molecules ($\alpha = 0$) and hard sphere molecules, we have

$$\phi_0(s) = \frac{2\sin(Rs)}{s}, \quad \phi_1(s) = \frac{2R\sin(Rs)}{s} - \frac{4\sin^2(Rs/2)}{s^2}, \tag{2.33}$$

while in the other cases, $\phi_{\alpha+\gamma}(s)$ and $\psi_\gamma(s)$ can be accurately calculated by Gauss-Legendre quadrature numerically. Figure 2.3 shows typical decaying-oscillating profiles of the two functions $\phi_{\alpha+\gamma}$ and ψ_γ, where the quasi-period of oscillation is about $2\pi/R$.

Note that in the VHS model, $-3 < \alpha \leq 1$. From Eq. (2.27) it follows that δ is restricted to the region $(-1, +\infty)$. Therefore, $\alpha + \gamma > -1$ and $1 - \gamma > -1$. In the original collision kernel proposed by Mouhot and Pareschi [1], $\gamma = 0$, so that α is restricted in the region $(-1, 1]$. This means that the original collision kernel cannot deal with general forms of soft potentials. In our modified collision kernel (2.9), if we

let $\gamma \to 2$, α can cover the whole region $(-3, 1]$, thus extending the applicability of the FSM to all inverse power-law potentials except the Coulomb potential.

2.3.3 Conservation enforcement

One of the drawbacks of the FSM, as with any spectral method for the approximation of the collision operator, is that it does not exactly conserve momentum and energy. To ensure the conservation of momentum and energy, we employ the method of Lagrangian multipliers [47, 48].

The procedure is simple and straightforward: after the collision operator Q is approximated, we construct Q^{new} by minimising the function $\sum_{\mathbf{j}}(Q_{\mathbf{j}} - Q^{new}_{\mathbf{j}})^2$ under the constraints $\sum_{\mathbf{j}} Q^{new}_{\mathbf{j}} = \sum_{\mathbf{j}} \mathbf{v} Q^{new}_{\mathbf{j}} = \sum_j |\mathbf{v}|^2 Q^{new}_{\mathbf{j}} = 0$, yielding

$$Q^{new} = Q - (\lambda_n + \lambda_{\mathbf{v}} \cdot \mathbf{v} + \lambda_e |\mathbf{v}|^2), \tag{2.34}$$

where the five Lagrangian multipliers satisfy

$$\begin{aligned}
\sum_{\mathbf{j}} Q &= \sum_j (\lambda_n + \lambda_{\mathbf{v}} \cdot \mathbf{v} + \lambda_e |\mathbf{v}|^2), \\
\sum_{\mathbf{j}} \mathbf{v} Q &= \sum_j \mathbf{v} (\lambda_n + \lambda_{\mathbf{v}} \cdot \mathbf{v} + \lambda_e |\mathbf{v}|^2), \\
\sum_{\mathbf{j}} |\mathbf{v}|^2 Q &= \sum_j |\mathbf{v}|^2 (\lambda_n + \lambda_{\mathbf{v}} \cdot \mathbf{v} + \lambda_e |\mathbf{v}|^2).
\end{aligned} \tag{2.35}$$

Since the errors for the momentum and energy in the FSM are spectrally small [1], the Lagrangian multipliers are very small. This is indeed confirmed in our numerical simulations. We also find that the Lagrangian multiplier method does not affect the accuracy of the FSM, while it ensures conservation of mass, momentum, and energy.

2.3.4 Detailed implementation

The detailed procedure to approximate the collision operator is now outlined. In the following, we assume Eq. (2.28) is approximated by the trapezoidal rule. First, the kernel modes should be pre-computed and stored. The storage of $\phi_{\alpha+\gamma}(\xi_{\mathbf{l}}, \theta_p, \varphi_q)$ and $\psi_\gamma(\xi_{\mathbf{m}}, \theta_p, \varphi_q)$ requires $2M(M-1)N_1N_2N_3$ units of compute memory. We also need

$N_1N_2N_3$ units of storage for

$$\phi_{loss} = \sum_{p,q=1}^{M-1,M} \phi_{\alpha+\gamma}(\xi_{\mathbf{m}}, \theta_p, \varphi_q)\psi_\gamma(\xi_{\mathbf{m}}, \theta_p, \varphi_q)\sin\theta_p, \tag{2.36}$$

which will be used to calculate the loss part of the collision operator. For space-homogeneous problems, such storage is relatively large when compared to the storage of the VDF. However, when it comes to space-inhomogeneous problems, the storage will be relatively small because different spatial grids could use the same kernel modes. Second, we get $\hat{f}$ by applying the inverse FFT to f, see Step 1 in algorithm 1 in the Appendix. Third, with Eq. (2.30), Eq. (2.25) becomes

$$\begin{aligned}\widehat{Q}_{\mathbf{j}} \approx & \underbrace{\frac{4\pi^2}{Kn'M^2} \sum_{p,q=1}^{M-1,M} \sum_{\substack{\mathbf{l}+\mathbf{m}=\mathbf{j} \\ \mathbf{l},\mathbf{m}=-(N_1,N_2,N_3)/2}}^{(N_1,N_2,N_3)/2-1} [\hat{f}_{\mathbf{l}}\phi_{\alpha+\gamma}(\xi_{\mathbf{l}}, \theta_p, \varphi_q)] \cdot [\hat{f}_{\mathbf{m}}\psi_\gamma(\xi_{\mathbf{m}}, \theta_p, \varphi_q)] \cdot \sin\theta_p}_{gain} \\ & \underbrace{-\frac{4\pi^2}{Kn'M^2} \sum_{\substack{\mathbf{l}+\mathbf{m}=\mathbf{j} \\ \mathbf{l},\mathbf{m}=-(N_1,N_2,N_3)/2}}^{(N_1,N_2,N_3)/2-1} \hat{f}_{\mathbf{l}} \cdot [\hat{f}_{\mathbf{m}}\phi_{loss}]}_{loss}.\end{aligned} \tag{2.37}$$

The loss term can be effectively calculated by FFT-based convolution, using the zero-padding technique [61]. For the gain term, one has to do an FFT-based convolution for each pair of (p, q), that is, $M(M-1)$ times. The implementation is listed in Steps 2, 3, and 4 in algorithm 1 [Appendix A]. Finally, the collision operator Q is calculated by applying FFT to $\widehat{Q}$ (Step 5).

Note that in algorithm 1, the zero-padding technique is employed to eliminate the aliasing error in the FFT-based convolution. This process is accurate for arbitrary values of t_1 and t_2 (defined in Appendix A) when the padding size in each direction is larger than one half of the velocity grid number. Considering the fact that the spectrum $\hat{f}$ is non-zero only in the central region of the frequency domain, we can expedite the calculation by ignoring the zero-padding. This leads to the simpler and faster algorithm 2. Numerical simulations on Test 1 below show that both algorithms produce identical results, but algorithm 2 is about 4 times faster than algorithm 1.

Now we see that the computational cost of the FSM is $O(M^2N^3 \log N)$, where

N is the same order as N_1, N_2 and N_3. Note that $\mathbf{l}$ and $\mathbf{m}$ are not separable in classical spectral methods, and the computational cost of Eq. (2.25) is $O(N^6)$ [47, 49]. A rough estimate of the speed-up can be given. In algorithm 2, one needs to do $2M(M-1)+2$ times FFT (the array size is $N_1 \times N_2 \times N_3$), while in classical spectral methods the computational cost is the same with one direct convolution of one complex and one real array of size $N_1 \times N_2 \times N_3$. For comparison, we take $M = 7$ and run our Matlab (version 2012a) programs on a PC with an Intel Xeon 3.3 GHz CPU. For $N = 32$ (or 64), algorithm 2 is about 18 (or 62) times faster than the classical spectral methods. Further speed-up can be achieved by reducing the value of M (say, to 5) and considering possible symmetry in the VDF. As will shown in Chapters 3 and 4, for the flows with large Knudsen number there are discontinuities in the VDF; to capture the discontinuities, one needs large number of velocity grids. In this case, the FSM could be faster than the classical spectral methods by two orders of magnitude.

Note that for the LJ potential, the storage of the kernel modes and computational cost of the collision operator is exactly the same as that for the single-term collision kernel (2.7) or (2.9). For the collision kernel (2.13), if we let $\gamma_1 = \gamma_2$, the storage and computational cost will also be the same as the single-term collision kernel. For the existence of $\phi_{1+\gamma_1}$, $\psi_{1-\gamma_1}$, $\phi_{-1+\gamma_2}$, and $\psi_{1-\gamma_2}$, one should choose $-2 < \gamma_1 < 2$ and $0 < \gamma_2 < 2$. Therefore, we choose $0 < \gamma_1 = \gamma_2 < 2$. Note, if $\gamma_1 \neq \gamma_2$, the storage and computational cost will be twice of that of the single-term collision kernel.

2.4 Accuracy of the fast spectral method

To check the accuracy of the FSM, the relax-to-equilibrium process of Maxwell molecules $(\alpha, \gamma = 0)$ is considered. This is a spatial-homogeneous problem, where the BE becomes

$$\frac{\partial f}{\partial t} = \frac{1}{Kn'} \int_{\mathbb{R}^3} \int_{\mathbb{S}^2} \sin^{-1}\left(\frac{\theta}{2}\right) [f(\mathbf{v}'_*) f(\mathbf{v}') - f(\mathbf{v}_*) f(\mathbf{v})] d\Omega d\mathbf{v}_*. \tag{2.38}$$

Without loss of generality, we choose $Kn' = 32\pi/5$.

Test 1. The BE (2.38) possesses the exact Bobylev-Krook-Wu (BKW) solution [62]:

$$f(\mathbf{v}, t) = \frac{1}{2(2\pi K)^{3/2}} \exp\left(-\frac{|\mathbf{v}|^2}{2K}\right) \left(\frac{5K-3}{K} + \frac{1-K}{K^2}|\mathbf{v}|^2\right), \tag{2.39}$$

where the "effective temperature" is $K = 1 - 0.4\exp(-t/6)$, $t \geq 0$. According to the exact solution, the evolution of the fourth- and sixth-order moments is given by

$$M_4 = \int f v_1^4 d\mathbf{v} = 6K - 3K^2, \quad M_6 = \int f v_1^6 d\mathbf{v} = 45K^2 - 30K^3. \tag{2.40}$$

The integration of Eq. (2.38) with respect to t will introduce some numerical error. In order to check how accurately the FSM can approximate the collision operator, we compare Q^{nu}, the numerical approximation of Q, to the analytical solution Q^{an}, which is calculated by $Q^{an} = [f(t = \Delta t) - f(t = 0)]/\Delta t$ with Δt=1.0E-5 (which is far smaller than the characteristic relaxation time). The following two factors affect the accuracy: the value of N, which decides the accuracy of the spectrum $\hat{f}$ of the VDF, and the value of M, which determines how accurately we approximate the integral in Eq. (2.28). The latter is qualitatively analysed as follows. For simplicity, let us ignore $\xi_{\mathbf{m}}$ and φ in Eq. (2.28). Notice that $\phi_{\alpha+\gamma}$ is a decaying-oscillating function with the quasi-period $2\pi/R$ (see Eq. (2.33) and Figure 2.3). Then, for a fixed value of $\xi_{\mathbf{l}}$, the integral kernel in Eq. (2.28) oscillates $R|\xi_{\mathbf{l}}|/\pi$ times as θ varies from 0 to π. In the worst cases ($\xi_{\mathbf{l}} \to N\pi/2L$), it oscillates $O(N)$ times. This implies that M should be $O(N)$. In practical calculations, however, M can be far less than N because, if the VDF has a support S, its spectrum has a support proportional to $1/S \sim 1/R$. Within this support, the integral kernel in Eq. (2.28) oscillates only a few times, and hence a small value of M can lead to accurate results.

We vary values of N and M to see their influence on the numerical accuracy; the results are tabulated in Table 2.1. When $N = 16$, the relative error is large because the resolution of the VDF is not high enough so that a large error exists in the spectrum $\hat{f}$. As N increases to 24, the error is reduced by one order of magnitude. When the trapezoidal rule is used, the error mainly comes from the approximation of Eq. (2.28), which decays at $O(1/M^2)$ when N is fixed. When M is fixed, the numerical accuracy does not improve when $N \geq 32$. If we increase the value of M by a factor of 2 when the value of N is increased by a factor of 2, we find that the spectral accuracy of the FSM is roughly maintained. When Eq. (2.28) is approximated by the Gauss-Legendre quadrature, the spectral accuracy is clear for $N \leq 32$ and $M \geq 6$. For $N > 32$, if M is increased linearly with N, spectral accuracy is maintained. For example, if we

Table 2.1: Relative error $\sum_{\mathbf{j}} |Q_{\mathbf{j}}^{nu} - Q_{\mathbf{j}}^{an}| / \sum_{\mathbf{j}} |Q_{\mathbf{j}}^{an}|$ in the approximation of the Boltzmann collision operator. T (G) stands for the trapezoidal rule (Gauss-Legendre quadrature) used in the approximation of Eq. (2.28). Parameters are $L = 8$ and $R = 6$.

N		$M = 5$	6	7	8	12	16
16	T	4.58E-1	4.73E-1	4.55E-1	4.52E-1	4.78E-1	4.83E-1
	G	2.10E-1	3.35E-1	2.48E-1	2.77E-1	2.74E-1	2.69E-1
24	T	7.94E-2	5.20E-2	4.73E-2	3.93E-2	2.92E-2	2.59E-2
	G	4.61E-2	2.09E-2	9.16E-3	2.10E-2	1.72E-2	1.37E-2
32	T	5.54E-2	3.51E-2	2.57E-2	1.93E-2	8.39E-3	4.75E-3
	G	4.26E-2	6.18E-3	6.49E-4	2.11E-4	1.86E-4	1.57E-4
48	T	4.26E-2	3.88E-2	2.77E-2	2.08E-2	8.99E-3	5.01E-3
	G	4.31E-2	6.17E-3	6.09E-4	4.56E-5	4.94E-6	3.85E-6
64	T	5.90E-2	3.87E-2	2.77E-2	2.08E-2	8.99E-3	5.02E-3
	G	4.30E-2	6.16E-3	6.10E-4	4.70E-5	3.87E-6	4.31E-6

choose the minimum error between $6 \leq M \leq 12$ for each N, the order of accuracy is 8.1 when N increases from 16 to 24; 13.5 when N increases from 24 to 32; and 8.9 when N increases from 32 to 48. Thus, in general, the approximation of Eq. (2.28) by Gauss-Legendre quadrature is better than that by the trapezoidal rule.

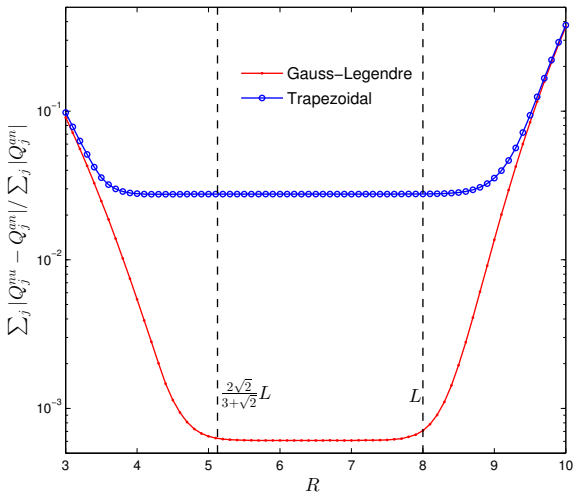

Figure 2.4: The relative error $\sum_{\mathbf{j}} |Q_{\mathbf{j}}^{nu} - Q_{\mathbf{j}}^{an}| / \sum_j |Q_{\mathbf{j}}^{an}|$ vs the truncation radius R. Parameters are $L = 8, N = 48$, and $M = 7$. Gauss-Legendre quadrature is used in the approximation of the kernel mode.

We now fix values of N and M to check the influence of R on the accuracy. Figure 2.4 indicates that R cannot be smaller than $2\sqrt{2}L/(3+\sqrt{2})$, which is roughly $\sqrt{2}$ times the support of the VDF; otherwise, some collisions will be ignored in the truncated collision

operator. Also, R cannot be larger than the size of the velocity domain, otherwise the aliasing error may destroy accuracy.

Next, we demonstrate the accuracy of the FSM as a function of time, where Eq. (2.38) is solved by the Euler forward method with a time step of 0.001. Figure 2.5 depicts the evolution of the VDF, and the fourth- and sixth-order moments. Excellent agreement is found between the numerical and BKW solutions, even when Eq. (2.28) is approximated by the trapezoidal rule with $M = 5$. Figure 2.6 shows the numerical errors in the VDF, the fourth- and sixth-order moments, and energy as functions of time. It can be seen that when Eq. (2.28) is approximated by Gauss-Legendre quadrature, the numerical error with $N = 32$ is one order of magnitude smaller than that with $N = 24$. Also, the accuracy of the results with $N = 24$ is even better than that with $N = 32$ when Eq. (2.28) is approximated by the trapezoidal rule. These results agree with what we found in Table 2.1.

Furthermore, we find that the use of the Lagrangian multiplier method does not affect the numerical accuracy. This could be explained as follows: from Figure 2.6(a) and (d) we see that the error in energy is far smaller than the error in the VDF. Therefore, the correction in Eq. (2.34) is negligible, which ensures conservation.

Comparing the kernel mode (2.30) with those in Refs. [1, 51, 54], the term $\sin\theta_p$ is missed in Refs. [1, 51] and an additional term $\sin\theta_2$ is added in Eq. (2.29) in Ref. [54]. We have carried out numerical simulations using these kernel modes and found that none of them can accurately capture the evolution of the VDF.

Test 2. For general forms of the initial condition, we cannot get the exact evolution of VDFs. However, we know the exact evolution of its velocity moments. For example, when the initial VDF takes the form

$$f(\mathbf{v}, t = 0) = \frac{1}{2(2\pi)^{3/2}} \exp\left(-\frac{|\mathbf{v} - \mathbf{V}_1|^2}{2}\right) + \frac{1}{2(2\pi)^{3/2}} \exp\left(-\frac{|\mathbf{v} - \mathbf{V}_2|^2}{2}\right), \quad (2.41)$$

with $\mathbf{V}_1 = (-2, 2, 0)$ and $\mathbf{V}_2 = (2, 0, 0)$, the exact evolution of the pressure tensor is

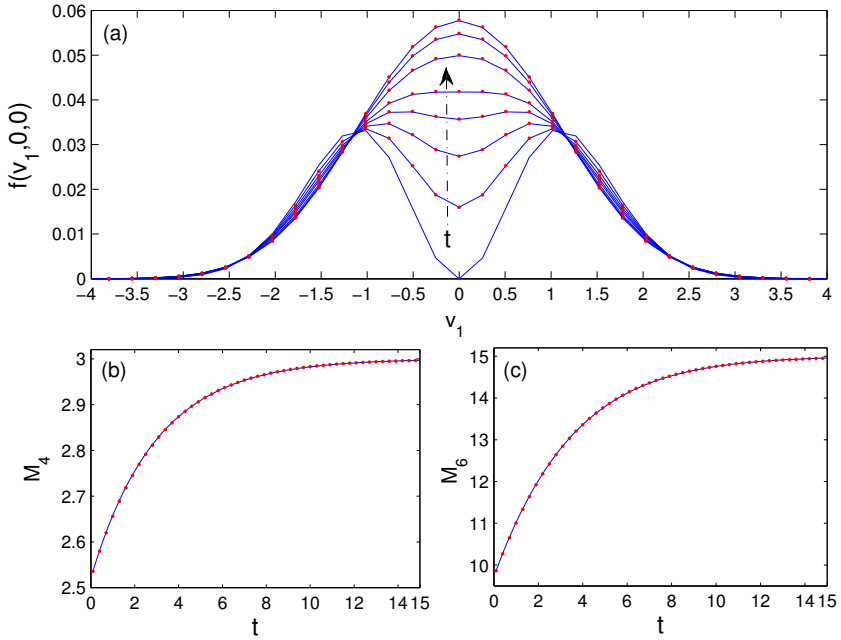

Figure 2.5: (a) Evolution of the VDF $f(v_1, 0, 0)$ of space-homogeneous Maxwell molecules, where the initial condition is given by Eq. (2.39). From bottom to top (near $v_1 = 0$), the time corresponding to each line is $0, 0.5, 1, 1.5, 2, 3, 4$, and 5. (b) and (c) Evolution of the fourth- and sixth-order moments, respectively. The solid lines represent the numerical results, while the dots are analytical predictions. The following parameters are used in the numerical simulation: $L = 8, R = 6$, $N = 64$, and $M = 5$ with Eq. (2.30).

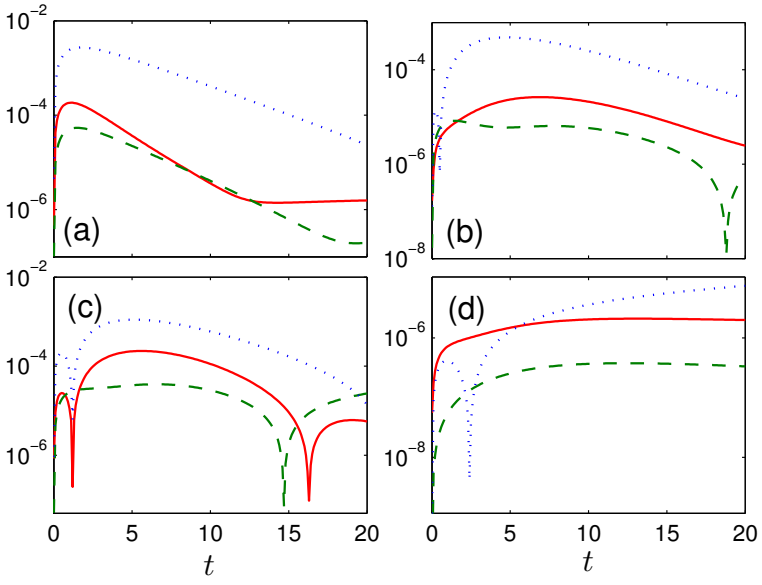

Figure 2.6: (a) Error $(\sum_{\mathbf{j}} |f^{nu} - f|^2 / \sum_{\mathbf{j}} |f|^2)^{1/2}$ in the VDF, (b) error in the fourth-order moment $|M_4^{nu} - M_4|/M_4$, (c) error in the sixth-order moment $|M_6^{nu} - M_6|/M_6$, and (d) error in the energy $|(P_{xx}^{nu} + P_{yy}^{nu} + P_{zz}^{nu})/6 - 1|$ vs time. The solid and dashed lines are the results using Eq. (2.31) with $N = 24$ and $N = 32$, respectively, while the dotted lines are the results using Eq. (2.30) with $N = 32$. Other parameters are $L = 8, R = 6$, and $M = 7$.

given by [47, 62]

$$P_{xx} = \frac{14}{3}\exp\left(-\frac{t}{2}\right) + \frac{16}{3}, \quad P_{yy} = -\frac{4}{3}\exp\left(-\frac{t}{2}\right) + \frac{16}{3},$$
$$P_{zz} = -\frac{10}{3}\exp\left(-\frac{t}{2}\right) + \frac{16}{3}, \quad P_{xy} = -4\exp\left(-\frac{t}{2}\right), \tag{2.42}$$

and the exact evolution of the third-order moments is given by

$$r_x = \int f v_1 |\mathbf{v}|^2 d\mathbf{v} = -4\exp\left(-\frac{t}{2}\right),$$
$$r_y = \int f v_2 |\mathbf{v}|^2 d\mathbf{v} = -\frac{4}{3}\exp\left(-\frac{t}{2}\right) + \frac{43}{3}. \tag{2.43}$$

Figure 2.7 compares the evolution of the second- and third-order moments. It demonstrates that our numerical simulation produces accurate results when compared to the analytical ones given by Eqs. (2.42) and (2.43). From Figure 2.8 we see that, the relative errors in P_{xx}, P_{yy}, and r_y are about 10^{-4}, while the errors are about 10^{-5} when Eq. (2.28) is approximated by Gauss-Legendre quadrature.

It is worthwhile to note that the spectral-Lagrangian method [47] cannot recover the third-order moments even when $N = 40$. Does this mean that the spectral-Lagrangian method is not spectrally accurate? We think that this is due to the integration region given in Eq. (2.29) of Ref. [47] (which is related to the parameter R in the FSM) being too large, so a significant aliasing error is introduced (see Figure 2.4). Indeed, we find in our simulations that r_x and r_y deviate from the analytical solutions when R is outside of the velocity domain.

Test 3. Notice that the initial VDFs used in the two test cases above are smooth, and the spectral accuracy of the FSM method has been proven [1]. Now we consider the case where the initial VDF is not smooth;, but has an abrupt jump at $v_1 = 0$:

$$f(\mathbf{v}, t=0) = \frac{1}{3(2\pi)^{3/2}} \begin{cases} 4\exp\left(-\frac{|\mathbf{v}|^2}{2}\right), & v_1 \geq 0, \\ \exp\left(-\frac{v_1^2}{8} - \frac{v_2^2+v_3^2}{2}\right), & v_1 < 0. \end{cases} \tag{2.44}$$

It can be shown analytically that the evolution of the second- and fourth-order moments

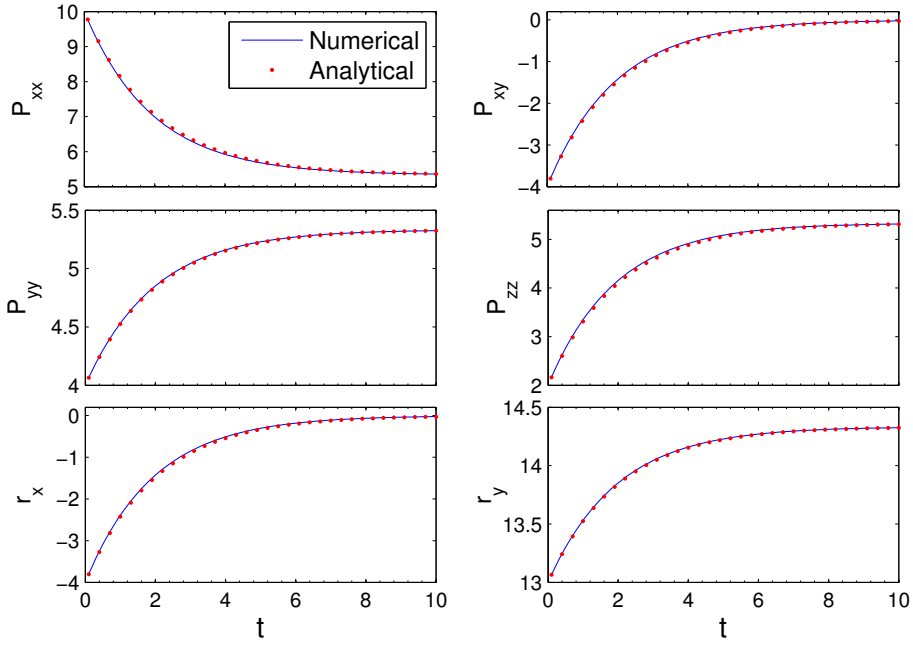

Figure 2.7: Evolution of the second- and third-order moments for space-homogeneous Maxwell molecules, where the initial VDF is given by Eq. (2.41). The following parameters are used in the numerical simulation: $L = 12, R = 10$, $N = 32$, and $M = 5$ with Eq. (2.30).

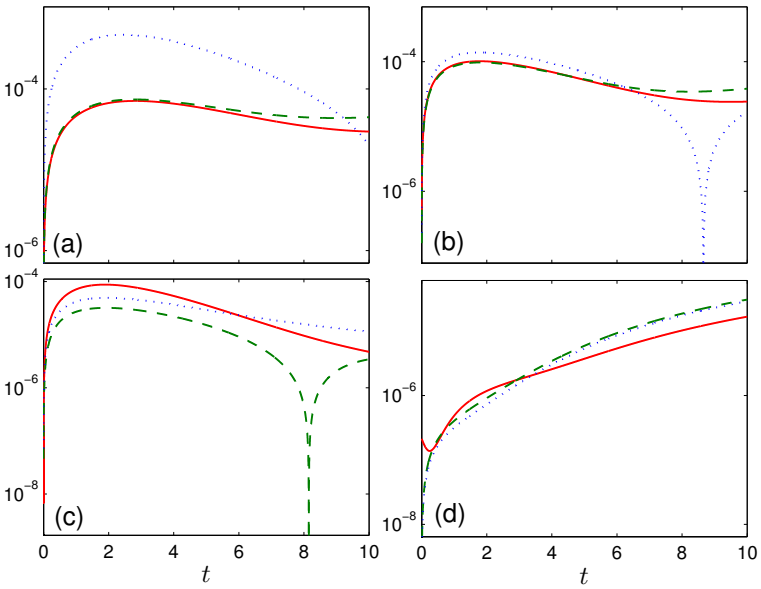

Figure 2.8: (a) Relative error $|P_{xx}^{nu} - P_{xx}|/P_{xx}$, (b) relative error $|P_{yy}^{nu} - P_{yy}|/P_{yy}$, (c) relative error $|r_y^{nu} - r_y|/r_y$, and (d) error in the energy $|(P_{xx}^{nu} + P_{yy}^{nu} + P_{zz}^{nu})/16 - 1|$ vs time. The solid and dashed lines are the results using Eq. (2.31) when $N = 24$ and $N = 32$, respectively, while the dotted lines are the results using Eq. (2.30) when $N = 32$. The other parameters are $L = 12, R = 10$, and $M = 7$.

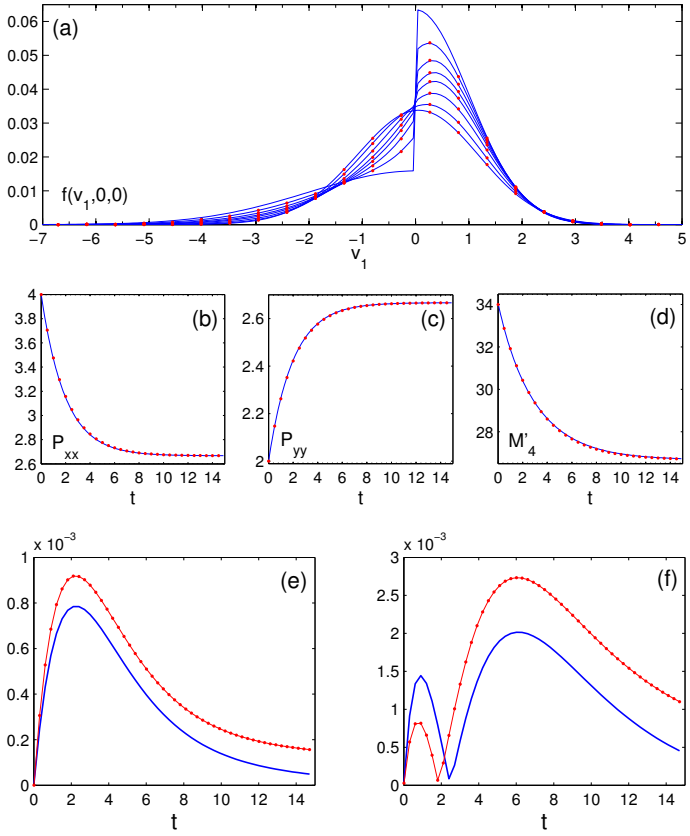

Figure 2.9: (a) Evolution of the VDF when the initial VDF at $v_1 = +0$ is four times larger than at $v_1 = -0$. From top to bottom (at $v_1 > 0$), the times corresponding to the lines are $t = 0, 0.5, 1, 1.5, 2, 3, 5$, and 9, respectively. (b-d) Evolution of the second- and fourth-order moments. Relative error (e) $|P_{xx}^{nu} - P_{xx}|/P_{xx}$ and (f) $|M_4^{'nu} - M_4^{'}|/M_4^{'}$ when $N = 42$. The dots are the numerical results when $N = 42$, the solid lines in (a), (e), and (f) are the numerical results with $N_1 = 256, N_2, N_3 = 42$, while the solid lines in (b-d) are analytical results. The other parameters are $L = 11$, $R = 2\sqrt{2}L/(3+\sqrt{2})$, and $M = 5$ with Eq. (2.30).

is given by

$$P_{xx} = \frac{4}{3}\exp\left(-\frac{t}{2}\right) + \frac{8}{3}, \quad P_{yy} = -\frac{2}{3}\exp\left(-\frac{t}{2}\right) + \frac{8}{3},$$
$$M_4' = \int f|\mathbf{v}|^4 d\mathbf{v} = \frac{22}{3}\exp\left(-\frac{t}{3}\right) + \frac{80}{3}. \tag{2.45}$$

Figure 2.9 demonstrates that the FSM can accurately capture the evolution of the second- and fourth-order moments, even when the initial VDF has a large jump at $v_1 = 0$. Also, no Gibbs oscillation has been observed in the central region of the VDF where the abrupt jump exists; only in the tails do we find small Gibbs oscillations. This is because the convolution in the Boltzmann collision operator can smear out the discontinuities.

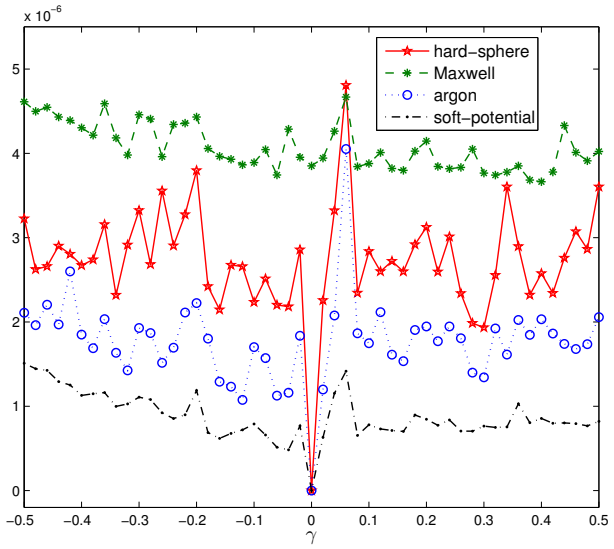

Figure 2.10: Relative error $\sum_{\mathbf{j}} |Q_{\mathbf{j}}^{nu} - Q_{\mathbf{j}}^{ref}| / \sum_{\mathbf{j}} |Q_{\mathbf{j}}^{ref}|$ in the approximation of the Boltzmann collision operator vs γ, where Q^{ref} is the collision term with $\gamma = 0$ for hard sphere, argon, and soft-potential molecules, while for Maxwell molecules, Q^{ref} is calculated according to the exact BKW solution (as done in Test 1). The other parameters are $L = 8, R = 6$, $N = 48$, and $M = 16$.

2.5 Comparison between different collision kernels

It is commonly thought that the solution of the BE is determined by the shear viscosity, rather than the details of the θ-dependence of the collision kernel. For instance, the VHS and variable soft sphere (VSS) models are used in DSMC and it is believed that as long as they recover the shear viscosity of a real gas, they produce the same results [14]. This is true to some extent; one example is the exact BKW solution for Maxwell molecules: different θ-dependence of the collision kernels with the same value of shear viscosity have the same BKW solution. However, this assumption has never been accurately checked for other potentials. Since the FSM can generate accurate numerical results, it is interesting to examine this assumption.

We take the hard sphere ($\alpha = 1$), argon ($\alpha = 0.38$), and soft-potential ($\alpha = -0.4$) molecules as examples. To be specific, we consider the BE (2.16) with $Kn = \sqrt{\pi}$. The VDF is given by Eq. (2.39) with $t = 0$. We vary the value of γ and compare the relative error of the collision operator Q. Figure 2.10 shows that the value of γ has almost no influence on the solution of the collision operator, as the relative errors are at the order of the numerical accuracy (when compared to Maxwell molecules) and seem to be random.

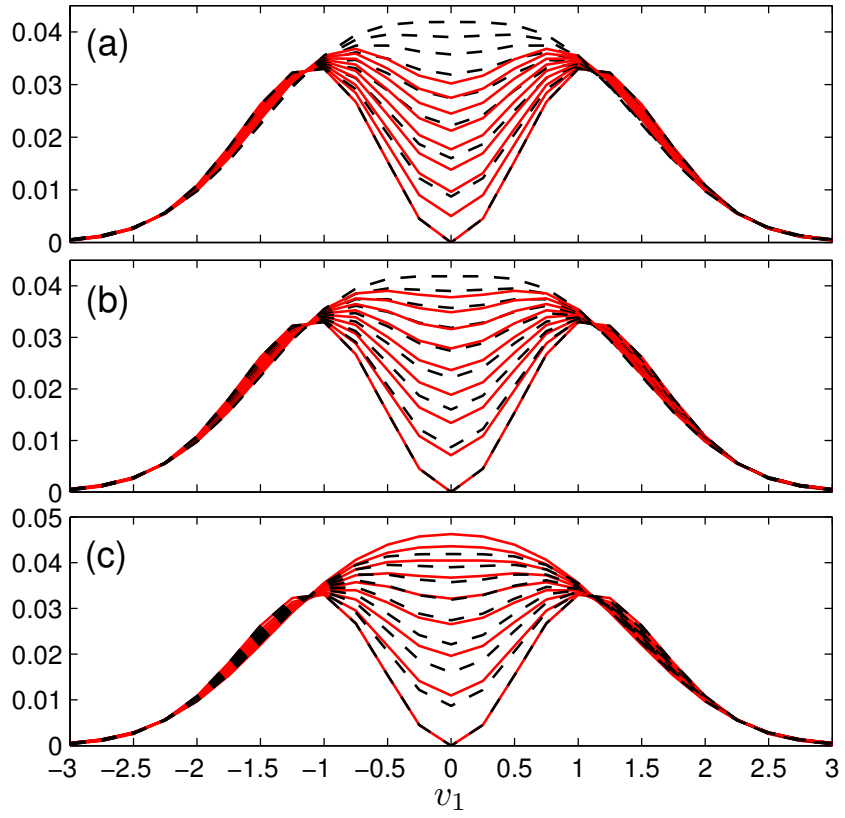

Figure 2.11: Evolution of the VDF $f(v_1, 0, 0)$ for space-homogeneous (a) hard sphere, (b) argon, and (c) soft-potential molecules, where the initial condition is given by Eq. (2.39). In each figure, from bottom to top (near $v_1 = 0$), the time corresponding to each line is $(0, 1, 2, 3, 4, 5, 6, 7, 8)\times 0.25$. Solid lines: the numerical solutions; dashed lines: analytical BKW solution for Maxwell molecules.

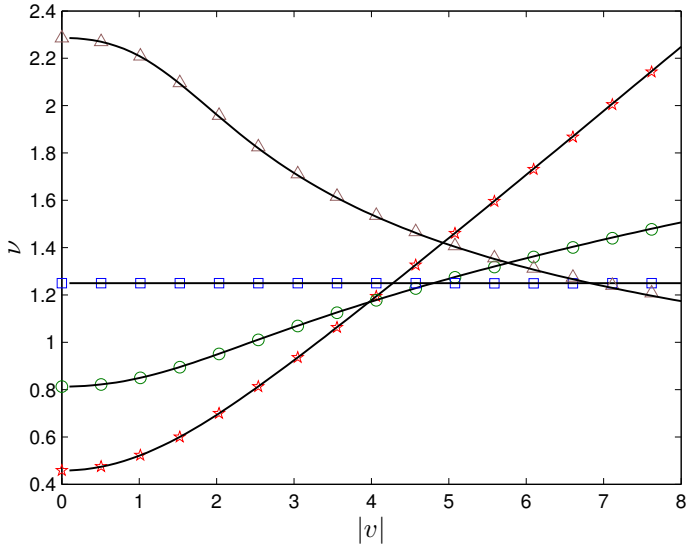

Figure 2.12: Collision frequency of hard sphere molecules (stars), argon with $\alpha = 0.38$ (circles), Maxwell molecules (squares), and soft-potential molecules with $\alpha = -0.4$ (triangles) vs molecular velocity. The lines are analytical results calculated according to equations in Ref. [6]. The VDF is given by Eq. (2.39) with $K = 1$.

Next we compare the relax-to-equilibrium processes between hard sphere, argon, Maxwell, and soft-potential molecules with $\gamma = 0$. Again, the initial VDF is given by Eq. (2.39). We choose $Kn = 2^{1-\omega}\sqrt{\pi}$, meaning different collision kernels have the same value of shear viscosity at $T = 2$. The evolution of the VDFs are shown in Figure 2.11. It is seen that for hard-potential molecules ($\alpha > 0$), in the central velocity region $[-1, 1]^3$, the relax-to-equilibrium process is slower than that for Maxwell molecules, and the larger the α, the slower the decay. In the outer velocity region, however, the decay is faster (although not clearly shown, this can be inferred according to the conservation of mass). For soft-potential molecules ($\alpha < 0$), however, the decay is faster than that for Maxwell molecules in the central velocity region. This may be qualitatively explained in terms of the collision frequency $\nu(\mathbf{v})$. Figure 2.12 shows that the collision frequency of hard sphere molecules is smaller (or larger) than that of Maxwell molecules when $|v| < 4$ (or $|v| > 4$). Therefore, in the central (outer) velocity region, there are less (more) effective collisions between hard sphere molecules than between Maxwell molecules, and hence the decay is slower (faster). Overall, from Figure 2.13 we see that, as compared to Maxwell molecules, the competition between the slower and faster decay results in the slower (faster) decay of the fourth- and sixth-order moments for hard-potential (soft-potential) molecules.

The different decay rates between different inverse power-law potential models with the same value of shear viscosity (see Figure 2.13) poses a question in the simulation of the LJ potential: since the shear viscosity can be recovered by different combinations of α_j and b_j, we can ask whether different values of α_j and b_j in Eq. (2.11) lead to different results? To answer this question, we compare the relax-to-equilibrium processes between argon with $\mu \propto T^{0.81}$ and the LJ potential with the collision kernel (2.11). The initial VDF is given by Eq. (2.39) with $t = 0$. For argon, we choose $Kn = 2^{0.19}\sqrt{\pi}$, while for the LJ potential we choose $Kn = 1.0758\sqrt{\pi}$ and $k_B T_0/\epsilon = 1.1$, so that the two models have the same value of shear viscosity and for the LJ potential the shear viscosity can be approximated by $T^{0.81}$ at $T/T_0 = 2$. The relative differences in the fourth- and sixth-order moments between the two models are depicted in Figure 2.14, where we see that the differences are very small. This example and the example shown in Figure 2.10 indicate that one can use different θ-dependence of the collision kernels

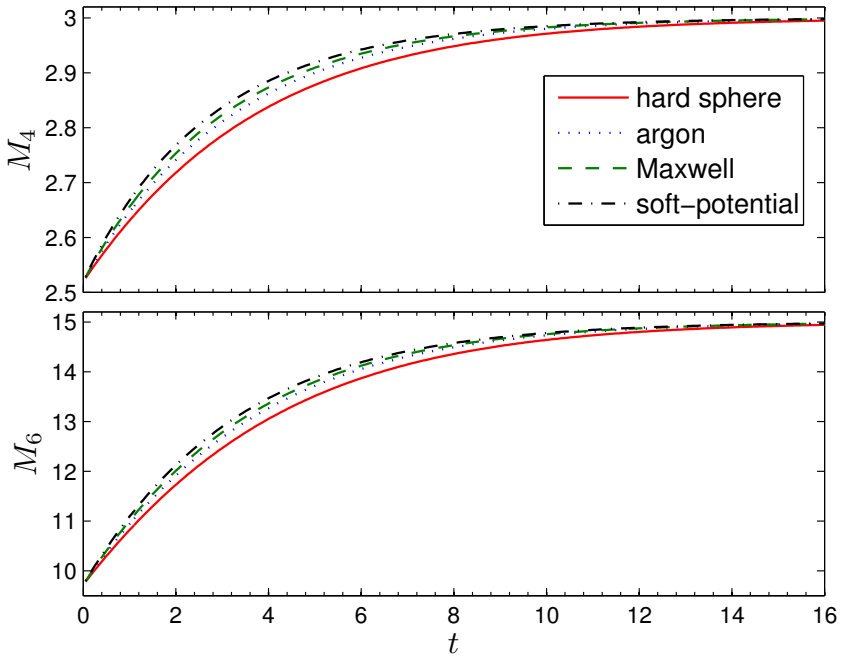

Figure 2.13: Evolution of the fourth- and sixth-order moments for different molecular models.

as long as the shear viscosity (not only its value, but also its temperature dependence) is recovered.

2.6 Solutions for space-inhomogeneous problems

2.6.1 Stationary solutions

To get stationary solutions of the BE, the time-dependent term is omitted, resulting in $v\partial f/\partial x + a\partial f/\partial v = Q(f, f_*)$. We then employ the iteration method to solve this equation: given the value of f at the k-th step, its value at the next iteration step is calculated by the following equation

$$\overline{\nu} f^{k+1} + v\frac{\partial f^{k+1}}{\partial x} = \overline{\nu} f^{k} - a\frac{\partial f^{k}}{\partial v} + Q(f^k, f_*^k), \tag{2.46}$$

where the spatial derivative $\partial f^{k+1}/\partial x$ is approximated by the second-order upwind scheme, and the acceleration term $a\partial f/\partial v$ is calculated according to the Fourier transform derivative theorem, when the VDF is smooth. The parameter $\overline{\nu}$ is the mean collision frequency.

The choice of the value of $\overline{\nu}$ is ad-hoc for space-inhomogeneous problems since

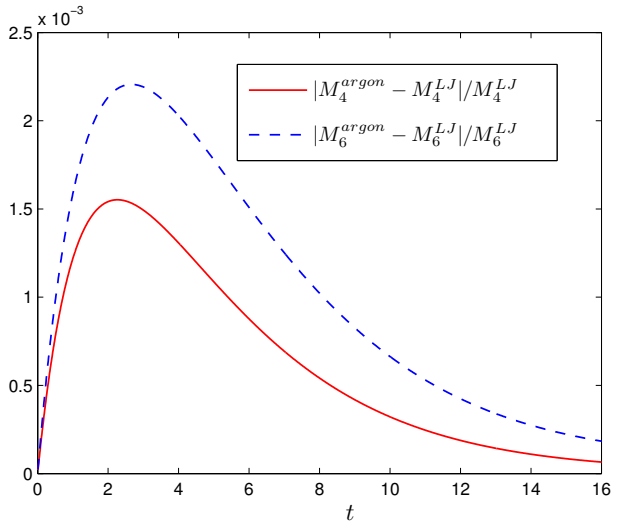

Figure 2.14: The relative differences in the fourth- and sixth-order moments between argon with $\mu \propto T^{0.81}$ and the LJ potential with collision kernel (2.11).

different locations have different mean collision frequency, and too large (small) a value of $\overline{\nu}$ results in slow convergence (numerical instability). A better way is to replace the mean collision frequency by the local collision frequency in the k-th iteration step, and change $f^k(v)$ in the loss term Q^- to $f^{k+1}(v)$, yielding

$$\nu(f^k)f^{k+1} + v\frac{\partial f^{k+1}}{\partial x} = -a\frac{\partial f^k}{\partial v} + Q^+(f^k, f_*^k). \tag{2.47}$$

Note that a similar scheme has been used in the study of the structure of shock waves [37, 39]. Also note that in the continuum regime $Kn \to 0$ and $\nu \to \infty$, the convergence rate to the stationary solutions is very slow. In this case, it may be better to solve the time-dependent BE by the asymptotic preserving scheme using relevant larger time step; see the recent review paper [63].

The iteration scheme to find the stationary solution is described in §2.6.1. The iteration process is terminated when the maximum L_1 norm of the macroscopic quantities (such as $n, \mathbf{V}, T, \mathbf{P}$, and $\mathbf{q}$) at two consecutive iteration steps is less than a fixed small value, say, 10^{-7}. Since there is only a small difference in macroscopic quantities for different values of M, a trick can be used to reduce the computational cost: we first choose a relatively small value of M; when the numerical solution is not far away from the true one we then switch to larger values of M. In the following calculations, it is found that the use of $M = 5$ generates satisfactory results. We use the trapezoidal rule

to approximate the kernel mode (2.28), since for $M = 5$ it has almost the same accuracy as that of Gauss-Legendre quadrature but with about 25% increase in computational efficiency.

A remaining issue is to determine the local collision frequency $\nu(\mathbf{v})$, see Eq. (2.47). We proposed a method in algorithm 2. In numerical simulations, we find that this method does not give accurate results over the whole velocity range $[-L, L]^3$, but only in the region with $|v| \leq R/\sqrt{2}$, i.e., the results are accurate within the support of the VDF. If one is not interested in the VDF when $|v| > S$, the value of ν can be fixed for $|v| > S$ at, say, the same value of ν at $|v| = S$. On the other hand, one can get an accurate collision frequency through enlarging the velocity domain by a factor of two. The details are given in algorithm 3 in Appendix A.

Figure 2.12 depicts the collision frequency ν for various kinds of collision kernels when $Kn = \sqrt{\pi}$, and good agreements between the numerical and analytical results are observed. It is seen that the collision frequency of the soft potential is finite at $|v| \to 0$.

2.6.2 Normal shock waves

The normal shock wave is ideal for testing the accuracy of the FSM in capturing highly nonequilibrium effects, since this is a spatially one-dimensional problem where the boundary effects are absent. We first consider the shock wave in a gas of hard sphere molecules. The structure of the planar shock wave varies in the x_2 direction. The flow is uniform at the upstream ($x_2 = -\infty$) and downstream ($x_2 = \infty$) ends. The upstream molecule number density, temperature, and Mach number are denoted by n_0, T_0, and Ma, respectively, while those of the downstream end can be determined through the Rankine-Hugoniot relations: the normalized VDF at the upstream end is

$$f = \frac{1}{\pi^{3/2}} \exp\left[-v_1^2 - (v_2 - \sqrt{\frac{5}{6}}Ma)^2 - v_3^2\right], \tag{2.48}$$

and that at the downstream end is

$$f = \frac{n_d}{(\pi T_d)^{3/2}} \exp\left[-\frac{v_1^2 + (v_2 - V_d)^2 + v_3^2}{T_d}\right], \tag{2.49}$$

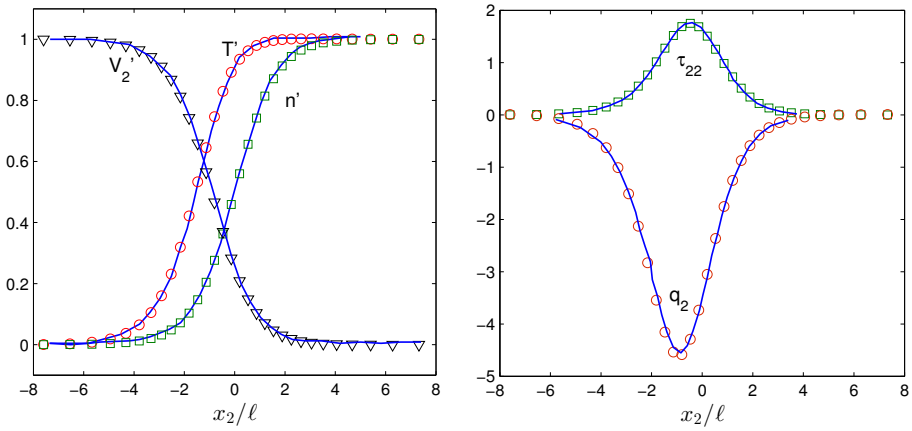

Figure 2.15: The normal shock wave for $Ma = 3$, where the reduced molecular number density is $n' = (n-1)/(n_r-1)$; temperature $T' = (T-1)/(T_r-1)$; bulk velocity, $V_2' = (V_2-V_r)/(\sqrt{5/6}Ma-V_r)$; shear stress $\tau_{22} = P_{22} - nT$; and heat flux q_2. The solid lines are the results from Ref. [37], while the symbols are our results from the FSM. The position of the shock wave is adjusted to $n'(0) = 1/2$. The velocity domain $[-10, 10]^3$ is uniformly divided into $42 \times 42 \times 42$ grid points, and $M = 5$.

where

$$n_d = \frac{4Ma^2}{Ma^2+3}, \quad V_d = \sqrt{\frac{5}{96}}\frac{Ma^2+3}{Ma}, \quad T_d = \frac{(5Ma^2-1)(Ma^2+3)}{16Ma^2}. \tag{2.50}$$

Ohwada solved this problem by means of the numerical kernel method [37]. For comparison, we set ℓ to be $\sqrt{\pi}/2$ times the mean free path of the hard sphere molecules ($\lambda_0 = (\sqrt{2}\pi d^2 n_0)^{-1}$, d is the diameter of the molecule) and the normalized Knudsen number $Kn' = 8\sqrt{2\pi}$. Figure 2.15 shows the shock wave structure for a Mach number of 3. It can be seen that the two deterministic numerical methods for the BE give identical results.

We then consider argon with the LJ potential. To compare with experimental data [64], we set the upstream temperature to be $T_0 = 298$ K, ℓ to be the mean free path in the upstream part ($\lambda_0 = (16/5\pi)\sqrt{\pi/2mk_BT_0}\mu/n_0$) and $Kn = 5\pi/16$ in Eq. (2.19). Good agreement between the numerical and experimental density profiles is seen in Figure 2.16. The agreement is due to the fact that we have correctly incorporated the shear viscosity of argon into the collision kernel, shown in Eq. (2.11).

Finally, we solve the BE for argon with the LJ potential and compare our results with that of MD simulation [65]. For comparison, we set the upstream temperature to be $T_0 = 300$ K, ℓ to be the mean free path in the upstream part and $Kn = 5\pi/16$.

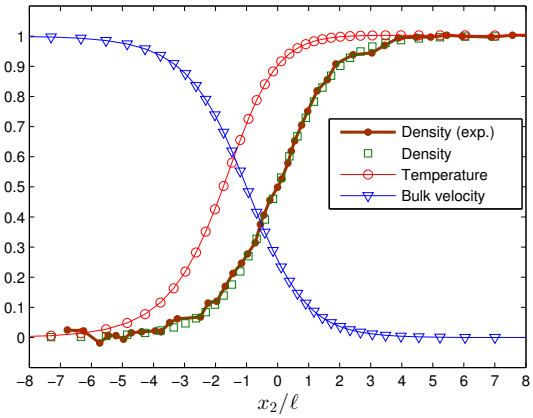

Figure 2.16: Reduced number density, temperature, and bulk velocity for the normal shock wave for $Ma = 2.80$. The experimental density is obtained from Ref. [64]. Numerical parameters are the same as those in Figure 2.15.

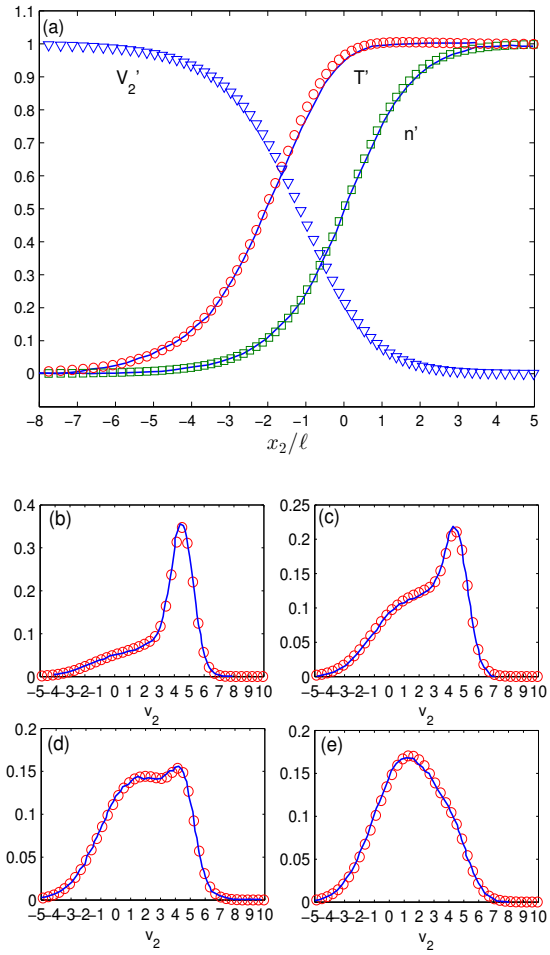

Figure 2.17: (a) Reduced molecular number density, temperature, and bulk velocity for the normal shock with $Ma = 5$ in argon gas (LJ potential). The marginal VDF $\int\int f dv_1 dv_3/n$ vs v_2 is presented in (b) $n' = 0.151$, (c) $n' = 0.350$, (d) $n' = 0.511$, and (e) $n' = 0.759$. The solid lines are the results from Ref. [65], while the symbols are our results from the FSM. The velocity domain $[-18, 18]^3$ is divided into $42 \times 84 \times 42$ grid points.

Figure 2.17 shows the shock wave structure for Mach number of 5, as well as the parallel VDFs (the perpendicular VDFs in Ref. [65] are actually parallel VDFs). As can be seen from this figure, the FSM produces nearly the same results as the MD simulation, not only in macroscopic quantities, but also in microscopic VDFs. Note that in this case the downstream temperature is about 2600K. The excellent agreement with MD data illustrates that the collision kernel (2.19) for the LJ potential works well in this temperature range.

2.6.3 Planar Fourier/Couette/force-driven Poiseuille flows

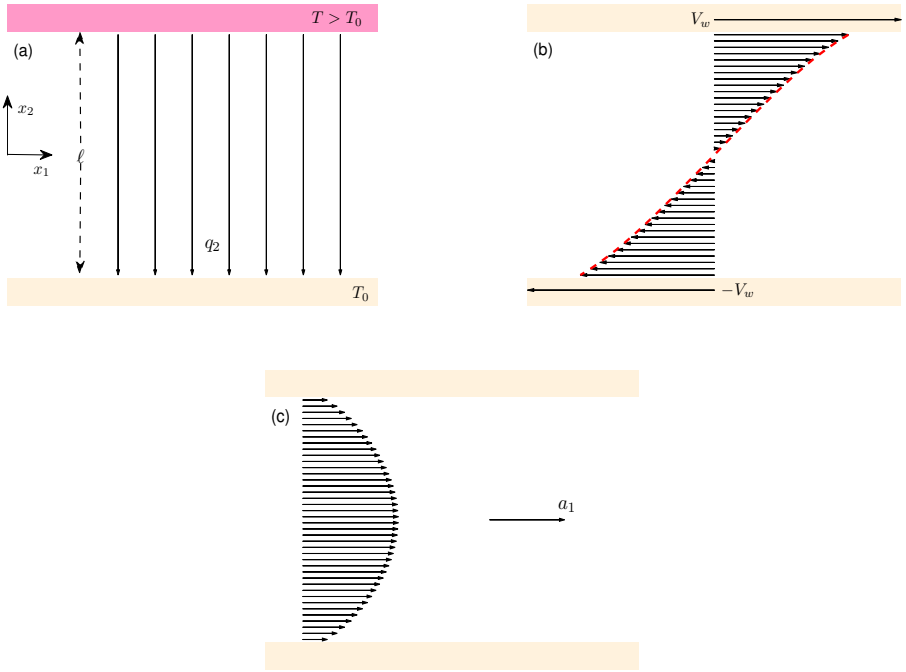

Figure 2.18: Sketch of (a) Fourier, (b) Couette, and (c) force-driven Poiseuille flows between parallel plates.

Consider a rarefied monatomic gas between two parallel infinite plates located at $x_2 = \ell/2$ and $x_2 = -\ell/2$. In Couette flow, the upper and lower plates move with velocity V_w and $-V_w$ in the direction parallel to the plates (the x_1 direction), while in Fourier and Poiseuille flows the plates are stationary (see Figure 2.18). No pressure gradient exists in the x_1 and x_3 directions. No external force is exerted in the Couette and Fourier flows, but in the Poiseuille flow the gas is subject to a uniform external force in the x_1 direction (the acceleration is denoted by a_1). In the Couette and Poiseuille

flows, the wall temperatures are kept at T_0, while in the Fourier flow the temperature of the upper wall is higher than that of the lower wall T_0. Maxwellian diffuse boundary condition is employed to account for the wall effects. When the average molecular number density n_0 and the intermolecular potential are known, the stationary state will be uniquely determined. We then analyse the density, velocity, temperature, shear stress, and heat flux profiles of the steady Fourier/Couette/force-driven Poiseuille flows.

In the planar Couette and Poiseuille flows, the symmetry of the problems with respect to the x_2 axis allows us to consider only half of the spatial region $-1/2 \leq x_2 \leq 0$. At the lower plate, according to Maxwellian diffuse boundary condition, the VDF for the reflected molecules is given by:

$$\begin{aligned} f =& \frac{n}{\pi^{3/2}} \exp[-(v_1 + V_w)^2 - v_2^2 - v_3^2], \quad \text{for } v_2 \leq 0, \\ n =& 2\sqrt{\pi} \int_{v_2<0} v_2 f(x_2 = -0.5, v) dv, \end{aligned} \tag{2.51}$$

while in the middle between the two plates, we have $f(v_1, v_2, v_3) = f(-v_1, -v_2, v_3)$ for Couette flow and $f(v_1, v_2, v_3) = f(v_1, -v_2, v_3)$ for Poiseuille flow.

For planar Fourier flow, however, we do not have this kind of symmetry. The boundary condition at the lower plate is the same as Eq. (2.51) with $V_w = 0$, while that at the upper plate is

$$\begin{aligned} f =& \frac{n}{(\pi T_r)^{3/2}} \exp\left(-\frac{v_1^2 + v_2^2 + v_3^2}{T_r}\right), \quad \text{for } v_2 < 0, \\ n =& 2\sqrt{\frac{\pi}{T_r}} \int_{v_2>0} v_2 f(x_2 = 0.5, v) dv, \end{aligned} \tag{2.52}$$

where T_r is the temperature ratio of the upper and lower plates.

In planar Couette flow of $Kn = 1$, we use argon with a shear viscosity proportional to $T^{0.81}$. The wall temperature is T_0=273K, and the wall velocity is $V_w = \sqrt{2} v_m$ in the first test case and $V_w = v_m/\sqrt{2}$ in the second one. The spatial region (halved due to the symmetry) is divided into 50 unequally spaced cells, with more cells near the boundary. The maximum velocity is at $L = 8$, and there are 42 velocity mesh points in each direction. Our numerical results are shown in Figure 2.19. In Figure 2.20 we show that, when using the iteration scheme given by Eq. (2.47), the relative error decays

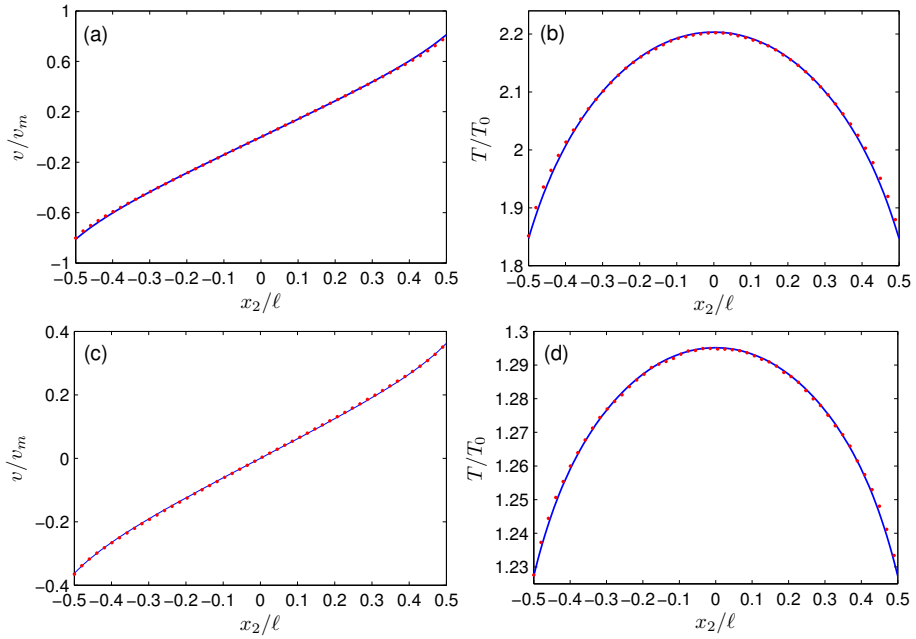

Figure 2.19: Profiles of the normalised velocity and temperature for planar Couette flow of argon gas at $Kn = 1$. (a, b) $V_w = \sqrt{2}v_m$ and (c, d) $V_w = v_m/\sqrt{2}$. The solid lines are numerical results from the FSM, while the dots are DSMC results.

exponentially, where, roughly speaking, the characteristic time of decay is inversely proportional to the Knudsen number. The FSM is very efficient when the Mach number is not very large, for instance, in the Couette flow shown in Figure 2.19(a) for which $Ma \approx 1.5$, the macroscopic quantities are obtained within 40 seconds (40 iterations, symmetry in the v_3 direction is considered) using our Matlab programme on a PC with an Intel Xeon 3.3 GHz CPU. Note that a corresponding Fortran program using one CPU is twice faster.

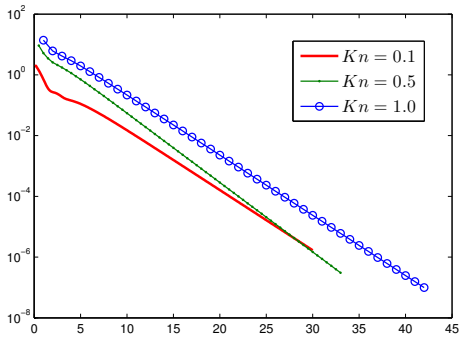

Figure 2.20: Decay of the relative error in the iteration process. The abscissa is the iteration step times the Knudsen number, while the ordinate is maximum relative error $max(\sum_j |T_j^k - T_j^{k-1}|/T_j^k, \sum_j |n_j^k - n_j^{k-1}|/n_j^k)$, where j is the position index.

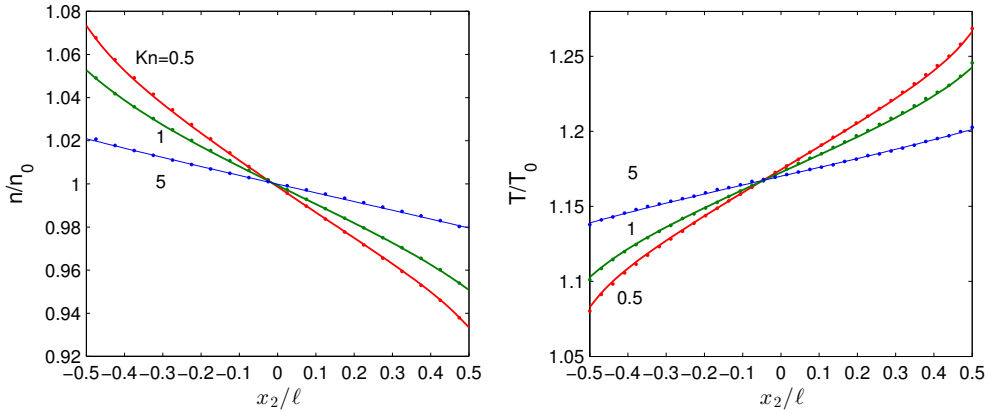

Figure 2.21: Density and temperature profiles for the planar Fourier flow of hard sphere molecules for unconfined Knudsen numbers of $0.5, 1$, and 5. The solid lines are our numerical results from the FSM, while the dots are DSMC results.

In Fourier flow, the temperatures of the lower and upper plates are chosen to be T_0=273K and 373K, respectively. We consider hard sphere molecules, and $Kn = 0.5, 1$, and 5. The spatial region is divided into 100 equally spaced cells. The maximum velocity is at $L = 6$, and there are 32 velocity mesh points in each direction. Nice agreements between the FSM and DSMC are shown in Figure 2.21.

In force-driven Poiseuille flow, we use hard sphere molecules and $Kn = 0.1$ and 0.5, respectively. The normalised acceleration is 0.11 and the wall temperature is T_0=273K. The spatial region (halved due to the symmetry) is divided into 50 unequally spaced cells with more cells near the boundary. The maximum velocity is at $L = 6$, and there are 32 velocity mesh points in each direction. The numerical results are depicted in Figure 2.22, where good agreements can be found.

2.7 Summary

The FSM for the approximation of the Boltzmann collision operator has been extended. A modified collision kernel, Eq. (2.9), is proposed, which enables the FSM to be applicable for all inverse power-law potentials except the Coulomb potential. By appropriate superposition of the modified collision kernels, we recovered the shear viscosity of the Lennard-Jones and rigid attracting potentials. Although many single-term collision kernels are added together, the computational efficiency of the Boltzmann collision operator is still the same as that for the single-term collision kernel. This unique prop-

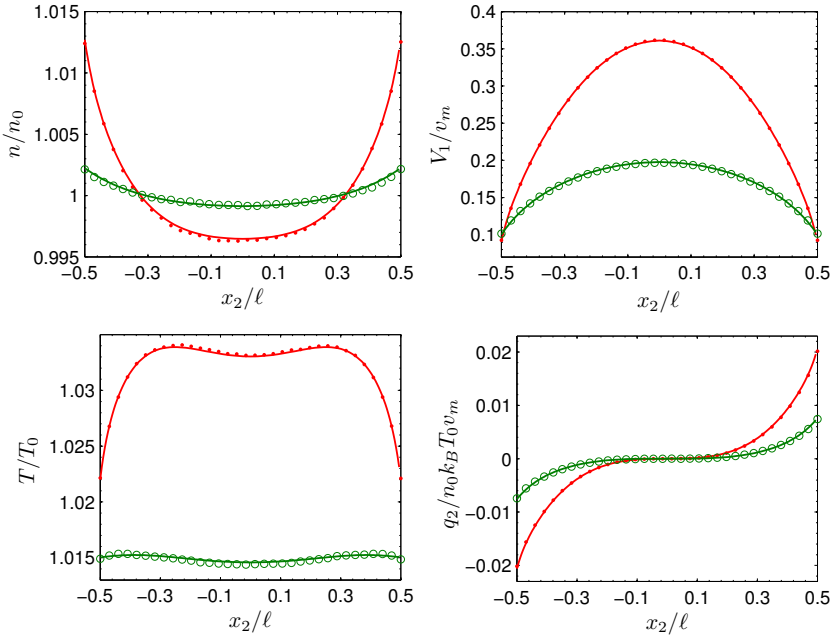

Figure 2.22: Profiles of the normalised number density, velocity, temperature, and heat flux for force-driven Poiseuille flow of hard sphere molecules when $Kn = 0.1$ (dots) and $Kn = 0.5$ (open circles). The solid lines are our results from the FSM, the symbols are DSMC results.

erty has advantages over the DSMC technique, where the simulation of soft potential molecules becomes inefficient because a large number of possible collision pairs are selected but each of which has only a small probability of actually participating in a collision [66]. For the simulation of particle systems interacting with the Coulomb potential, the following two solutions might be used. The first is to adopt the Fokker-Planck-Landau equation instead of the BE when all the collisions become grazing. For this case, the FSM has already been developed [67]. The second way is to use the Sutherland formula for shear viscosity, where the BE with the collision kernel (2.13) can be solved by the FSM.

The trapezoidal rule and Gauss-Legendre quadrature has been used to approximate the kernel mode. By comparing the numerical solutions with the analytical BKW solutions, we found that the latter is more accurate when $M > 5$. When $M = 5$, the accuracy is almost the same. We have also found that the spectrally small errors in conservation of momentum and energy in the FSM can be eliminated by using the Lagrangian multiplier method, while spectral accuracy is retained.

With accurate solutions provided by the FSM, we checked whether the solution

of the BE is affected by the θ-dependence of the collision kernel or not. Within the numerical accuracy (relative error is about 10^{-6}) we found that, for the same inverse power-law potential with the same value of shear viscosity but different forms of the θ-dependence of the collision kernel, solutions to the BE are the same. This justifies the fact that one can use different forms of the collision kernel provided that the shear viscosity (not only its value, but also its temperature dependence) is recovered.

The method has also been applied to space-inhomogeneous problems, including the normal shock wave and planar Fourier/Couette/force-driven Poiseuille flows. The numerical results of the FSM are found to agree well with those of the finite-difference solution to the BE, the experimental data, and the MD and DSMC solutions.

Since the FSM solves the BE deterministically, it is useful for developing a hybrid solver, where in the continuum regime kinetic model (or NS) equations are used, while in the rarefied regime the BE is solved. The open question remains as how to determine the location of the continuum/rarefied interface.

The dealiasing condition requires the velocity domain to be about two times larger than the support of the VDF, which wastes more than half of the compute memory and time in three-dimensional velocity space. A better way to do this is to introduce the non-uniform FFT [68], where the velocity space is non-uniformly discretised but the frequency space is equally divided. The only change we need is to get the spectrum $\hat{f}$ from f and the collision operator Q from $\hat{Q}$ by non-uniform FFTs, while the FFT-based convolution remains unchanged. Since the main computational effort is devoted to the calculation of FFT-based convolution, the non-uniform FFT will not increase the computation time much, especially when many efficient non-uniform FFT algorithms are available. Therefore, the use of fewer non-uniform velocity mesh points (with most of the points lying in the support of the VDF) will need less computation memory and time, without sacrificing accuracy.

Chapter 3

Fast spectral method for linearised Boltzmann equation

In this Chapter, the FSM is applied to the linearised BE. Two classical problems are solved, namely, the Poiseuille flow and thermal transpiration between parallel plates and rectangular tubes. Because of the singular (over-concentration) behaviour in the VDF [69], the numerical simulation of a highly rarefied gas is a difficult task; for a long time the accurate numerical results have been limited to hard sphere molecules when $Kn \leq 20$ [40, 70]. Recently, some progresses have been achieved both analytically and numerically, where the results are obtained at large Knudsen numbers [69, 71–73]. Here the linearised BE for various types of molecular models is solved accurately and efficiently by the FSM, up to $Kn \sim 10^6$.

3.1 The linearised Boltzmann equation and FSM

If the state of gas is weakly nonequilibrium, the BE may be linearised. The standard method is to write the VDF as $f(t, \mathbf{x}, \mathbf{v}) = f_{eq}[1 + h(t, \mathbf{x}, \mathbf{v})]$, where $|h| \ll 1$, so that the collision operator [say, in Eq. (2.16)] is linearised to $\int\int B(\theta, |\mathbf{u}|) f_{eq}(\mathbf{v}'_*)[h(\mathbf{v}'_*) + h(\mathbf{v}') - h(\mathbf{v}_*) - h(\mathbf{v})] d\Omega d\mathbf{v}_*$ with $B(\theta, |\mathbf{u}|) = \sin^{\alpha+\gamma-1}(\theta/2) \cos^{-\gamma}(\theta/2) |\mathbf{u}|^{\alpha} / Kn'$. The FSM developed in the previous Chapter, however, cannot be directly applied to this version of the linearised collision operator, because of the term $f_{eq}(\mathbf{v}'_*)h(\mathbf{v}_*)$. Instead, we seek another form of linearisation. We express the VDF as $f(t, \mathbf{x}, \mathbf{v}) = f_{eq} + h(t, \mathbf{x}, \mathbf{v})$, so

that the collision operator in Eq. (2.16) can be linearised to $\mathcal{L}_g(h) - \nu(v)h$, where

$$\mathcal{L}_g(h) = \int\int B(\theta, |\mathbf{u}|)[f_{eq}(\mathbf{v}')h(\mathbf{v}'_*) + f_{eq}(\mathbf{v}'_*)h(\mathbf{v}') - f_{eq}(\mathbf{v})h(\mathbf{v}_*)]d\Omega d\mathbf{v}_*, \tag{3.1}$$

can be viewed as a linear gain term and $\nu(v) = \int\int B(\theta, |\mathbf{u}|)f_{eq}(\mathbf{v}_*)d\Omega d\mathbf{v}_*$ is the equilibrium collision frequency.

The equilibrium collision frequency can be calculated analytically, or approximated by algorithm 2 (see Appendix A), if $\hat{f}$ is replaced by $\hat{f}_{eq}$, the spectrum of the equilibrium distribution function. This term only needs to be calculated once, since each spatial cell uses the same equilibrium collision frequency. For the linearised gain term $\mathcal{L}_g$, if Eq. (2.28) is approximated by the Gauss-Legendre quadrature for a higher accuracy (compared to the trapezoidal rule), its jth Fourier mode is

$$\begin{aligned}\widehat{\mathcal{L}}_{g\mathbf{j}} \approx & \frac{4}{Kn'}\sum_{p,q=1}^{M}\sum_{\substack{\mathbf{l}+\mathbf{m}=\mathbf{j}\\ \mathbf{l},\mathbf{m}=-(N_1,N_2,N_3)/2}}^{(N_1,N_2,N_3)/2-1} \omega_p\omega_q[\hat{f}_{eq}(\mathbf{l})\phi_{\alpha+\gamma}(\xi_{\mathbf{l}},\theta_p,\varphi_q)]\cdot[\hat{h}_{\mathbf{m}}\psi_\gamma(\xi_{\mathbf{m}},\theta_p,\varphi_q)]\cdot\sin\theta_p \\ & + \frac{4}{Kn'}\sum_{p,q=1}^{M}\sum_{\substack{\mathbf{l}+\mathbf{m}=\mathbf{j}\\ \mathbf{l},\mathbf{m}=-(N_1,N_2,N_3)/2}}^{(N_1,N_2,N_3)/2-1} \omega_p\omega_q[\hat{h}_{\mathbf{l}}\phi_{\alpha+\gamma}(\xi_{\mathbf{l}},\theta_p,\varphi_q)]\cdot[\hat{f}_{eq}(\mathbf{m})\psi_\gamma(\xi_{\mathbf{m}},\theta_p,\varphi_q)]\cdot\sin\theta_p \\ & - \frac{4}{Kn'}\sum_{\substack{\mathbf{l}+\mathbf{m}=\mathbf{j}\\ \mathbf{l},\mathbf{m}=-(N_1,N_2,N_3)/2}}^{(N_1,N_2,N_3)/2-1} \hat{f}_{eq}(\mathbf{l})\cdot[\hat{h}_{\mathbf{m}}\phi_{loss}],\end{aligned} \tag{3.2}$$

where $\phi_{loss} = \sum_{p,q=1}^{M}\omega_p\omega_q\phi_{\alpha+\gamma}(\xi_{\mathbf{m}},\theta_p,\varphi_q)\psi_\gamma(\xi_{\mathbf{m}},\theta_p,\varphi_q)\sin\theta_p$ and $\hat{h}$ is the spectrum of the VDF h.

Obviously, the gain term $\mathcal{L}_g$ can be calculated in a way similar to algorithm 2. Since the Fourier transform of the terms $\hat{f}_{eq}(\mathbf{l})\phi_{\alpha+\gamma}(\xi_{\mathbf{l}},\theta_p,\varphi_q)$and $\hat{f}_{eq}(\mathbf{m})\psi_\gamma(\xi_{\mathbf{m}},\theta_p,\varphi_q)$ can be precomputed and stored, the computational time of the linearised collision operator is nearly the same as that of the full Boltzmann collision operator. Therefore, it seems that there is no need to consider the BE in a linearized form. However, special values of γ can be used to reduce the computational cost by half[1]: choosing $\gamma = (1-\alpha)/2$, the linearised gain term $\int\int B(\theta,|\mathbf{u}|)[f_{eq}(\mathbf{v}')h(\mathbf{v}'_*) + f_{eq}(\mathbf{v}'_*)h(\mathbf{v}')]d\Omega d\mathbf{v}_*$ becomes $\frac{4}{Kn'}\int_{\mathbb{R}^3}\int_{\mathbb{R}^3}\delta(\mathbf{y}\cdot\mathbf{z})(|\mathbf{y}||\mathbf{z}|)^{-\gamma}[f_{eq}(\mathbf{v}+\mathbf{z})h(\mathbf{v}+\mathbf{y}) + h(\mathbf{v}+\mathbf{z})f_{eq}(\mathbf{v}+\mathbf{y})]d\mathbf{y}d\mathbf{z}$ after

[1] The use of special collision kernels has been justified in the previous Chapter.

the Carleman-like representation. Since the interchange of $\mathbf{y}$ and $\mathbf{z}$ does not change the linearised gain term, Eq. (3.2) can be simplified to the following form

$$\begin{aligned}\widehat{\mathcal{L}}_{g\mathbf{j}} \approx & \frac{8}{Kn'} \sum_{p,q=1}^{M} \sum_{\substack{\mathbf{l}+\mathbf{m}=\mathbf{j} \\ \mathbf{l},\mathbf{m}=-(N_1,N_2,N_3)/2}}^{(N_1,N_2,N_3)/2-1} \omega_p \omega_q [\hat{f}_{eq}(\mathbf{l}) \phi_{\alpha+\gamma}(\xi_{\mathbf{l}}, \theta_p, \varphi_q)] \cdot [\hat{h}_{\mathbf{m}} \psi_{\gamma}(\xi_{\mathbf{m}}, \theta_p, \varphi_q)] \cdot \sin\theta_p \\ & - \frac{4}{Kn'} \sum_{\substack{\mathbf{l}+\mathbf{m}=\mathbf{j} \\ \mathbf{l},\mathbf{m}=-(N_1,N_2,N_3)/2}}^{(N_1,N_2,N_3)/2-1} \hat{f}_{eq}(\mathbf{l}) \cdot [\hat{h}_{\mathbf{m}} \phi_{loss}],\end{aligned}$$

or

$$\begin{aligned}\widehat{\mathcal{L}}_{g\mathbf{j}} \approx & \frac{8}{Kn'} \sum_{p,q=1}^{M} \sum_{\substack{\mathbf{l}+\mathbf{m}=\mathbf{j} \\ \mathbf{l},\mathbf{m}=-(N_1,N_2,N_3)/2}}^{(N_1,N_2,N_3)/2-1} \omega_p \omega_q [\hat{h}_{\mathbf{l}} \phi_{\alpha+\gamma}(\xi_{\mathbf{l}}, \theta_p, \varphi_q)] \cdot [\hat{f}_{eq}(\mathbf{m}) \psi_{\gamma}(\xi_{\mathbf{m}}, \theta_p, \varphi_q)] \cdot \sin\theta_p \\ & - \frac{4}{Kn'} \sum_{\substack{\mathbf{l}+\mathbf{m}=\mathbf{j} \\ \mathbf{l},\mathbf{m}=-(N_1,N_2,N_3)/2}}^{(N_1,N_2,N_3)/2-1} \hat{f}_{eq}(\mathbf{l}) \cdot [\hat{h}_{\mathbf{m}} \phi_{loss}].\end{aligned} \tag{3.3}$$

Note that Eq. (3.3) works for all the power-law potentials except for the Coulomb potential. For LJ potential, however, the half reduction in the computational time cannot be achieved. In this case, one may directly use the full BE instead of the linearised one.

3.2 Poiseuille flow between infinite parallel plates

The configuration is similar to that in Figure 2.18(c). Instead of the external acceleration a_1, a uniform pressure gradient is imposed on the gas in the x_1 direction: the pressure is given by $n_0 k_B T_0(1 + \beta_P x_1/\ell)$, where $|\beta_P| \ll 1$. The BE can be linearised around the reference equilibrium state at rest with number density n_0 and temperature T_0, i.e., the VDF is expressed as $f = f_{eq} + \beta_P(x_1 f_{eq} + h)$. The normalisation is presented in Eq. (2.15); the normalised flow velocity is $V_1 = \int v_1 h d\mathbf{v}$, the normalized heat flux is $q_1 = \int \left(|\mathbf{v}|^2 - \frac{5}{2}\right) v_1 h d\mathbf{v}$, and the linearised BE in the dimensionless form reads

$$v_2 \frac{\partial h}{\partial x_2} = \mathcal{L}_g(h) - \nu(v) h - \underbrace{\frac{v_1}{\pi^{3/2}} \exp(-|\mathbf{v}|^2)}_{source}, \tag{3.4}$$

where the source term comes from the pressure gradient.

Because of symmetry, we only consider the half spatial region $-1/2 \leq x_2 \leq 0$ with the specular-reflection boundary condition being imposed at $x_2 = 0$. The diffuse boundary condition is adopted at the wall, i.e., $h(x_2 = -1/2, v_2 > 0) = 0$. The spatial region is divided into 100 uniform cells.

The maximum molecular velocity is at $L = 6$. Because of the symmetry and smoothness of the VDF in the $v_1(> 0)$ and $v_3(> 0)$ directions, 12×12 uniform grids are used. In the discretisation of v_2, $N_2 = 256$ uniform grids are used when $Kn < 1$ and 128 nonuniform velocity grids are used (because of the over-concentration in the VDF) when $Kn \geq 1$. Let $i = -N_2/2 + 1/2, -N_2/2 + 3/2, \cdots, N_2/2 - 1/2$, the velocity is discretised as $v_2 = i^n L/(N_2/2 - 1/2)^n$. For $Kn < 1$, $1 \leq Kn \leq 10^4$, and $Kn > 10^4$, we choose $n = 1$, 3, and 7, respectively.

The number of the frequency components in the ξ_1 and ξ_3 directions are 24. For uniform velocity discretisation, the multi-resolution scheme [50] is used in the ξ_2 direction: in the evolution of the collision operator, only $N_2' = 32 \sim 64$ central frequency components are used. For nonuniform velocity discretisation, the corresponding frequency domain is still divided into $32 \sim 64$ equidistant points. The FFT is used in the v_1 and v_3 directions, while in the v_2 direction, the direct sum is employed to implement the Fourier transformation, resulting in the computational cost at the order of $O[N_2 N_2' N_1 N_3 \ln(N_1 N_3)]$, which becomes comparable to the convolution sum of Eq. (2.25). In the approximation of the kernel mode (2.28), the Gauss-Legendre quadrature with $M = 6 \sim 8$ is used. The symmetry in the v_3 direction and the antisymmetry in the v_1 direction allow us to use $p, q = 1, 2, \cdots, M/2$ in Eq. (3.3).

To obtain the stationary solution, the following implicit iteration scheme is used:

$$\nu h^{k+1} + v_2 \frac{\partial h^{k+1}}{\partial x_2} = \mathcal{L}_g(h^k) - \frac{v_1}{\pi^{3/2}} \exp(-|\mathbf{v}|^2). \tag{3.5}$$

where $\partial h/\partial x_2$ is approximated by the second-order up-wind finite difference method. The iteration is terminated when the net massflow rate $M[h_P] = 2\int_{-1/2}^{0} V_1 dx_2$ and heat flow rate $Q[h_P] = 2\int_{-1/2}^{0} q_1 dx_2$ between two consecutive iteration step are less than 10^{-8}. As shown in Figure 2.20, the number of iterations is roughly in inverse proportion to the Kundsen number. At large Kn, the results are obtained within 1 minute because several iterations are enough. Typical profiles of VDFs demonstrating

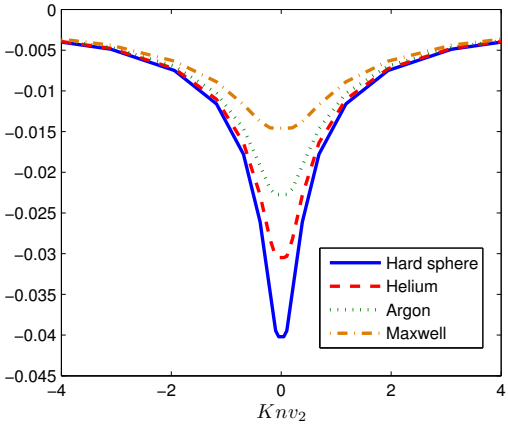

(a) $x_2 = 0$

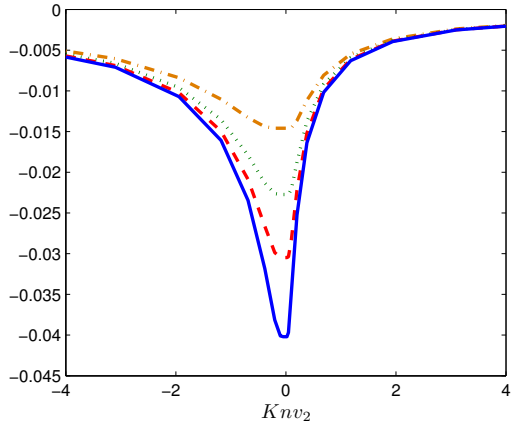

(b) $x_2 = -\frac{1}{4}$

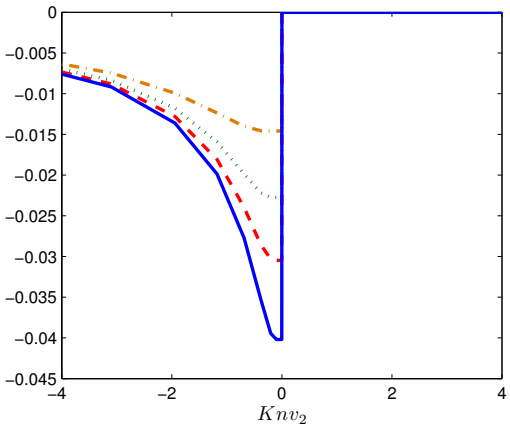

(c) $x_2 = -\frac{1}{2}$

Figure 3.1: VDFs h_P at $v_1, v_3 = 6/31$ in the Poiseuille flow when $Kn = 10^4$.

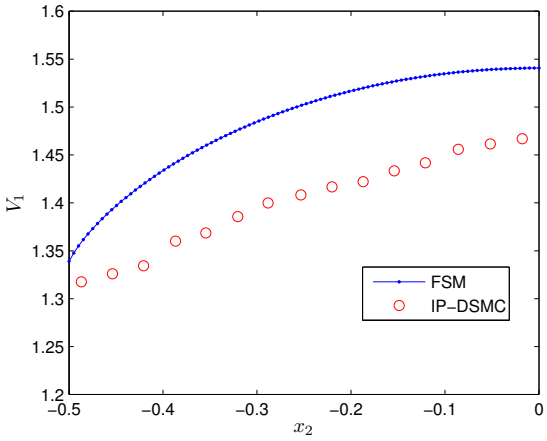

Figure 3.2: Comparison of the velocity profiles obtained from the FSM and IP-DSMC in a gas of hard sphere molecules when $Kn_{VHS} = 100$.

Table 3.1: Comparisons between the mass and heat flow rates in the Poiseuille flow between parallel plates in a gas of hard sphere molecules. The heat flow rate in the last column is obtained by the Onsager-Casimir relation. Note that for hard sphere molecules, we have $k = 8Kn/5\sqrt{\pi}$.

	FSM		Ref. [70]		Ref. [69]	
k	$-M[h_P]$	$Q[h_P]$	$-M[h_P]$	$Q[h_P]$	$-M[h_P]$	$Q[h_P]$
0.1	1.1957	0.0550	1.1930	0.0553	-	-
0.15	0.9948	0.0759	0.9938	0.0761	-	-
0.2	0.9003	0.0933	0.8999	0.0935	-	-
0.3	0.8152	0.1207	0.8152	0.1209	-	-
0.4	0.7802	0.1418	0.7801	0.1419	-	-
0.6	0.7563	0.1730	0.7562	0.1730	-	-
0.8	0.7533	0.1959	0.7533	0.1958	-	-
1	0.7575	0.2140	0.7574	0.2140	-	-
1.5	0.7771	0.2477	0.7771	0.2477	-	-
2	0.7991	0.2724	0.7991	0.2724	-	-
3	0.8399	0.3083	0.8398	0.3082	-	-
4	0.8750	0.3346	0.8749	0.3345	-	-
6	0.9322	0.3731	0.9321	0.3730	-	-
8	0.9779	0.4016	0.9778	0.4015	-	-
10	1.0160	0.4242	1.0159	0.4242	1.0159	0.4241
15	1.0908	0.4669	1.0908	0.4669	-	-
20	1.1478	0.4984	1.1479	0.4984	1.1477	0.4982
10^2	1.5143	0.6901	-	-	1.5143	0.6900
10^3	2.1210	0.9960	-	-	2.1210	0.9960
10^4	2.7614	1.3165	-	-	2.7615	1.3166
10^5	3.4094	1.6405	-	-	3.4094	1.6406
10^6	4.0587	1.9652	-	-	4.0587	1.9652

the over-concentration phenomena are shown in Figure 3.1. For larger Kn, the width and height of the VDFs scale linearly with Kn, that is, the width is proportional to $1/Kn$, while the height is proportional to Kn (see also the first order soltuion in Ref. [69]).

To validate the FSM for the linearised BE, our numerical results are compared to those in Refs. [69, 70] for a gas of hard sphere molecules. It is seen from Table 3.1 that for $k \geq 0.3$, the absolute errors between the two methods in the mass and heat flow rates are less than 2×10^{-4} (the errors are less than 2×10^{-3} when $M = 6$). When k is small, the maximum absolute errors between the mass flow rate and heat flow rate are 2.7×10^{-3} and 3×10^{-4}, respectively. This demonstrates the high accuracy of our method. We also compare our numerical results with those from the IP-DSMC [17]. Figure 3.2 demonstrates that the IP-DSMC are not so accurate at large Kn, where the

Table 3.2: Comparisons between the mass and heat flow rates in the Poiseuille flow between parallel plates for different molecular models.

	Hard Sphere		Helium		Argon		Maxwell	
Kn	$-M[h_P]$	$Q[h_P]$	$-M[h_P]$	$Q[h_P]$	$-M[h_P]$	$Q[h_P]$	$-M[h_P]$	$Q[h_P]$
0.3	0.8331	0.1135	0.8375	0.1144	0.8419	0.1155	0.8477	0.1175
0.4	0.7909	0.1341	0.7938	0.1343	0.7969	0.1349	0.8013	0.1362
0.6	0.7599	0.1649	0.7606	0.1636	0.7618	0.1630	0.7641	0.1629
0.8	0.7531	0.1875	0.7522	0.1850	0.7520	0.1832	0.7526	0.1818
1	0.7550	0.2056	0.7527	0.2018	0.7513	0.1989	0.7505	0.1963
2	0.7908	0.2636	0.7840	0.2553	0.7785	0.2485	0.7727	0.2413
3	0.8287	0.2992	0.8191	0.2879	0.8109	0.2784	0.8018	0.2680
4	0.8620	0.3252	0.8502	0.3117	0.8399	0.3002	0.8282	0.2873
6	0.9168	0.3632	0.9019	0.3465	0.8885	0.3320	0.8727	0.3155
8	0.9609	0.3912	0.9437	0.3722	0.9280	0.3554	0.9091	0.3362
10	0.9979	0.4134	0.9789	0.3927	0.9613	0.3742	0.9398	0.3527
20	1.1264	0.4863	1.1019	0.4602	1.0784	0.4361	1.0480	0.4072
10^2	1.4883	0.6762	1.4532	0.6398	1.4168	0.6042	1.3643	0.5570
10^3	2.0927	0.9815	2.0502	0.9381	2.0035	0.8934	1.9299	0.8287
10^4	2.7284	1.2964	2.6860	1.2537	2.6382	1.2084	2.5589	1.1394
10^5	3.3806	1.6261	3.3356	1.5804	3.2853	1.5324	3.2031	1.4607
10^6	4.0299	1.9508	3.9849	1.9050	3.9345	1.8569	3.8520	1.7849

maximum error in the velocity profile reaches about 7%.

Next we compare the mass and heat flow rates between the hard sphere molecules, helium ($\omega = 0.66$), argon ($\omega = 0.81$), and the Maxwell molecules. Different behaviours between the four molecular models are observed in Table 3.2. These differences, although small, can be seen when the Knudsen number is large, see Figure 3.3. Denoting Kn_c (≈ 0.9) the Knudsen number where the Knudsen minimum in the mass flow rate exists. When $Kn > Kn_c$ ($Kn < Kn_c$), the mass flow rate decreases (increases) when ω increases, for fixed value of Kn. For instance, at $Kn = 10$, the mass flow rate of the Maxwell molecules is 94% of the hard sphere molecules. The underlying mechanism can be explained as follows: from Figure 2.12 we see that, for the same value of shear viscosity, the average collision frequency $\int \nu(v) f_{eq} dv / \int f_{eq} dv$ increases as ω increases. Therefore, the Maxwell molecules have larger average collision frequency than the hard sphere molecules. Since at large Kn the mass flow rate increases with Kn (the collision frequency decreases), the Maxwell molecules have less mass flow rate than the hard sphere molecules. On contrary, when $Kn < Kn_c$, the Maxwell molecules have more mass flow rate than the hard sphere molecules. The heat flow rate behaves similarly to

the mass flow rate; that is, when $Kn > 0.5$ (or $Kn < 0.5$), the heat flow rate decreases (or increases) as increases, for a fixed value of Kn. Similar behaviours have been observed when the LJ potential is considered [74].

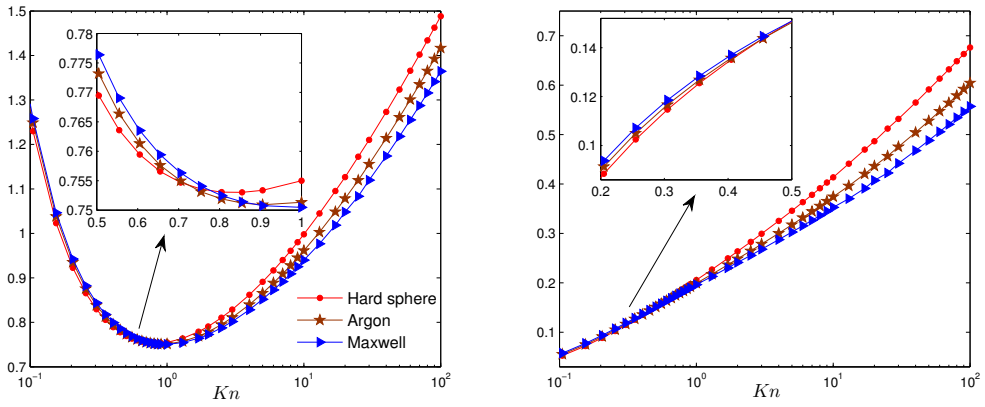

(a) Mass flow rate $-M$ **(b)** Heat flow rate Q

Figure 3.3: Comparisons in mass and heat flow rates for different molecular models in the Poiseuille gas flow between parallel plates. For clarity, the flow rates for helium is not plotted.

3.3 Thermal transpiration between parallel plates

In thermal transpiration, the wall temperature is $T = T_0(1 + \beta_T x_1/\ell)$, where $|\beta_T| \ll 1$. The VDF is expressed as $f = f_{eq} + \beta_P[x_1 f_{eq}(|\mathbf{v}|^2 - \frac{5}{2}) + h]$ and the linearised BE is given by Eq. (3.4) except the source term now becomes $\frac{v_1}{\pi^{3/2}}\left(|\mathbf{v}|^2 - \frac{5}{2}\right)\exp(-|\mathbf{v}|^2)$.

The spatial and velocity discretisations as well as the iteration scheme are the same as these in the Poiseuille flow. The mass and heat flow rates are tabulated in Table 3.3. When the molecular model is fixed, the mass and heat flow rates increase monotonically with Kn. Like the Poiseuille flow, different molecular model has different flow rates: for $Kn \geq 0.5$ ($Kn \leq 0.5$), the mass flow rate decreases (increases) when the value of ω increases; the heat flow rate, however, always decreases when ω increases.

The Onsager-Casimir relation states that the mass flow rate in the thermal transpiration is equal to the heat flow rate in the Poiseuille flow. Comparisons in Tables 3.2 and 3.3 show that this relation is held with the absolute error smaller than 10^{-4}. Recently, Takata and Funagane [69] made the important observation that at large Kn, $V_1[h_T]$ and $q_1[h_P]$ are even identical at the level of spatial profile, i.e.,

Table 3.3: Comparisons between the mass flow rate and heat flow in the thermal transpiration between parallel plates for different molecular models.

	Hard Sphere		Helium		Argon		Maxwell	
Kn	$-Q[h_T]$	$M[h_T]$	$-Q[h_T]$	$M[h_T]$	$-Q[h_T]$	$M[h_T]$	$-Q[h_T]$	$M[h_T]$
0.3	0.4767	0.1136	0.4700	0.1144	0.4651	0.1156	0.4607	0.1175
0.4	0.5781	0.1342	0.5700	0.1344	0.5640	0.1350	0.5583	0.1362
0.6	0.7354	0.1649	0.7253	0.1636	0.7175	0.1630	0.7099	0.1629
0.8	0.8546	0.1875	0.8429	0.1849	0.8337	0.1832	0.8245	0.1817
1	0.9501	0.2056	0.9370	0.2018	0.9266	0.1989	0.9160	0.1963
2	1.2575	0.2636	1.2389	0.2553	1.2237	0.2485	1.2073	0.2413
3	1.4429	0.2992	1.4202	0.2879	1.4011	0.2784	1.3799	0.2680
4	1.5769	0.3252	1.5508	0.3117	1.5284	0.3002	1.5031	0.2873
6	1.7696	0.3632	1.7382	0.3465	1.7106	0.3320	1.6784	0.3155
8	1.9095	0.3911	1.8741	0.3722	1.8423	0.3554	1.8044	0.3362
10	2.0200	0.4134	1.9813	0.3927	1.9460	0.3742	1.9034	0.3527
20	2.3755	0.4863	2.3263	0.4601	2.2793	0.4361	2.2192	0.4072
10^2	3.2709	0.6762	3.2003	0.6398	3.1266	0.6041	3.0198	0.5570
10^3	4.6666	0.9815	4.5806	0.9381	4.4851	0.8934	4.3321	0.8287
10^4	6.1043	1.2964	6.0189	1.2537	5.9211	1.2084	5.7557	1.1394
10^5	7.5728	1.6261	7.4817	1.5804	7.3783	1.5324	7.2067	1.4606
10^6	9.0339	1.9508	8.9426	1.9050	8.8390	1.8569	8.6668	1.7849

$V_1[h_T] = q_1[h_P] + O(Kn^{-1}(\ln Kn)^2)$. Our numerical results in Figure 3.4 further show that the agreement is even at the microscopic level, where $h_T \approx (|\mathbf{v}|^2 - \frac{5}{2})h_P$.

The asymptotic mass flow rates at large Kn in the Poiseuille flow and thermal transpiration have also been obtained [69]. It has been found that they increase logarithmically with respect to Kn. For the heat flow rate in the thermal transpiration, we find it can also be well fitted by the logarithmic function of Kn: $Q[h_T] = -0.6345 \ln(Kn) - Q_0$ in the region $10^5 < Kn < 2 \times 10^6$, where the constant Q_0 is 0.2679, 0.1762, 0.07371, and -0.09903 for the hard sphere molecules, helium, argon, and the Maxwell molecules, respectively.

3.4 Poiseuille flow through a rectangular channel

Consider a rarefied gas in a long straight channel along the x_3 axis. The cross section is uniform and rectangle, so that $-\ell/2 < x_1 < \ell/2$ and $-A\ell/2 < x_1 < A\ell/2$, where A

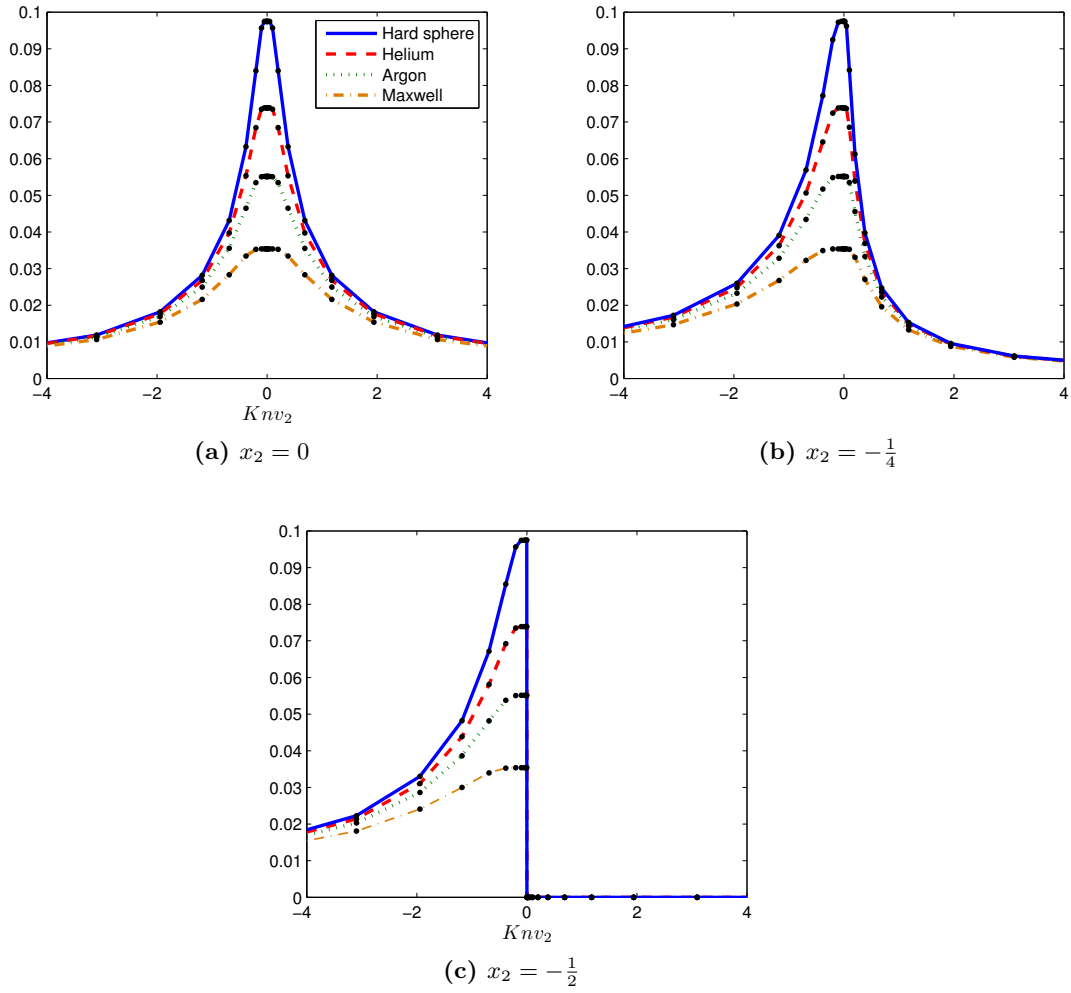

(a) $x_2 = 0$ **(b)** $x_2 = -\frac{1}{4}$ **(c)** $x_2 = -\frac{1}{2}$

Figure 3.4: The Onsager-Casimir relation at the microscopic level. Dots: VDFs h_T in the thermal transpiration with $Kn = 10^4$. Lines: $(|v|^2 - \frac{5}{2})h_P$, where h_P are the VDFs in the Poiseuille flow shown in Figure 3.1. Here $v_1, v_3 = 6/31$.

is the aspect ratio. The linearised BE in the dimensionless form reads

$$v_1 \frac{\partial h}{\partial x_1} + v_2 \frac{\partial h}{\partial x_2} = \mathcal{L}_g(h) - \nu(v)h - \frac{v_3}{\pi^{3/2}} \exp(-|\mathbf{v}|^2). \tag{3.6}$$

The normalised mass and heat flow rates are $M[h_P] = (4/A)\int_{-A/2}^{0}\int_{-1/2}^{0} V_3 dx_1 dx_2$ and $M[h_P] = (4/A)\int_{-A/2}^{0}\int_{-1/2}^{0} q_3 dx_1 dx_2$, respectively, where $V_3 = \int v_3 h d\mathbf{v}$ and $q_3 = \int \left(|\mathbf{v}|^2 - \frac{5}{2}\right) v_3 h d\mathbf{v}$. Unlike the Poiseuille flow between parallel plates where the mass and heat flow rates increase logarithmically with Kn, here they saturate when $Kn \to$

Table 3.4: Comparisons between the mass and heat flow rates in the Poiseuille flow through a rectangular channel for hard sphere molecules. The last row: the analytical solutions at $k = \infty$. Note that $Kn = 5\pi k'/16$.

	$A = 1$				$A = 2$			
	FSM		Ref. [40]		FSM		Ref. [40]	
k'	$-M[h_P]$	$Q[h_P]$	$-M[h_P]$	$Q[h_P]$	$-M[h_P]$	$Q[h_P]$	$-M[h_P]$	$Q[h_P]$
0.1	0.6116	0.0445	0.613	0.045	0.9009	0.0476	0.905	0.048
0.2	0.4691	0.0716	0.470	0.072	0.6676	0.0790	0.668	0.079
0.3	0.4260	0.0889	0.426	0.089	0.5950	0.1013	0.595	0.101
0.4	0.4066	0.1010	0.407	0.101	0.5616	0.1175	0.562	0.118
0.5	0.3960	0.1103	0.396	0.110	0.5433	0.1301	0.544	0.130
0.6	0.3898	0.1174	0.390	0.117	0.5322	0.1401	0.532	0.140
0.8	0.3833	0.1280	0.383	0.128	0.5203	0.1554	0.520	0.156
1	0.3811	0.1356	0.381	0.136	0.5141	0.1664	0.515	0.167
2	0.3806	0.1558	0.380	0.156	0.5108	0.1977	0.512	0.198
3	0.3835	0.1656	0.383	0.166	0.5148	0.2131	0.516	0.214
4	0.3862	0.1717	0.386	0.172	0.5191	0.2230	0.520	0.223
5	0.3886	0.1760	0.388	0.176	0.5228	0.2300	0.523	0.230
6	0.3906	0.1792	0.390	0.179	0.5261	0.2352	0.527	0.236
8	0.3938	0.1837	0.394	0.184	0.5314	0.2428	0.532	0.243
10	0.3963	0.1869	0.396	0.187	0.5354	0.2481	0.536	0.248
20	0.4033	0.1948	-	-	0.5479	0.2613	-	-
50	0.4102	0.2016	-	-	0.5596	0.2734	-	-
10^2	0.4136	0.2048	-	-	0.5657	0.2791	-	-
10^3	0.4183	0.2089	-	-	0.5742	0.2865	-	-
10^4	0.4191	0.2095	-	-	0.5758	0.2878	-	-
∞	0.4194	0.2097	0.4194	0.2097	0.5762	0.2881	0.5762	0.2881

∞: the mass flow rate is

$$M_P = \frac{-1}{4\sqrt{\pi}}\left[\frac{2(A^3+1)}{3A} - \frac{2(A^2+1)^{3/2}}{3A} + \ln\frac{(A^2+1)^{1/2}+A}{(A^2+1)^{1/2}-A} + A\ln\frac{(A^2+1)^{1/2}+1}{(A^2+1)^{1/2}-1}\right], \tag{3.7}$$

and the heat flow rate is $Q_P = -M_P/2$, which are only functions of the aspect ratio of the rectangular channel and independent of the molecular model [75].

This problem was first solved by the numerical kernel method [40] and then by the low-noise DSMC [25] for hard sphere molecules. It is reported that the agreement in the mass flow rate between the two methods is better than 1%. We solve this problem in a 80×80 spatial-uniform cells for $A = 1$ and 2. In the discretisation of velocity space, we set $v_1, v_2 = i^n L/(N_2/2-1/2)^n$ with $i = -N_2/2+1/2, -N_2/2+3/2, \cdots, N_2/2-1/2$. We choose $L = 4$, $N_2 = 48$ and $i = 3$ for $Kn \leq 10$ and $N_2 = 64$ and $i = 5$ otherwise.

Due to symmetry, v_3 is uniformly discretised in the region of $[0, 6]$ by 12 cells. Nice agreement in the mass and heat flow rates with Doi's are shown in Table 3.4.

To compare the numerical efficiency with the low-noise DSMC, we consider the hard sphere gas inside a square channels; with a 25×25 spatial cell mesh, $32 \times 32 \times 24$ frequency components, and $M = 6$, we obtain $\mathcal{M} = 0.3808$ and 0.3966, $\mathcal{Q} = 0.1365$ and 0.1874 for $Kn_{vhs} = 1$ and 10, respectively, compared to Doi's 0.381 and 0.396 for $\mathcal{M}$, and 0.136 and 0.187 for $\mathcal{Q}$. The computational time is 100 and 40 *seconds*[2], respectively, compared to the low-noise DSMC that takes 66 and 12 *minutes*[3], respectively. These comparisons indicate that the FSM is an accurate and efficient new numerical method. For smaller Kn, the efficiency of FSM over low-variance DSMC increases more.

We then compare our numerical results with the recent experiment [76], where the aspect ratio is $A = 52.45$ and the working gas is helium ($\omega = 0.66$). Several methods are proposed to explain the experiment [77–79], but none of them is based on the solutions of the BE. In the discretisation of spatial space, 50 and 200 nonuniform grids are used in the x_1 and x_2 directions, respectively, while the same velocity grids are used as that of $A = 1$. To gain better agreement with the experiment, different values of accommodation coefficient α are used[4]. The obtained mass flow rate $Q[h_p]$ has to be transformed to the reduce mass flow rate G by the following equation

$$G(\delta_{in}, \delta_{out}) = \frac{1}{\delta_{out} - \delta_{in}} \int_{\delta_{in}}^{\delta_{out}} Q[h_p](\delta) d\delta, \tag{3.8}$$

where $\delta = \sqrt{\pi}/2Kn$ is a rarefaction parameter, and the subscripts in and out stand for the inlet and outlet, respectively. The reduced mass flow rate no longer depends on the local pressure gradient, but only on the mean value of pressure. Hence the rarefaction parameter δ_m at the mean pressure of the channel is introduced. We consider the experiment data where the inlet to outlet pressure ratio is five, so that $\delta_{in} = 5\delta_m/3$ and $\delta_{out} = \delta_m/3$.

[2]Our Fortran program runs on a computer with an Intel Xeon 3.3 GHz CPU, where only one core is used)

[3]The Fortran program runs on a single core of an Intel Q9650 (3.0 GHz Core 2 Quad processor). The time is obtained when there is 0.1% statistical uncertainty in the mass flow rate. To achieve the same level of uncertainty in the velocity field, the low-noise DSMC would need 240 and 120 minutes, respectively

[4] The wall boundary condition is $h(v_1, v_2, v_3, x_1, x_2 = -A/2) = (1-\alpha)h(-v_1, v_2, v_3, x_1, x_2 = -A/2)$ for $v_1 > 0$ and $h(v_1, v_2, v_3, x_1 = -1/2, x_2) = (1-\alpha)h(v_1, -v_2, v_3, x_1 = -1/2, x_2)$ for $v_2 > 0$.

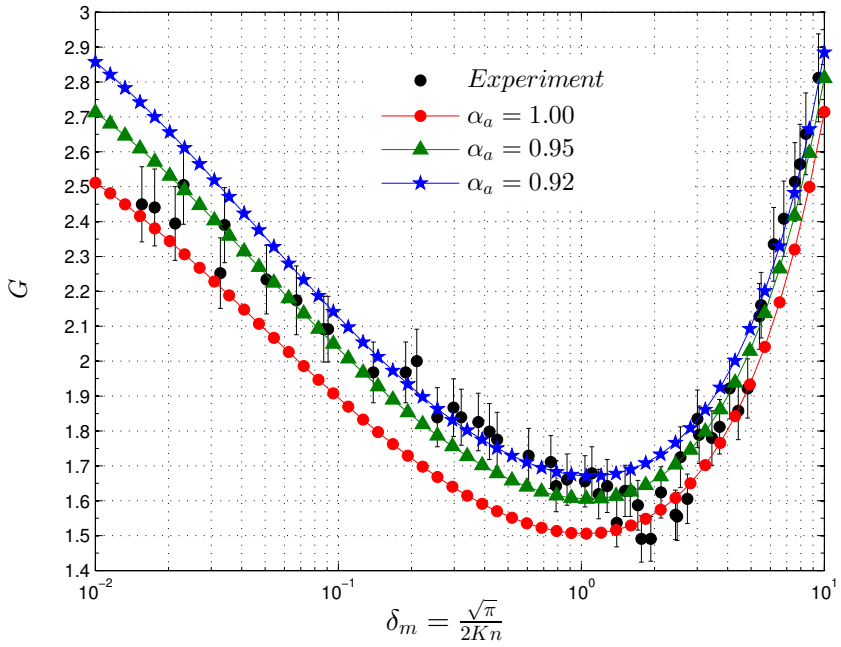

Figure 3.5: Comparison of the mass flow rate in the Poiseuille flow in rectangular tube with the experiment by Ewart *et al* [76] for various values of the accommodation coefficient.

In numerical simulations, the mass flow rate $Q[h_p]$ is obtained at discrete values of the rarefaction parameter. Then the reduced mass flow rate is calculated by Eq. (3.8), where $Q[h_p]$ is obtained by cubic interpolation. Results of the reduced mass flow rate are visualised in Figure 3.5. In the near continuum regime ($\delta \geq 6$), the experimental mass flow rates can be well fitted by the numerical results from the BE with the accommodation coefficient $\alpha = 0.92$. In the region $1 \leq \delta < 6$, the experimental data can be fitted by the numerical results $\alpha = 0.92 \sim 1$. For $0.2 \leq \delta \leq 1$, the mass flow rates from the BE with $\alpha = 0.92$ agree with the experimental measurements. When $\delta \leq 0.1$, the BE with $\alpha = 0.95 \sim 1$ agrees well with the experiment.

3.5 Thermal transpiration through a rectangular channel

In the thermal transpiration through a rectangular tube, the source term in Eq. (3.6) is replaced by $v_3\left(|\mathbf{v}|^2 - \frac{5}{2}\right)\exp(-|\mathbf{v}|^2)/\pi^{3/2}$. At the highly rarefied limit [75], the mass flow rate is $M_T = -M_P/2$ and the heat flow rate is $Q_T = 9M_P/4$, where M_P is given by Eq. (3.7). The comparison in the mass and heat flow rates with Doi's results are

Table 3.5: Comparisons between the mass and heat flow rates in the thermal transpiration through a channel with rectangular cross section for hard sphere molecules. Note that $Kn = 5\pi k'/16$.

	$A = 1$				$A = 2$			
	FSM		Ref. [40]		FSM		Ref. [40]	
k'	$-M[h_T]$	$Q[h_T]$	$-M[h_T]$	$Q[h_T]$	$-M[h_T]$	$Q[h_T]$	$-M[h_T]$	$Q[h_T]$
0.1	0.0450	0.1759	0.045	0.176	0.0479	0.1842	0.048	0.185
0.2	0.0719	0.2936	0.072	0.294	0.0793	0.3199	0.079	0.320
0.3	0.0891	0.3748	0.089	0.375	0.1014	0.4205	0.101	0.421
0.4	0.1012	0.4341	0.102	0.434	0.1176	0.4976	0.118	0.498
0.5	0.1103	0.4794	0.110	0.479	0.1302	0.5587	0.130	0.560
0.6	0.1174	0.5153	0.118	0.514	0.1403	0.6085	0.140	0.609
0.8	0.1279	0.5690	0.128	0.568	0.1556	0.6852	0.155	0.686
1	0.1356	0.6077	0.136	0.606	0.1668	0.7433	0.167	0.743
2	0.1560	0.7098	0.156	0.708	0.1980	0.9003	0.198	0.900
3	0.1658	0.7571	0.166	0.756	0.2135	0.9762	0.214	0.976
4	0.1719	0.7856	0.172	0.784	0.2233	1.0229	0.223	1.023
5	0.1761	0.8052	0.176	0.804	0.2303	1.0553	0.230	1.055
6	0.1793	0.8197	0.179	0.818	0.2355	1.0795	0.236	1.079
8	0.1839	0.8399	0.184	0.839	0.2431	1.1136	0.243	1.113
10	0.1870	0.8536	0.187	0.852	0.2484	1.1370	0.248	1.136
20	0.1950	0.8867	-	-	0.2618	1.1942	-	-
50	0.2017	0.9138	-	-	0.2736	1.2420	-	-
10^2	0.2048	0.9258	-	-	0.2792	1.2636	-	-
10^3	0.2089	0.9406	-	-	0.2866	1.2909	-	-
10^4	0.2095	0.9430	-	-	0.2878	1.2954	-	-
∞	0.2097	0.9436	0.2097	0.9436	0.2881	1.2965	0.2881	1.2965

shown in Table 3.5, where very good agreements can be found.

3.6 Summary

The FSM has been extended to solve the linearised BE for the Poiseuille flow and thermal transpiration in both one- and two-dimensional geometry. Comparison with the existing experimental data and numerical method demonstrates that the FSM is an efficient and accurate method.

Chapter 4

Kinetic model equations for classical gases

The complicated nature of the Boltzmann collision operator has stimulated the search for several kinetic models. The general idea of kinetic modelling is to replace the Boltzmann collision operator by simpler expressions, not only making the problems tractable analytically, but also reducing the computational cost to the order of $O(N^3)$ or even less (by introducing reduced VDFs). In this Chapter, as an application of the FSM, we check the accuracy of the well-known kinetic models by comparing their solutions to these of the BE. A new kinetic model, which can minimise the difference between its collision operator to that of the BE, is proposed.

4.1 Kinetic modelling

Several considerations are suggested to simplify the Boltzmann collision operator [6]. First, the simplified collision operator must guarantee conservation of mass, momentum and energy. Second, the VDF must reduce to the equilibrium distribution function when the system is in equilibrium. Third, the transport coefficients (such as the shear viscosity and thermal conductivity) derived from the kinetic model equation by the Chapman-Enskog expansion should coincide with those obtained from the BE. Fourth, the H-theorem, which states that production of entropy is always positive and vanishes only if the system is in equilibrium, should be satisfied. Note that while the first and

second requirements are fundamental, and the third one yields consistent solutions with the NSF equations in the continuum flow regime, the fourth one is just a physical requirement which does not guarantee accurate numerical results.

There are two categories of kinetic models, classified by whether the collision frequency is a function of the molecular velocity [80–84] or not. Here we focus on kinetic models with velocity-independent collision frequencies, since they are frequently used in rarefied gas dynamics, although the collision frequency is generally velocity-dependent (except for the ideal Maxwell molecules).

The general form of the kinetic modelled collision operator is

$$Q(f, f_*) = \nu(f_r - f), \tag{4.1}$$

where ν is the collision frequency independent of the molecular velocity and f_r is the reference VDF. The collision frequency is always positive, so the loss term νf shows that molecules are lost at a constant rate, irrespective of their velocities. Different kinetic models have different gain terms (reference VDFs).

4.1.1 BGK model

This model was proposed by Bhatnagar, Gross and Krook [85] and independently by Welander in 1950s [86]. It is the simplest kinetic model ever known, since the reference VDF is the local equilibrium distribution function f_{eq}, defined in Eq. (1.16). The collision frequency is determined in various ways. One of them is to choose

$$\nu = \frac{p}{\mu}, \tag{4.2}$$

so that by solving the BGK equation using the Chapman-Enskog expansion the expression of the shear viscosity μ is the same as that given in the BE.

On the other hand, to recover the correct expression of the thermal conductivity, one chooses

$$\nu = \frac{2p}{3\mu}. \tag{4.3}$$

A shortcoming of the BGK equation is that the correct expressions of the shear

viscosity and thermal conductivity cannot be given simultaneously. As a result, the Prandtl number of the BGK model is unity, instead of 2/3 for monoatomic gases. Nevertheless, the BGK model has been widely used and intensively studied. Usually, for shear-dominated problems, Eq. (4.2) is selected, while for heat-dominated ones, Eq. (4.3) is used. In the following, if without specification, the collision frequency of the BGK model is given by Eq. (4.2).

4.1.2 Ellipsoidal-statistical model

To correct the Prandtl number in the BGK model, Holway proposed a kinetic model by means of the H-theorem in 1966 [87]: he constructed the reference VDF by minimising the entropy function under the conservation of mass, momentum, and energy, and the assumption that the pressure tensor $\mathbf{P}$ is known:

$$\begin{aligned} f_r^{ES} &= \frac{n}{\sqrt{\det[\pi\lambda_{ij}]}} \exp(-\lambda_{ij}^{-1} v_{r_i} v_{r_j}), \\ \lambda_{ij} &= \frac{2k_B T(1-b)}{m}\delta_{ij} + \frac{2bP_{ij}}{nm}, \end{aligned} \tag{4.4}$$

where b is directly related to the Prandtl number, $\mathrm{Pr} = 1/(1-b)$.

The resulting model is known as the ellipsoidal-statistical (ES) model. To recover the correct value of shear viscosity, the collision frequency is chosen as

$$\nu = \frac{p}{\mu(1-b)}. \tag{4.5}$$

Clearly, b should be smaller than unity. There are, however, low bound for b: for f_r^{ES} to have a finite norm, one must choose $b \geq -1/2$. Therefore, the Prandtl number of the ES model varies from 2/3 to positive infinity as b increases from $-1/2$ to 1. Fortunately, to get the correct Prandtl number for monoatomic gas, one chooses the minimum available value $b = -1/2$. In this case, Eq. (4.5) is the same as Eq. (4.3). If $b = 0$, the BGK model can be recovered.

The H-theorem has been proved in 2000, making this model the only kinetic model satisfying the H-theorem and having the correct value of transport coefficients [88]. Since then, the ES model has attracted great attentions.

4.1.3 Shakhov model

The Shakhov (S) model proposed by Shakhov [89–91] is another modification of the BGK model giving the correct Prandtl number, where the reference VDF is

$$f_r^S = f_{eq}\left[1 + \frac{2(1-\mathrm{Pr})m}{5n(k_BT)^2} q \cdot v_r \left(\frac{mv_r^2}{2k_BT} - \frac{5}{2}\right)\right], \tag{4.6}$$

and the collision frequency is given by Eq. (4.2).

Although it has the correct Prandtl number, this model has two shortcomings. First, the H-theorem can be proved only for the linearised S model. In the nonlinear form one can neither prove nor disprove the H-theorem. Second, the VDF may become negative, which is not physical. Despite the two deficiencies, the S model has also been widely used. In most of cases, this model gives quite satisfactory results.

4.1.4 Liu model

A general method for constructing the kinetic model was proposed by Liu in 1990. The reference VDF takes the form of [92]

$$\begin{aligned} f_r^L = f_{eq} &+ f_{eq}\left(\frac{1}{\nu} - \frac{\mu}{nk_BT}\right)\frac{m}{k_BT}\left(v_{r_i}v_{r_j} - \frac{1}{3}v_r^2\delta_{ij}\right)\nabla_j V_i \\ &+ f_{eq}\left(\frac{1}{\nu} - \frac{3\mu}{2nk_BT}\right)\left(\frac{mv_r^2}{2k_BT} - \frac{5}{2}\right)v_{r_i}\nabla_i \ln T. \end{aligned} \tag{4.7}$$

The shortcomings of the Liu model is exactly the same as the S model. The advantage of the Liu model is that, unlike the ES and S models, here ν is a free parameter, due to the fact that the shear stress and heat flux are incorporated simultaneously in a unique way. This freedom allows the possibility to get nice agreements with the BE by adjusting the value of the collision frequency. For instance, for Kramers' problem, choosing $0 \leq 1 - \nu\mu/p \leq 1/5$ can produce accurate slip velocities for hard sphere gases [93].

The Liu model, however, has been rarely used in real applications [93, 94]. The critical reason is that, one just does not know how to choose the collision frequency. In addition, the spatial derivatives make the collision operator nonlocal, whereas the Boltzmann collision operator is localised in space.

4.1.5 Combined ES and S model

Since the ES and S models have explicitly treated the shear stress and heat flux, one may use the combined ES and S model, where the collision frequency can also be arbitrarily chosen. We consider the following reference VDF:

$$f_r^C = \nu_{ES} f_r^{ES} + (1-\nu_{ES}) f_{eq}\left[1 + \frac{1-\Pr(1-b\nu_{ES})}{1-\nu_{ES}} \frac{2m}{5n(k_BT)^2} q\cdot v_r \left(\frac{mv_r^2}{2k_BT} - \frac{5}{2}\right)\right]. \tag{4.8}$$

In order to recover the expressions for shear viscosity and thermal conductivity, we have to choose the collision frequency as

$$\nu = \frac{p}{\mu(1-b\nu_{ES})}. \tag{4.9}$$

The new kinetic model can be viewed as a linear combination of the ES and S models. It reduces to the ES model when $\nu_{ES} = 1$ and to the S model when $\nu_{ES} = 0$. Note that we have two free parameters b and ν_{ES}. Again, b is restricted over the region $[-1/2, +\infty)$ for the finite norm of f_r^{ES}, but ν_{ES} can be an arbitrary value as long as the collision frequency ν is positive. Numerical simulations reveal that, however, the solutions are only sensitive to the product of b and ν_{ES}, instead of the separated values. This may be qualitatively explained as follows. When the traceless shear stress σ_{ij} is small, f_r^{ES} is linearized to $\approx f_{eq}[1 + mb\sigma_{ij}v_{r_i}v_{r_j}/2nk_B^2T^2]$. Hence the reference VDF becomes

$$f_r^C \approx f_{eq} + f_{eq}\frac{mb\nu_{ES}}{2n(k_BT)^2}\sigma_{ij}v_{r_i}v_{r_j} + f_{eq}[1-\Pr(1-b\nu_{ES})]\frac{2m}{5n(k_BT)^2} q\cdot v_r\left(\frac{mv_r^2}{2k_BT} - \frac{5}{2}\right), \tag{4.10}$$

which is solely determined by the product of b and ν_{ES}.

It should be noted that, if the first-order Chapman-Enskog expressions for σ_{ij} and q are used, Eq. (4.10) can be casted into Eq. (4.7) by setting $\Pr = 2/3$. Thus, the combined ES and S model is more general and accurate than the Liu model due to the fact that σ_{ij} and q contain not only the first-order informations, but also other orders.

The open problem in the Liu model and the combined model is how to determine the collision frequency ν. Physically, one should choose the collision frequency so that the collision operator approaches to that of BE as closely as possible.

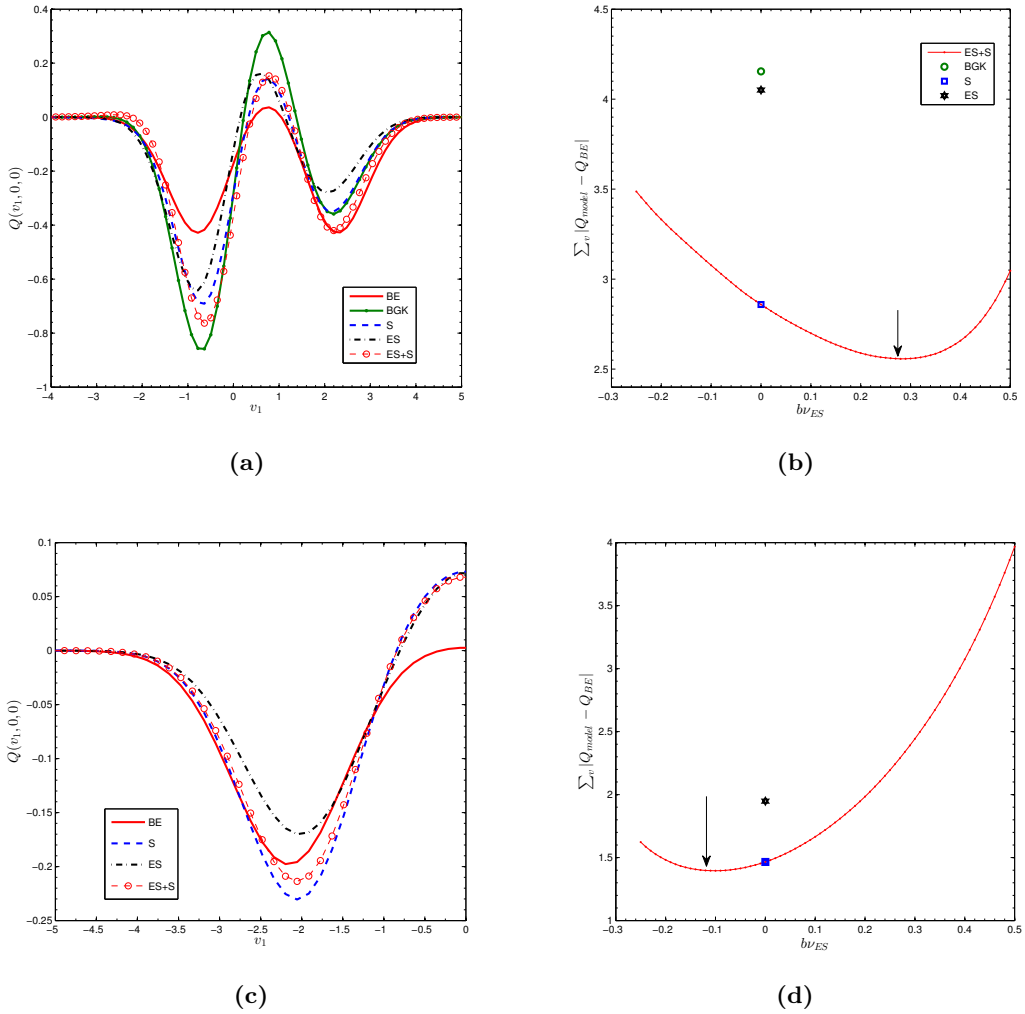

Figure 4.1: Comparison between different collision operators in the spatial-homogeneous relaxation problem. The circles show the collision operator from the combined ES and S model, with $\nu_{ES} = 0.5$ and the value of b being indicated by the arrow.

4.2 Accuracy of the kinetic collision operators

It is interesting to show how accurately the collision operators $Q(f, f_*)$ in various kinetic models approximate the Boltzmann collision operator. Let us first consider a gas of hard sphere molecules. The VDF is $f = \pi^{-3/2} \exp[-(v_1 - 2)^2 - v_2^2 - v_3^2] + 4\pi^{-3/2} \exp[-(v_1 + 0.5)^2 - v_2^2 - v_3^2]$. Profiles of the collision operators are shown in Figure 4.1(a), while deviations of the kinetic collision operators from the Boltzmann collision operator, simply defined as $\sum |Q_{model} - Q_{BE}|$, are shown in Figure 4.1(b). It is seen that, among the BGK, ES, and S models, the deviation is largest for the BGK model and smallest

for the S model. For the combined ES and S model, the deviation is tuned by the values of ν_{ES} and b. Here we set $\nu_{ES} = 0.5$ and vary the value of b. The minimum deviation is achieved at $b \approx 0.56$.

The accuracy of the kinetic collision operators is strongly related to the VDF. We then consider another VDF: $f = \pi^{-3/2}\exp[-(v_1-2)^2-v_2^2-v_3^2]+\pi^{-3/2}\exp[-(v_1+2)^2-v_2^2-v_3^2]$. Due to symmetry, profiles of the collision operators are shown in Figure 4.1(c), with $v_1 \leq 0$. In this case, the S model is the same as the BGK model as the heat flux is zero. The BGK and S models are better than the ES model in terms of the deviation, shown in Figure 4.1(d). For the combined ES and S model, the minimum deviation is achieved at $b \approx -0.2$.

Different behaviours of the kinetic collision operators may be related to the different collision frequencies (relaxation rates of VDFs). Here we only consider the ES, S, and the combined models, since the BGK model does not have the correct Prandtl number. Among the three models, we find that the relaxation of the second- and third-order moments are the same, i.e., $\frac{\partial \sigma_{ij}}{\partial t} = -\frac{p}{\mu}\sigma_{ij}$ and $\frac{\partial q_i}{\partial t} = -\frac{2}{3}\frac{p}{\mu}q_i$, while the relaxation of the VDF is generally different:

$$\begin{aligned}
\frac{\partial f}{\partial t} &= -\frac{2}{3}\frac{p}{\mu}(f - f_r^{ES}), \\
\frac{\partial f}{\partial t} &= -\frac{p}{\mu}(f - f_r^{S}), \\
\frac{\partial f}{\partial t} &= -\frac{1}{1-b\nu_{ES}}\frac{p}{\mu}(f - f_r^{C}).
\end{aligned} \tag{4.11}$$

While the collision frequencies of the VDF in the ES and S models are fixed, the collision frequency in the combined ES and S model varies as the product of b and ν_{ES} changes. Thus, adjusting the values of b and ν_{ES}, one may get different collision frequencies (hence different relaxation rates of high-order moments which may be important in specific problems). This flexibility allows us to get closer results to the Boltzmann collision operator if we let the relaxation rates in the combined ES and S model approach to the "true" ones.

One example is in a gas of hard sphere molecules, where the initial VDF is given by Eq. (2.39) with $t = 0$. Figures 4.2(a) and (b) show that the fourth- and sixth-order moments in S and ES models increase faster than the BE's, and these moments in

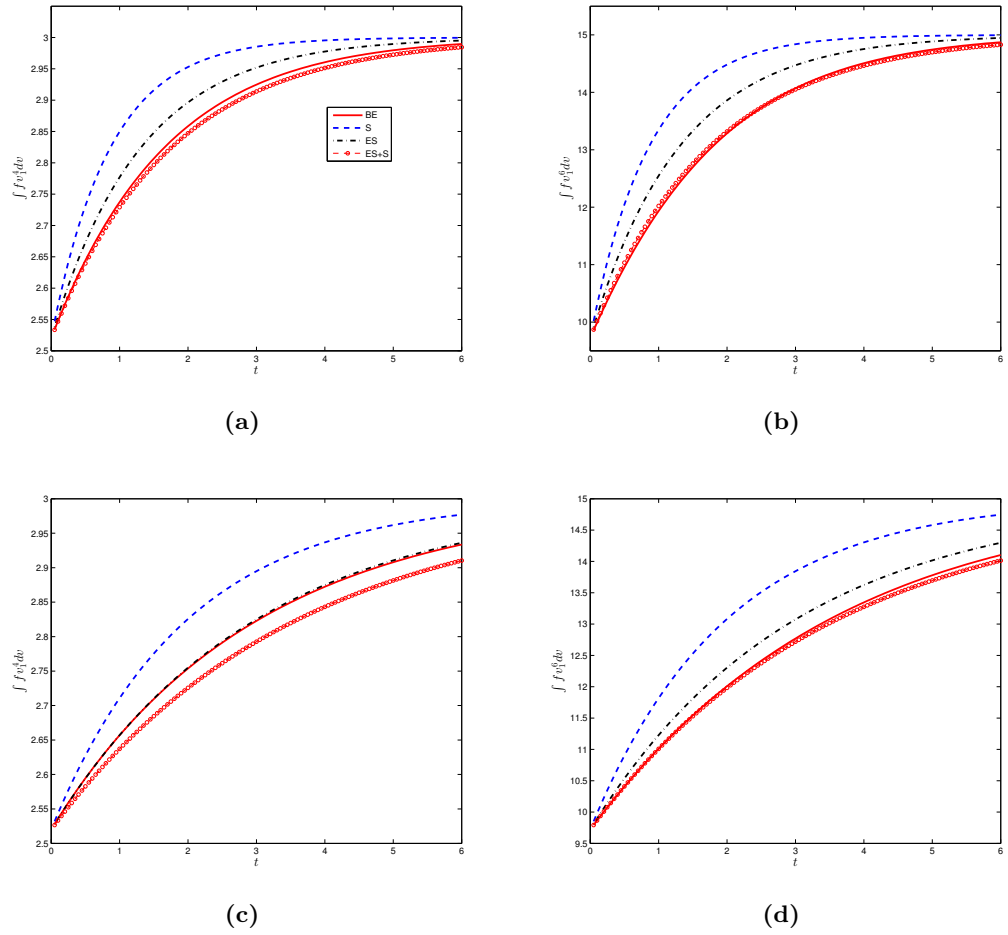

Figure 4.2: Relaxation of the fourth- and sixth-order moments in a gas of (a, b) hard sphere molecules and (c, d) Maxwell molecules.

the S model grow faster than the ES's. From Eq. (4.11) it can be inferred that one should choose $b\nu_{ES} < -0.5$ in the combined model. Indeed, by choosing $\nu_{ES} = 2.5$ and $b\nu_{ES} = -1$, the fourth- and sixth-order moments of the combined ES and S model almost increase in the same rates as those of the BE.

Another example is in a gas of Maxwell molecules. Figure 4.2(c) shows the fourth-order moments of the S model increases faster than these of the BE, while that in the ES model increases in the same rate with the BE. Figure 4.2(d) shows that the sixth-order moments of the S and ES models grow faster than the BE. By choosing $\nu_{ES} = 2.5$ and $b\nu_{ES} = -0.8$, the sixth-order moment in the combined model grows almost in the same rate with the BE's. Unfortunately, the fourth-order moment in the combined model increases slower than the BE.

4.3 Accuracy of the kinetic models

In this section, we will check the accuracy of the kinetic model equations by comparing solutions of the BGK, ES, S, and the combined model equations with the BE in spatial-inhomogeneous problems, both in 1D and 2D geometries.

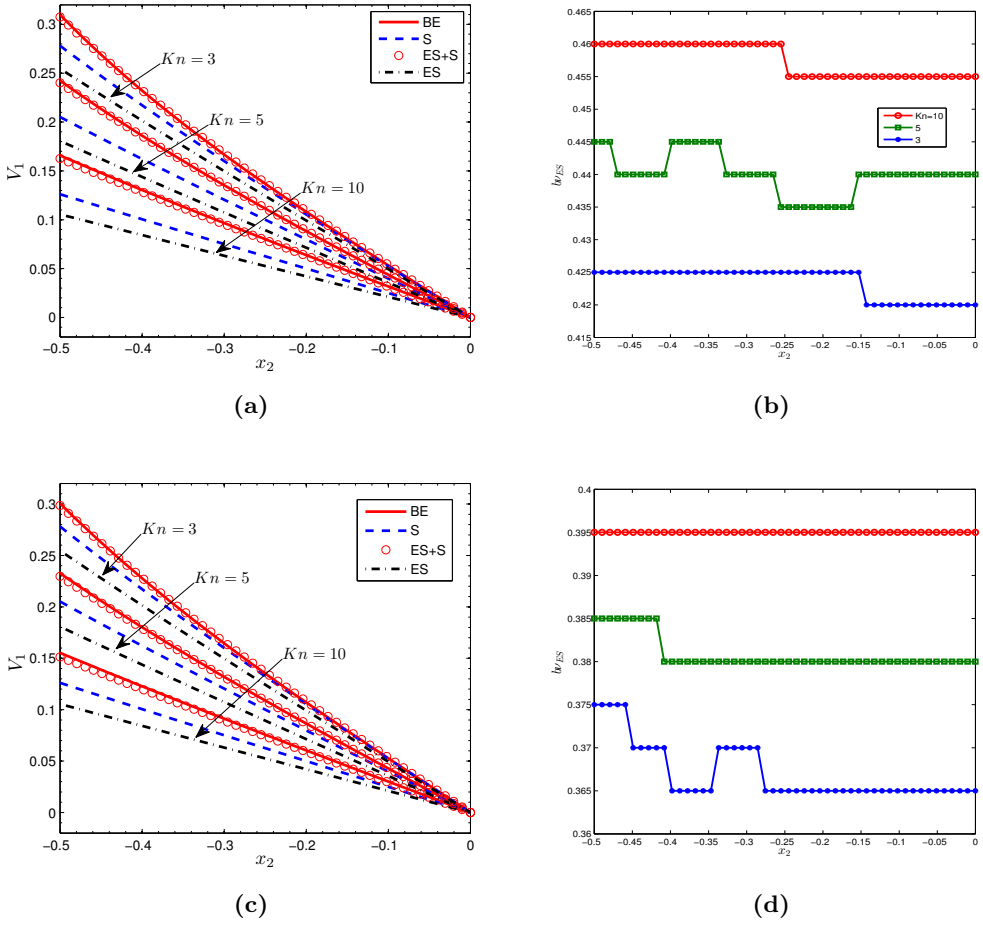

Figure 4.3: Velocity profiles (see also Figure 2.19) in the Couette flow and values of $b\nu_{ES}$ used in the combined ES and S model (ν_{ES} is fixed to be 0.5). The first row: Maxwell molecules. The second row: argon. Note that velocities have been normalised by the wall velocity.

4.3.1 Planar Couette flow

The configuration is shown in Figure 2.18(b). We consider the case where the wall velocity is very small, say, $V_w = 0.01v_m$, so that the system is essentially isothermal. Figures 4.3(a) and (c) show that both ES and S models over-predict velocity slips. From Eq. (4.11) we find that the collision frequency of the ES model is smaller than

the S model. Since the S model has better accuracy than the ES model, we may get close results to the BE by choosing appropriate positive values of $b\nu_{ES}$ in the combined ES and S model, to make the collision frequency larger than that of the S model. For example, for Maxwell gas with $Kn = 10$, 5, and 3, $b\nu_{ES} \approx 0.46$, 0.44, and 0.42 yield very close results to the BE; for argon gas with $Kn = 10$, 5, and 3, $b\nu_{ES} \approx 0.395$, 0.38, and 0.37 yield nice agreements with the BE. It should be noted that, if we increase the collision frequency in the S model or the ES model, the results can be improved, but we cannot get nice velocity profiles in the whole spatial domain.

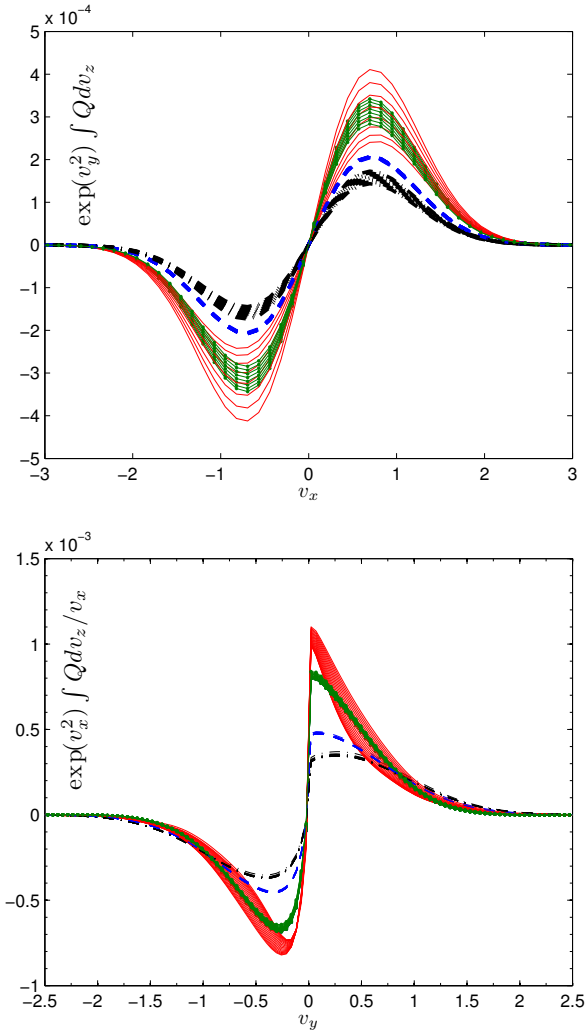

Figure 4.4: Comparison of the collision operator between the kinetic models and BE for Maxwell gas, where the distribution function is chosen at the down plate, obtained by use of the S model when $Kn = 10$. The solid lines, BE; the dashed lines: S model; the dash-dotted lines: ES model; the dotted lines: combined model.

The nice agreements between the combined model and BE are attributed to the fact that, the collision operator of the combined model is close to that of BE in average sense, as clearly illustrated in Figure 4.4. To be specific, the ES model is the worst here because the difference between its collision operator and that of BE is the largest. The combined model is better than the S model because its collision operator is closer to that of BE. This suggests that, in order to get accurate results by use of the combined model, one should minimise the difference between collision operators of the combined model and BE, by varying the value of $b\nu_{ES}$. From many numerical tests, we find that the following parameter

$$\mathcal{D} = \int |Q^C - Q^{BE}| v_r^2 dv \tag{4.12}$$

is a nine measure of the difference between Boltzmann collision operator and the collision operator Q^C of the combined ES and S model.

The procedure in obtaining solutions of the combined ES and S model is: first, we solve the problem by one of the kinetic models (BGK, S, or ES model) and get a nearly converged solutions; second, using the obtained VDFs we calculate the Boltzmann collision operator by the FSM; third, we fixed the value of ν_{ES} (say, 0.5) and vary the value of b to minimize the parameter $\mathcal{D}$. For the planar Couette flow, the obtained values of b are shown in Figure 4.3(b) and (d); finally, we solve the same problem by the combined ES and S model with the obtained b and ν_{ES}, until the stationary state is reached. In this way, the time-consuming FSM is applied only once, hence the computational time can be greatly reduced.

4.3.2 Poiseuille flow

The comparison between the model equations and BE is summarised in Figure 4.5(a) when $0.1 \leq Kn \leq 100$. The Knudsen minimum in the mass flow rate is clearly seen. The BGK and S models produce almost the same results so that only the results of BGK model are shown. For a gas of hard sphere molecules, the ES model overpredicts the mass flow rate by about 10% when the Knudsen number is large, whereas the BGK model only overpredicts it by about 5%. For a gas of Maxwell molecules, the deviations between model equations (BGK and ES models) and the BE are even larger.

Figure 4.5 shows that, when the combined ES and S model is used, we get very

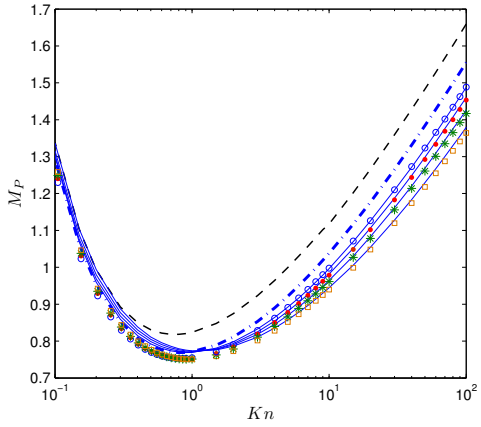

(a) Mass flow rate

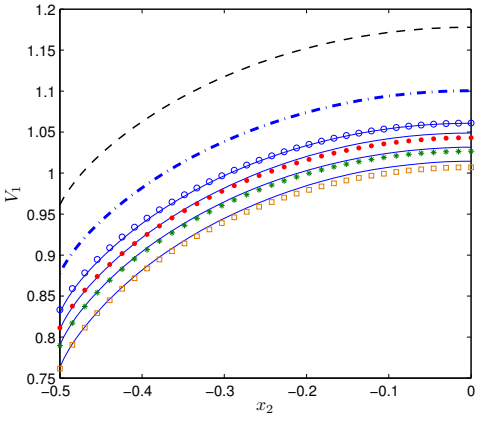

(b) $Kn = 10$

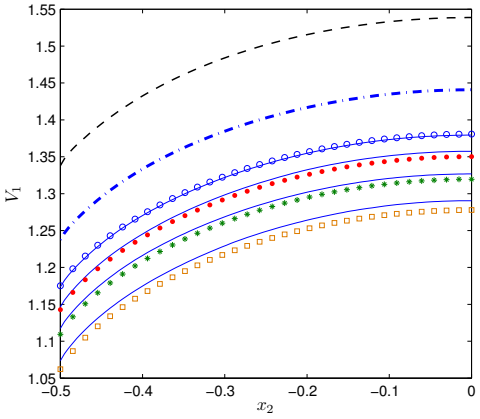

(c) $Kn = 50$

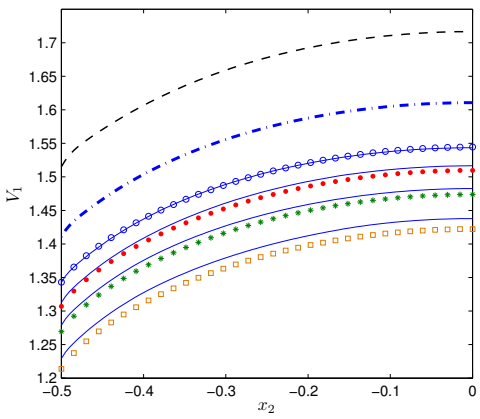

(d) $Kn = 100$

Figure 4.5: Comparisons of mass flow rates and velocity profiles between the model equations and BE in the Poiseuille flow. Dashed line: ES; Dash-dotted line: BGK; Circles: BE for hard sphere molecules; Dots: BE for helium; Stars: BE for argon; Squares: BE for Maxwell molecules. Solid lines: the combined ES and S model ($b\nu_{ES}$ are shown in Figure 4.6).

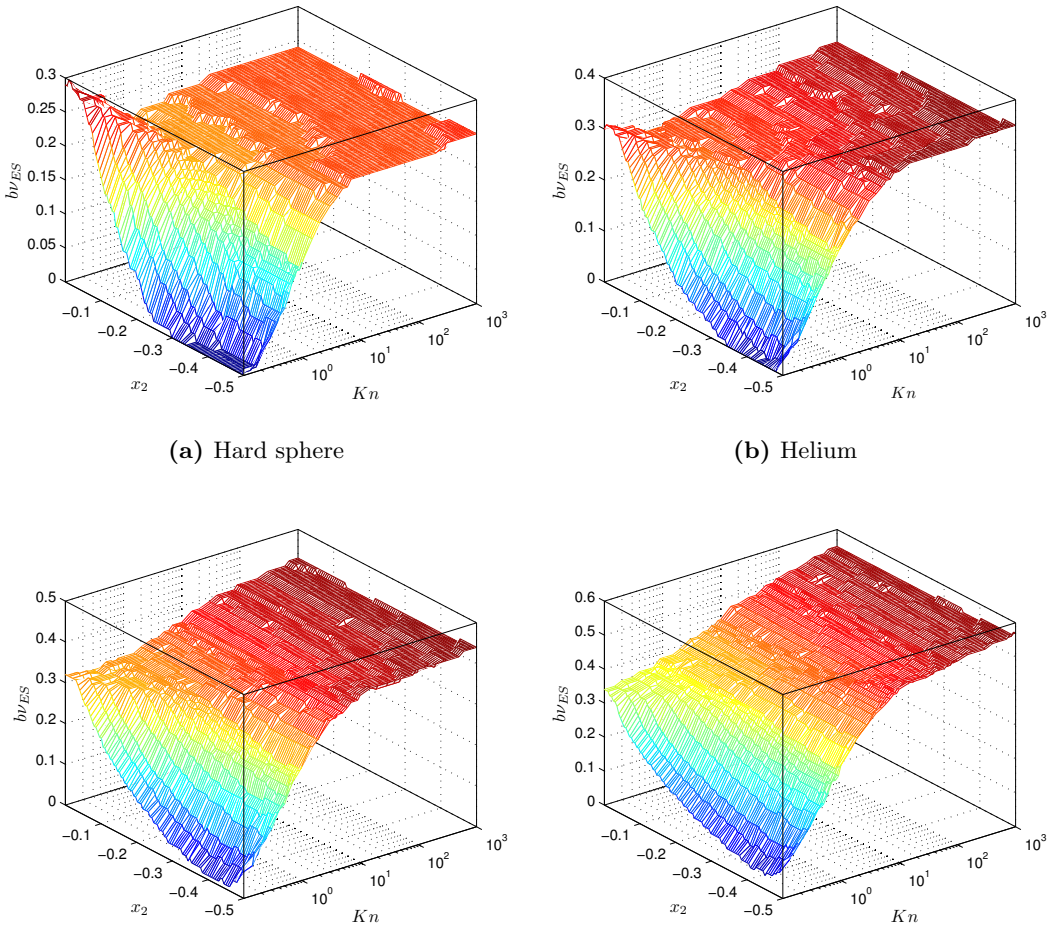

(a) Hard sphere

(b) Helium

(c) Argon

(d) Maxwell

Figure 4.6: Values of $b\nu_{ES}$ used in the combined ES and S model in the Poiseuille flow for different molecular models.

close mass flow rate and velocity profiles to the BE for $Kn \geq 2$, when the distance $\mathcal{D} = \int |Q^C - Q^{BE}| v^2 dv$ is minimised[1]. Interestingly, from Figure 4.6 we see that for large Knudsen numbers, the value of $b\nu_{ES}$ approaches to a constant value. This property has great applications. If we use the combined ES and S model and introduce the reduced VDFs [95], we can get very accurate results for large Knudsen numbers, where $b\nu_{ES}$ is a fixed constant independent of the Knudsen numbers. Furthermore, the computation time is much less than that of BE solvers.

[1] Since it is a linearised problem, the flow velocity is very small. Therefore, v_r in Eq. (4.12) is replaced by v.

4.3.3 Normal shock waves

This case has also been solved by the FSM and the numerical accuracy has been checked by comparisons with DSMC, MD, and experimental data in §2.6.3. Figure 4.7 compares the shock wave structures obtained from the kinetic model equations with the BE in hard sphere gas. It is found that the solution of S model equation is closest to the BE, although there are great deviations in temperature at the upstreaming parts. The BGK model, however, is the worst. When different molecular models are used, the S model is still better than the BGK and ES models. As ω increases from 0.5 to 1, the agreement between the S model and BE gets better and better. For Maxwell molecules, there is almost no difference in the shock structures between the S model and BE (not shown). When the combined ES and S model is used, the results can be improved [96]. However, it is hard to find the appropriate values of b and ν_{ES}.

4.3.4 Rayleigh problem

Sudden change of wall temperature

Consider a semi-infinite expanse of a rarefied Maxwell gas in contact with a stationary plane wall (at $x_1 = 0$, parallel to the x_2 axis, temperature T_0) and in a uniform equilibrium state at rest (temperature T_0, pressure p_0). Suppose that the wall temperature changes discontinuously to another uniform temperature $T_1 = 2T_0$ at time $t = 0$ and is kept at T_1 for all $t > 0$. In order to compare with the results from the BGK model [97], we set $Kn = \pi/4$, so the the BGK model and BE have the same value of shear viscosity. The gas molecules are reflected diffusely on the wall. The BE and kinetic equations are solved by the operator-splitting method.

We are interested in the transition regime, since at early times (compared with the mean collision time) the transport is ballistic, while at late times the NSF equations become appropriate [98, 99]. The results are shown in Figure 4.8. Among all the kinetic models, the BGK model performs the worst, while the S and ES models produce very close results to the BE. Between the S and ES models, in a relative short period of time $t < 10$, it can be found that near the peaks of the velocity profiles, the ES model is better than the S mode, while at the fronts of shocks, the S model is better. For long

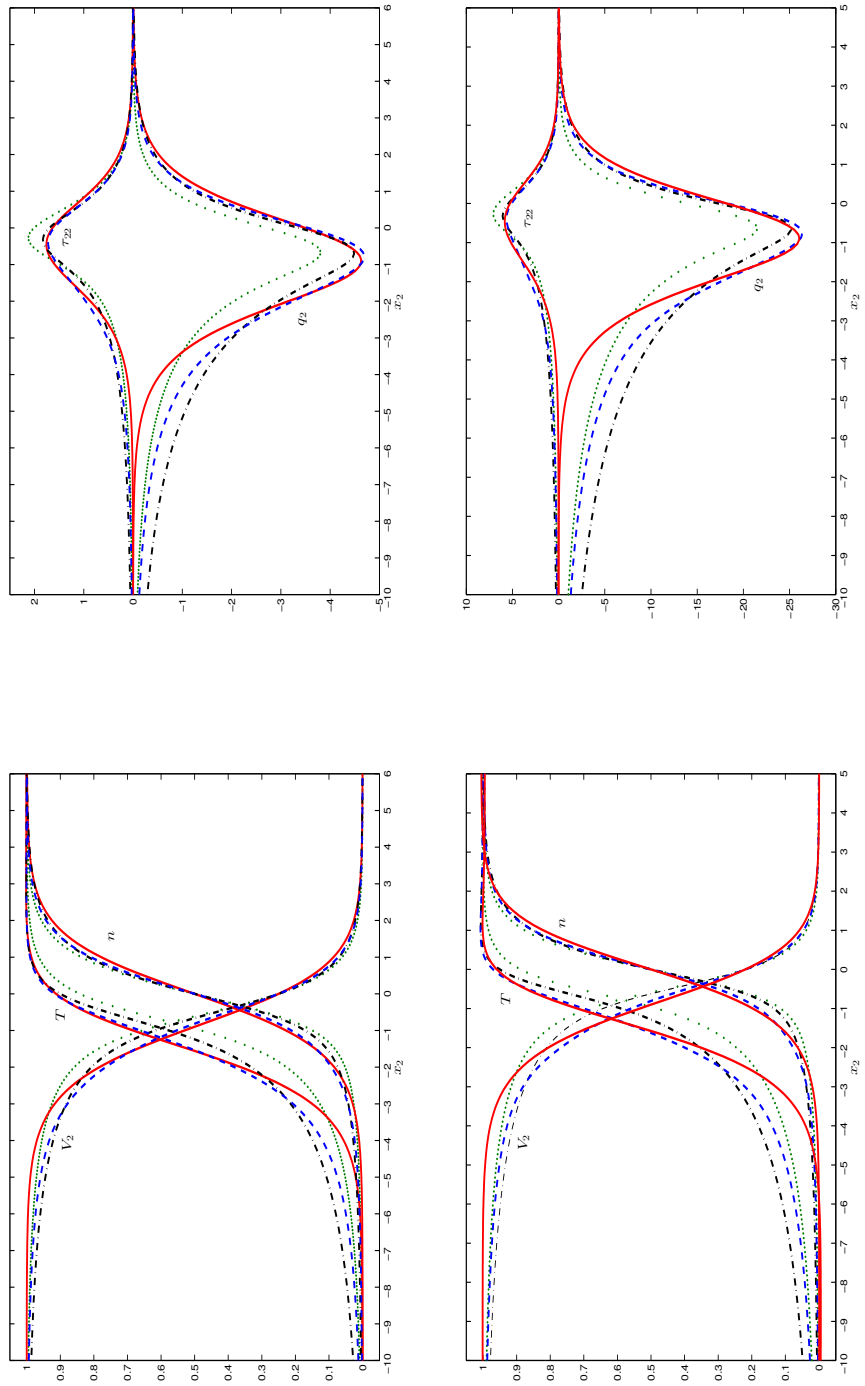

Figure 4.7: Shock wave structures of $Ma = 3$ (the first row, see also Figure 2.15) and 5 (the second row). S model: the blue dashed line, BGK: the green dots, ES: the black dash-dotted lines, and BE: the red solid lines.

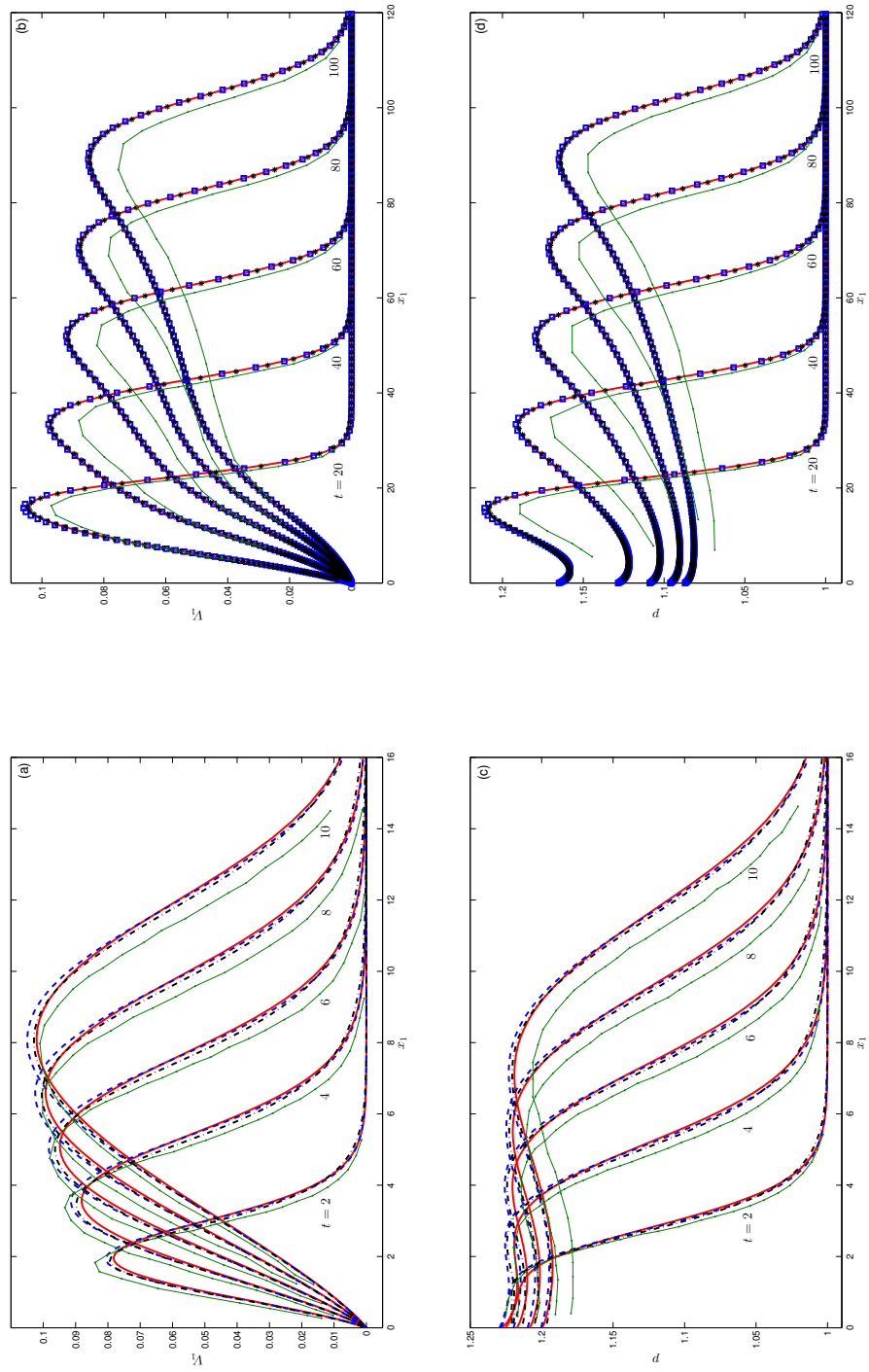

Figure 4.8: Comparison between solutions of the kinetic models and BE for the sudden heat problem. S: blue dashed lines or squares, ES: black dash-dotted lines or stars, BGK: green dotted lines, and BE: red solid lines. The BGK solutions are obtained from [97]. The velocity grids number is $64 \times 24 \times 24$.

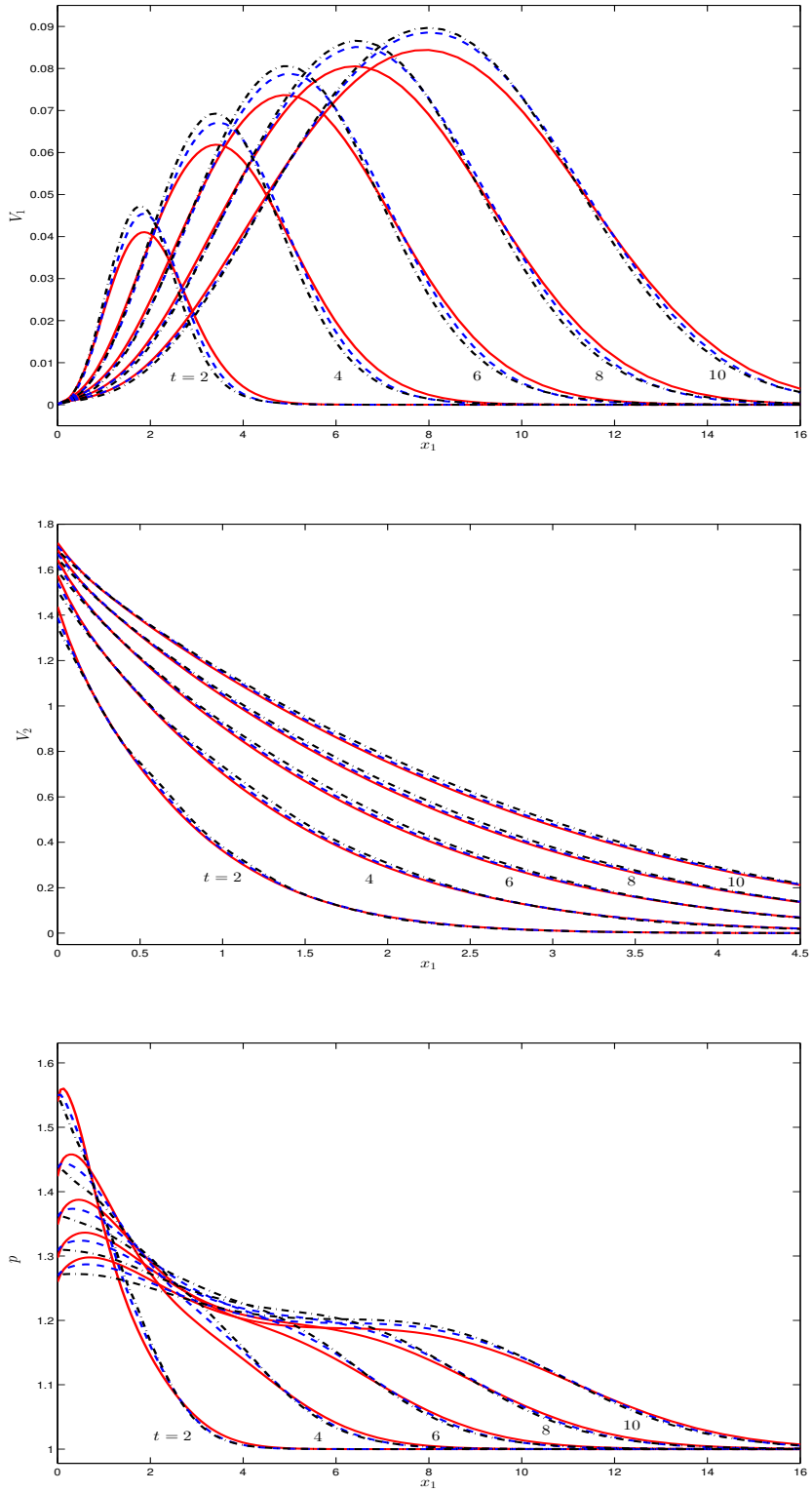

Figure 4.9: Comparison between solutions of the kinetic models and BE for the Rayleigh problem. S: blue dashed lines or squares, ES: black dash-dotted lines or stars, and BE: red solid lines. The velocity grids number is $64 \times 24 \times 24$.

times, both ES and S models yield the identical results with BE.

Sudden change of wall velocity

This case studies the gas flow in the semi-infinite space, where the wall suddenly acquires a velocity $V_w = 2v_m$ in the x_2 direction. Figure 4.9 compares the solutions between the ES, S model, and BE, where it can be found that the S model performs better than the ES model, in contrast to the case where the wall temperature suddenly changes. For long time behaviours, both kinetic models have the same results (not shown).

4.3.5 Lid-driven flow

Consider the lid-driven flow in a square cavity, as was firstly studied using DSMC by John, Gu, and Emerson [100, 101]. Since the velocity near the bottom wall is very small, the computational time of DSMC is extremely high. Even when the velocity of the upper wall is small so that the BE can be linearized, the low-noise DSMC developed by Radtke, Hadjiconstantinou, and Wagner [25] takes more than 1 day to get a resolved result for $Kn_{vhs} = 0.1$. We solve the problem (wall velocity $V_{wall} = 50\text{m/s}$, $T_0 = 273\text{K}$) in a 51×51 non-uniform spatial grids, with $32 \times 32 \times 12$ grids in the velocity space for $Kn_{vhs} = 0.1$ and 1, and $64 \times 64 \times 12$ for $Kn_{vhs} = 10$. For $Kn = 0.1$, our method needs only 90 minutes to produce a converged solution, where the error between the two consecutive iteration steps $\sqrt{\int |V^{k+1} - V^k|^2 dx_1 dx_2 / \int |V^k|^2 dx_1 dx_2}$ is less than 10^{-7}.

Figure 4.10 shows the temperature contours, velocity and heat flux streamlines in the lid-driven flow of argon gas with the diffuse boundary condition. We have also simulated the same problem using the hard sphere molecules. Comparisons in the velocity, temperature, and heat flux profiles between the two molecular models with the same value of shear viscosity are shown in Figure 4.11. The numerical results suggest that the molecular model has little influence on the flow pattern. This may explain why the BGK model with the correct value of shear viscosity can give nice agreements with the DSMC [102].

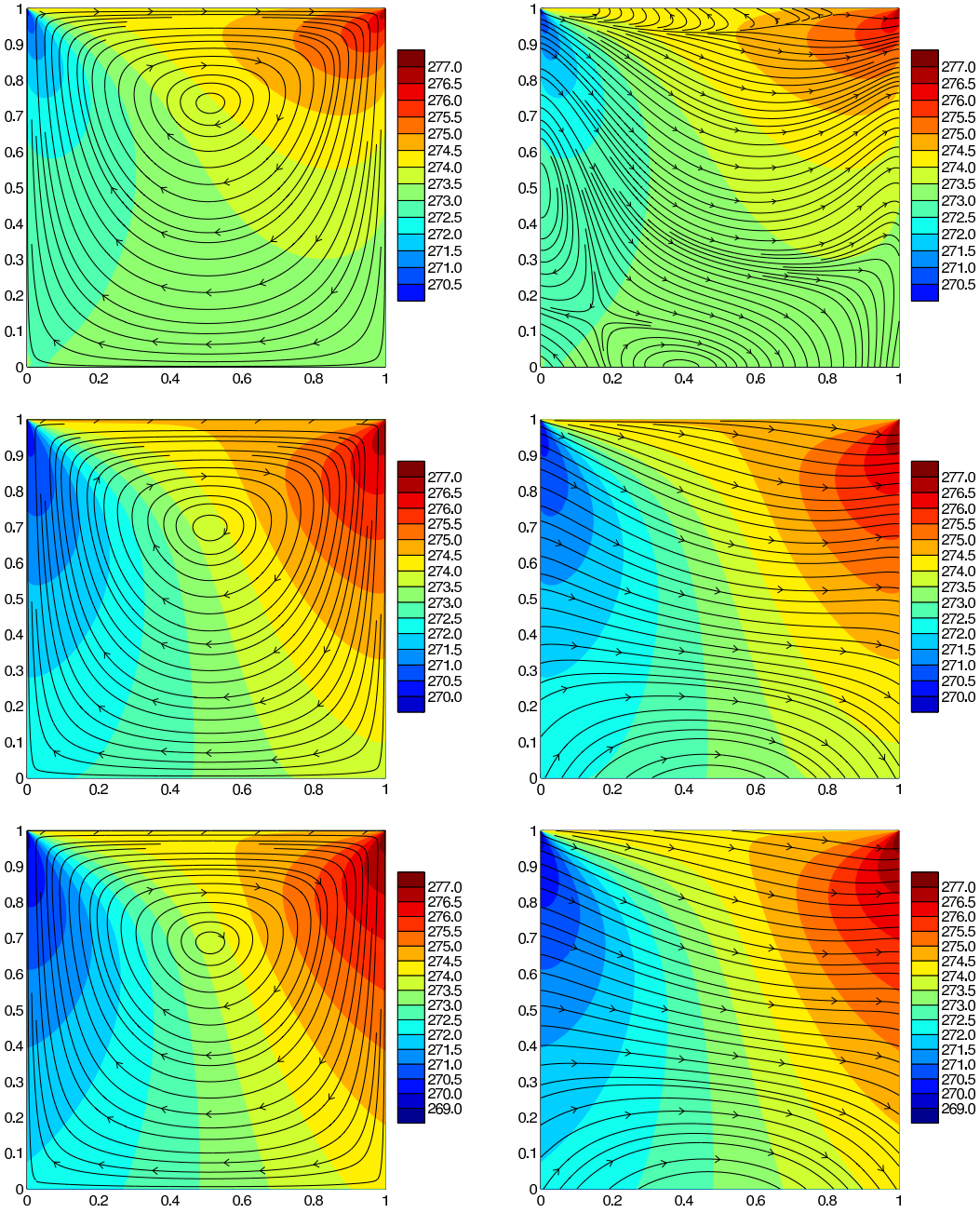

Figure 4.10: Temperature contours and streamlines (velocity: first column; heat flux: second column) in the lid-driven flow of argon gas. From top to bottom, the Knudsen number of each row is $Kn_{vhs} = 0.1$, 1, and 10, respectively.

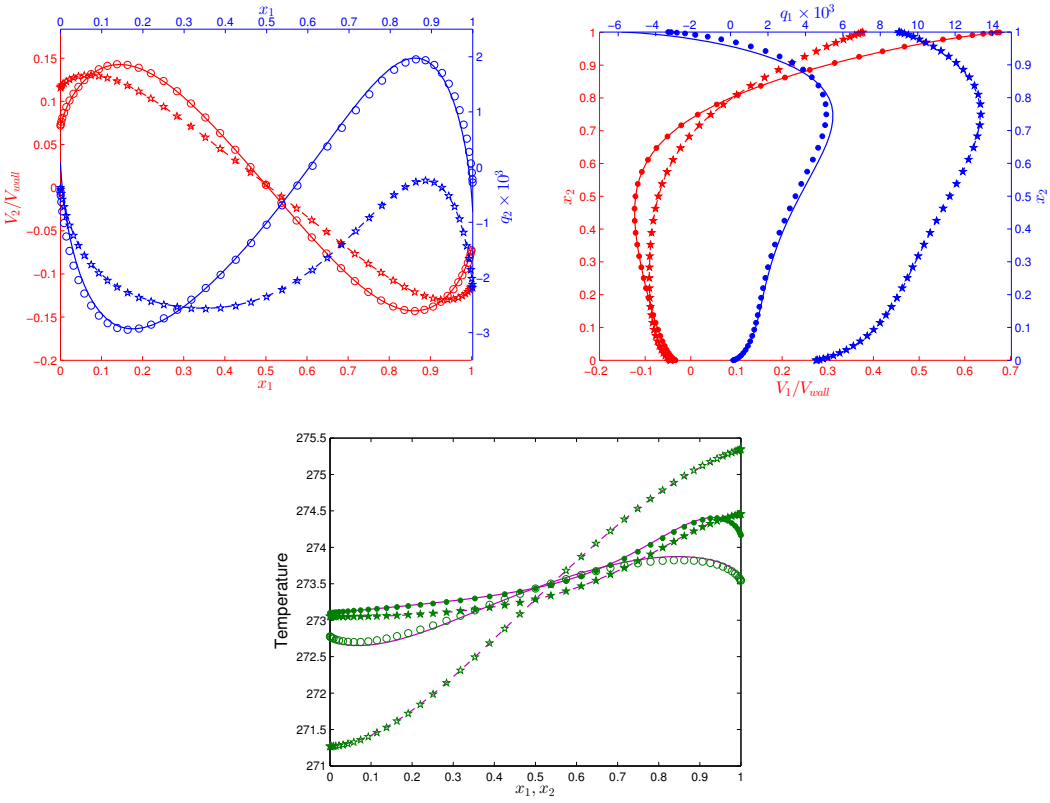

Figure 4.11: Comparisions in velocity, temperature, and heat flux profiles between the argon and hard sphere molecules. The solid (or dashed) lines, results of argon when $Kn_{vhs} = 0.1$ (or 10). The circles (or pentagram), results of hard sphere molecules when $Kn_{vhs} = 0.132$ (or 13.2). The opened (or closed) markers are the results along the central horizontal (vertical) lines.

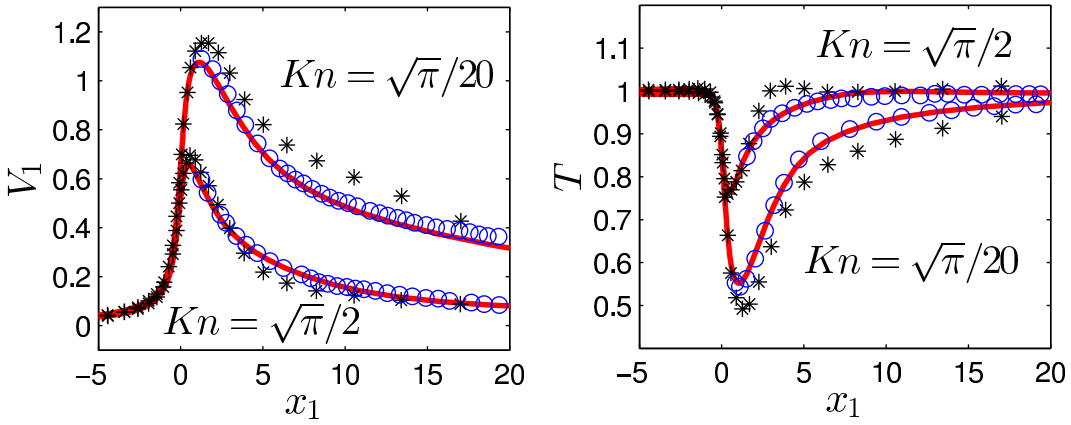

Figure 4.12: Velocity and temperature profiles along the symmetric line through the slit centre. The red solid lines: BE solutions by the FSM. The stars: BE solutions by Tcheremissine's method [33]. The circles, solutions of the S model equations.

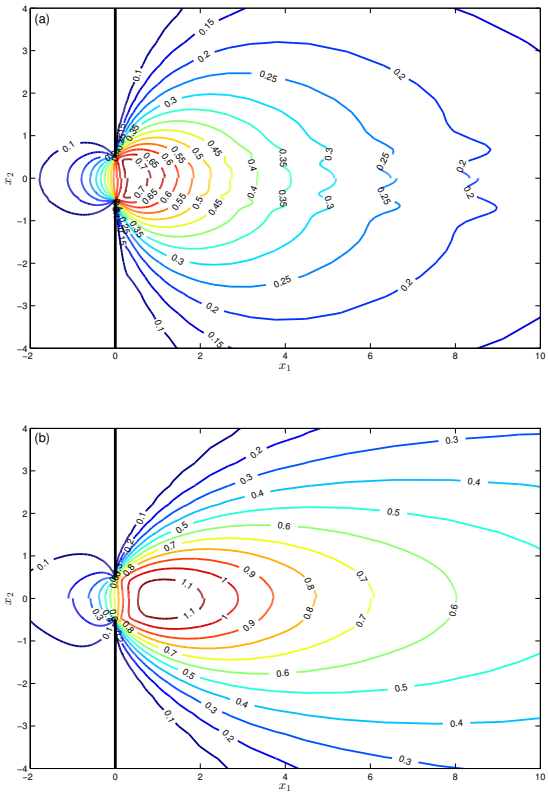

Figure 4.13: Contour of the Mach number $\sqrt{6(V_1^2+V_2^2)/5}$ in the slit flow for (a) $Kn=\sqrt{\pi}/2$ and (b) $Kn=\sqrt{\pi}/20$. The region $x_2>0$ is the solution of the S model equation, while the region $x_2<0$ is that of the BE by the FSM.

4.3.6 Slit flow

This case is exactly the same as the one reported in Ref. [103], where solutions of the S model and the BE were compared. The BE was solved by Tcheremissine's method [33] with $24\times24\times12$ velocity nodes, and the authors claimed that double the grid points number in the velocity space led to the relative error less then 1%. This contradicts with our previous observation that, for large Knudsen number, the velocity grids should be increased to capture the discontinuity in VDFs. Here, we simulate the case where the pressure ratio between the left and right reservoirs is 10. The Knudsen numbers Kn are $\sqrt{\pi}/2$ and $\sqrt{\pi}/20$, respectively, corresponding to $\delta=1$ and $\delta=10$ in Ref. [103]. Flow distributions along the symmetric line through the slit centre are shown in Figure 4.12, where solutions of the S model and the BE (obtained from the FSM) agree very well, while the solutions from Tcheremissine's method deviate a lot from our BE solutions.

These deviations are due to the fact that $24 \times 24 \times 12$ velocity nodes are not enough (for $\delta = 1$ we used $48 \times 96 \times 12$ velocity grids) when the Knudsen number is large.

Figure 4.13 compares the Mach contours between the results of the S model and the BE, where one can find that the two solutions are very close to each other. We have also simulated the ES model and found that the S model is much better. Therefore, the BE can be replaced by the S model equation, to greatly reduce the computational time and memory (since the VDF can be integrated in the v_3 direction in the S model).

4.3.7 Flows arising from temperature variations/discontinuities

Response to spatial-periodic boundary temperature

Consider the response of argon gas to a boundary temperature with a sinusoidal spatial variation. The upper $x_2 = L$ and lower boundary $x_2 = 0$ is diffusely reflecting with a temperature given by $T_w = T_0(1 - \epsilon \cos 2\pi x_1/L)$. The unconfined Knudsen number Kn is 1.3 when the spatial length is normalised by L so that the Knudsen number based on the VHS model is 1. Due to the symmetries in the x_1 and x_2 directions, the simulation domain is chosen as $0 < x_1, x_2 < L/2$. The reflecting boundary condition is chosen for the left, upper, and right walls, while the diffuse boundary condition is used in the bottom wall.

The temperature and velocity profiles are shown in Figure 4.14. When the temperature variation in the wall is small ($\epsilon = 0.05$), the BGK, S, and ES models give close results to the BE, with the ES model being the closest (see at $x_1 \approx 0,1$ and $x_2 \approx 0.5$). However, when the temperature variation is huge ($\epsilon = 0.5$), the BGK and S models do not give accurate results, while the ES model gives almost identical result with the BE for the temperature field. The reduced VDFs are also shown when $\epsilon = 0.5$, demonstrating the necessity of using 128 velocity grids in the v_1 and v_2 directions.

Thermal creep flows with closed walls

Consider the thermal creep flow in a two-dimensional closed rectangular channel with a length-to-width ratio of 5. The temperature at the right side is set to be twice that of the left side, while the temperature of the top and bottom walls varies linearly along the channel. Using the mean density, the temperature of the left wall, and the

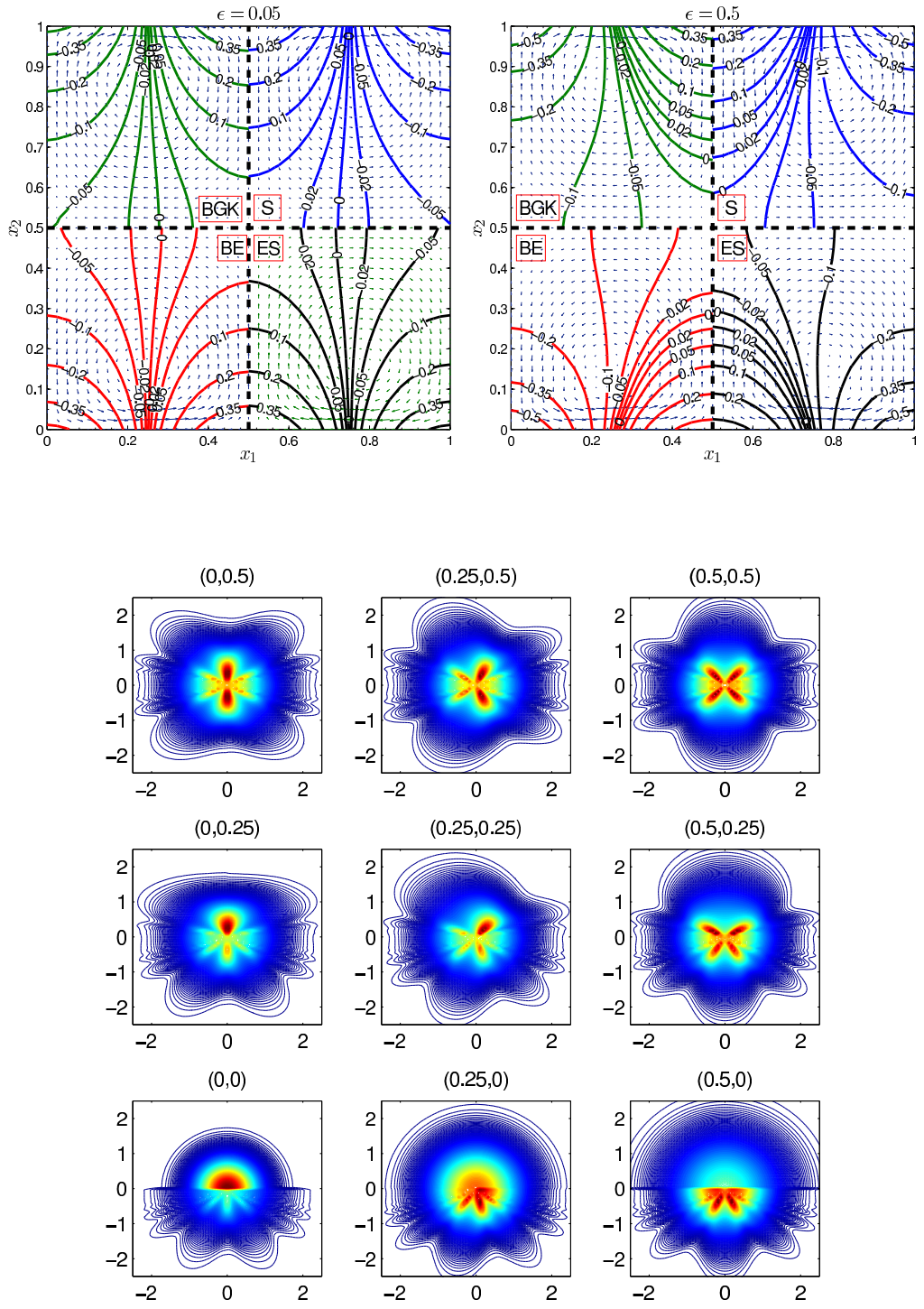

Figure 4.14: Upper: Comparison between solutions of the kinetic models and BE. The solid lines are the temperature contours $(T-1)/\epsilon$, while the arrows are the velocity vectors. Down: Contours of the reduced VDF $\int f dv_3$ when $\epsilon = 0.5$. The vertical axis is v_2 and the horizontal axis is v_1. The titles in each figure show the locations (x_1, x_2). The velocity grid numbers are huge: $128 \times 128 \times 12$ in $[-7.5, 7.5] \times [-7.5, 7.5] \times [-7.5, 0]$.

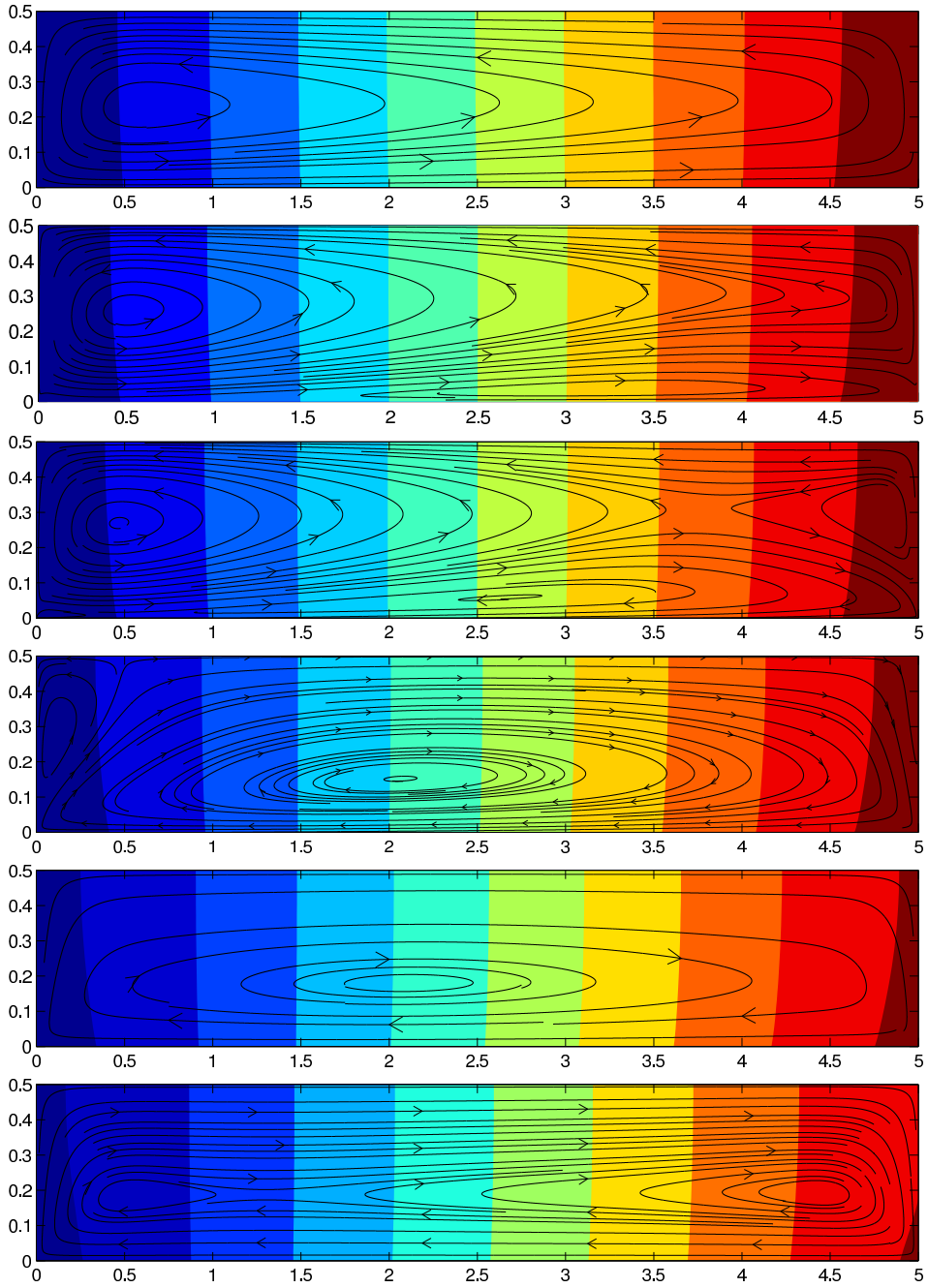

Figure 4.15: Temperature contours and velocity streamlines in the thermal creep flow of argon gas within a closed channel. From top to bottom, the Knudsen number is $Kn = 0.08$, 0.2, 0.25, 0.6, 2, and 10, respectively. In each figure, from left to right, the temperature of each contour is $1 + 0.1i$, $i = 1, 2, \cdots, 9$.

channel width, Kn is set to be 0.08, 0.2, 0.25, 0.6, 2, and 10 in the cases we investigate. Figure 4.15 presents the resulting streamlines and the temperature distributions inside the channel for the flow of argon gas. The S model can predicts nice temperature field. The ES model is not as good as the S model.

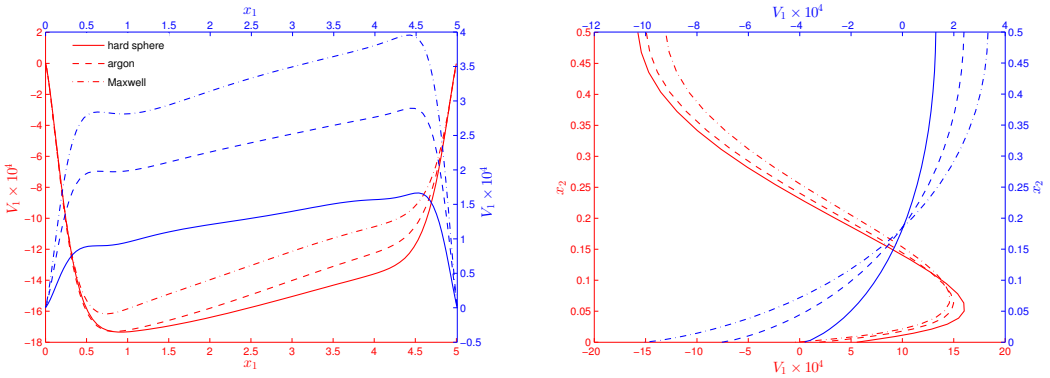

(a) Velocity along the central horizontal line **(b)** Velocity along the central vertical line

Figure 4.16: Velocity profiles for thermal creep flow within a closed channel. $Kn = 0.08$ (10) is represented for the red (blue) lines.

Unlike thermal creep in an open channel, where the flow moves towards the hot region, the thermal creep flow in a closed channel exhibits richer phenomena. At $Kn = 0.08$, the gas flows from the cold region to the hot region along the boundary, and returns in the central region. At $Kn = 0.2$, the flow still moves from hot to cold in the central region, however, near the lower wall the flow moves towards the hot region when $x_1 < 2$ and towards the cold region for at $x_1 > 2$, i.e., a circulation emerges near the lower corner of the domain. At $Kn = 0.25$, the circulation near the lower wall expands, which divides the flow in the central region into two circulation zones. The lower circulation zone keeps expanding, and pushes the other two circulations in the central region towards the left and right boundaries as Kn increases. At $Kn = 0.6$, the flow direction is reversed (as compared to that when $Kn = 0.08$) and only one circulation zone remains near the left wall. The reversal of the flow direction continues but the circulations near the left wall gradually disappear as the Knudsen number increases further, for instance, to $Kn = 2$. Finally, at larger Kn, the gas near the lower surface moves from hot to cold, and two clockwise circulations emerge near the left and right sides. The streamline profiles stay the same as when Kn is further increased, but

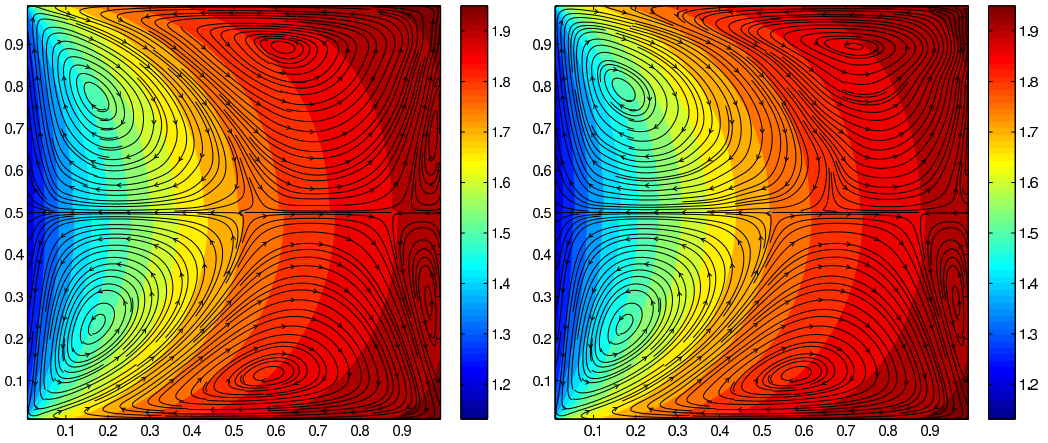

(a) S model and BE **(b)** ES model and BE

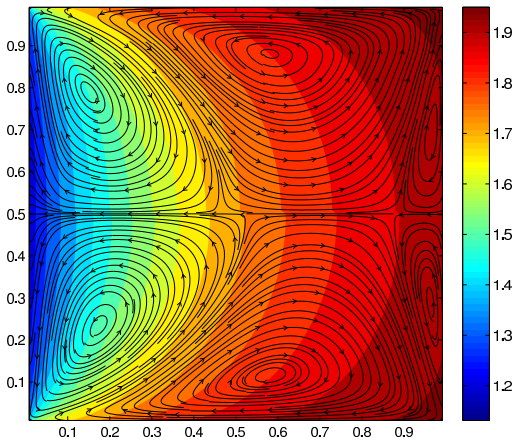

(c) Combined model and BE

Figure 4.17: Comparison between the kinetic models and the BE. In each figure, the upper (down) half region shows the results of the kinetic models (BE). The Knudsen number is $Kn = \pi/20$. In the combined ES and S model, we have $\nu_{ES} = 0.5$ and the values of b are shown in Figure 4.18(a).

the flow velocity decreases almost linearly with the Knudsen number. Comparison of the velocity profiles for different molecular models are shown in figure 4.16; it can be seen that the molecular models greatly affect the results.

Flows arising from temperature discontinuity

We consider a rarefied argon gas confined in the 2D square container, where the left wall of the container is kept at a temperature of T_l, while the other three walls are kept at a temperature of T_r. Figure 4.17(a) shows the temperature and streamline profiles when $T_r = 2T_l$ and $Kn = \pi/20$. Only slight differences in the temperature and streamline

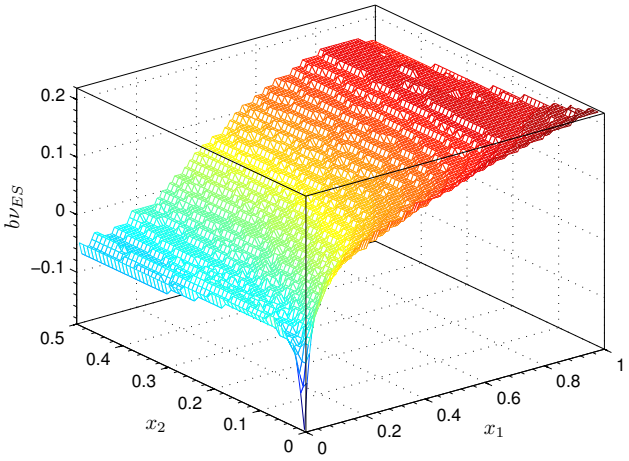

(a)

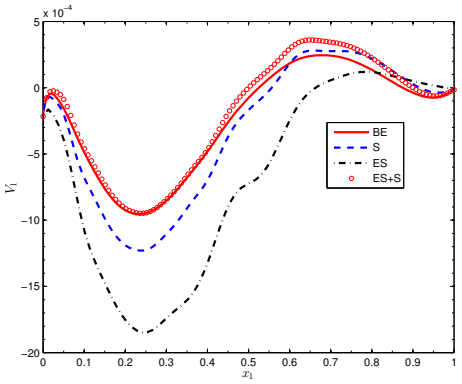

(b)

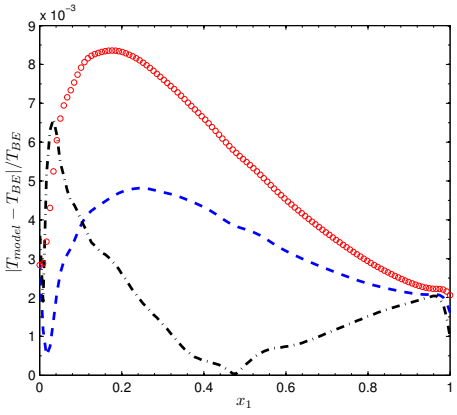

(c)

Figure 4.18: (a) Values of $b\nu_{ES}$ used in the combined ES and S model, where $\nu_{ES} = 0.5$; (b) Velocities in the central line; (c) Relative error of temperature in the central line. The Knudsen number is $Kn = \pi/20$.

profiles are observed between the S model and the BE. When the ES model is used, the temperature profile is slightly improved [Figures 4.17(b) and 4.18(c)], but the velocity profiles deviate significantly from the these of BE [Figures 4.17(b) and 4.18(b)]. The combined ES and S model is also applied to this case. From Figures 4.17(c) and 4.18(b) we see that the agreements in the velocity profiles are improved, while the error in the temperature profile slightly grows, with the maximum error being less than one percentage.

4.4 Summary

The accuracy of various existing kinetic models with velocity-independent collision frequency (the BGK, ES, and S models) are checked by comparing their solutions with these of the BE. It is found that it is difficult to conclude which kinetic model is the best, since the accuracy depends on individual flow problem.

A new kinetic model, which is a linear combination of the ES and S models, is proposed. Since the shear stress and heat flux terms are added simultaneously in a unique way, the velocity-independent collision frequency can be arbitrarily chosen. Based on a significant number of numerical simulations, we have empirically proposed a criterion to determine the collision frequency of the combined model, which can make the collision operator approach to that of the BE as closely as possible. The new model has been successfully applied to the problems with small velocities such as the planar Couette flow, force driven Poiseuille flow, and the flow arising from temperature discontinuities. An open question remains as how to determine the value of $b\nu_{ES}$ for other kind of flows. This deservers further analytical and numerical investigations.

Chapter 5

Fast spectral method for gas mixtures

5.1 The Boltzmann equation for binary gas mixture

Consider the binary gas mixture of monoatomic gases, where the mass of a molecular of the first component c_1 is m_1, while that of the second component c_2 is m_2. Let $f^{c_1}(t, \mathbf{x}, \mathbf{v})$ and $f^{c_2}(t, \mathbf{x}, \mathbf{v})$ be respectively the VDFs of the first and second components. The macroscopic quantities, such as the molecular number density, bulk velocity, and temperature of each component ($\imath$ is the species index), are defined as

$$n^{\imath} = \int f^{\imath} d\mathbf{v}, \quad \mathbf{V}^{\imath} = \frac{1}{n^{\imath}} \int \mathbf{v} f^{\imath} d\mathbf{v}, \quad T^{\imath} = \frac{m_{\imath}}{3n^{\imath} k_B} \int |\mathbf{v} - \mathbf{V}^{\imath}|^2 f^{\imath} d\mathbf{v}, \tag{5.1}$$

while the molecular number density, bulk velocity, and temperature of the mixture are defined as

$$n = \sum_{\imath} n^{\imath}, \quad \overline{\mathbf{V}} = \frac{\sum_{\imath} m_{\imath} n^{\imath} \mathbf{V}^{\imath}}{\sum_{\imath} m_{\imath} n^{\imath}}, \quad T = \frac{1}{3nk_B} \sum_{\imath} \int m_{\imath} |\mathbf{v} - \mathbf{V}^{\imath}|^2 f^{\imath} d\mathbf{v}. \tag{5.2}$$

In the absence of external force, the BE for the binary gas mixture of monatomic molecules takes the form of

$$\frac{\partial f^{\imath}}{\partial t} + \mathbf{v} \cdot \frac{\partial f^{\imath}}{\partial \mathbf{x}} = \sum_{\jmath=1,2} Q^{\imath\jmath}, \tag{5.3}$$

where collision operators $Q^{\imath\jmath}(f^\imath, f_*^\jmath)$ consist of the gain parts $Q^{\imath\jmath+}$ and loss parts $Q^{\imath\jmath-}$. They are self-collision operators when $\imath = \jmath$ and cross-collision operators when $\imath \neq \jmath$. The collision operators are local in time and spatial space. For simplicity, t and $\mathbf{x}$ will be omitted in writing the collision operators

$$Q^{\imath\jmath}(f^\imath, f_*^\jmath) = \underbrace{\int_{\mathbb{R}^3}\int_{\mathbb{S}^2} B^{\imath\jmath}(\cos\theta, |\mathbf{u}|) f^\jmath({}'\mathbf{v}_*^{\imath\jmath}) f^\imath({}'\mathbf{v}^{\imath\jmath}) d\Omega d\mathbf{v}_*}_{Q^{\imath\jmath+}} - \underbrace{\nu^{\imath\jmath} f^\imath(\mathbf{v})}_{Q^{\imath\jmath-}}, \tag{5.4}$$

where

$$\nu^{\imath\jmath}(\mathbf{v}) = \int_{\mathbb{R}^3}\int_{\mathbb{S}^2} B^{\imath\jmath}(\cos\theta, |\mathbf{u}|) f^\jmath(\mathbf{v}_*) d\Omega d\mathbf{v}_* \tag{5.5}$$

are the collision frequencies, and the relation between the post- and pre-collision velocities becomes

$${}'\mathbf{v}^{\imath\jmath} = \mathbf{v} + \frac{m_\jmath}{m_\imath + m_\jmath}(|\mathbf{u}|\Omega - \mathbf{u}), \quad {}'\mathbf{v}_*^{\imath\jmath} = \mathbf{v}_* - \frac{m_\imath}{m_\imath + m_\jmath}(|\mathbf{u}|\Omega - \mathbf{u}). \tag{5.6}$$

The cross-collision operators conserve the mass ($\int Q^{\imath\jmath} d\mathbf{v} = 0$), total momentum ($\int m_\imath \mathbf{v} Q^{\imath\jmath} d\mathbf{v} + \int m_\jmath \mathbf{v} Q^{\jmath\imath} d\mathbf{v} = 0$), and total energy ($\int m_\imath |\mathbf{v}|^2 Q^{\imath\jmath} d\mathbf{v} + \int m_\jmath |\mathbf{v}|^2 Q^{\jmath\imath} d\mathbf{v} = 0$), instead of the momentum and energy of each species. For Maxwell molecules, however, we have the following exact relations for each cross-collision operators:

$$\int m_\imath \mathbf{v} Q^{\imath\jmath} d\mathbf{v} = -\tilde{\nu}^{\imath\jmath} \frac{m_\imath m_\jmath}{m_\imath + m_\jmath} n^\imath n^\jmath (\mathbf{V}^\imath - \mathbf{V}^\jmath), \tag{5.7}$$

$$\int \frac{m_\imath}{2} |\mathbf{v} - \mathbf{V}^\imath|^2 Q^{\imath\jmath} d\mathbf{v} = -\tilde{\nu}^{\imath\jmath} \frac{m_\imath m_\jmath}{(m_\imath + m_\jmath)^2} n^\imath n^\jmath [3k_B(T^\imath - T^\jmath) - m_\jmath |\mathbf{V}^\imath - \mathbf{V}^\jmath|^2], \tag{5.8}$$

where $\tilde{\nu}^{\imath\jmath} = 2\pi \int_0^\pi (1 - \cos\theta) \sin\theta B(\cos\theta) d\theta$.

5.2 Cross-collision kernels

Detailed forms of the self-collision kernels $B^\imath(\cos\theta, |\mathbf{u}|)$ suitable for the FSM have been discussed and given in §2.1, where the use of simpler collision kernels is justified by the observation that solutions of the BE are determined by the coefficient of shear viscosity (not only its value, but also its temperature dependence), instead of the detailed θ-dependence of the collision kernel, see §2.5.

The situation becomes more complicated for gas mixtures. In addition to the shear viscosity and thermal conductivity, there are mass diffusion and thermal diffusion, and the inverse effect to thermal diffusion. Two kinds of cross-collision kernels will be considered separately.

5.2.1 Collision kernels for power-law potentials

The simplest form of the cross-collision kernel is for a gas of hard sphere molecules, where $B^{\imath\jmath} = (d^{c_1} + d^{c_2})^2|\mathbf{u}|/4$, with $d^{\imath}$ being the molecular diameters. For other type of intermolecular interactions, it is a difficult task to recover all the transport coefficients by a simple collision kernel. In DSMC, it is usually assumed that solutions of the BE are determined by both of the coefficients of shear viscosity and mass diffusion. For instance, the VSS model which gives the correct coefficients of shear viscosity and mass diffusion is widely adopted by DSMC in the simulation of gas mixtures [14].

Therefore, if we recover the coefficients of shear viscosity and mass diffusion, our deterministic solutions are compatible with those of DSMC. To do this, we choose the following cross-collision kernels [see also Eq. (2.9)]:

$$B^{\imath\jmath}(\cos\theta, |\mathbf{u}|) = B_0^{\imath\jmath} \sin^{\alpha^{\imath\jmath}+\gamma^{\imath\jmath}-1}\left(\frac{\theta}{2}\right) \cos^{-\gamma^{\imath\jmath}}\left(\frac{\theta}{2}\right) |\mathbf{u}|^{\alpha^{\imath\jmath}}, \tag{5.9}$$

where the symmetry requires $B_0^{\imath\jmath} = B_0^{\jmath\imath}$, $\alpha^{\imath\jmath} = \alpha^{\jmath\imath}$, and $\gamma^{\imath\jmath} = \gamma^{\jmath\imath}$.

According to the Chapman-Enskog expansion [5], the coefficient of the mass diffusion is given by

$$\begin{aligned} D_m^{\imath\jmath} &= \frac{3\sqrt{2\pi k_B T/m_r^{\imath\jmath}}}{16(m_r^{\imath\jmath}/2k_BT)^3 n \int_0^\infty u^5 \sigma_M^{\imath\jmath} \exp\left(-m_r^{\imath\jmath}u^2/2k_BT\right) du} \\ &= \frac{3\sqrt{(m_r^{\imath\jmath})^{\alpha^{\imath\jmath}} 2^{2-\alpha^{\imath\jmath}}/\pi}}{64 B_0^{\imath\jmath} \Gamma(\frac{\alpha^{\imath\jmath}+\gamma^{\imath\jmath}+3}{2}) \Gamma(1-\frac{\gamma^{\imath\jmath}}{2})} \frac{(k_BT)^{\omega^{\imath\jmath}}}{n m_r^{\imath\jmath}}, \end{aligned} \tag{5.10}$$

where $\omega^{\imath\jmath}$ is given by Eq. (2.6), $m_r^{\imath\jmath} = m_\imath m_\jmath/(m_\imath + m_\jmath)$ is the reduced mass, n is the total mass density, i.e., $n = n^{c_1} + n^{c_2}$ when $\imath \neq \jmath$, and $\sigma_M^{\imath\jmath}$ is the momentum transfer cross-section defined below.

In the practical calculations, when the mass diffusion $D_m^{\imath\jmath}$ (not only its value, but its temperature dependence) is known, the value of $\alpha^{\imath\jmath}$ can be determined from the

value of ω^{ij} according to Eq. (2.6), while the value of γ^{ij} is determined by the ratio of the viscosity cross-section σ_μ^{ij}

$$\begin{aligned}\sigma_\mu^{ij} =& 2\pi|\mathbf{u}|^{\alpha^{ij}-1}B_0^{ij}\int_0^\pi \sin^{\alpha^{ij}+\gamma^{ij}-1}\left(\frac{\theta}{2}\right)\cos^{-\gamma^{ij}}\left(\frac{\theta}{2}\right)\sin^3\theta d\theta \\ =& 16\pi|\mathbf{u}|^{\alpha^{ij}-1}B_0^{ij}\Gamma\left(\frac{\alpha^{ij}+\gamma^{ij}+3}{2}\right)\Gamma\left(2-\frac{\gamma^{ij}}{2}\right)/\Gamma\left(\frac{\alpha^{ij}+7}{2}\right),\end{aligned} \tag{5.11}$$

to the momentum transfer cross-section σ_M^{ij}

$$\begin{aligned}\sigma_M^{ij} =& 2\pi|\mathbf{u}|^{\alpha^{ij}-1}B_0^{ij}\int_0^\pi \sin^{\alpha^{ij}+\gamma^{ij}-1}\left(\frac{\theta}{2}\right)\cos^{-\gamma^{ij}}\left(\frac{\theta}{2}\right)(1-\cos\theta)\sin\theta d\theta \\ =& 8\pi|\mathbf{u}|^{\alpha^{ij}-1}B_0^{ij}\Gamma\left(\frac{\alpha^{ij}+\gamma^{ij}+3}{2}\right)\Gamma\left(1-\frac{\gamma^{ij}}{2}\right)/\Gamma\left(\frac{\alpha^{ij}+5}{2}\right).\end{aligned} \tag{5.12}$$

That is, γ^{ij} is obtained from the following equation

$$\frac{\sigma_\mu^{ij}}{\sigma_M^{ij}} = \frac{4-2\gamma^{ij}}{\alpha^{ij}+5}. \tag{5.13}$$

After α^{ij} and γ^{ij} are determined, one can determine the vale of B_0^{ij} by Eq. (5.10).

For example, for the He-Ar mixture [14], since $\omega^{ij} = 0.725$, from Eq. (2.6) we choose $\alpha^{ij} = 0.55$; since the ratio of the viscosity cross-section to the momentum transfer cross-section is about 0.9, we choose $\gamma^{ij} = -0.5$.

5.2.2 Collision kernel for the Lennard-Jones potential

To recover all the transport coefficients, it is better to take into account the realistic LJ potential and consider the original collision kernel given by Eqs. (2.1)-(2.2). For simplicity, we assume the collision kernel can be written as

$$B^{ij} = B_{LJ}^{ij}(\theta, |\mathbf{u}|)\mathbf{u}, \tag{5.14}$$

where the function $B_{LJ}^{ij}(\theta, |\mathbf{u}|)$ can always be constructed from the relation between the aiming distance b_a, relative velocity $|\mathbf{u}|$, and the deflection angle θ, for instance, using the method and data in Refs. [56, 104].

5.3 Fast spectral method for cross-collision operators

As in the approximation of the self-collision operators presented in §2.3, we rewrite the cross-collision operator $Q^{\imath\jmath}(f^\imath, f^\jmath_*)$ using the Carleman-like representation. We introduce $\Theta = B_0^{\imath\jmath}\sin^{\alpha^{\imath\jmath}+\gamma^{\imath\jmath}-1}(\theta/2)\cos^{-\gamma^{\imath\jmath}}(\theta/2)|\mathbf{u}|^{\alpha^{\imath\jmath}-1}$ when the collision integral is given by Eq. (5.9) and $\Theta = B_{LJ}^{\imath\jmath}(\theta,|\mathbf{u}|)$ when the collision integral is given by Eq. (5.14). With the basic identity $2\int_{\mathbb{R}^3}\delta(2\mathbf{y}\cdot\mathbf{u}+|\mathbf{y}|^2)f(\mathbf{y})d\mathbf{y} = |\mathbf{u}|\int_{\mathbb{S}^2} f(|\mathbf{u}|\Omega-\mathbf{u})d\Omega$, the cross-collision operator can be rewritten as

$$
\begin{aligned}
Q^{\imath\jmath} =& \int_{\mathbb{R}^3}\int_{\mathbb{S}^2}\Theta|\mathbf{u}|[f^\jmath({}'\mathbf{v}_*^{\imath\jmath})f^\imath({}'\mathbf{v}^{\imath\jmath}) - f^\jmath(\mathbf{v}_*)f^\imath(\mathbf{v})]d\Omega d\mathbf{v}_* \\
=& \int\int\Theta|\mathbf{u}|\left[f^\jmath\left(\mathbf{v}_* - (1-b)\frac{|\mathbf{u}|\Omega-\mathbf{u}}{2}\right)f^\imath\left(\mathbf{v}+a\frac{|\mathbf{u}|\Omega-\mathbf{u}}{2}\right) - f^\jmath(\mathbf{v}_*)f^\imath(\mathbf{v})\right]d\Omega d\mathbf{v}_* \\
=& 2\int_{\mathbb{R}^3}\int_{\mathbb{R}^3}\Theta\delta(2\mathbf{y}\cdot\mathbf{u}+|\mathbf{y}|^2)\left[f^\jmath\left(\mathbf{v}_* - \frac{(1-b)\mathbf{y}}{2}\right)f^\imath\left(\mathbf{v}+\frac{a\mathbf{y}}{2}\right) - f^\jmath(\mathbf{v}_*)f^\imath(\mathbf{v})\right]d\mathbf{y}d\mathbf{v}_* \\
=& 4\int_{\mathbb{R}^3}\int_{\mathbb{R}^3}\Theta\delta(\mathbf{y}\cdot\mathbf{u}+|\mathbf{y}|^2)[f^\jmath(\mathbf{v}_*-(1-b)\mathbf{y})f^\imath(\mathbf{v}+a\mathbf{y}) - f^\jmath(\mathbf{v}_*)f^\imath(\mathbf{v})]d\mathbf{y}d\mathbf{v}_* \\
=& 4\int_{\mathbb{R}^3}\int_{\mathbb{R}^3}\Theta\delta(\mathbf{y}\cdot\mathbf{z})[f^\jmath(\mathbf{v}+\mathbf{z}+b\mathbf{y})f^\imath(\mathbf{v}+a\mathbf{y}) - f^\jmath(\mathbf{v}+\mathbf{y}+\mathbf{z})f^\imath(\mathbf{v})]d\mathbf{y}d\mathbf{z},
\end{aligned}
$$

where

$$
a = \frac{2m_\jmath}{m_\imath+m_\jmath}, \qquad b = \frac{m_\jmath-m_\imath}{m_\imath+m_\jmath}. \tag{5.15}
$$

According to Eq. (2.21), the deflection angle θ and relative velocity $|\mathbf{u}|$ can be expressed as functions of $|\mathbf{y}|$ and $|\mathbf{z}|$. We therefore denote 4Θ by $B(|\mathbf{y}|,|\mathbf{z}|)$. For example, we have $B(|\mathbf{y}|,|\mathbf{z}|) = 4B_0^{\imath\jmath}|\mathbf{y}|^{\alpha^{\imath\jmath}+\gamma^{\imath\jmath}-1}|\mathbf{z}|^{-\gamma^{\imath\jmath}}$ when the collision integral is given by Eq. (5.9). The cross-collision operator is simplified to

$$
Q^{\imath\jmath} = \int_{\mathbb{R}^3}\int_{\mathbb{R}^3}\delta(\mathbf{y}\cdot\mathbf{z})B(|\mathbf{y}|,|\mathbf{z}|)[f^\jmath(\mathbf{v}+\mathbf{z}+b\mathbf{y})f^\imath(\mathbf{v}+a\mathbf{y}) - f^\jmath(\mathbf{v}+\mathbf{y}+\mathbf{z})f^\imath(\mathbf{v})]d\mathbf{y}d\mathbf{z}. \tag{5.16}
$$

Suppose both VDFs have the support S, the relative velocity is then $|\mathbf{u}| \le 2S$, and the infinite integration region $\mathbb{R}^3$ in Eq. (5.16) can also be reduced to $\mathcal{B}_R$, i.e., $|\mathbf{x}|,|\mathbf{y}| \le R$ with $R = \sqrt{2}S$. Expanding the truncated collision operator in the truncated Fourier series, we find that the $\mathbf{j}$-th mode of the truncated cross-collision operator is

related to the Fourier coefficients $\hat{f}^\imath$ and $\hat{f}^\jmath$ as

$$\widehat{Q}^{\imath\jmath}_{\mathbf{j}} = \sum_{\substack{\mathbf{l}+\mathbf{m}=\mathbf{j} \\ \mathbf{l},\mathbf{m}=-(N_1,N_2,N_3)/2}}^{(N_1,N_2,N_3)/2-1} \hat{f}^\imath_{\mathbf{l}} \hat{f}^\jmath_{\mathbf{m}} \beta(a\mathbf{l}+b\mathbf{m},\mathbf{m}) - \hat{f}^\imath_{\mathbf{l}} \hat{f}^\jmath_{\mathbf{m}} \beta(\mathbf{m},\mathbf{m}), \tag{5.17}$$

where the kernel mode $\beta(\mathbf{l},\mathbf{m})$ is

$$\beta(\mathbf{l},\mathbf{m}) = \int_{\mathcal{B}_R}\int_{\mathcal{B}_R} B(|\mathbf{x}|,|\mathbf{y}|)\delta(\mathbf{y}\cdot\mathbf{z})\exp(i\xi_{\mathbf{l}}\cdot\mathbf{y} + i\xi_{\mathbf{m}}\cdot\mathbf{z})d\mathbf{y}d\mathbf{z}. \tag{5.18}$$

Note that the second term in Eq. (5.17) can be calculated by the FFT-based convolution with the computational cost $O(N^3 \log N)$. For the first term, however, the direct calculation requires the computational cost to be $O(N^6)$. The main goal here is to separate $\xi_{\mathbf{l}}$ and $\xi_{\mathbf{m}}$ in $\beta(a\mathbf{l}+b\mathbf{m},\mathbf{m})$ so that Eq. (5.17) can be calculated effectively by the FFT-based convolution, maintaining the computational cost at the order of $O(N^3 \log N)$. If $b \neq 0$, the separation is different from that in §2.3.2.

Similar to Eq. (2.26), Eq. (5.18) can be transformed to

$$\frac{1}{2}\int \left[\int_0^R \rho B(\rho,|\rho'|)\cos(\rho\xi_{\mathbf{l}}\cdot\mathbf{e})d\rho\right]\left\{\int \delta(\mathbf{e}\cdot\mathbf{e}')\left[\int_{-R}^R |\rho'|\exp(i\rho'\xi_{\mathbf{m}}\cdot\mathbf{e}')d\rho'\right]d\mathbf{e}'\right\}d\mathbf{e},$$

where the integration with respect to ρ can be approximated by Gauss-Legendre quadrature of order M_2 (ρ_r and ω_r ($r = 1, 2, \cdots, M_2$) are the abscissas and weights of the Gauss-Legendre quadrature for $\rho \in [0, R]$), yielding

$$\frac{1}{2}\int \sum_{r=1}^{M_2} \omega_r\rho_r \cos(\rho_r\xi_{\mathbf{l}}\cdot\mathbf{e})\left\{\int \delta(\mathbf{e}\cdot\mathbf{e}')\left[\int_{-R}^R |\rho'|B(\rho_r,|\rho'|)\exp(i\rho'\xi_{\mathbf{m}}\cdot\mathbf{e}')d\rho'\right]d\mathbf{e}'\right\}d\mathbf{e}.$$

According to the calculation adopted in Eq. (2.28), we have

$$\beta(\mathbf{l},\mathbf{m}) = \int \sum_{r=1}^{M_2} \omega_r\rho_r\cos(\rho_r\xi_{\mathbf{l}}\cdot\mathbf{e})\psi(\rho_r,|\xi_{\mathbf{m}}|\cos\theta_1)d\mathbf{e}, \tag{5.19}$$

where

$$\psi(\rho_r,s) = 2\pi\int_0^R |\rho'|B(\rho_r,|\rho'|)J_0(\rho's)d\rho'. \tag{5.20}$$

The integration with respect to $\mathbf{e}$ in Eq. (5.19) can be approximated either by the

trapezoidal rule [see Eq. (2.30)] or by the Gauss-Legendre quadrature [see Eq. (2.31)]. For clarity, we only give the result when using the Gauss-Legendre quadrature, i.e., $\beta(\mathbf{l},\mathbf{m}) \approx \sum_{p,q,r=1}^{M,M,M_2} \omega_p\omega_q\omega_r\rho_r \cos(\rho_r\xi_\mathbf{l}\cdot\mathbf{e}_{\theta_p,\phi_q})\psi(\rho_r, |\xi_\mathbf{m}|\cos\theta_1)\sin\theta_p$, where $|\xi_\mathbf{m}|\cos\theta_1 = \sqrt{|\xi_\mathbf{m}|^2 - (\xi_\mathbf{m}\cdot\mathbf{e}_{\theta_p,\varphi_q})^2}$.

Finally, we expand the kernel mode into the following form:

$$\begin{aligned}\beta(a\mathbf{l}+b\mathbf{m},\mathbf{m}) \approx \sum_{p,q,r=1}^{M,M,M_2} &\omega_p\omega_q\omega_r\rho_r\psi(\rho_r,|\xi_\mathbf{m}|\cos\theta_1)\cdot\sin\theta_p \\ &\times[\cos(\rho_r a\xi_\mathbf{l}\cdot\mathbf{e}_{\theta_p,\varphi_q})\cdot\cos(\rho_r b\xi_\mathbf{m}\cdot\mathbf{e}_{\theta_p,\varphi_q}) \\ &-\sin(\rho_r a\xi_\mathbf{l}\cdot\mathbf{e}_{\theta_p,\varphi_q})\cdot\sin(\rho_r b\xi_\mathbf{m}\cdot\mathbf{e}_{\theta_p,\varphi_q})].\end{aligned} \tag{5.21}$$

Now we see $\xi_\mathbf{l}$ and $\xi_\mathbf{m}$ are completely separated, hence Eq. (5.17) can be computed by the FFF-based convolution, with the computational cost at the order of $O(M_2M^2N^3\log_2 N)$.

Special forms of the kernel mode

When the cross-collision kernel is given by Eq. (5.9), we have

$$\beta(a\mathbf{l}+b\mathbf{m},\mathbf{m}) \approx 4B_0^{\imath\jmath}\sum_{p,q=1}^{M}\omega_p\omega_q I(\xi_\mathbf{l},\xi_\mathbf{m})\cdot\psi_{\gamma^{\imath\jmath}}\left\{\sqrt{|\xi_\mathbf{m}|^2-(\xi_\mathbf{m}\cdot\mathbf{e}_{\theta_p,\varphi_q})^2}\right\}\sin\theta_p, \tag{5.22}$$

where

$$I(\xi_\mathbf{l},\xi_\mathbf{m}) = 2\int_0^R \rho^{\alpha^{\imath\jmath}+\gamma^{\imath\jmath}}\cos[\rho(a\xi_\mathbf{l}+b\xi_\mathbf{m})\cdot\mathbf{e}]d\rho, \tag{5.23}$$

and the function $\psi_\gamma(s)$ is defined in Eq. (2.29).

Due to the presence of b in Eq. (5.23), three different cases will be considered for the calculation of $I(\xi_\mathbf{l},\xi_\mathbf{m})$:

- When the two types of molecules have identical mass, we have $a=1$ and $b=0$. Thus,

$$I(\xi_\mathbf{l}) = 2\int_0^R \rho^{\alpha^{\imath\jmath}+\gamma^{\imath\jmath}}\cos(\rho a\xi_\mathbf{l}\cdot\mathbf{e}_{\theta_p,\varphi_q})d\rho, \tag{5.24}$$

  which can be calculated accurately by Gauss-Legendre quadrature. In this case, $\xi_\mathbf{l}$ and $\xi_\mathbf{m}$ appear in two different functions. Hence Eq. (5.17) can be calculated

effectively by the FFT-based convolution. The computational cost of the cross-collision operators is exactly the same as that of the self-collision operators, which is $O(M^2N^3\log_2 N)$.

- For cross-collision operators when the two types of molecules have nearly identical mass, i.e., $|m_A - m_B| \ll m_A + m_B$, we have $|b| \ll 1$. Then, according to the Taylor expansion, we have $\cos[\rho(a\xi_{\mathbf{l}} + b\xi_{\mathbf{m}})\cdot\mathbf{e}_{\theta_p,\varphi_q}] \approx \sum_{r=0}^{M_1-1}\cos(\rho a\xi_{\mathbf{l}}\cdot\mathbf{e}_{\theta_p,\varphi_q} + r\pi/2)(b\rho\xi_{\mathbf{m}}\cdot\mathbf{e}_{\theta_p,\varphi_q})^r/r!$, where '!' stands for the factorial. Hence we have

$$I(\xi_{\mathbf{l}},\xi_{\mathbf{m}}) \approx 2\sum_{r=0}^{M_1-1}\frac{(b\xi_{\mathbf{m}}\cdot\mathbf{e}_{\theta_p,\varphi_q})^r}{r!}\int_0^R \rho^{\alpha^{ij}+\gamma^{ij}+r}\cos\left(\rho a\xi_{\mathbf{l}}\cdot\mathbf{e}_{\theta_p,\varphi_q}+\frac{r\pi}{2}\right)d\rho, \tag{5.25}$$

where each term in the summation can be calculated accurately by Gauss-Legendre quadrature. From Eqs. (5.22) and (5.25) we find that $\xi_{\mathbf{l}}$ and $\xi_{\mathbf{m}}$ appear in two different functions. Hence Eq. (5.17) can be calculated effectively by the FFT-based convolution, with the computational cost $O(M_1M^2N^3\log_2 N)$, which is M_1 times larger than the self-collision operators.

- For general cases, Eq. (5.22) can be approximated by the Gauss-Legendre quadrature so that $\xi_{\mathbf{l}}$ and $\xi_{\mathbf{m}}$ are separated by the property of the cosine function

$$\begin{aligned} I(\xi_{\mathbf{l}},\xi_{\mathbf{m}}) \approx 2\sum_{r=1}^{M_2}\omega_r\rho_r^{\alpha^{ij}+\gamma^{ij}}\cdot[\,&\cos(\rho_r a\xi_{\mathbf{l}}\cdot\mathbf{e}_{\theta_p,\varphi_q})\cdot\cos(\rho_r b\xi_{\mathbf{m}}\cdot\mathbf{e}_{\theta_p,\varphi_q}) \\ &-\sin(\rho_r a\xi_{\mathbf{l}}\cdot\mathbf{e}_{\theta_p,\varphi_q})\cdot\sin(\rho_r b\xi_{\mathbf{m}}\cdot\mathbf{e}_{\theta_p,\varphi_q})]. \end{aligned} \tag{5.26}$$

Then, Eq. (5.17) can be calculated with the computation cost $O(M_2M^2N^3\log_2 N)$, which is $2M_2$ times larger than the self-collision operators.

5.4 Conservation enforcement

The procedure in deriving the FSM for gas mixtures is essentially the same as that for single species [1]. Therefore, it can be proved that the present FSM conserves the mass and satisfies the H-theorem, while the approximation errors of momentum and energy are spectrally small. These errors, however, can be eliminated using the method of

Lagrangian multiplier.

For Maxwell molecules, the Lagrangian method is similar to that of self-collision operators (see §2.3.3). After Q^{ij} is obtained, we minimise $\sum_{\mathbf{j}}(Q^{ij}_{\mathbf{j}} - \tilde{Q}^{ij}_{\mathbf{j}})^2$ under the constraints of mass conservation, Eqs. (5.7) and (5.8), yielding

$$\widetilde{Q}^{ij} = Q^{ij} - (\lambda_n^{ij} + \lambda_{\mathrm{v}}^{ij} \cdot \mathbf{v} + \lambda_e^{ij}|\mathbf{v}|^2), \tag{5.27}$$

where the Lagrangian multipliers satisfy

$$\begin{aligned}
\sum_{\mathbf{j}} Q^{ij} &= \sum_{\mathbf{j}} (\lambda_n^{ij} + \lambda_{\mathrm{v}}^{ij} \cdot \mathbf{v} + \lambda_e^{ij}|\mathbf{v}|^2), \\
\sum_{\mathbf{j}} m_i \mathbf{v} Q^{ij} &= \sum_{\mathbf{j}} m_i \mathbf{v} (\lambda_n^{ij} + \lambda_{\mathrm{v}}^{ij} \cdot \mathbf{v} + \lambda_e^{ij}|\mathbf{v}|^2) \\
&\quad - \sum_{\mathbf{j}} \tilde{\nu}^{ij} \frac{m_i m_j}{m_i + m_j} n^i n^j (\mathbf{V}^i - \mathbf{V}^j), \\
\sum_{\mathbf{j}} \frac{m_i}{2} |\mathbf{v}|^2 Q^{ij} &= \sum_{\mathbf{j}} \frac{m_i}{2} |\mathbf{v}|^2 (\lambda_n^{ij} + \lambda_{\mathrm{v}}^{ij} \cdot \mathbf{v} + \lambda_e^{ij}|\mathbf{v}|^2) \\
&\quad - \sum_{\mathbf{j}} \tilde{\nu}^{ij} \frac{m_i m_j}{(m_i + m_j)^2} n^i n^j [3k_B(T^i - T^j) - m_j |\mathbf{V}^i - \mathbf{V}^j|^2].
\end{aligned} \tag{5.28}$$

For other types of intermolecular interactions, we minimise the function $\sum_{\mathbf{j}}(Q^{c_1c_2}_{\mathbf{j}} - \tilde{Q}^{c_1c_2}_{\mathbf{j}})^2 + (Q^{c_2c_1}_{\mathbf{j}} - \tilde{Q}^{c_2c_1}_{\mathbf{j}})^2$ under the conservation of mass, total momentum, and total energy, yielding $\widetilde{Q}^{ij} = Q^{ij} - (\lambda_n^{ij} + m_i\lambda_{\mathrm{v}} \cdot \mathbf{v} + m_i\lambda_e|\mathbf{v}|^2)$, where the 6 Lagrangian multipliers satisfy

$$\begin{aligned}
\sum_{\mathbf{j}} Q^{c_1c_2} &= \sum_{\mathbf{j}} (\lambda_n^{c_1c_2} + m_1\lambda_{\mathrm{v}} \cdot \mathbf{v} + m_1\lambda_e|\mathbf{v}|^2), \\
\sum_{\mathbf{j}} Q^{c_2c_1} &= \sum_{\mathbf{j}} (\lambda_n^{c_2c_1} + m_2\lambda_{\mathrm{v}} \cdot \mathbf{v} + m_2\lambda_e|\mathbf{v}|^2), \\
\sum_{\mathbf{j}} (m_1 Q^{c_1c_2} + m_2 Q^{c_2c_1})\mathbf{v} &= \sum_{\mathbf{j}} m_1 (\lambda_n^{c_1c_2} + m_1\lambda_{\mathrm{v}} \cdot \mathbf{v} + m_1\lambda_e|\mathbf{v}|^2)\mathbf{v} \\
&\quad + \sum_{\mathbf{j}} m_2 (\lambda_n^{c_2c_1} + m_1\lambda_{\mathrm{v}} \cdot \mathbf{v} + m_1\lambda_e|\mathbf{v}|^2)\mathbf{v}, \\
\sum_{\mathbf{j}} (m_1 Q^{c_1c_2} + m_2 Q^{c_2c_1})|\mathbf{v}|^2 &= \sum_{\mathbf{j}} m_1 (\lambda_n^{c_1c_2} + m_1\lambda_{\mathrm{v}} \cdot \mathbf{v} + m_1\lambda_e|\mathbf{v}|^2)|\mathbf{v}|^2 \\
&\quad + \sum_{\mathbf{j}} m_2 (\lambda_n^{c_2c_1} + m_1\lambda_{\mathrm{v}} \cdot \mathbf{v} + m_1\lambda_e|\mathbf{v}|^2)|\mathbf{v}|^2.
\end{aligned} \tag{5.29}$$

5.5 Comparison with exact BKW solutions

We check accuracy of the FSM by comparing the numerical solutions with the analytical BKW solutions for Maxwell molecules ($\alpha^{ij} = 0$). Without loss of generality, we take $\gamma^{ij} = 0$ in Eq. (5.9) and consider the spatial-homogeneous BE. The exact BKW solutions can be written as follows [105]:

$$f^{i}_{BKW}(v,t) = n^{i}\left(\frac{m_i}{2\pi K}\right)^{3/2}\exp\left(-\frac{m_i|v|^2}{2K}\right)\left(1 - 3rp_i + \frac{rp_i}{K}m_i|v|^2\right), \tag{5.30}$$

where

$$\begin{aligned} p_1 &= \frac{4n^{c_2}}{5}[2B_0^{c_2c_2} - m_0 B_0^{c_1c_2}(5 - 3m_0)], \\ p_2 &= \frac{4n^{c_1}}{5}[2B_0^{c_1c_1} - m_0 B_0^{c_1c_2}(5 - 3m_0)], \\ r &= \frac{\widetilde{A}}{\widetilde{A}\exp[4\pi\widetilde{A}(t+t_0)] - \widetilde{B}}, \\ K &= \frac{n^{c_1} + n^{c_2}}{n^{c_1} + n^{c_2} + 2(n^{c_1}p_1 + n^{c_2}p_2)r}, \end{aligned} \tag{5.31}$$

with

$$\begin{aligned} \widetilde{A} &= \frac{4n^{c_1}B_0^{c_1c_1} + 2n^{c_2}m_0B_0^{c_1c_2}(5 - 3m_0p_2/p_1)}{15}, \\ \widetilde{B} &= \frac{8n^{c_1}B_0^{c_1c_1}p_1 + 4n^{c_2}m_0B_0^{c_1c_2}(5 - 3m_0)p_2}{15}, \end{aligned} \tag{5.32}$$

and $m_0 = 4m_1m_2/(m_1 + m_2)^2$.

The additional conditions below should be satisfied for the existence of exact solutions:

- Exact solution of type I exists when p_1 is equal to p_2, i.e., this solution exists only for special values of relative density

$$\frac{n^{c_2}}{n^{c_1}} = \frac{2B_0^{c_1c_1} - m_0(5 - 3m_0)B_0^{c_1c_2}}{2B_0^{c_2c_2} - m_0(5 - 3m_0)B_0^{c_1c_2}}. \tag{5.33}$$

- Exact solution of type II exists for arbitrary values of n^{c_1} and n^{c_2} when the following relation is satisfied

$$\frac{1}{2B_0^{c_1c_1}/B_0^{c_1c_2} - m_0(5 - 3m_0)} + \frac{1}{2B_0^{c_2c_2}/B_0^{c_1c_2} - m_0(5 - 3m_0)} = \frac{1}{3m_0^2}. \tag{5.34}$$

We first consider the case where the two types of molecules have the mass ratio of $m_1/m_2 = 4$. In our numerical simulations, we use Eq. (5.26) with $M_2 = 7$ to approximate Eq. (5.23). In the angular discretisation, we take $M = 6$. Figure 5.1 shows the relax-to-equilibrium process of the two types of solutions. One can see that the numerical obtained VDFs agree well with the BKW solutions, and the relative errors in the fourth-order moments are about 10^{-4}. This demonstrates accuracy of the FSM.

We then consider the case that the two types of molecules have nearly identical mass, i.e., $m_1/m_2 = 1.25$. We use Eq. (5.25) with $M_1 = 7$ to approximate Eq. (5.23), while in the angular discretisation we take $M = 6$. Figure 5.2 compares the evolution of the VDFs and the fourth-order moments. Again, they agree with the BKW solutions very well.

5.6 Space-inhomogeneous problems

We employ the iteration method to get the stationary solutions of the BE for space-inhomogeneous problems. Given the VDFs $f_k^{c_1}$ and $f_k^{c_2}$ at the k-th iteration step, their values at the next iteration step is calculated by the following equations

$$[\nu^{c_1c_1}(f_k^{c_1}) + \nu^{c_1c_2}(f_k^{c_2})]f_{k+1}^{C_1} + \mathbf{v}\cdot\frac{\partial f_{k+1}^{c_1}}{\partial \mathbf{x}} = Q_k^{c_1c_1+} + Q_k^{c_1c_2+},$$
$$[\nu^{c_2c_2}(f_k^{c_2}) + \nu^{c_2c_1}(f_k^{c_1})]f_{k+1}^{c_2} + \mathbf{v}\cdot\frac{\partial f_{k+1}^{c_2}}{\partial \mathbf{x}} = Q_k^{c_2c_2+} + Q_k^{c_2c_1+}.$$

5.6.1 Normal shock waves

We compare our numerical solutions for normal shock waves with those obtained from a finite-difference method [39]. The mixture is composed of hard sphere molecules with the diameters of the molecular c_1 and c_2 being d^{c_1} and d^{c_2}, respectively. For comparison, we set $B^{c_1c_1} = (d^{c_1})^2/4$, $B^{c_2c_2} = (d^{c_2})^2/4$, and $B^{c_1c_2} = (d^{c_1} + d^{c_2})^2/16$. Figures 5.3 and 5.4 show the shock wave structures with different concentrations. It is seen that our numerical results compare well with those of a finite-difference method.

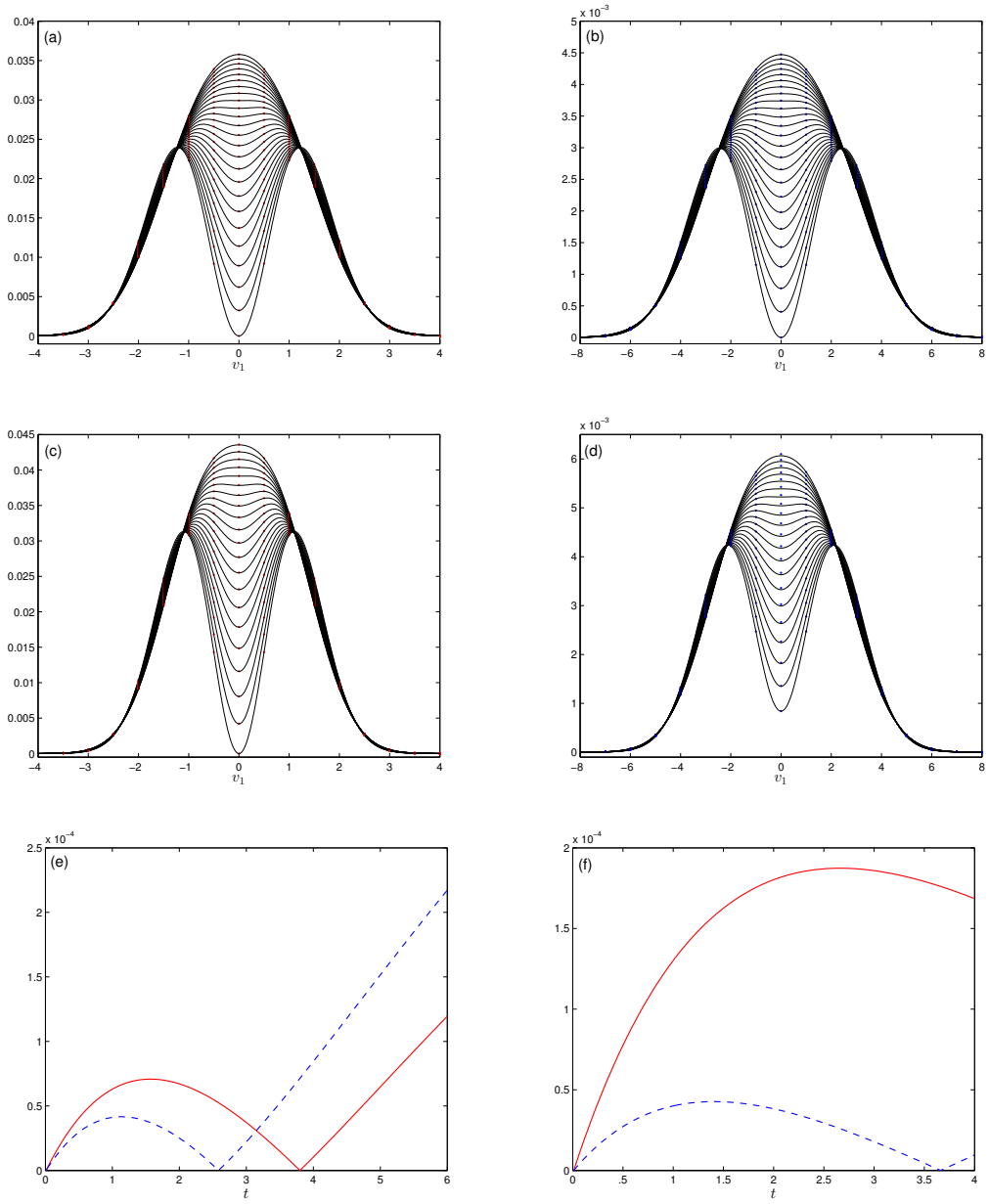

Figure 5.1: (a-d) Evolution of VDFs in the spatial-homogeneous Maxwell molecules. The solid lines are the BKW solutions of type I (a,b) and type II (c,d), while the dots are the numerical ones. (a,c): $f^{c_1}(v_1, 0, 0)$ and (b,d): $f^{c_2}(v_1, 0, 0)$. In each figure, from bottom to top (near $v_1 = 0$), the time in (a,c) is $(0, 1, 2, \cdots, 24) \times 0.25$, while in (b,d) is $(0, 1, 2, \cdots, 20) \times 0.1$. (e) The relative errors of the fourth-order moments vs time for type I solutions. Solid line: $\int (f^{c_1} - f^{c_1}_{BKW}) v_1^4 dv / \int f^{c_1}_{BKW} v_1^4 dv$, dashed line: $\int (f^{c_2} - f^{c_2}_{BKW}) v_1^4 dv / \int f^{c_2}_{BKW} v_1^4 dv$. (f) The relative errors of the fourth-order moments vs time for type II solutions. The parameters are $m_1 = 4m_2 = 4$. (a,b,e): $B_0^{c_2 c_2} = B_0^{c_1 c_1} = 4B_0^{c_1 c_2} = 1/4\pi$, $n^{c_1} = n^{c_2} = 1$, and $t_0 = \log[(B + 3Ap_1)/A]/4A\pi$ so that at the initial time $t = 0$, $1 - 3rp_1 = 1 - 3rp_2 = 0$. (c,d,f): $B_0^{c_1 c_2} = 1/16\pi$, $B_0^{c_2 c_2} = B_0^{c_1 c_1} = B_0^{c_1 c_2}(3m_0^2 + 5m_0)/2$, $n^{c_1} = 0.95$, $n^{c_2} = 1$, and $t_0 = \max\{\log[(\widetilde{B} + 3\widetilde{A}p_1)/\widetilde{A}], \log[(\widetilde{B} + 3\widetilde{A}p_2)/\widetilde{A}]\}/4\widetilde{A}\pi$. The velocity bound L is 8 for the distribution function f^{c_1} and 16 for the distribution function f^{c_2}. The other parameters are $N = 64$, $M = 6$, and $M_2 = 7$.

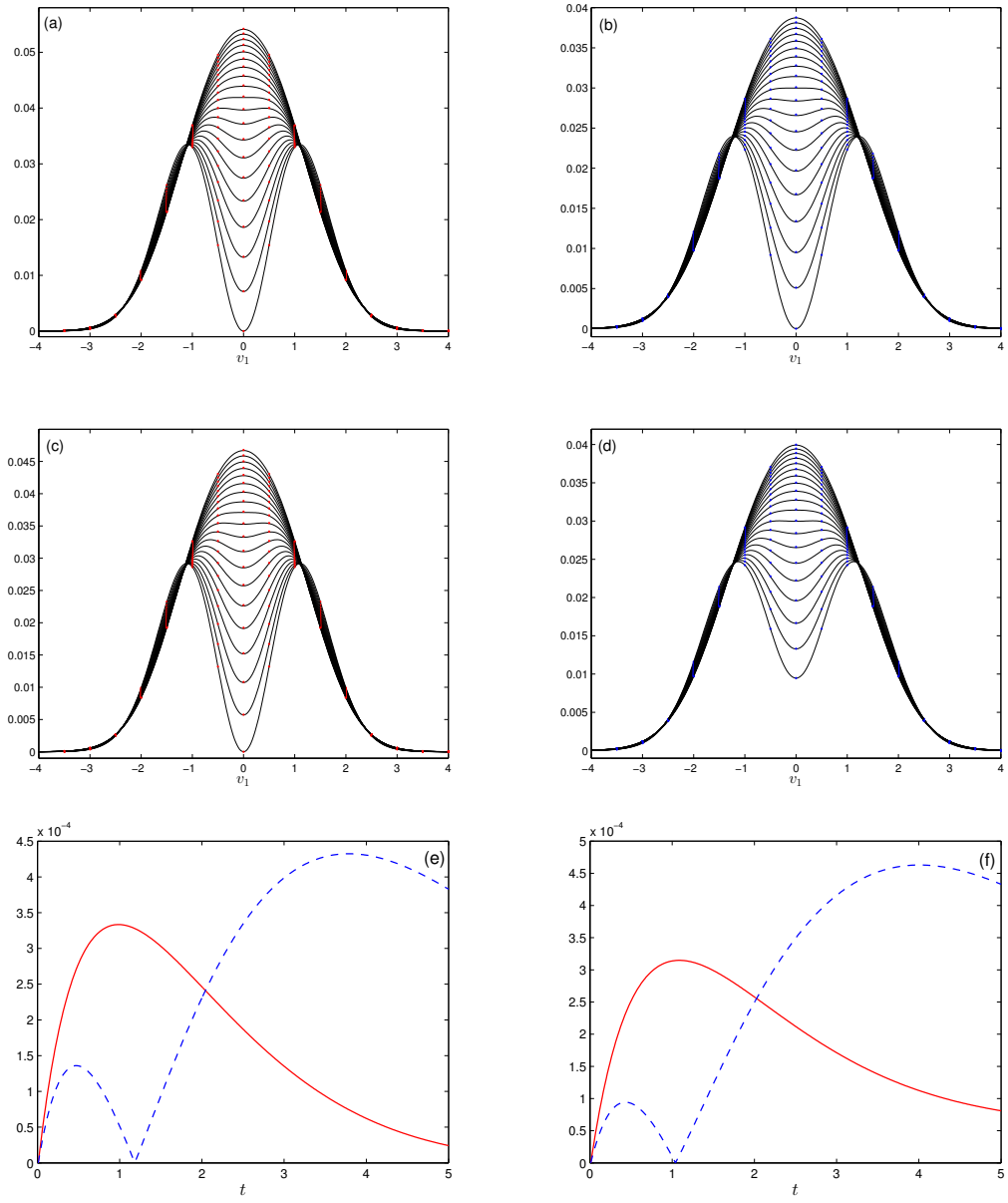

Figure 5.2: (a-d) Evolution of VDFs in the spatial-homogeneous Maxwell molecules. The solid lines in (a,b) and (c,d) are respectively the BKW solutions of type I and II, while the dots are the numerical ones. (a,c): $f^{c_1}(v_1, 0, 0)$ and (b,d): $f^{c_2}(v_1, 0, 0)$. In each figure, from bottom to top (near $v_1 = 0$), the time is $(0, 1, 2, \cdots, 19) \times 0.1$. (e) and (f) The relative errors of the fourth-order moments in the simulation of exact solutions of types I and II, respectively. The parameters are $m_1 = 1, m_2 = 0.8$, (a,b,e) $B_0^{c_2c_2} = B_0^{c_1c_1} = 4B_0^{c_1c_2} = 1/4\pi$, $n^{c_1} = n^{c_2} = 1$, and $t_0 = \log[(\widetilde{B} + 3\widetilde{A}p_1)/\widetilde{A}]/4\widetilde{A}\pi$, (c,d,f) $B_0^{c_1c_2} = 1/16\pi$, $B_0^{c_2c_2} = B_0^{c_1c_1} = B_0^{c_1c_2}(3m_0^2 + 5m_0)/2$, $n^{c_1} = 0.9, n^{c_2} = 1$, and $t_0 = \max\{\log[(\widetilde{B}+3\widetilde{A}p_1)/\widetilde{A}], \log[(\widetilde{B}+3\widetilde{A}p_2)/\widetilde{A}]\}/4\widetilde{A}\pi$. We choose $N = 32$, $M = 6$, and $M_1 = 7$.

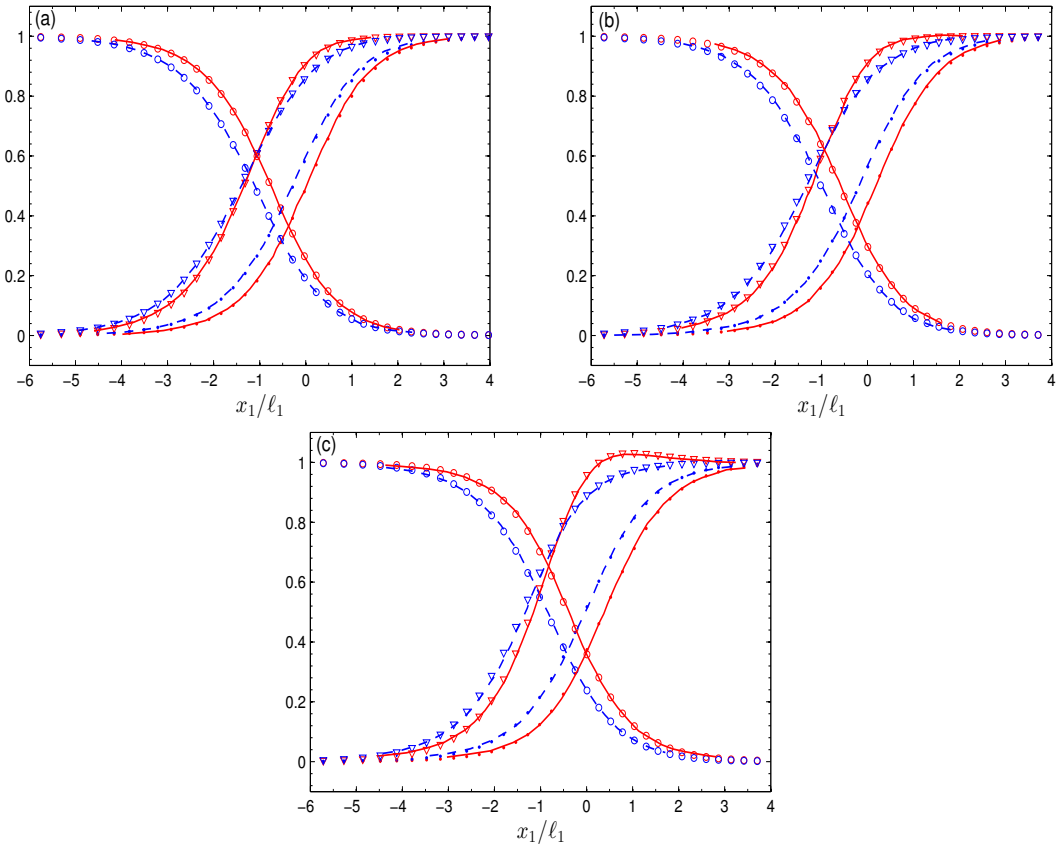

Figure 5.3: Profiles of molecular number densities (dots), flow velocities (circles), and temperature (triangles) for upstream Mach number 3, $m^{c_2}/m^{c_1} = 0.5$, and $d^{c_2}/d^{c_1} = 1$: (a) $\chi_{c_2} = 0.1$, (b) $\chi_{c_2} = 0.5$, and (c) $\chi_{c_2} = 0.9$. Here χ_{c_2} is the concentration of the c_2-component at the upstream infinity and l_1 is the mean free path of the molecules of the c_1-component at the upstream infinity. The markers are our numerical results, while the lines (solid: c_1-component, dashed: c_2-component) are the results of the finite-difference method (note that components c_1 and c_2 are correspondingly the A and B components in Ref. [39]).

5.6.2 Heat transfer between two parallel plates

We further compare our numerical results for the Fourier heat transfer problem between two parallel plates with that of a finite-difference method [106]. The mixture is again composed of hard sphere molecules, confined in the domain $0 \le x_1 \le \ell$. The diffuse boundary condition is adopted, where the wall temperature at $x_1 = 0$ is T_I and that at $x_1 = d$ is $2T_I$. The Knudsen number is defined as $Kn = l_0/\ell$, where the mean-free path $l_0 = [\sqrt{2}\pi(d^{c_1})^2(n_{av}^{c_1} + n_{av}^{c_2})]^{-1}$.

Figure 5.5 shows the temperature profiles with $Kn = 1$, $m_2/m_1 = 0.25$, $d^{c_2}/d^{c_1} = 0.5$, and $n_{av}^{c_2}/n_{av}^{c_1} = 0.1, 1$, and 10. In our numerical simulations, we have used $128 \times 48 \times 48$ velocity grids. The agreements with those from a finite-difference method are

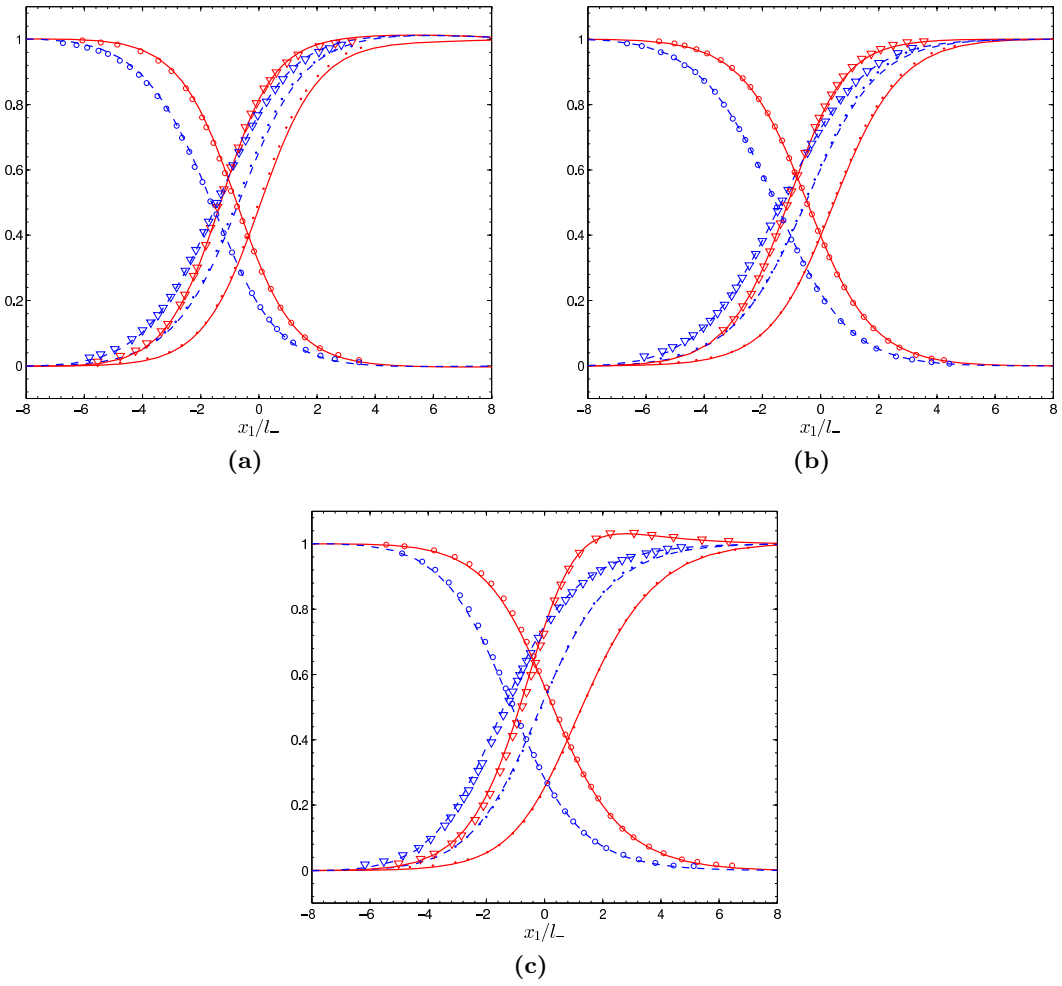

Figure 5.4: Same as Figure 5.3, expect here $m^{c_2}/m^{c_1} = 0.25$ and the Mach number is 2.

quite satisfactory. Note that the smaller molecules (c_2 component) have a larger mean free path. Therefore, the density profile of the component c_2 is flatter than that of the component c_1. Also note that the effective Knudsen number at the same Kn increases with the value of $n_{av}^{c_2}/n_{av}^{c_1}$, since Kn is based on the average number density of the total mixture and on the diameter of the larger molecules. Therefore, the temperature profiles become flatter as $n_{av}^{c_2}/n_{av}^{c_1}$ increases.

5.6.3 Thermal creep flow in closed channel

Finally we consider the thermal creep flow of binary gas mixture in a 2D closed channel with the length-to-width ratio being 5. The temperature in the right end of the channel is 1.5 times higher than that in the left end. The temperature in the top and bottom

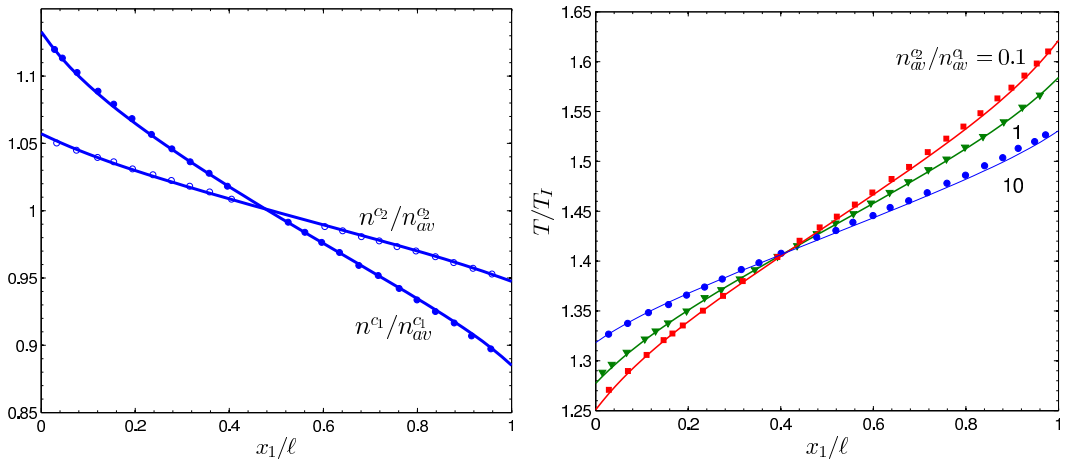

Figure 5.5: Normalized molecular number densities (at $n^{c_2}_{av}/n^{c_1}_{av} = 10$) and temperature profiles of Fourier heat flow between two parallel plates. Solid lines: our numerical results; Markers: results from the finite-difference method (components c_1 and c_2 are correspondingly the components A and B in Ref. [106]).

walls varies linearly. We consider the hard sphere molecules with $m_1 = m_2$, $d^{c_2}/d^{c_1} = 0.25$, and $n^{c_2}_{av}/n^{c_1}_{av} = 0.1$. The mean free path is defined as that in the Fourier flow and the channel width is chosen as the character length. Figures 5.6 and 5.7 show the temperature and streamline profiles. The flows gradually reverse their directions, as happened in a single species (see §4.3.7). Since the component c_2 has a larger Kn, its flow pattern changes earlier than that of the component c_1.

5.7 Summary

We have extended the FSM to the binary gas mixture of monoatomic gases. The accuracy of the FSM has been checked by comparing the numerical solutions with the analytical BKW solutions as well as the numerical results of the finite-difference method from the Kyoto kinetic theory group. The present method can be straightforwardly applied to multiple gas mixtures.

The mass difference between the two kinds of molecules makes the FSM less efficient as that for the single component gas, however, it is still faster than the conventional spectral methods where the computational complexity is at the order of $O(N^6)$, especially when a large number of velocity grids are needed.

In the current implementation, we have used the same number of grids for the velocity discretisation, and L is chosen as the support of the VDF of the lighter molecules.

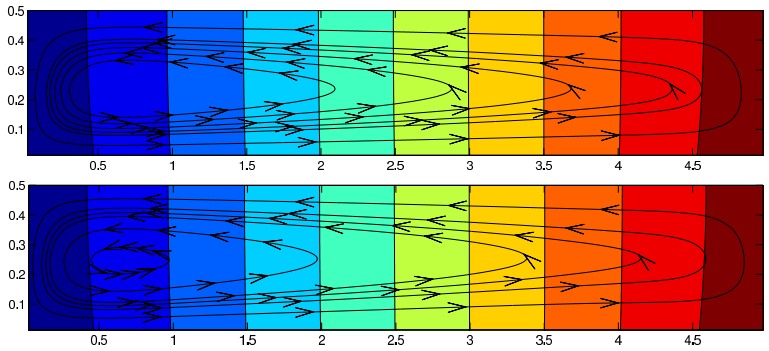

(a) $Kn = 0.1$

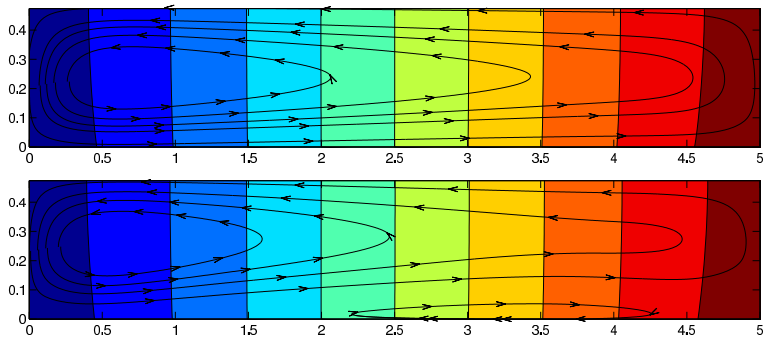

(b) $Kn = 0.15$

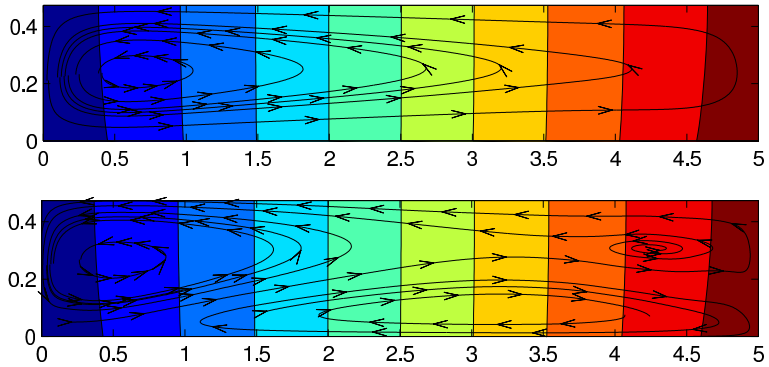

(c) $Kn = 0.2$

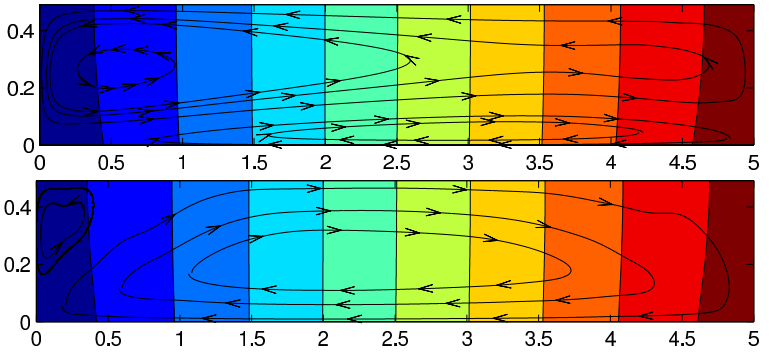

(d) $Kn = 0.25$

Figure 5.6: The temperature and streamline profiles in the thermal creep flow of a binary gas mixture. Near the bottom wall, from $x_2 = 0.5$ to $x_2 = 4.5$, the isothermal lines have the temperature ranging from 1.05 to 1.45. In each sub figure, the first one is the results of the component c_1, while the second one is that of the component c_2.

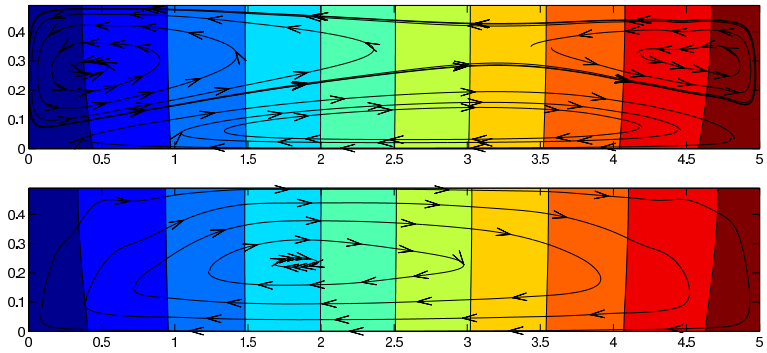

(a) $Kn = 0.3$

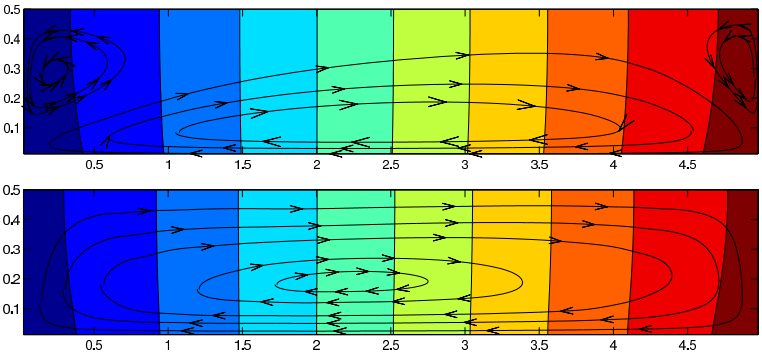

(b) $Kn = 0.5$

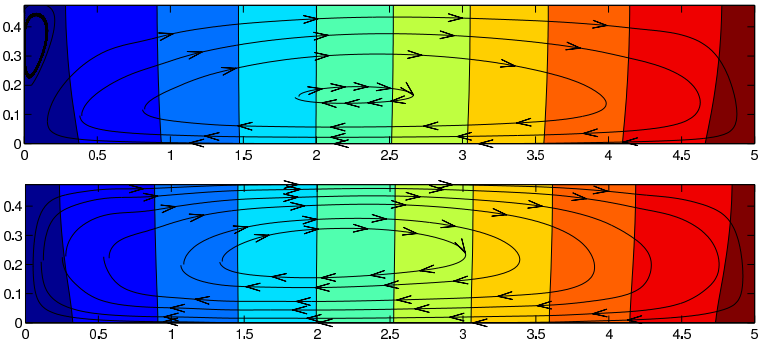

(c) $Kn = 0.7$

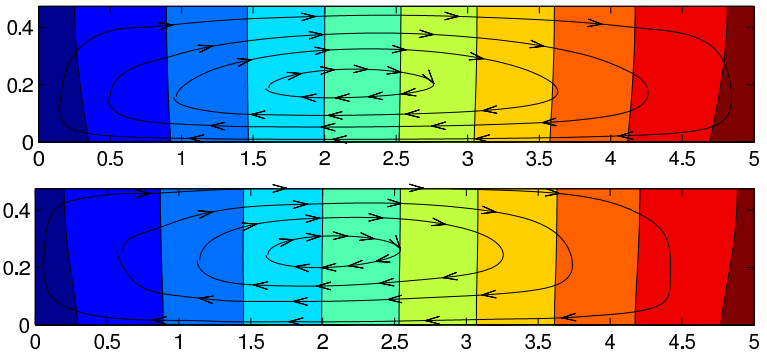

(d) $Kn = 1$

Figure 5.7: Same as Figure 5.6 but for different Kn.

As a consequence, the velocity grid number are 8 and 27 times larger than that for single component gas when the mass ratio are 4 and 9, respectively. This wastes not only the computer memory, but also the computational time. Further efforts will be needed to optimise the algorithm, for example, to use a non-uniform velocity grids.

Chapter 6

Fast spectral method for quantum Fermi gases

6.1 The quantum Boltzmann equation for Fermi gases

Consider a system of two-component fermions with the atom mass m_1 and m_2 in the normal phase, so that it can be described semiclassically by the VDFs $f^{c_1}(t, \mathbf{x}, \mathbf{v})$ and $f^{c_2}(t, \mathbf{x}, \mathbf{v})$. The component c_1 has up spin while the component c_2 has down spin. We take into account only the interaction between opposite spins via the s-wave scattering. In the three-dimensional geometry ($d_v = 3$), the differential cross-section is given by (in the units where $\hbar = k_B = 1$)

$$\frac{d\sigma}{d\Omega} = \frac{a_s^2}{1 + a_s^2 m_r^2 |\mathbf{u}|^2}, \tag{6.1}$$

while in the 2D geometry ($d_v = 2$), the differential cross-section is given by

$$\frac{d\sigma}{d\Omega} = \frac{2\pi}{m_r |\mathbf{u}|} \frac{1}{\log^2(a_s^2 m_r^2 |\mathbf{u}|^2) + \pi^2}, \tag{6.2}$$

where a_s is the s-wave scattering length, which can be tunnelled by the external magnetic field according to the Feshbach resonance. Note that m_r is the reduced mass.

The quantum Boltzmann equations are derived from a heuristic argument of the

classical BE [107]. For Fermi gas, it takes the form of

$$\frac{\partial f^\imath}{\partial t} + \mathbf{v} \cdot \frac{\partial f^\imath}{\partial \mathbf{x}} - \frac{\partial U^\imath}{\partial \mathbf{x}} \cdot \frac{\partial f^\imath}{\partial \mathbf{v}} = Q^{\imath\jmath}(f^\imath, f^\jmath_*), \tag{6.3}$$

where $U^\imath(\mathbf{x}, t)$ are the effective potentials, and $Q^{\imath\jmath}$ are quantum collision operators:

$$\begin{aligned} Q^{\imath\jmath}(f^\imath, f^\jmath_*) = \int_{\mathbb{R}^d_v} \int_{\mathbb{S}^{d_v-1}} |\mathbf{u}| \frac{d\sigma}{d\Omega} \{ & f^\jmath('\mathbf{v}^{\imath\jmath}_*) f^\imath('\mathbf{v}^{\imath\jmath})[1 - f^\jmath(\mathbf{v}_*)][1 - f^\imath(\mathbf{v})] \\ & - f^\jmath(\mathbf{v}_*) f^\imath(\mathbf{v})[1 - f^\jmath('\mathbf{v}^{\imath\jmath}_*)][1 - f^\imath('\mathbf{v}^{\imath\jmath})] \} d\Omega d\mathbf{v}_*, \end{aligned} \tag{6.4}$$

with the relation between the post- and pre-collision velocities given by Eq. (5.6).

When the VDFs are known, one can obtain the macroscopic quantities. For example, the atom number density, bulk velocity, shear stress, and heat flux of each component can be obtained as below ($\mathbf{v}_r = \mathbf{v} - \mathbf{V}$):

$$\begin{aligned} n^\imath &= \left(\frac{m_\imath}{2\pi}\right)^{d_v} \int f^\imath d\mathbf{v}, \quad \mathbf{V}^\imath = \left(\frac{m_\imath}{2\pi}\right)^{d_v} \frac{1}{n^\imath} \int \mathbf{v} f^\imath d\mathbf{v}, \\ P^\imath_{ij} &= \left(\frac{m_\imath}{2\pi}\right)^{d_v} m_\imath \int v_{ri} v_{rj} f^\imath d\mathbf{v}, \quad q_i = \left(\frac{m_\imath}{2\pi}\right)^{d_v} \frac{m_\imath}{2} \int v_{ri} |v_r|^2 f^\imath d\mathbf{v}. \end{aligned} \tag{6.5}$$

Introducing the entropy function $H = -\sum_\imath \int d\mathbf{v}[f^\imath \ln f^\imath + (1 - f^\imath)\ln(1 - f^\imath)]$ to Eq. (6.3), one gets the equilibrium distribution function

$$f_{eq} \equiv \left\{ Z^{-1} \exp\left[\frac{m(\mathbf{v} - \mathbf{V})^2}{2k_B T}\right] + 1 \right\}^{-1}, \tag{6.6}$$

where $Z(\mathbf{x}, t)$ is the local fugacity satisfying $\ln Z = (\mu' - U)/k_B T$, with μ' being the chemical potential.

When the quantum system is in equilibrium, we have

$$n = \left(\frac{m k_B T}{2\pi}\right)^{d_v/2} G_{d_v/2}(Z), \quad P_{\alpha\beta} = n k_B T \frac{G_{d_v/2+1}(Z)}{G_{d_v/2}(Z)} \delta_{\alpha\beta}, \tag{6.7}$$

where $G_n(Z) = \frac{1}{\Gamma(n)} \int_0^\infty \frac{x^{n-1}}{Z^{-1} e^x - \theta} dx$ is the Fermi-Dirac function. When $Z \to 0$, $G_n(Z) \to Z$, the quantum gas is in the near classical limit, where the equilibrium VDF is very close to the Maxwellian equilibrium VDF for classical gases and the behaviour of quantum gases is similar to the classical ones.

6.2 Fast spectral method

Following Refs. [53, 54], we separate the quantum collision operator to $Q^{\imath\jmath}(f^\imath, f^\jmath_*) = Q^{\imath\jmath}_c - Q^{\imath\jmath}_1 - Q^{\imath\jmath}_2 + Q^{\imath\jmath}_3 + Q^{\imath\jmath}_4$, where $Q^{\imath\jmath}_c(f^\imath, f^\jmath_*) = \int_{\mathbb{R}^d_v}\int_{\mathbb{S}^{d_v-1}} |\mathbf{u}|\frac{d\sigma}{d\Omega}[f^\jmath(\prime\mathbf{v}^{\imath\jmath}_*)f^\imath(\prime\mathbf{v}^{\imath\jmath}) - f^\jmath(\mathbf{v}_*)f^\imath(\mathbf{v})]d\Omega d\mathbf{v}_*$ is the classical quadratic collision operator, and

$$\begin{aligned}
Q^{\imath\jmath}_1 &= \int_{\mathbb{R}^d_v}\int_{\mathbb{S}^{d_v-1}} |\mathbf{u}|\frac{d\sigma}{d\Omega} f^\jmath(\prime\mathbf{v}^{\imath\jmath}_*)f^\imath(\prime\mathbf{v}^{\imath\jmath})f^\jmath(\mathbf{v}_*)d\Omega d\mathbf{v}_*,\\
Q^{\imath\jmath}_2 &= \int_{\mathbb{R}^d_v}\int_{\mathbb{S}^{d_v-1}} |\mathbf{u}|\frac{d\sigma}{d\Omega} f^\jmath(\prime\mathbf{v}^{\imath\jmath}_*)f^\imath(\prime\mathbf{v}^{\imath\jmath})f^\imath(\mathbf{v})d\Omega d\mathbf{v}_*,\\
Q^{\imath\jmath}_3 &= \int_{\mathbb{R}^d_v}\int_{\mathbb{S}^{d_v-1}} |\mathbf{u}|\frac{d\sigma}{d\Omega} f^\jmath(\mathbf{v}_*)f^\imath(\mathbf{v})f^\jmath(\prime\mathbf{v}^{\imath\jmath}_*)d\Omega d\mathbf{v}_*,\\
Q^{\imath\jmath}_4 &= \int_{\mathbb{R}^d_v}\int_{\mathbb{S}^{d_v-1}} |\mathbf{u}|\frac{d\sigma}{d\Omega} f^\jmath(\mathbf{v}_*)f^\imath(\mathbf{v})f^\imath(\prime\mathbf{v}^{\imath\jmath})d\Omega d\mathbf{v}_*,
\end{aligned} \tag{6.8}$$

are the cubic collision operators.

We rewrite these collision operators using the Carleman-like representation. With the basic identity $2\int_{\mathbb{R}^{d_v}} \delta(2\mathbf{y}\cdot\mathbf{u} + |\mathbf{y}|^2)f(\mathbf{y})d\mathbf{y} = |\mathbf{u}|^{d_v-2}\int_{\mathbb{S}^{d_v-1}} f(|\mathbf{u}|\Omega - \mathbf{u})d\Omega$, the classical collision operator becomes $Q^{\imath\jmath}_c = 2^{d_v-1}\int_{\mathbb{R}^d_v}\int_{\mathbb{R}^{d_v}} \frac{d\sigma}{d\Omega}|\mathbf{u}|^{3-d_v}\delta(\mathbf{y}\cdot\mathbf{z})[f^\jmath(\mathbf{v}+\mathbf{z}+b\mathbf{y})f^\imath(\mathbf{v}+a\mathbf{y}) - f^\jmath(\mathbf{v}+\mathbf{y}+\mathbf{z})f^\imath(\mathbf{v})]d\mathbf{y}d\mathbf{z}$, where a and b are defined in Eq. (5.15). Note that the delta function poses the condition that $\mathbf{z}$ should be perpendicular to $\mathbf{y}$, which leads to $|\mathbf{u}|^2 = |\mathbf{y}|^2 + |\mathbf{z}|^2$. Hence for $d_v = 3$ we define the collision kernel as

$$B(|\mathbf{y}|, |\mathbf{z}|) = 4\frac{d\sigma}{d\Omega} = \frac{4a_s^2}{1 + a_s^2 m_r^2(|\mathbf{y}|^2 + |\mathbf{z}|^2)}, \tag{6.9}$$

while for $d_v = 2$ we have

$$B(|\mathbf{y}|, |\mathbf{z}|) = 2\frac{d\sigma}{d\Omega}|\mathbf{u}| = \frac{4\pi}{m_r}\frac{1}{\log^2[a_s^2 m_r^2(|\mathbf{y}|^2 + |\mathbf{z}|^2)] + \pi^2}. \tag{6.10}$$

Since the distribution functions have the support S, the relative velocity $|\mathbf{u}| \le 2S$. Therefore, the infinite integration region in the collision operator is reduced to $\mathcal{B}_R$, i.e., $|\mathbf{y}|, |\mathbf{z}| \le R$ with $R = \sqrt{2}S$, which results in the truncated collision operator

$$Q^{\imath\jmath}_c = \int_{\mathcal{B}_R}\int_{\mathcal{B}_R} B(|\mathbf{y}|, |\mathbf{z}|)\delta(\mathbf{y}\cdot\mathbf{z})[f^\jmath(\mathbf{v}+\mathbf{z}+b\mathbf{y})f^\imath(\mathbf{v}+a\mathbf{y}) - f^\jmath(\mathbf{v}+\mathbf{y}+\mathbf{z})f^\imath(\mathbf{v})]d\mathbf{y}d\mathbf{z}. \tag{6.11}$$

Similarly, the cubic collision operators can be rewritten as

$$\begin{aligned}
Q_1^{\imath\jmath} &= \int_{\mathcal{B}_R}\int_{\mathcal{B}_R} B(|\mathbf{y}|,|\mathbf{z}|)\delta(\mathbf{y}\cdot\mathbf{z}) f^\jmath(\mathbf{v}+\mathbf{z}+b\mathbf{y}) f^\imath(\mathbf{v}+a\mathbf{y}) f^\jmath(\mathbf{v}+\mathbf{y}+\mathbf{z}) d\mathbf{y}d\mathbf{z},\\
Q_2^{\imath\jmath} &= \int_{\mathcal{B}_R}\int_{\mathcal{B}_R} B(|\mathbf{y}|,|\mathbf{z}|)\delta(\mathbf{y}\cdot\mathbf{z}) f^\jmath(\mathbf{v}+\mathbf{z}+b\mathbf{y}) f^\imath(\mathbf{v}+a\mathbf{y}) f^\imath(\mathbf{v}) d\mathbf{y}d\mathbf{z},\\
Q_3^{\imath\jmath} &= \int_{\mathcal{B}_R}\int_{\mathcal{B}_R} B(|\mathbf{y}|,|\mathbf{z}|)\delta(\mathbf{y}\cdot\mathbf{z}) f^\jmath(\mathbf{v}+\mathbf{z}+b\mathbf{y}) f^\jmath(\mathbf{v}+\mathbf{y}+\mathbf{z}) f^\imath(\mathbf{v}) d\mathbf{y}d\mathbf{z},\\
Q_4^{\imath\jmath} &= \int_{\mathcal{B}_R}\int_{\mathcal{B}_R} B(|\mathbf{y}|,|\mathbf{z}|)\delta(\mathbf{y}\cdot\mathbf{z}) f^\imath(\mathbf{v}+a\mathbf{y}) f^\jmath(\mathbf{v}+\mathbf{y}+\mathbf{z}) f^\imath(\mathbf{v}) d\mathbf{y}d\mathbf{z}.
\end{aligned} \tag{6.12}$$

Expanding the truncated collision operators in the truncated Fourier series, we find that, for the classical collision operator, the $\mathbf{j}$-th model $\widehat{Q}_c^{\imath\jmath}(\xi_\mathbf{j})$ is given by Eq. (5.17). Similarly, the $\mathbf{j}$-th mode of the truncated cubic collision operators can be expressed as

$$\begin{aligned}
\widehat{Q}_1^{\imath\jmath}(\xi_\mathbf{j}) &= \sum_{\substack{\mathbf{l}+\mathbf{m}+\mathbf{n}=\mathbf{j}\\ \mathbf{l},\mathbf{m},\mathbf{n}=-N/2}}^{N/2-1} \hat{f}_\mathbf{l}^\imath \hat{f}_\mathbf{m}^\jmath \hat{f}_\mathbf{n}^\jmath \beta(a\mathbf{l}+b\mathbf{m}+\mathbf{n},\mathbf{m}+\mathbf{n}),\\
\widehat{Q}_2^{\imath\jmath}(\xi_\mathbf{j}) &= \sum_{\substack{\mathbf{l}+\mathbf{m}+\mathbf{n}=\mathbf{j}\\ \mathbf{l},\mathbf{m},\mathbf{n}=-N/2}}^{N/2-1} \hat{f}_\mathbf{l}^\imath \hat{f}_\mathbf{m}^\jmath \hat{f}_\mathbf{n}^\imath \beta(a\mathbf{l}+b\mathbf{m},\mathbf{m}),\\
\widehat{Q}_3^{\imath\jmath}(\xi_\mathbf{j}) &= \sum_{\substack{\mathbf{l}+\mathbf{m}+\mathbf{n}=\mathbf{j}\\ \mathbf{l},\mathbf{m},\mathbf{n}=-N/2}}^{N/2-1} \hat{f}_\mathbf{l}^\imath \hat{f}_\mathbf{m}^\jmath \hat{f}_\mathbf{n}^\imath \beta(\mathbf{m}+a\mathbf{n},\mathbf{m}),\\
\widehat{Q}_4^{\imath\jmath}(\xi_\mathbf{j}) &= \sum_{\substack{\mathbf{l}+\mathbf{m}+\mathbf{n}=\mathbf{j}\\ \mathbf{l},\mathbf{m},\mathbf{n}=-N/2}}^{N/2-1} \hat{f}_\mathbf{l}^\imath \hat{f}_\mathbf{m}^\jmath \hat{f}_\mathbf{n}^\jmath \beta(\mathbf{m}+b\mathbf{n},\mathbf{m}+\mathbf{n}),
\end{aligned} \tag{6.13}$$

where the kernel mode $\beta(\mathbf{l},\mathbf{m})$ is given by Eq. (5.18).

When $d_v = 3$, the kernel mode is simplified to (suppose here the integral with respect to the unit vector $\mathbf{e}$ in Eq. (5.19) is approximated by the trapezoidal rule)

$$\beta(\mathbf{l},\mathbf{m}) \simeq \frac{\pi^2}{M^2} \sum_{r,p,q=1}^{M_2,M-1,M} \omega_r|\rho_r| \exp(i\rho_r\xi_\mathbf{l}\cdot\mathbf{e}_{\theta_p,\varphi_q})\psi(\rho_r,|\xi_\mathbf{m}|\cos\theta_1)\sin\theta_p, \tag{6.14}$$

where

$$\psi(\rho_r,s) = 8\pi a_s^2 \int_0^R \frac{\rho' J_0(\rho' s)d\rho'}{1+a_s^2 m_r^2(\rho'^2+\rho_r^2)}, \tag{6.15}$$

and ρ_r and ω_r $(r = 1, 2, \cdots, M_2)$ are the abscissas and weights of the Gauss-Legendre quadrature in the region $[-R, R]$.

Analogously, for $d_v = 2$, the kernel mode is simplified to

$$\beta(\mathbf{l}, \mathbf{m}) \simeq \frac{\pi}{M} \sum_{r,p=1}^{M_2,M} \omega_r \exp(i\rho_r \xi_{\mathbf{l}} \cdot \mathbf{e}_{\theta_p}) \psi(\xi_{\mathbf{m}} \cdot \mathbf{e}_{\theta_{p+\frac{\pi}{2}}}), \tag{6.16}$$

where $e_{\theta_p} = (\cos\theta_p, \sin\theta_p)$ with $\theta_p = p\pi/M$, and

$$\psi(\rho_r, s) = \frac{8\pi}{m_r} \int_0^R \frac{\cos(\rho' s) d\rho'}{\log^2[a_s^2 m_r^2 (\rho'^2 + \rho_r^2)] + \pi^2}. \tag{6.17}$$

Notice that the procedure in deriving the FSM for quantum BE is essentially the same as that for classical BE, therefore, it can be proved that the present fast spectral method conserves the mass and satisfies the H-theorem, while the error on the approximation of momentum and energy is spectrally small.

6.3 Detailed implementation

We take the 2D case as an example. With Eq. (6.16), we have

$$\begin{aligned} \widehat{Q}_c^{ij}(\xi_{\mathbf{j}}) \simeq & \frac{\pi}{M} \sum_{g,p=1}^{M_2,M} \sum_{\substack{\mathbf{l}+\mathbf{m}=\mathbf{j} \\ \mathbf{l},\mathbf{m}=-N/2}}^{N/2-1} \underbrace{\omega_r \exp(ia\rho_r \xi_{\mathbf{l}} \cdot \mathbf{e}_{\theta_p}) \hat{f}_{\mathbf{l}}^i \times \exp(ib\rho_r \xi_{\mathbf{m}} \cdot \mathbf{e}_{\theta_p}) \psi(\xi_{\mathbf{m}} \cdot e_{\theta_{p+\frac{\pi}{2}}}) \hat{f}_{\mathbf{m}}^j}_{C_1^{gp}(l+m)} \\ & - \frac{\pi}{M} \sum_{\substack{\mathbf{l}+\mathbf{m}=\mathbf{j} \\ \mathbf{l},\mathbf{m}=-N/2}}^{N/2-1} \hat{f}_{\mathbf{l}}^i \times \sum_{g,p=1}^{M_2,M} \omega_r \exp(i\rho_r \xi_{\mathbf{m}} \cdot \mathbf{e}_{\theta_p}) \psi(\xi_{\mathbf{m}} \cdot \mathbf{e}_{\theta_{p+\frac{\pi}{2}}}) \hat{f}_{\mathbf{m}}^j. \end{aligned} \tag{6.18}$$

It is clearly seen that, if using the FFT-based convolution, the computational cost of the classical collision operator Q_c is at the order of $O(MM_2N^2 \log N)$. In real computations, we take $M = 4 \sim 8$ and $M_2 = 10 \sim 20$. It should be noted that, if $\mathbf{y}$ and $\mathbf{z}$ are separable in the collision kernel $B(|\mathbf{y}|, |\mathbf{z}|)$, the cost can be reduced to $O(MN^2 \log N)$ and our scheme is exactly the same as that in Refs. [54].

Similarly, the cubic collision operators Q_1 and Q_3 can also be computed at the cost

of $O(MM_2N^2\log N)$:

$$\widehat{Q}_1^{ij}(\xi_{\mathbf{j}}) \simeq \frac{\pi}{M}\sum_{g,p=1}^{M_2,M}\sum_{l=-N/2}^{N/2-1}\exp(ia\rho_r\xi_l\cdot\mathbf{e}_{\theta_p})\hat{f}_{\mathbf{l}}^i \times \sum_{\substack{\mathbf{m}+\mathbf{n}=\mathbf{j}-\mathbf{l}\\ m,n=-N/2}}^{N/2-1}\underbrace{\left[\omega_r\exp(ib\rho_r\xi_{\mathbf{m}}\cdot\mathbf{e}_{\theta_p})\hat{f}_{\mathbf{m}}^j\times\exp(i\rho_r\xi_{\mathbf{n}}\cdot\mathbf{e}_{\theta_p})\hat{f}_{\mathbf{n}}^j\right]\psi(\xi_{\mathbf{m}+\mathbf{n}}\cdot\mathbf{e}_{\theta_p+\frac{\pi}{2}})}_{C_2^{gp}(\mathbf{m}+\mathbf{n})},$$

$$\widehat{Q}_3^{ij}(\xi_{\mathbf{j}}) \simeq \frac{\pi}{M}\sum_{l=-N/2}^{N/2-1}\hat{f}_{\mathbf{l}}^i \times \sum_{g,p=1}^{M_2,M}\sum_{\substack{\mathbf{m}+\mathbf{n}=\mathbf{j}-\mathbf{l}\\ m,n=-N/2}}^{N/2-1}\omega_r\exp(ia\rho_r\xi_{\mathbf{n}}\cdot\mathbf{e}_{\theta_p})\hat{f}_{\mathbf{n}}^i\times\exp(i\rho_r\xi_{\mathbf{m}}\cdot\mathbf{e}_{\theta_p})\hat{f}_{\mathbf{m}}^j\psi(\xi_{\mathbf{m}}\cdot\mathbf{e}_{\theta_p+\frac{\pi}{2}}),$$

while for the cubic collision operators Q_2 and Q_4, based on the computed C_1^{gp} and C_2^{gp}, the computational costs can be reduced to $O(N^2\log N)$:

$$\widehat{Q}_2^{ij}(\xi_{\mathbf{j}}) \simeq \frac{\pi}{M}\sum_{n=-N/2}^{N/2-1}\hat{f}_{\mathbf{n}}^i \times \sum_{g,p=1}^{M_2,M}C_1^{gp}(\mathbf{j}-\mathbf{n}),\quad \widehat{Q}_4^{ij}(\xi_{\mathbf{j}}) \simeq \frac{\pi}{M}\sum_{l=-N/2}^{N/2-1}\hat{f}_{\mathbf{l}}^i \times \sum_{g,p=1}^{M_2,M}C_2^{gp}(\mathbf{j}-\mathbf{l}).$$

Therefore, for $d_v = 2$, the overall computational cost is $O(MM_2N^3\log N)$, while for $d_v = 3$, the computational cost is $O(M^2M_2N^3\log N)$.

6.4 Spin diffusion in a harmonic potential

As an application of the FSM for the quantum Fermi equation, we consider the spin diffusion in a harmonic potential. Initially, the spin-up component locates at $x = -1$ (centre-of-mass), while the spin-down component is at $x = 1$. The two components have the same atom number and small mass. If there is no interaction between the two components, the two components will pass through each other repeatedly and the centre-of-mass each component will oscillate sinusoidally, due to the harmonic potential. If there exists strong interaction between the two components, however, each component would rather be scattered away than goes to the trap centre.

To quantitatively show the centre-of-mass evolution, we carry out the direct numer-

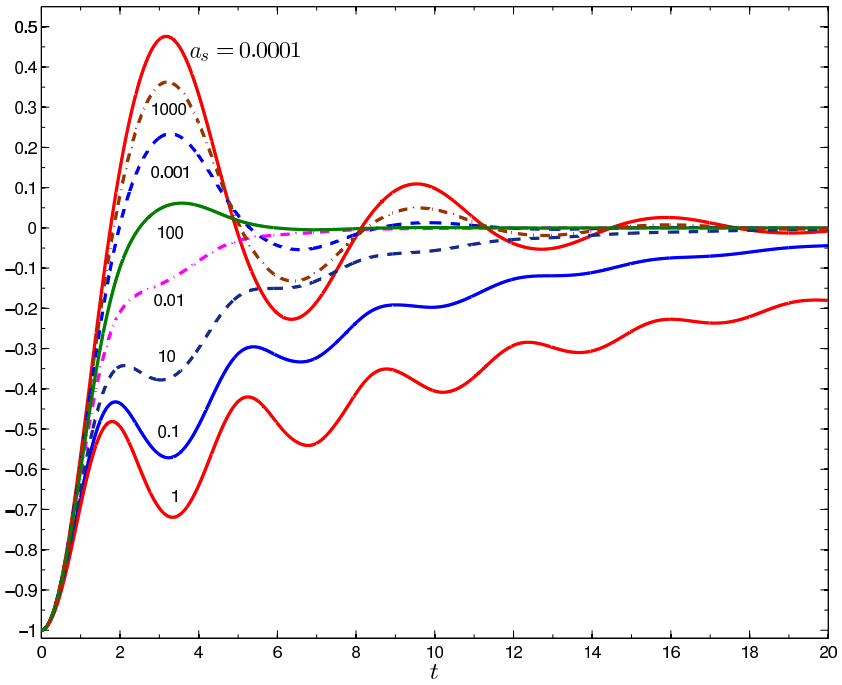

Figure 6.1: Centre-of-mass evolution of the spin down component.

ical simulations at various value of s-wave scattering length. The results are shown in Figure 6.1. The reflection dynamics is observed when the collision frequencies are high, at $a_s = 0.1, 1$, and 10. The approaching dynamic is observed at $a_s = 0.01$, while the pass through effects are observed at $a_s = 0.0001, 0.001, 100$, and 1000. This is because the differential cross-section in 2D geometry first increases with a_s and then decreases, with its maximum value achieved at $a_s^2 m_r T \approx 1$.

6.5 Summary

The FSM is applied to the BE for quantum Fermi gases with realistic collision kernels. The interesting spin-diffusion problem in harmonic potential is considered. The method may be used to explain the recent experiments [108–110]. The method can be directly applied to quantum Bose gases, where $(1-f)$ in Eq. (6.4) should be replaced by $(1+f)$.

Chapter 7

Collective oscillations in dilute quantum gas

7.1 Background

The realisation of quantum degeneracy in the ultracold atomic gases has attracted intensive research efforts to understand the interacting quantum systems [111, 112]. The experimental controllability of the interactions, energy, and spin population makes these systems ideal to study the crossover from a Bose-Einstein condensation (BEC) to a Bardeen-Cooper-Schrieffer (BCS) superfluid, which is ubiquitous in high-temperature superconductivity, neutron stars, nuclear matter, and quark-gluon plasma [113].

In the zero-temperature limit, the superfluid behaviour of the Fermi gases is well understood [112, 114, 115]. At high temperatures, the dilute quantum gases are in the normal phase and their dynamics can be described by the quantum BE [107]. On the other hand, when the temperature is below the critical temperature for superfluidity, the superfluid and normal phases coexist. In this case, the BE for the dynamics of the quasiparticle distribution function and the Euler equations for the superfluid order parameter can be combined to describe the quantum gas dynamics [116, 117].

The study of the low-lying excitation modes (see Figure 7.1) is important for probing the properties of strongly correlated systems, revealing the underlying mechanics of BEC-BCS crossover. So far, the effects of temperature on the collective mode remain unclear. For instance, experimentally, in the same temperature range, Kinast *et*

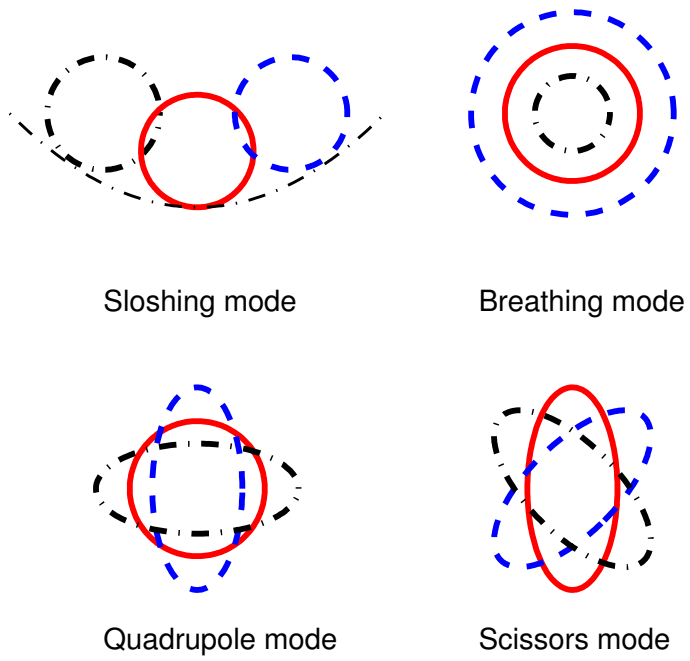

Figure 7.1: Sketch of the four typical collective oscillations in the external harmonic potential. The solid lines: density shapes of the quantum gas at equilibrium. The dashed and dash-dotted lines: intermediate states. For the excitation of the breathing mode, the strength of the external potential is suddenly decreased and held at its new value hereafter, so that the density shape goes from the solid circle to the dashed one, and then back to the solid again, forming half of the oscillation period. Later on, the density shape changes to the dash-dotted circle and return to the solid-line shape, completing another half period of oscillation.

al. demonstrated that the frequency of the radial breathing mode stayed close to the hydrodynamic value [118], while Wright *et al.* measured the scissors mode and found a clear transition from the hydrodynamic to collisionless behavior [119]. This discrepancy motivated Riedl *et al.* to measure the frequency and damping of the radial compression (breathing), quadrupole, and scissors modes in a similar experimental condition and to compare the experimental data with the analytical prediction of the moment method [120]. However, there are discrepancies between the experimental and theoretical results, especially for the radial quadrupole mode.

The analytical expressions for the mode frequency and damping were obtained by applying the method of moments to the linearised BE [120–124]. However, this method may not provide accurate predictions for the quantum gas in the transition regime [120, 125], which is caused by i) the spatially-dependent relaxation time is replaced by the spatially-average one and/or ii) only low orders of moments are included in the analytical method, which may not be adequate for capturing the important

features of the collective oscillations. For example, one needs to consider high-order terms for the cloud surface deformation at large radii in the quadrupole mode if using average relaxation time [125]. The other major drawback of the analytical method is that it is only limited to the external harmonic potentials, while experimentally anharmonic effects emerge at high temperatures where the external potential has a Gaussian profile [119, 120]. Therefore, it is necessary to solve the BE numerically to get the accurate mode frequency and damping. Only in this way can we know the applicability of the Boltzmann description in quantum gases.

Here we put forward a deterministic method to numerically solve the Boltzmann model equation in the hydrodynamic, transition, and collisionless regimes. This Chapter is divided into two parts. First, we solve the classical BGK model. We extract the frequency and damping of the radial quadrupole and scissors modes and compare them with the analytical and experimental data [119–121, 124]. With the numerical results, we find that the difference between the experimental data and the analytical results of the BE in Refs. [119, 120] is reduced. Second, we solve the quantum BGK model and indicates the applicability of this model in describing the quadrupole oscillations in 2D Fermi gases.

7.2 Classical BGK model

We consider two-component balanced Fermi gases well above the degeneracy temperature, where the gases are statistically classical but the collisions are quantum. The dilute Fermi gas is in the normal phase and the up-spin and down-spin components have the same atom mass m. Due to the Pauli's exclusion principle, collision happens between atoms with different spins. For most of the experiments the two components move together and one needs only consider one VDF. Furthermore, the experiments of Wright *et al.* and Riedl *et al.* are conducted in elongated traps so that one can focus only on the radial collective oscillations, neglecting the axial motion [119, 120, 126]. Thus, the problem is effectively 2D. In general, due to the presence of the Gaussian

laser beam, the gas is trapped in the two-dimensional Gaussian potential

$$U(x,y) = U_0\left[1 - \exp\left(-\frac{x^2}{W_a^2} - \frac{y^2}{W_b^2}\right)\right], \tag{7.1}$$

where U_0 is trap depth and W_a, W_b are the trap widths. At low temperatures, the atom cloud is far smaller than the trap widths, so that the potential is nearly harmonic

$$U(x,y) = \frac{m}{2}(\omega_x^2 x^2 + \omega_y^2 y^2), \tag{7.2}$$

where the trap frequencies satisfy $\omega_x = \sqrt{2U_0/m}/W_a$ and $\omega_y = \sqrt{2U_0/m}/W_b$.

Instead of the quantum BE, we first begin with the classical BGK model; this model can capture the essential physics of the problem and has been widely used to describe rarefied gas dynamics. It reads

$$\frac{\partial f}{\partial t} + v_x\frac{\partial f}{\partial x} + v_y\frac{\partial f}{\partial y} + a_x\frac{\partial f}{\partial v_x} + a_y\frac{\partial f}{\partial v_y} = \frac{f_{le} - f}{\tau(x,y)}, \tag{7.3}$$

where $(a_x, a_y) = -(\partial/\partial x, \partial/\partial y)U(x,y)/m$ are the accelerations, $\tau(x,y)$ is the local relaxation time, and f_{le} is the local equilibrium distribution function

$$f_{le} = \frac{mn}{2\pi k_B T}\exp\left[-m\frac{(v_x - V_x)^2 + (v_y - V_y)^2}{2k_B T}\right], \tag{7.4}$$

which is defined in terms of the local particle density $n(x,y)$, local temperature $T(x,y)$, and local macroscopic velocities $V_x(x,y)$ and $V_y(x,y)$. When the system is in global thermal equilibrium, $n = n_0\exp[-U(x,y)/k_B T_0]$, with n_0 being the particle density at the trap centre and T_0 the global equilibrium temperature.

The shear viscosity plays a dominant role in the collective oscillations; the atom cloud remains nearly isothermal and the experiments [127, 128] are not sensitive to the thermal conductivity. Therefore, the local relaxation time can be determined by equating the shear viscosity of the quantum BE with that derived from the BGK model (7.3), yielding $\tau = \mu/nk_B T$. When the vacuum expression for the cross-section is used [123], we have $\tau(x,y) = 15\sqrt{m\pi/k_B T}/16\sigma n\int_0^\infty d\xi\xi^7 e^{-\xi^2}(1 + \xi^2 T/T_B)^{-1}$, where $\sigma = 4\pi a_s^2$ is the total energy-independent cross-section and $T_B = \hbar^2/mk_B a_s^2$ is the binding temperature of the dimer state. Two limiting cases will be considered. When

the scattering length a_s is small, the differential cross-section is energy-independent, and atoms behave like hard spheres. The local relaxation timeis given by [123, 129, 130]

$$\tau(x,y) = \frac{5}{16\sigma n(x,y)}\sqrt{\frac{m\pi}{k_B T(x,y)}}. \tag{7.5}$$

On the contrary, in the unitarity limit where $a_s \to \infty$ (atoms interact through soft potentials), we have

$$\tau(x,y) = \frac{15m^{3/2}}{64\hbar^2 n(x,y)}\sqrt{\frac{k_B T(x,y)}{\pi}}. \tag{7.6}$$

7.2.1 Asymptomatic preserving numerical scheme

The relaxation time is a crucial parameter in the collective oscillations. A spatially uniform gas is in the hydrodynamic regime when $\omega_0\tau \ll 1$. Here ω_0 is the external trap frequency (the mode frequency is of the same order). In this circumstance, the Euler and NS equations can be derived from the BE by the Chapman-Enskog expansion [129]. On the contrary, the gas is collisionless when $\omega_0\tau \gg 1$. When the gas is trapped, however, it could be in the hydrodynamic, transition ($\omega_0\tau \sim 1$), or collisionless regime in the central region of the trap, whereas in the surface region it is always collisionless. The different order-of-magnitude of τ across the trap poses difficulty in numerical simulations: if one wants to resolve the details of the collision, the time step Δt should be smaller than τ, which is not practical for the long time behaviour when the gas is in the hydrodynamic regime ($\tau \to 0$). Therefore, in a practical calculation, it is desirable to use a numerical scheme that can have practical time step across hydrodynamic and collisionless regimes as we are interested in the macroscopic behaviour of the gas.

In order to have practical time step in hydrodynamic regime, we adopt the asymptotic preserving scheme to solve the BGK model numerically [131, 132]. The virtue of this scheme is that it can capture the macroscopic gas dynamics in the hydrodynamic limit even if the small scale determined by the relaxation time τ is not numerically resolved. The computational accuracy in the hydrodynamic regime is guaranteed by the fact that, using the Chapman-Enskog expansion [5], this numerical scheme yields the correct Euler equations when holding the spatial steps and time step fixed and letting τ goes to zero. Therefore, the computation of a hydrodynamic flow can be as

fast and accurate as that of the transition and collisionless flows. This unique feature cannot be implemented by the probabilistic methods such as DSMC and MD.

The transport part of the BGK model is treated explicitly, while the collision is treated implicitly to overcome its stiffness in the hydrodynamic regime, resulting

$$\frac{f^{j+1}-f^{j}}{\Delta t}+Tr[f^{j}]=\frac{1}{\tau^{j+1}(x,y)}(f_{le}^{j+1}-f^{j+1}), \tag{7.7}$$

where the variables with superscript j denote the values of these variables at the j-th time step and $Tr[f^j]$ represents the spatial and velocity discretisation of the transport term. If the spatial and velocity ranges are wide enough such that f is negligible small at the boundaries, $Tr[f^j]$ can be handled by the fast Fourier transformation to achieve the spectral accuracy. By using the conservative properties of the collision term, the nonlinear implicit equation (7.7) can be solved explicitly. That is, given f^j, one can get n^{j+1}, u_x^{j+1}, u_y^{j+1}, and T^{j+1} from the following equations: $n^{j+1}=\int F dv_x dv_y$, $(V_x^{j+1},V_y^{j+1})=\int(v_x,v_y)F dv_x dv_y/n^{j+1}$, and $T^{j+1}=m[\int(v_x^2+v_y^2)F dv_x dv_y/n^{j+1}-(V_x^{j+1})^2-(V_y^{j+1})^2]/2k_B$, where $F=f^j-\Delta t T[f^j]$ and the numerical integration can be carried out by direct discrete sum or by the Simpson's rule. The above four macroscopic quantities at the $(j+1)$-th time step determine f_{le}^{j+1} according to Eq. (7.4) and τ^{j+1} according to Eq. (7.5) or (7.6). Therefore, f^{j+1} can be solved explicitly.

In practice, since $n(x,y)$ is very small near the boundary, numerical error emerges when calculating the macroscopic velocity. Hence it is possible to get negative temperature, which is not physical. To tackle this problem, the collision term in Eq. (7.7) is neglected near the spatial boundary. This is justified by the fact that far from the trap centre the gas is in the collisionless limit so the collision term is negligible. Another point one should pay attention to is that, the maximum CourantFriedrichsLewy number $\Delta t\cdot\max\{|v_x|/\Delta x+|v_y|/\Delta y+|a_x|/\Delta v_x+|a_y|/\Delta v_y\}$ with $\Delta x,\Delta y$ the spatial steps and $\Delta v_x,\Delta v_y$ the velocity steps, must be smaller than 1.

7.2.2 Numerical validations

To validate the numerical scheme, we simulate the radial sloshing and breathing modes in the isotropic harmonic trap with $\omega_x,\omega_y=\omega_0$. The local relaxation time is given by Eq. (7.5). However, the use of Eq. (7.6) will give the same result because the cloud is

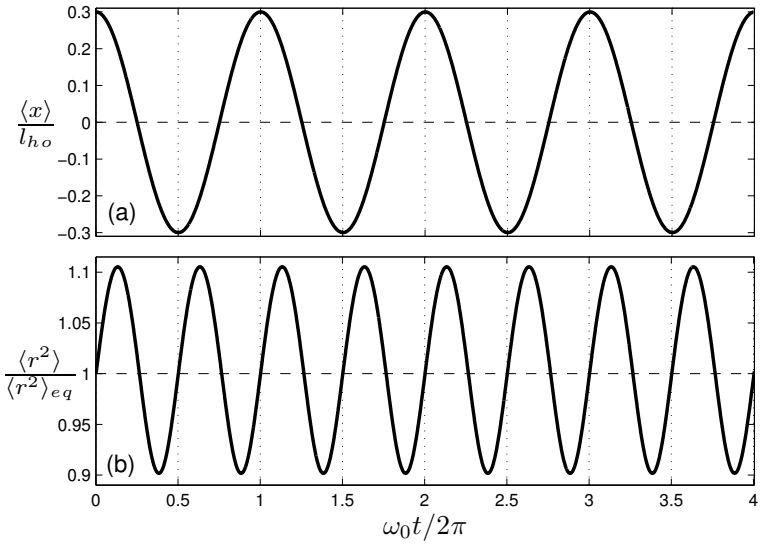

Figure 7.2: Numerical simulation of the (a) sloshing mode and (b) breathing mode. The initial distribution function is $f = \exp\{-[\omega_0^2(x-0.3l_{ho})^2 + \omega_0^2 y^2 + v_x^2 + v_y^2]/2\}/2\pi$ for the sloshing mode and $f = \exp\{-[\omega_0^2(x^2+y^2) + (v_x - 0.8x)^2 + (v_y - 0.8y)^2]/2\}/2\pi$ for the breathing mode. In both simulations, $m = k_B = T_0 = 1, \omega_0 = \sigma = 4$, so that the characteristic length l_{ho} is 0.25 and the system is in the transition regime. The spatial region $[-1.5, 1.5]^2$ and the velocity region $[-8, 8]^2$ are uniformly discretized into 64×64 and 32×32 meshes, respectively. The time step is $\Delta t = 0.002$ and the maximum CFL number is 0.875. Here <> means the spatial average.

nearly isothermal, i.e., after normalisation, only $n(x, y)$ affects $\tau(x, y)$. The numerical results in Figure 7.2 show that, as expected, the sloshing and breathing modes oscillate with the frequency ω_0 and $2\omega_0$, respectively [122, 125]. Note that the simulations were carried out in the transition regime, where damped modes decay rapidly. The two perfectly undamped modes prove the accuracy of the numerical scheme.

7.2.3 Results for the harmonic potential

Now we simulate the radial quadrupole mode and compare the results with the analytical and experimental ones. Analytically, replacing the local relaxation time $\tau(x, y)$ by the average relaxation time $\widetilde{\tau} = 2\sqrt{2}\tau(0, 0)$ and applying the method of moments up to the second-order, one finds that the mode frequency ω_r and damping rate ω_i satisfy [121, 133]

$$\omega^2 - 2\omega_0^2 - i\omega\widetilde{\tau}(\omega^2 - 4\omega_0^2) = 0, \tag{7.8}$$

where $\omega = \omega_r - i\omega_i$. This equation clearly shows that in the hydrodynamic regime, the mode frequency is $\omega_r = \sqrt{2}\omega_0$, while in the collisionless regime, it is $\omega_r = 2\omega_0$.

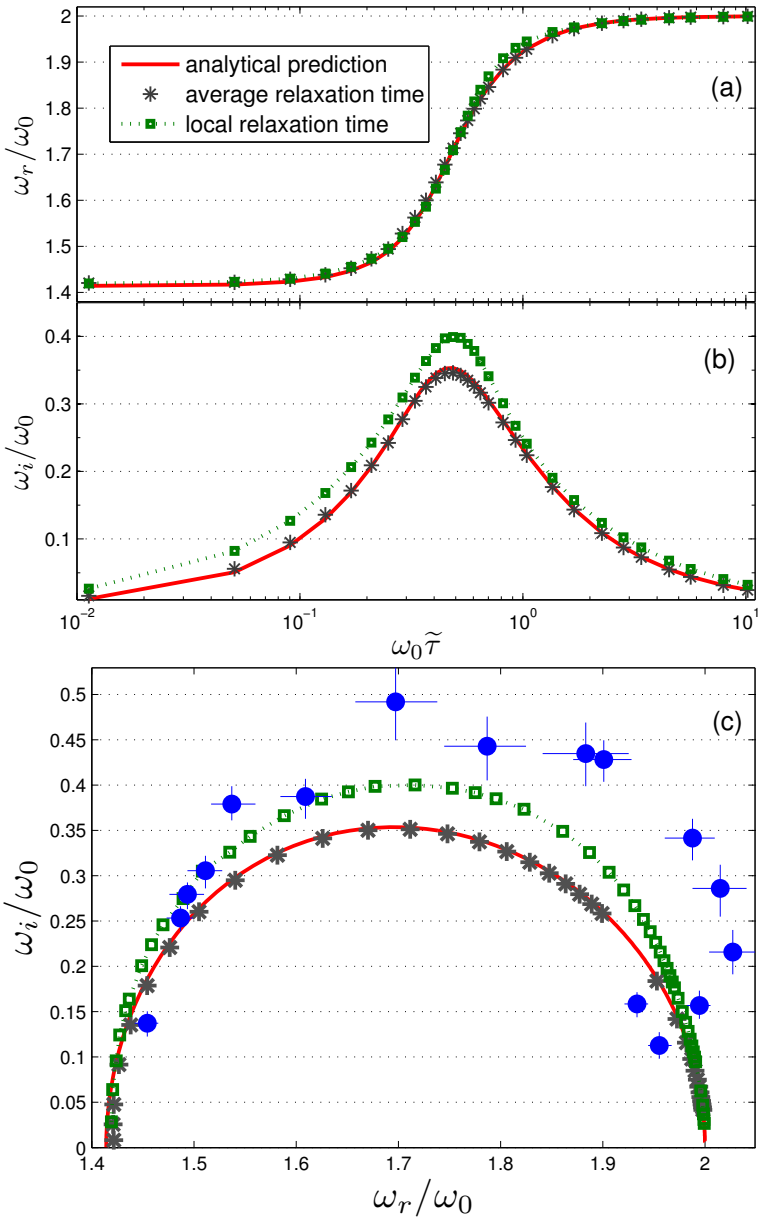

Figure 7.3: (a) The normalised collective frequency and (b) damping of the radial quadrupole mode vs the nondimensional variable $\omega_0\widetilde{\tau}$. The results are obtained by fitting the quadrupole moment $Q = \langle x^2 - y^2 \rangle$ through the equation $Q(t) = A\exp(-\omega_i t)\sin(\omega_r t + \phi) + B\exp(-Ct)$. The quadrupole mode is excited by initial distribution function $\exp\{-[\omega_0^2(x^2+y^2)+(v_x-0.8x)^2+(v_y+0.8y)^2]/2\}/2\pi$. The value of cross-section σ is varied to change the system from the hydrodynamic limit to the collisionless limit. Other parameters are the same as those in Figure 7.2. (c) Damping ω_i versus collective frequency ω_r of the radial quadrupole mode. For the experimental data (solid circles), ω_0 represents the frequency of the sloshing mode when the gas is trapped in the Gaussian potential [120].

As mentioned above, the analytical solution (7.8) are not accurate due to the local relaxation time is replaced by the average one and/or only the second-order moments are included. Thus, in the numerical simulations, we use both the local and average relaxation times to see which factor affects the accuracy of the analytical results. Numerically extracted mode frequency and damping are depicted in Figure 7.3. When the average relaxation time is used, the numerical obtained mode frequency, damping, and their relations (stars) agree with the analytical results very well, so it is sufficient to include up to the second-order moments. The inaccuracy of the analytical results is therefore caused solely by replacing the local relaxation time with the average one. Comparing the analytical results with the numerical (squares, when the local relaxation time is used) and experimental ones (solid circles), one finds that the analytical mode frequency coincides with the numerical one [Figure 7.3(a)], while the analytical method underestimates the damping, especially in the transition regime [Figure 7.3(b) and (c)]. With the numerical results (squares), the difference between the experimental data and that of the BE in Ref. [120] is greatly reduced.

Finally, we simulate the radial scissors mode in the elliptical harmonic potential with $\omega_x = 2\omega_y = 4$. Analytically, the method of moments up to second-order predicts the following relation between the mode frequency and damping [124]

$$i\omega(\omega^2 - \omega_h^2) + \widetilde{\tau}(\omega^2 - \omega_{c1}^2)(\omega^2 - \omega_{c2}^2) = 0, \tag{7.9}$$

where $\omega_h = (\omega_x^2 + \omega_y^2)^{1/2}$ is the frequency in the hydrodynamic limit and $\omega_{c1} = \omega_x + \omega_y$, $\omega_{c2} = |\omega_x - \omega_y|$ are the frequencies at the collisionless limit.

Typical oscillation sceneries of the radial scissors mode are shown in Figure 7.4. In the collisionless limit ($\sqrt{\omega_x\omega_y}\widetilde{\tau} = 28$), the angle of atom cloud oscillates with two frequencies of 5.999 and 2, and the damping rate of 0.036. As the value of $\sqrt{\omega_x\omega_y}\widetilde{\tau}$ decreases, both of the frequencies decrease, with the larger one gradually reducing to $2\sqrt{2}$ [Figure 7.5(a)] and the smaller one quickly approaching to zero. For example, when $\sqrt{\omega_x\omega_y}\widetilde{\tau} = 0.316$, $\omega_r = 4.609$ and the smaller frequency is already 0.012; however, the damping corresponding to the larger frequency decreases with an initial increase [Figure 7.5(b)]. The largest damping is achieved when $\sqrt{\omega_x\omega_y}\widetilde{\tau} = 0.72$, where the scissors mode damps out within 2 oscillations. When the average relaxation time is used

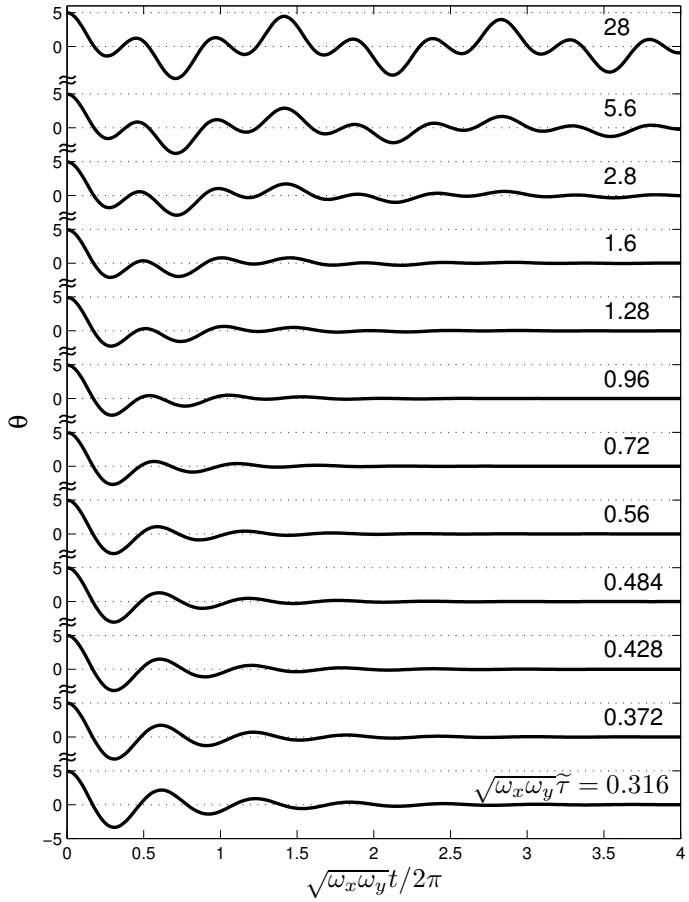

Figure 7.4: The angle (in degrees) of atom cloud vs the normalized time. The scissors mode is excited by sudden rotation of the trap angle $\theta(0)$ by 5^o. The trap frequencies are $\omega_x = 2\omega_y = 4$. The time step is $\Delta t = 0.0025$ and the maximum CFL number is 0.82. Other parameters are the same as those in Fiure 7.2, except the spatial region in the y direction is now $[-3, 3]$. The angle is obtained by $\theta(t) = 90\,\mathrm{atan}[\langle xy\rangle/\langle x^2 - y^2\rangle]/\pi$.

in the numerical simulation, the mode frequency (stars) overlaps with the analytical prediction [Figure 7.5(a)], while the damping agrees with the analytical prediction only in the hydrodynamic and collisionless regimes [Figure 7.5(b)]; in the transition regime the damping is slightly larger than that of the analytical prediction. This implies that, unlike the radial quadrupole mode, the analytical ansatz (see Eq. (4) in Ref. [124]) is not accurate enough. When the local relaxation time is used, both the mode frequency and damping do not agree with the analytical prediction, especially in the transition regime: the mode frequency is always larger than the analytical one, while the damping could be smaller or larger than the analytical one, depending on the value of $\sqrt{\omega_x\omega_y}\widetilde{\tau}$. For the relation between mode frequency and damping, the numerical results are always larger than the analytical one, see Figure 7.5(c). Like the

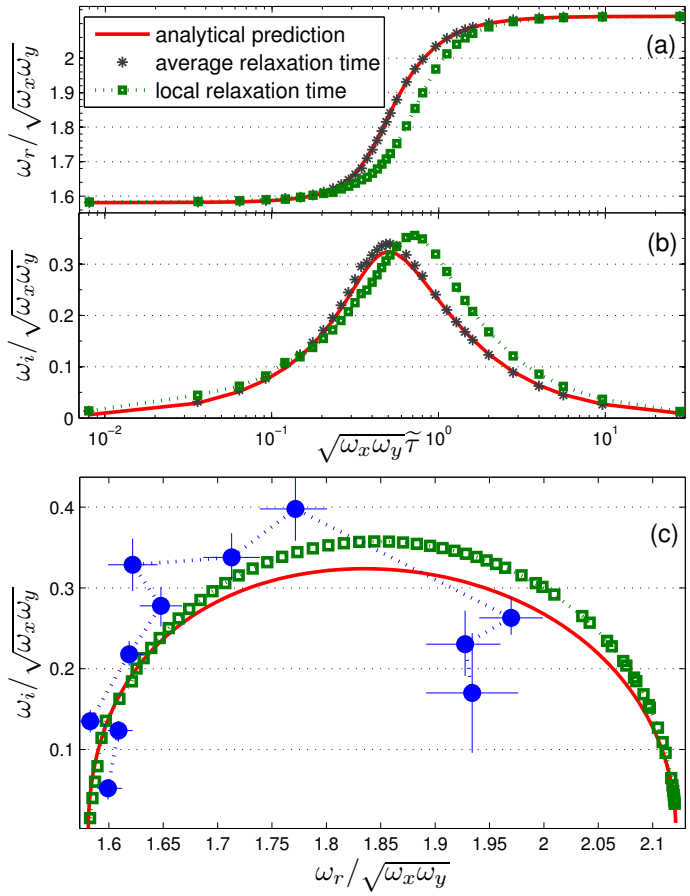

Figure 7.5: The normalized (a) collective frequency and (b) damping of the radial scissors mode vs the average relaxation time. The results are obtained by fitting the cloud angle to a sum of two damped sine functions each with their own free parameters. Only the higher frequency and the corresponding damping rate is plotted. (c) Damping ω_i versus collective frequency ω_r of the radial scissors mode. The experimental data (solid circles) are collected from Ref. [119].

radial quadrupole, the numerical results are closer to the experimental data than the analytical results at low temperatures. At higher temperatures, the anharmonic effect of the external Gaussian potential becomes important, and there are large errors in the frequency and damping, see the last three experimental data in Figure 7.5(c).

7.2.4 Numerical results for the Gaussian potential

Instead of the harmonic potential, the gases are trapped in the Gaussian potential at higher temperatures. The moment method fails to provide analytical solution for the Gaussian potential, so we have to rely on numerical simulations. To calculate the collective frequency and damping of the radial quadrupole mode, the following experimental data are used [120]: $U_0 = 50k_B(\mu K)$, $W_a, W_b = 32.8\mu m$, with the corre-

sponding trap frequency $\omega_x, \omega_y = 1800 \times 2\pi(\text{Hz})$. The trap frequency in the z direction is $\omega_z = 32 \times 2\pi\text{Hz}$, and the total number of atoms is $N_a = 6 \times 10^5$. In the numerical simulations, the time, spatial coordinates, velocity, and temperature are respectively normalised by $a\sqrt{m/k_B T_F}$, a, $\sqrt{k_B T_F/m}$, and the Fermi temperature $T_F = 2.73\mu K$. The distribution function is also normalised by the particle density at the trap centre. Therefore, the normalized accelerations in the x and y directions are respectively $-36.6x\exp(-x^2 - y^2)$ and $-36.6y\exp(-x^2 - y^2)$, and at the unitarity limit, the normalised local relaxation time is $\tau(x, y) = 0.09(T/T_F)^2/n(x, y)$.

Figure 7.6(a) shows the frequency of the sloshing mode decreases as the temperature increases, which coincides with the experimental observations. This can be explained by the fact that the anharmonicity becomes stronger and stronger as the cloud size increases due to the temperature rise. Also, we find that the frequency decreases as the cloud's initial centre x_0 increases. Note that the sloshing mode is excited by shifting the Gaussian potential by x_0 in the x direction.

Figure 7.6(b) demonstrates the relation between the mode frequency and damping, where the local relaxation time is $\tau(x, y) = \alpha\widetilde{T}^2/n(x, y)$, the initial distribution function is $f = \exp\{-18.3[1 - e^{-x^2/1.05^2 - 1.05^2 y^2}]/\widetilde{T}\}\exp[-(v_x^2 + v_y^2)/2\widetilde{T}]/2\pi\widetilde{T}$, and $\widetilde{T} = T/T_F$. In the numerical simulation we use two values of α, because if the repulsive mean-field potential is presented in the experiment, the atom density at the trap center will decrease and hence the coefficient will be lager than 0.09. When $\alpha = 0.09$, as the temperature increases (corresponding to the data from left to right), the mode frequency first increases, remains almost unchanged at $\omega_r/\omega_x \approx 1.8$, and then slightly decreases. The constant frequency is due to the balance between the anharmonic and collisionless effects: the anharmonic effect reduces the effective trap frequency (and hence the mode frequency) while the collisionless effect tends to increase the mode frequency. When $\alpha = 0.18$, the trend of the relation between the mode frequency and damping agrees with the experimental finding reasonably well. That is, from the hydrodynamic regime to the collisionless regime, the mode frequency first increases and then decreases. These results indicate that our numerical scheme can provide reasonable predictions for the collective oscillations in the Gaussian potentials. Also, it indicates that the difference between the numerical and experiment results may be

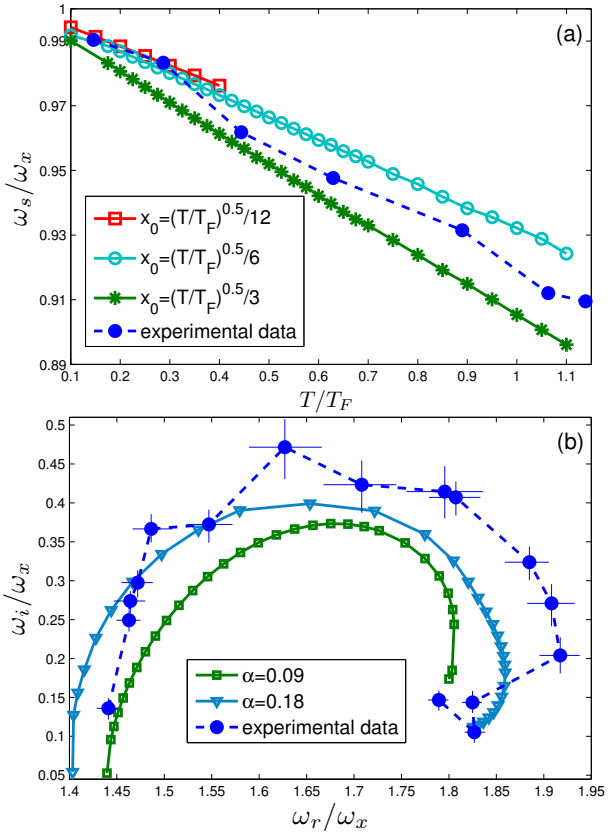

Figure 7.6: (a) The sloshing mode frequency versus the temperature in the Gaussian potential. (b) Damping rate ω_i versus collective frequency ω_r of the radial quadrupole mode. The spatial region $[-\sqrt{\widetilde{T}}, \sqrt{\widetilde{T}}] \times [-\sqrt{\widetilde{T}}, \sqrt{\widetilde{T}}]$ and the velocity region $[-8\sqrt{\widetilde{T}}, 8\sqrt{\widetilde{T}}] \times [-8\sqrt{\widetilde{T}}, 8\sqrt{\widetilde{T}}]$are uniformly discretized into 64×64 and 32×32 meshes, respectively. The time step is $\Delta t = 0.0013$.

a consequence of the approximation of the relaxation rate or the neglected mean-field potential term in Eq. (7.3), rather than the anharmonic effect [120].

7.3 Quantum BGK model

Recently, the damping of the collective modes in the 2D Fermi gas has been investigated experimentally [134]: the constant oscillation frequency (two times of the trap frequency) and small damping rate (the same order as that of the dipole mode, which is mainly caused by the anharmonicity of the external trap) of the breathing mode suggested the classical dynamic scaling symmetry of the 2D Fermi gas. In addition, the damping of the 2D quadrupole oscillations was also measured and the shear viscosity was extracted as a function of the temperature and the coupling strength. Theoretically, the shear viscosity has been calculated using the kinetic theory [135, 136] and

the damping rates of the quadrupole mode were obtained [135], which agreed with the experimental data qualitatively. Generally speaking, kinetic theory is applicable at high temperature and weak coupling limits. However, for 3D Fermi gas at the unitary limit, it was shown qualitatively that the applicability can be down to $T \sim 0.4T_F$ [123], where T_F is the Fermi temperature. Numerically, the damping of the radial quadrupole and scissors modes extracted from the numerical solution of the BE [125, 137] agrees with the experiment data [120] qualitatively. Also, regarding the spin transport in the strong collision of two spin-polarized fermionic clouds [108, 109], the numerical simulation shows that the BE can reproduce the passing through, approaching, and bouncing off dynamics [138], although no comparison to the experimental data was made.

Here we numerically solve the quantum BGK model and check its applicability range by comparing the damping of the quadrupole oscillations with the experimental data [134]. Unlike the probabilistic method [138], we solve the Boltzmann model equation deterministically and observe the quantitative agreement between the numerical and experimental data in certain parameter regions. These parameter regions demonstrate the applicability range of the BE.

Again, we consider the two-component Fermi gas in the normal fluid phase, where the up-spin and down-spin components have the same atom mass m and atom numbers $N_a/2$. As experiment, the gas is tightly confined in the z direction, so that the system is effectively 2D. The quantum BE is given by Eq. (6.3) with the differential cross-section given by Eq. (6.2). The form of quantum BGK model is like Eq. (7.3), but the local equilibrium VDF f_{le} is replaced by the quantum one, given by Eq. (6.6). For isothermal problems, the local relaxation time τ is determined by equating the shear viscosity obtained from the quantum BGK model with that derived from the quantum BE, i.e., $\tau = \mu G_1(Z)/nk_BTG_2(Z)$. The expression for the shear viscosity of the quantum BE has been calculated in [135, 136]. It can be rewritten as

$$\mu = -\frac{\pi m k_B T}{8\hbar I_B(Z)} G_2^2(Z), \tag{7.10}$$

where $I_B = \int d\xi(\xi_x\xi_y)L[\xi_x\xi_y]$ and the linearized collision integral is

$$L[\psi] = \int d\xi_2 \int_0^{2\pi} d\Omega \frac{F}{K}\Delta\psi, \tag{7.11}$$

with $\Delta\psi = \psi_4+\psi_3-\psi_2-\psi$, $F = f^0 f_2^0(1-f_3^0)(1-f_4^0)$, $K = \log^2(|\xi-\xi_2|^2 T/2T_B)+\pi^2$. Note that here $f^0(\xi) = (Z^{-1}e^{\xi^2}+1)^{-1}$ with the dimensionless quantity $\xi = m(\mathbf{v}-\mathbf{V})/\sqrt{2mk_BT}$. In the near-classical limit ($z \to 0$), the shear viscosity is [136]

$$\mu_{cl} = \frac{mk_BT}{2\pi^2\hbar}\left[\log^2\left(\frac{5T}{2T_B}\right)+\pi^2\right]. \tag{7.12}$$

We study the quadrupole oscillations of the 2D Fermi gas in the isotropic harmonic potential with the trapping frequency $\omega_\perp = 2\pi \times 125$Hz [134]. We normalise the time by $1/\omega_\perp$, the velocity by v_F, spatial length by $v_F/\omega_\perp$, the chemical potential by the Fermi energy $E_F = \hbar^2k_F^2/2m$, the temperature by the Fermi temperature $T_F = E_F/k_B$, the acceleration by $v_F\omega_\perp$, and the particle density by n_0/π, where $v_F = \hbar k_F/m$ with $k_F = \sqrt{2\pi n_0}$ being the Fermi wave vector. Note that n_0 is the particle density at the trap centre when the system is in equilibrium. Then, the quantum BGK model becomes

$$\frac{\partial f}{\partial t}+v_x\frac{\partial f}{\partial x}+v_y\frac{\partial f}{\partial y}-x\frac{\partial f}{\partial v_x}-y\frac{\partial f}{\partial v_y} = -\frac{f-f_{le}}{\tau(x,y)}, \tag{7.13}$$

where $f_{le} = \{Z^{-1}\exp[-(\mathbf{v}-\mathbf{V})^2/T]+1\}^{-1}$ is the normalised local equilibrium VDF, and

$$\tau(x,y) = -\frac{\pi^3 G_1(Z)G_2(Z)}{8I_B}\frac{\hbar\omega_\perp}{E_F}\frac{1}{n(x,y)}, \tag{7.14}$$

is the normalised relaxation time. The normalised particle density is $n(x,y) = \int d\mathbf{v} f$ and the normalised bulk velocity is $\mathbf{v}(x,y) = \int d\mathbf{v}\mathbf{v}f/n(x,y)$.

Unlike the 3D Fermi gas in the unitary limit, the collision frequency $1/\tau$ here is not a linear function of the particle density n [123]. Since the fugacity is a function of the particle density (see Eq. (6.7), the larger the particle density the larger the fugacity), the collision frequency, increases more slowly than n [Figure 7.7].

We use the asymptomatic preserving scheme to solve Eq. (7.13). The initial chemical potential μ' satisfies $N = 2E_F^2T^2G_2(e^{\mu'/T})/\hbar^2\omega_\perp^2$, and the initial fugacity corresponding to the excitation of quadrupole mode is $Z = \exp[(\mu'-1.1x^2-0.91y^2)/T]$.

We first investigate the damping of the quadrupole modes as a function of the interaction strength for a fixed temperature $T = 0.47T_F$ and the Fermi energy $E_F = 2\pi\hbar \times 8.2$kHz, corresponding to the experimental condition described in Figure 1 in Ref. [134]. The particle number is estimated to be $3500 \sim 4300$ [135]. Note that the

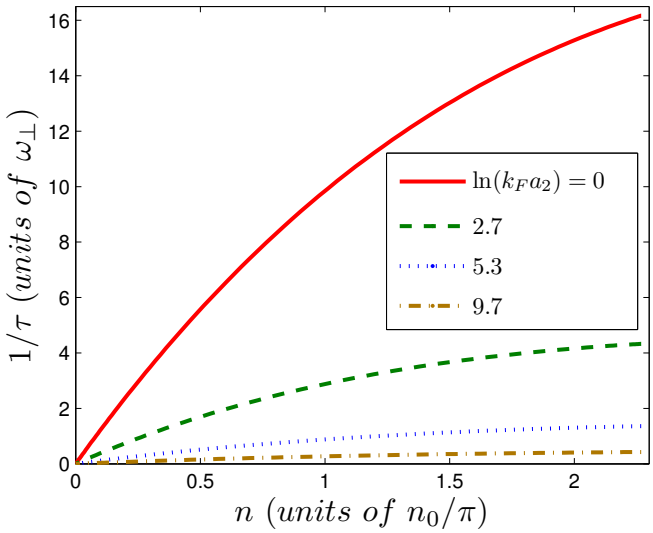

Figure 7.7: The collision frequency vs the particle density for different values of interaction strength $\ln(k_F a_2)$ at $T = 0.47T_F$, $E_F = 2\pi\hbar \times 8.2$kHz, and $N_a = 4300$. The system is in the hydrodynamic regime ($\omega_\perp \tau_{min} \ll 1$) at $\ln(k_F a_2) = 0$, in the transition regime ($\omega_\perp \tau_{min} \sim 1$) at $\ln(k_F a_2) = 2.7, 5.3$, and in the collisionless regime ($\omega_\perp \tau_{min} \gg 1$) at $\ln(k_F a_2) = 9.7$. Here a_2 is the s-wave scattering length in 2D velocity space.

experiments are conducted in the presence of slightly anharmonic potential, where even the dipole modes decay at rate of $\Gamma_D = (0.04 \pm 0.01)\omega_\perp$ and the breathing modes decay near the average value $\Gamma_B \simeq 0.05\omega_\perp$. In order to eliminate the effects of anharmonicity, the numerical and analytical damping rates will be added by $0.05\omega_\perp$. Also note that the analytical results, i.e., Eq. (12) in Ref. [135], are based on the hydrodynamics, so it should be accurate in the hydrodynamic regime. From Figure 7.7 we can see that the hydrodynamic regime is realised in the strong coupling regime when $\ln(k_F a_2) \sim 0$. Indeed, from Figure 7.8 we see that, the analytical (the dashed line) and numerical (the lines with crosses) damping rates agree with each other at $\ln(k_F a_2) \leq 1.5$. This demonstrates the accuracy of our numerical scheme. As the value of $\ln(k_F a_2)$ increases, the system first enters into the transition regime and then the collisionless regime, where the hydrodynamic method breaks down. When $\ln(k_F a_2) \geq 1.5$, one can see the large deviation of the analytical results from the experimental data. However, our numerical results are in quantitative agreement with the experimental data. This indicates that the semi-classical BE can describe the damping of the quadrupole mode well, up to the strong interaction limit, i.e., $\ln(k_F a_2) \simeq 1.5$.

For the oscillation frequency of the quadrupole mode, however, there are some

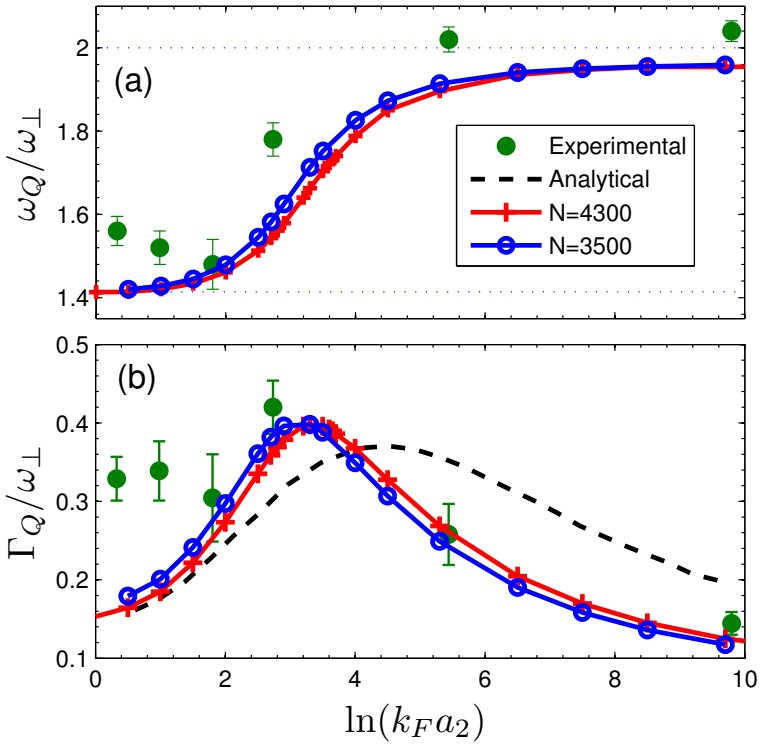

Figure 7.8: (a) Frequency and (b) damping vs the interaction strength in the quadrupole oscillations of 2D Fermi gas at $T/T_F = 0.47$ and $E_F = 2\pi\hbar \times 8.2$kHz. The experimental data are from Figure 1(a) and (b) of Ref. [134], the analytical results are obtained from Figure 3 in Ref. [135] using $N_a = 4300$, while the solid lines are the numerical results of Eq. (7.13) for different particle number N_a. Note that N in the legend is the atom number N_a.

discrepancies between the numerical and experimental data, see Figure 7.8(a). This may be caused by the anharmonicity of the effective potential, which includes the external potential and additional potential caused by the mean-field or beyond mean-filed effects. Due to the anharmonicity of the external trap, the normalised quadrupole frequency should be increased by multiplying a prefactor which is larger than 1 [126]. Since the detailed trap anharmonicity is not given in the experiment, it is hard to estimate the value of the prefactor. On the other hand, the ellipticity of the trap, i.e., $e = |\omega_x - \omega_y|/\omega_\perp$, increases the normalised frequency by a factor of the order e^2. However, this incensement is negligible because of the small value of e ($e \leq 0.04$). As for the mean-field effect, when the gas is confined in harmonic trap, it has been shown that at the zero temperature the normalised frequency at the collisionless regime is $2\sqrt{(1-\widetilde{g}/2)/(1-\widetilde{g})}$, where $\widetilde{g} = 1/\ln(k_F a_2)$ [134, 139]. That is, the normalised frequency is 2.12 at $\ln(k_F a_2) = 5$ and 2.05 at $\ln(k_F a_2) = 10$. Thus in the numerical

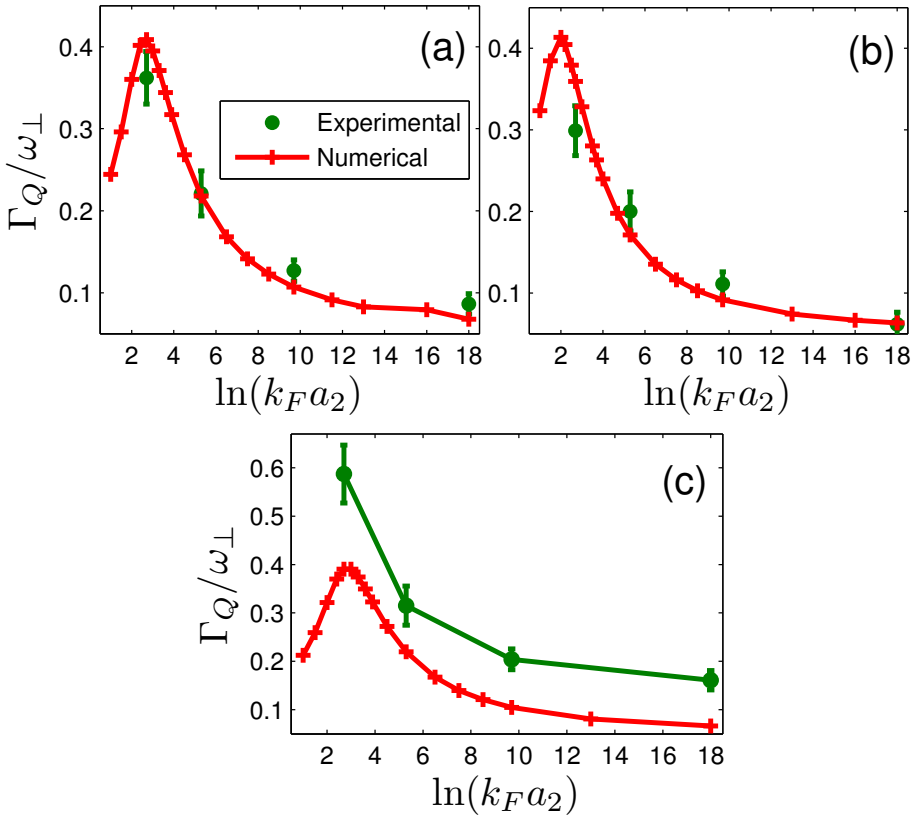

Figure 7.9: The damping vs the interaction strength in the quadrupole oscillations of 2D Fermi gas at (a) $T = 0.65T_F$, $E_F = 2\pi\hbar \times 9.0$kHz, (b) $T = 0.89T_F$, $E_F = 2\pi\hbar \times 9.1$kHz, and (c) $T = 0.30T_F$, $E_F = 2\pi\hbar \times 6.4$kHz. The particle number is $N_a = 3500$. The experimental data are from Figure 1(a) and (b) of Ref. [134].

simulations, it is equivalent to set the effective harmonic trap frequency to be $\sim 1.05\omega_\perp$. If we magnify the numerically extracted normalised frequency in Figure 7.3(a) by a factor of 1.05, the results agree with the experimental date very well (not shown). With this kind of magnification, the numerically extracted damping in Figure 7.8(b) agrees with the experimental data slightly better.

The good prediction of the BE on the damping of quadrupole oscillation continues to hold at higher temperatures, see Figure 7.9 (a) and (b). However, at a lower temperature ($T = 0.3T_F$), the BE ceases to give the correct prediction for the damping of quadrupole mode in the entire region of interaction strength, see Figure 7.9(c).

7.4 Summary

To improve the accuracy and overcome the limitation of the method of moments, we have demonstrated a computationally efficient numerical scheme to solve the Boltzmann model equation. The advantage of the asymptotic preserving scheme is that it can deal with the harmonic and Gaussian potentials, as well as other forms of the potential, including the mean-field and other self-energy terms, which will help us to understand the properties of strongly interacting particles. In particular, the asymptotic preserving nature of the numerical scheme makes the computation of a hydrodynamic flow as fast and accurate as that of the transition and collisionless flows, which cannot be implemented by the probabilistic methods.

The extracted mode frequency and damping of the radial quadrupole and scissors modes provide better agreement with the experimental data than the analytical solutions obtained from the method of moments. We have solved the quantum BGK model numerically. Eliminating the effect of the anharmonicity of the external potential, we have observed quantitative agreements between the numerically extracted damping of the 2D quadrupole oscillation and the experimental data. This indicates that the quantum BGK model can describe the collective oscillations of 2D Fermi gas at least in the parameter regions $T/T_F \geq 0.47$ and $\ln(k_F a_2) \geq 1.5$.

In addition to the study of collective oscillations, the present method can be useful for investigation of many other problems. For example, one can use it to study the expansion of the atom cloud after the trap being switched off; to examine the collision of two initially separated atom clouds to see the formation of quantum shock waves [140]; to determine the effective transport coefficients such as the heat conductivity in very elongated traps [141]. Also, the deterministic nature of the numerical scheme makes it suitable to solve the two-fluid equations (one for the normal phase and the other for the superfluid phase [116]), where the numerical simulations will help us to understand the coupled dynamics of the superfluid and normal phases, i.e., the damping of superfluid flow by a thermal cloud [142]. Furthermore, it can help us to analyse the value spin drag coefficients in recent experiments [108, 109].

Chapter 8

Conclusions

8.1 Summary

We have presented an accurate and efficient deterministic numerical method to solve the BE for monoatomic gases. Specifically, we focused on the numerical approximation of the Boltzmann collision operator by the FSM. Instead of the velocity space, the FSM handles the complicated collision in a corresponding frequency space. If the direct sum is applied to calculate the spectrum of the Boltzmann collision operator, the computational cost is at the order of $O(N_\xi^6)$, where N_ξ is the number of frequency components which is not necessary equal to the number of velocity grids N. The main idea of the FSM is to approximate the kernel mode Eq. (2.28) by the numerical quadrature to separate the frequency components $\xi_{\mathbf{l}}$ and $\xi_{\mathbf{m}}$, so that the spectrum of the Boltzmann collision operator Eq. (2.25) can be calculated by the FFT-based convolution, resulting in the computational cost at the order of $O(M^2 N_\xi^3 \log N_\xi)$. The separation of the frequency components in the kernel mode needs special forms of the collision kernel. One of the main contribution of this thesis is that we constructed special forms of the collision kernel, making the FSM applicable to all inverse-power law potentials (except for the Coulomb potential) and the realistic LJ potential. The original FSM conserves the mass, while the error in the conservation of momentum and energy is spectrally small. By use of the Lagrangian multiplier method, momentum and energy conservation can be easily satisfied while the spectral accuracy is retained. Thus, in terms of accuracy and efficiency, the FSM is the best method for deterministic

approximation of Boltzmann collision operator. The accuracy of the FSM has been evaluated by comparing the numerical solutions with the analytical BKW solutions. The factors affecting the accuracy of FSM have been analysed in depth. With the accurate numerical results provided by FSM, we have also justified the use of special collision kernels.

The FSM has been successfully applied to the linearised BE, where the symmetry can reduce the computational cost by half. Also, the FSM has been extended to the BE for monoatomic gas mixtures, both in the classical and quantum mechanics regimes.

The velocity distribution functions have discontinuities when the Knudsen number is large. To capture these discontinuities one needs relatively large number of velocity grids. Since the FSM works in the frequency space, however, the number of frequency components do not have to be very large. The reason is that, in the calculation of Eq. (2.25), the spectrum of the VDF is multiplied by a weight function (kernel mode) which is very small when the frequency is large. Therefore, very high frequency components can be safely ignored. In real calculations, $32 \sim 64$ frequency components in each direction are enough, for examples see Chapter 3. This is one of the main advantage of the spectral method over other deterministic methods like DVM.

The number of the discrete angles M in the approximation of kernel model by the quadrature also affects accuracy. In the most cases, the kernel mode can be approximated by the trapezoidal rule with $M = 5$. In some extreme (highly rarefied) cases where $N_\xi \sim 64$, the kernel mode can be approximated by the Gauss-Legendre quadrature with $M \sim 8$, in order to obtain highly accurate results.

An implicit iteration scheme has been adopted to find the stationary solutions in the space-inhomogeneous problems, where the convergence to the steady state has been found to be exponential, with the typical number of iterations being inversely proportional to the Knudsen number. In the transition and free molecular regimes, the iteration scheme is very efficient. The accuracy of the numerical method (FSM+iteration scheme) has been benchmarked through the comparison with the numerical kernel method from the Kyoto Kinetic Group, the experimental data, DSMC, and the MD. Very good agreements are observed in all tested cases. The computational time of our method has also been compared to the low-noise DSMC. Comparisons demonstrate the

merit of our method as a computationally accurate and efficient (for lid-driven flow, our method is at least 10 times faster than the low-noise DSMC) method for rarefied gas dynamics. The only drawback of the FSM, like all other deterministic numerical methods, is that a large amount of compute memory is required (relative to that of the DSMC method).

The complicated nature of the Boltzmann collision operator has stimulated the search of kinetic models. We have proposed a kinetic model which can be viewed as a linear combination of the ES and S models. By adjusting the free parameter in the combined ES and S model, we can minimise the difference between its collision operator to that of the BE. With the accurate numerical solution provided by the fast spectral method, we have checked accuracy of kinetic model equations and found out the flow regimes where the complicated Boltzmann collision kernel can be replaced by the simple kinetic models. We have also solved the collective oscillation of quantum gas confined in external trap and compare the numerical solutions with the experimental data, indicating applicability of the quantum kinetic model.

8.2 Future works

The work developed in this thesis leads to new opportunities:

1. The accurate and efficient method proposed in this thesis can be used to produce some benchmarking data, e.g. to calculate the mass and heat flow rates in the Poiseuille flow through the rectangular tube with arbitrary aspect ratio.

2. The comparison between numerical solutions of the Boltzmann and kinetic model equations may help us to establish a criterion to judge flow conditions that the BE can be replaced by the kinetic model equations. This criterion may help to develop a hybrid scheme (near the boundary the BE solver is used, while in the bulk the kinetic model equations are adopted) to solve big problems.

3. The fast spectral method for the approximation of BE can be straightforwardly applied to solve the granular BE where the inelastic binary collisions are taken into account. For this purpose, the collision operator in granular BE should be written in the weak form.

References

[1] C. Mouhot and L. Pareschi. Fast algorithms for computing the Boltzmann collision operator. *Math. Comput*, 75(256):1833–1852, 2006.

[2] M. Gad-el-Hak. The fluid mechanics of microdevices - the Freeman Scholar lecture. *J. Fluids Eng.*, 121(1):5–33, 1999.

[3] Y. Sone. *Kinetic theory and fluid dynamics*. Birkhauser Boston, 2002.

[4] C. Cercignani. *Mathematical Methods in Kinetic Theory*. Plenum Publishing Inc., 223 Spring Street, New York, N.Y. 10013, 1990.

[5] S. Chapman and T.G. Cowling. *The Mathematical Theory of Non-uniform Gases*. Cambridge University Press, 1970.

[6] H. Struchtrup. *Macroscopic Transport Equations for Rarefied Gas Fows: Approximation Methods in Kinetic Theory*. Heidelberg, Germany: Springer, 2005.

[7] K. Xu and Z. H. Li. Microchannel flow in the slip regime: gas-kinetic BGK-Burnett solutions. *J. Fluid Mech.*, 513:87–110, 2004.

[8] Y. Zheng, A. L. Garcia, and B. J. Alder. Comparison of kinetic theory and hydrodynamics for Poiseuille flow. *J. Stat. Phys.*, 109:495–505, 2002.

[9] L. S. Garcia-Colin, R. M. Velasco, and F. J. Uribe. Beyond the Navier-Stokes equations: Burnett hydrodynamics. *Phys. Rep.*, 465:149–189, 2008.

[10] H. Grad. On the kinetic theory of rarefied gases. *Comm. Pure Appl. Math.*, 2:331–407, 1949.

[11] W. Weiss. Continuous shock structure in extended thermodynamics. *Phys. Rev. E*, 52: 5760, 1995.

[12] A. Rana, M. Torrilhon, and H. Struchtrup. A robust numerical method for the R13 equations of rarefied gas dynamics: Application to lid driven cavity. *J. Comput. Phys.*, 236:169–186, 2013.

[13] X. J. Gu and D. R. Emerson. A high-order moment approach for capturing non-equilibrium phenomena in the transition regime. *J. Fluid Mech.*, 636:177–216, 2009.

[14] G. A. Bird. *Molecular Gas Dynamics and the Direct Simulation of Gas Flows*. Oxford Science Publications, Oxford University Press Inc, New York, 1994.

[15] K. Nanbu. Direct simulation scheme derived from the Boltzmann equation. i. Monocomponent gases. *J. Phys. Soc. Japan*, 52:2042–2049, 1983.

[16] W. Wagner. A convergence proof for Bird's direct simulation Monte Carlo method for the Boltzmann equation. *J. Stat. Phys.*, 66:1011–1044, 1992.

[17] J. Fan and C. Shen. Statistical simulation of low-speed rarefied gas flows. *J. Comput. Phys.*, 167:393–412, 2001.

[18] N. D. Masters and W. J. Ye. Octant flux splitting information preservation DSMC method for thermally driven flows. *J. Comput. Phys.*, 226(2):2044–2062, 2007.

[19] F. Fei and J. Fan. A diffusive information preservation method for small Knudsen number flows. *J. Comput. Phys.*, 243:179–193, 2013.

[20] Q. H. Sun, I. D. Boyd, and G. V. Boyd. A hybrid continuum/particle approach for micro-scale gas flows. *Rar. Gas. Dynam*, page 663, 2003.

[21] T. E. Schwartzentruber, L. C. Scalabrin, and I. D. Boyd. A modular particle-continuum numerical method for hypersonic non-equilibrium gas flows. *J. Comput. Phys.*, 225:1159–1174, 2007.

[22] J. M. Burt and Iain D. Boyd. A hybrid particle approach for continuum and rarefied flow simulation. *J. Comput. Phys.*, 228(2):460–475, 2009.

[23] L. L. Baker and N. G. Hadjiconstantinou. Variance reduction for Monte Carlo solutions of the Boltzmann equation. *Phys. Fluids*, 17(5):051703, 2005.

[24] T. M. M. Homolle and N. G. Hadjiconstantinou. A low-variance deviational simulation Monte Carlo for the Boltzmann equation. *J. Comput. Phys.*, 226(2):2341–2358, 2007.

[25] G. A. Radtke, N. G. Hadjiconstantinou, and W. Wagner. Low-noise Monte Carlo simulation of the variable hard sphere gas. *Phys. Fluids*, 23(3):030606, 2011.

[26] D. Goldstein, B. Sturtevant, and J. E. Boardwell. Investigation of the motion of discrete-velocity gases. *Rar. Gas. Dynam. Progress in Aeronautics and Astronautics*, 118, 1989.

[27] A. V. Bobylev, A. Palczewski, and J. Schneider. On approximation of the Boltzmann equation by discrete velocity models. *C. R. Acad. Sci. Pairs*, 320:639–644, 1995.

[28] V. V. Aristov and F. G. Tcheremissine. Direct numerical solutions for the kinetic Boltzmann equation. *Comput. Ceneter Russ. Acad. Sci. Moscow*, 1992.

[29] W. Wagner. Approximation of the Boltzmann by discrete velocity models. *J. Stat. Phys.*, 78:1555–1570, 1995.

[30] C. Buet. A discrete-velocity scheme for the Boltzmann operator of rarefied gas dynamics. *Trans. Theory Stat. Phys.*, 25:33–60, 1996.

[31] A. B. Morris, P. L. Varghese, and D. B. Goldstein. Monte Carlo solution of the Boltzmann equation via a discrete velocity model. *J. Comput. Phys.*, 230(4):1265–1280, 2011.

[32] F. G. Tcheremissine. Direct numerical solution of the Boltzmann equation. *Rar. Gas. Dynam*, pages 677–685, 2005.

[33] Tcheremissine F. G. Solution to the Boltzmann kinetic equation for high-speed flows. *Comput. Math. Math. Phys.*, 46:315, 2006.

[34] Y. Y. Kloss, P. V. Shuvalov, and F. G. Tcheremissine. Solving Boltzmann equation on GPU. *Procedia Computer Science*, 1(1):1083–1091, 2010.

[35] C. Mouhot, L. Pareschi, and T. Rey. Convolutive decomposition and fast summation methods for discrete-velocity approximations of the Boltzmann equation. *ESAIM: Mathematical Modelling and Numerical Analysis*, 10.1051/m2an/2013078, 2013.

[36] Y. Sone, T. Ohwada, and K. Aoki. Temperature jump and knudsen layer in a rarefied-gas over a plane wall: Numerical-analysis of the linearized boltzmann-equation for hard-sphere molecules. *Phys. Fluids A-Fluid Dynamics*, 1(2):363–370, 1989.

[37] T. Ohwada. Structure of normal shock-waves: Direct numerical analysis of the Boltzmann equation for hard-sphere molecules. *Phys. Fluids A-Fluid Dynamics*, 5(1):217–234, 1993.

[38] T. Ohwada. Heat flow and temperature and density distributions in a rarefied gas between parallel plates with different temperatures. Finite-difference analysis of the nonlinear Boltzmann equation for hard-sphere molecules. *Phys. Fluids*, 8(8):2153–2160, 1996.

[39] S. Kosuge, K. Aoki, and S. Takata. Shock-wave structure for a binary gas mixture: finite-difference analysis of the Boltzmann equation for hard-sphere molecules. *Eur. J. Mech. B/Fluids*, 20(1):87–126, 2001.

[40] T. Doi. Numerical analysis of the Poiseuille flow and thermal transpiration of a rarefied gas through a pipe with a rectangular cross section based on the linearized Boltzmann equation for a hard sphere molecular gas. *J. Vac. Sci. Technol. A*, 28:603–612, 2010.

[41] A. V. Bobylev. The theory of the nonlinear spatially uniform Boltzmann equation for Maxwell molecules. *Math. Phys. Rev.*, 7:111–233, 1988.

[42] L. Pareschi and B. Perthame. A Fourier spectral method for homogeneous Boltzmann equation. *Trans.Theory Stat. Phys.*, 25:369–382, 1996.

[43] A. V. Bobylev and S. Rjasanow. Difference scheme for the Boltzmann equation based on the Fast Fourier Transform. *Eur. J. Mech. B/Fluids*, 16(2):293–306, 1997.

[44] C. Watchararuangwit, Y. N. Grigoriev, and S. V. Meleshko. A deterministic spectral method for solving the Boltzmann equation for one-dimensional flows. *ScienceAsia*, 35 (1):70–79, 2009.

[45] A. V. Bobylev and S. Rjasanow. Fast deterministic method of solving the Boltzmann equation for hard spheres. *Eur. J. Mech. B/Fluids*, 18(5):869–887, 1999.

[46] I. Ibragimov and S. Rjasanow. Numerical solution of the Boltzmann equation on the uniform grid. *Conputing*, 69(2):163–186, 2002.

[47] I. M. Gamba and S. H. Tharkabhushanam. Spectral-Lagrangian methods for collisional models of non-equilibrium statistical states. *J. Comput. Phys.*, 228(6):2012–2036, 2009.

[48] I. M. Gamba and S. H. Tharkabhushanam. Shock and boundary structure formation by spectral-Lagrangian methods for the inhomogeneous Boltzmann transport equation. *J. Comput. Math.*, 28:430–460, 2010.

[49] L. Pareschi and G. Russo. Numerical solution of the Boltzmann equation I: Spectrally accurate approximation of the collision operator. *SIAM J. Numerical Analysis*, 37(4): 1217–1245, 2000.

[50] F. Filbet and G. Russo. High order numerical methods for the space non-homogeneous Boltzmann equation. *J. Comput. Phys.*, 186(2):457–480, 2003.

[51] F. Filbet, C. Mouhot, and L. Pareschi. Solving the Boltzmann equation in NlogN. *SIAM J. Scientific Computing*, 28(3):1029–1053, 2006.

[52] F. Filbet. On deterministic approximation of the Boltzmann equation in a bounded domain. *Multiscale. Model. Simul*, 10(3):792–817, 2012.

[53] F. Filbet, Jingwei Hu, and Shi Jin. A numerical scheme for the quantum Boltzmann equation with stiff collision terms. *Math. Model. Num. Anal*, 46(2):443–463, 2012.

[54] Jingwei Hu and Lexing Ying. A fast spectral algorithm for the quantum Boltzmann collision operator. *Commun. Math. Sci*, 10(3):989–999, 2012.

[55] P. T. Gressman and R. M. Strain. Global classical solutions of the Boltzmann equation with long-range interactions. *PNAS*, 107(13):5744–5749, 2010.

[56] F. Sharipov and G. Bertoldo. Numerical solution of the linearized Boltzmann equation for an arbitrary intermolecular potential. *J. Comput. Phys.*, 228(9):3345–3357, 2009.

[57] H. A. Hassan and D. B. Hash. A generalized hard-sphere model for Monte-Carlo simulation. *Phys. Fluids A: Fluid Dynamics*, 5(3):738–744, 1993.

[58] H. Matsumoto. Variable sphere molecular model for inverse power law and Lennard-Jones potentials in Monte Carlo simulations. *Phys. Fluids*, 14(12):4256–4265, 2002.

[59] J. Fan. A generalized soft-sphere model for Monte Carlo simulation. *Phys. Fluids*, 14 (12):4399–4405, 2002.

[60] Y. Shi, P. L. Brookes, Y. W. Yap, and J. E. Sader. Accuracy of the lattice Boltzmann method for low-speed noncontinuum flows. *Phys. Rev. E*, 83:045701, 2011.

[61] C. Canuto, M. Y. Hussaini, and A. Quarteroni. *Spectral Method in Fluid Dynamics*. Springer-verlag, 1998.

[62] M. Krook and T. T. Wu. Exact solutions of the Boltzmann equation. *Phys. Fluids*, 20: 1589, 1977.

[63] L. Pareshci and G. Russo. Efficient asymptotic preserving deterministic methods for the Boltzmann equation. *AVT-194 RTO AVT/VKI, Models and Computational Methods for Rarefied Flows*, 2011.

[64] P. Kowalczyk, A. Palczewski, G. Russo, and Z. Walenta. Numerical solutions of the Boltzmann equation: comparison of different algorithms. *Eur. J. Mech.B/Fluids*, 27(1): 62–74, 2008.

[65] P. Valentini and T. E. Schwartzentruber. Large-scale molecular dynamics simulations of normal shock waves in dilute argon. *Phys. Fluids*, 21(6), 2009.

[66] M. N. Macrossan and C. R. Lilley. Modified generalized hard sphere collision model for direct simulation Monte-Carlo calculations. *J. Thermophys. Heat Transfer*, 17:289–291, 2003.

[67] L. Pareschi, G. Russo, and G. Toscani. Fast spectral methods for the Fokker-Planck-Landau collision operator. *J. Comput. Phys.*, 165(1):216–236, 2000.

[68] A. Heintz, P. Kowalczyk, and R. Grzhibovskis. Fast numerical method for the Boltzmann equation on non-uniform grids. *J. Comput. Phys.*, 227:6681–6695, 2008.

[69] S. Takata and H. Funagane. Poiseuille and thermal transpiration flows of a highly rarefied gas: over-concentration in the velocity distribution function. *J. Fluid Mech.*, 669:242–259, 2011.

[70] T. Ohwada, Y. Sone, and K Aoki. Numerical analysis of the Poiseuille and thermal transpiration flows between two parallel plates on the basis of the Boltzmann equation for hard sphere molecules. *Phys. Fluids*, 1:2042, 1989.

[71] H. Funagane and S. Takata. Hagen-Poiseuille and thermal transpiration flows of a highly rarefied gas through a circular pipe. *Fluid Dyn. Res.*, 44:055506, 2012.

[72] T. Doi. Plane thermal transpiration of a rarefied gas in the presence of gravitation. *Vacuum*, 86:1541–1546, 2012.

[73] T. Doi. Effect of weak gravitation on the plane Poiseuille flow of a highly rarefied gas. *Zeitschrift für angewandte Mathematik und Physik*, 63:1091–1102, 2012.

[74] F. Sharipov and G. Bertoldo. Poiseuille flow and thermal creep based on the Boltzmann equation with the Lennard-Jones potential over a wide range of the Knudsen number. *Phys. Fluids*, 21:067101, 2009.

[75] S. K. Loyalka, T. S. Storvick, and H. S. Park. Poiseuille flow and thermal creep flow in long, rectangular channels in the molecular and transition flow regimes. *J. Vac. Sci. Technol.*, 13:1188, 1976.

[76] T. Ewart, P. Perrier, I. A. Graur, and J. G. Méolans. Mass flow rate measurements in a microchannel, from hydrodynamic to near free molecular regimes. *J. Fluid Mech.*, 584: 337–356, 2007.

[77] N. Dongari, Y. H. Zhang, and J. M. Reese. Modeling of Knudsen layer effects in micro/nanoscale gas flows. *Journal of Fluid Engineering–Transactions of the ASME*, 133: 071101, 2011.

[78] N. Dongari and A. Agrawal. Modeling of Navier-Stokes equations for high Knudsen number gas flows. *International Journal of Heat and Mass Transfer*, 55:4352–4358, 2012.

[79] S. Kokou Dadzie and H. Brenner. Predicting enhanced mass flow rates in gas microchannels using nonkinetic models. *Phys. Rev. E*, 86:036318, 2012.

[80] C. Cercignani. The method of elementary solutions for kinetic models with velocity-dependent collision frequency. *Ann. Phys.*, 40:469, 1966.

[81] S. K. Loyalka and J. H. Ferziger. Model dependence of the slip coefficient. *Phys. Fluids*, 10:1833–1839, 1967.

[82] S. K. Loyalka and J. H. Ferziger. Model dependence of the temperature slip coefficient. *Phys. Fluids*, 11:1168–1671, 1968.

[83] H. Struchtrup. The BGK-model with velocity-dependent collision frequency. *Cont. Mech. Theromodyn.*, 9:23–32, 1997.

[84] Y. S. Zheng and H. Struchtrup. Ellipsoidal statistical Bhatnagar-Gross-Krook model with velocity-dependent collision frequency. *Phys. Fluids*, 17(12):127103, 2005.

[85] P. L. Bhatnagar, E. P. Gross, and M. Krook. A model for collision processes in gases. I. Small amplitude processes in charged and neutral one-component systems. *Phys. Rev.*, 94:511–525, 1954.

[86] P. Welander. On the temperature jump in a rarefied gas. *Ark. Fys.*, 7:507–553, 1954.

[87] L. H. Holway. New statistical models for kinetic theory: methods of construction. *Phys. Fluids*, 9:1658–1673, 1966.

[88] P. Andries, P. Le Tallec, J. Perlat, and B. Perthame. The Gaussian-BGK model of Boltzmann equation with small Prandtl number. *Eur. J. Mech. B Fluids*, 19:813830, 2000.

[89] E. M. Shakhov. Approximate kinetic equations in rarefied gas theory. *Fluid Dynamics*, 3(1):112–115, 1968.

[90] E. M. Shakhov. Generalization of the Krook kinetic relaxation equation. *Fluid Dynamics*, 3(5):95–96, 1968.

[91] E. M. Shakhov. *Method of investigation of rarefied gas dynamics*. NauKa, Moscow, 1974.

[92] Guangjun Liu. A method for constructing a model form for the Boltzmann equation. *Phys. Fluids A*, 2:277, 1990.

[93] A. V. Latyshev and A. A. Yushkanov. Thermal and isothermal slip in a new Liu model transport equation. *Tech. Phys. Lett.*, 23(7):540–541, 1997.

[94] V. Garzo and M. Lopez de Haro. Kinetic model for heat and momentum transport. *Phys. Fluids*, 6:3787, 1994.

[95] K. Aoki, S. Takata, and T. Nakanishi. Poiseuille-type flow of a rarefied gas between two parallel plates driven by a uniform external force. *Phys. Rev. E*, 65:026315, 2002.

[96] C. Z. Chen, K. Xu, and Q. D. Cai. A comparison and unification of ellipsoidal statistical and Shakhov BGK models. *arxiv:1304.0865*.

[97] K. Aoki, Y. Sone, K. Nishino, and H. Sugimoto. Numerical analysis of unsteady motion of a rarefied gas caused by sudden change of wall temperature with special interest in the propagation of discontinuity in the velocity distribution function. *Rarefied gas dynamics; Proceedings of the 17th International Symposium*, pages 222–231, 1990.

[98] A. Manela and N. G. Hadjiconstantinou. On the motion induced in a gas confined in a small-scale gap due to instantaneous boundary heating. *J. Fluid Mech.*, 593:453–462, 2007.

[99] A. Manela and N. G. Hadjiconstantinou. Gas motion induced by unsteady boundary heating in a small-scale slab. *Phys. Fluids*, 20:117104, 2008.

[100] B. John, X. J. Gu, and D. R. Emerson. Investigation of heat and mass transfer in a lid-driven cavity under nonequilibrium flow conditions. *Num Heat Transfer B*, 52:287–303, 2011.

[101] B. John, X. J. Gu, and D. R. Emerson. Effects of incomplete surface accommodation on non-equilibrium heat transfer in cavity flow: A parallel DSMC study. *Computers & Fluids*, 45:197–201, 2011.

[102] J. C. Huang, K. Xu, and P. B. Yu. A unified gas-kinetic scheme for continuum and rarefied flows II: Multi-dimensional cases. *Commun. Comput. Phys.*, 12:662–690, 2012.

[103] O. I. Rovenskaya, A. Ph. Polikarpov, and I. A. Graur. Comparison of the numerical solutions of the full Boltzmann and S-model kinetic equations for gas flow through a slit. *Computers & Fluids*, 80(0):71–78, 2013.

[104] A. Venkattraman and A. A. Alexeenko. Binary scattering model for Lennard-Jones potential: Transport coefficients and collision integrals for non-equilibrium gas flow simulations. *Phys. Fluids*, 24:027101, 2012.

[105] M. Krook and T. T. Wu. Exact solution of Boltzmann equation for multicomponent systems. *Phys. Rev. Lett.*, 38:991–993, 1997.

[106] S. Kosuge and and S. Takata K. Aoki. Heat transfer in a gas mixture between two parallel plates: Finite-difference analysis of the Boltzmann equation. *AIP Conf. Proc.*, 585:289–296, 2000.

[107] E. A. Uehling and G. E. Uhlenbeck. Transport phenomena in Einstein-Bose and Fermi-Dirac gases. I. *Phys. Rev*, 43(7):0552–0561, 1933.

[108] A. Sommer, M. Ku, G. Roati, and M. W. Zwierlein. Universal spin transport in a strongly interacting Fermi gas. *Nature*, 472:201–204, 2011.

[109] A. Sommer, M. Ku, and M. W Zwierlein. Spin transport in polaronic and superfluid Fermi gases. *New J. Phys.*, 13:055009, 2011.

[110] M. Koschorreck, D. Pertot, E. Vogt, and M. Köhl. Universal spin dynamics in two-dimensional Fermi gas. *Nat. Phys.*, Doi:10.1038/NPHYS2637, 2013.

[111] F. Dalfovo, S. Giorgini, L. P. Pitaevskii, and S. Stringari. Theory of Bose-Einstein condensation in trapped gases. *Rev. Mod. Phys.*, 71:463, 1999.

[112] S. Giorgini, L. P. Pitaevskii, and S. Stringari. Theory of ultracold atomic Fermi gases. *Rev. Mod. Phys.*, 80:1215, 2008.

[113] C. Cao, E. Elliott, J. Joseph, H. Wu, J. Petricka, T. Schaefer, and J. E. Thomas. Universal quantum viscosity in a unitary Fermi gas. *Science*, 331(6013):58–61, 2011.

[114] C. Menotti, P. Pedri, and S. Stringari. Expansion of an interacting Fermi gas. *Phys. Rev. Lett.*, 89(25):250402, 2002.

[115] M. Cozzini and S. Stringari. Fermi gases in slowly rotating traps: Superfluid versus collisional hydrodynamics. *Phys. Rev. Lett.*, 91(7):070401, 2003.

[116] B. Jackson and E. Zaremba. Quadrupole collective modes in trapped finite-temperature Bose-Einstein condensates. *Phys. Rev. Lett.*, 88(18):180402, 2002.

[117] M. Urban and P. Schuck. Dynamics of a trapped Fermi gas in the BCS phase. *Phys. Rev. A*, 73(1):013621, 2006.

[118] J. Kinast, A. Turlapov, and J. E. Thomas. Damping of a unitary Fermi gas. *Phys. Rev. Lett.*, 94(17):170404, 2005.

[119] M. J. Wright, S. Riedl, A. Altmeyer, C. Kohstall, E. R. Sanchez Guajardo, J. Hecker Denschlag, and R. Grimm. Finite-temperature collective dynamics of a Fermi gas in the BEC-BCS crossover. *Phys. Rev. Lett.*, 99(15):150403, 2007.

[120] S. Riedl, E. R. Sanchez Guajardo, C. Kohstall, A. Altmeyer, M. J. Wright, J. Hecker Denschlag, R. Grimm, G. M. Bruun, and H. Smith. Collective oscillations of a Fermi gas in the unitarity limit: Temperature effects and the role of pair correlations. *Phys. Rev. A*, 78(5):053609, 2008.

[121] U Al Khawaja, C. J. Pethick, and H. Smith. Kinetic theory of collective modes in atomic clouds above the Bose-Einstein transition temperature. *J. Low Temp. Phys.*, 118(1-2): 127–141, 2000.

[122] D. Guery-Odelin, F. Zambelli, J. Dalibard, and S. Stringari. Collective oscillations of a classical gas confined in harmonic traps. *Phys. Rev. A*, 60(6):4851–4856, 1999.

[123] P. Massignan, G. M. Bruun, and H. Smith. Viscous relaxation and collective oscillations in a trapped Fermi gas near the unitarity limit. *Phys. Rev. A*, 71:033607, 2005.

[124] G. M. Bruun and H. Smith. Frequency and damping of the scissors mode of a Fermi gas. *Phys. Rev. A*, 76(4):045602, 2007.

[125] T. Lepers, D. Davesne, S. Chiacchiera, and M. Urban. Numerical solution of the Boltzmann equation for the collective modes of trapped Fermi gases. *Phys. Rev. A*, 82(2): 023609, 2010.

[126] A. Altmeyer, S. Riedl, M. J. Wright, C. Kohstall, J. Hecker Denschlag, and R. Grimm. Dynamics of a strongly interacting Fermi gas: The radial quadrupole mode. *Phys. Rev. A*, 76(3):033610, 2007.

[127] G. M. Kavoulakis, C. J. Pethick, and H. Smith. Damping of hydrodynamic modes in a trapped Bose gas above the Bose-Einstein transition temperature. *Phys. Rev. A*, 57(4): 2938–2941, 1998.

[128] M. Braby, J. Y. Chao, and T. Schäfer. Thermal conductivity and sound attenuation in dilute atomic Fermi gases. *Phys. Rev. A*, 82:033619, 2010.

[129] T. Nikuni and A. Griffin. Hydrodynamic damping in trapped Bose gases. *J. Low Temp. Phys.*, 111(5-6):793–814, 1998.

[130] S. Watabe, A. Osawa, and T. Nikuni. Zero and first sound in normal Fermi systems. *J. Low Temp. Phys.*, 158(5-6):773–805, 2010.

[131] S. Jin. Efficient asymptotic-preserving (AP) schemes for some multiscale kinetic equations. *SIAM J. Sci. Comput.*, 21(2):441–454, 1999.

[132] F. Filbet and S. Jin. An asymptotic preserving scheme for the ES-BGK model of the Boltzmann equation. *J. Sci. Comput.*, 46(2):204–224, 2011.

[133] C. Buggle, P. Pedri, W. von Klitzing, and J. T. M. Walraven. Shape oscillations in nondegenerate Bose gases: Transition from the collisionless to the hydrodynamic regime. *Phys. Rev. A*, 72(4):043610, 2005.

[134] E. Vogt, M. Feld, B. Fröhlich, D. Pertot, M. Koschorreck, and M. Köhl. Scale invariance and viscosity of a two-dimensional Fermi gas. *Phys. Rev. Lett.*, 108:070404, 2012.

[135] G. M. Bruun. Shear viscosity and spin-diffusion coefficient of a two-dimensional Fermi gas. *Phys. Rev. A*, 85:013636, 2012.

[136] T. Schäfer. Shear viscosity and damping of collective modes in a two-dimensional Fermi gas. *Phys. Rev. A*, 85:033623, 2012.

[137] D. Davesne S. Chiacchiera, T. Lepers and M. Urban. Role of fourth-order phase-space moments in collective modes of trapped Fermi gases. *Phys. Rev. A*, 84:043634, 2011.

[138] O. Goulko, F. Chevy, and C. Lobo. Collision of two spin-polarized fermionic clouds. *Phys. Rev. A*, 84:051605(R), 2011.

[139] T. K. Ghosh and S. Sinha. Splitting between quadrupole modes of dilute quantum gas in a two-dimensional anisotropic trap. *Eur. Phys. J. D*, 19:371, 2002.

[140] J. A. Joseph, J. E. Thomas, M. Kulkarni, and A. G. Abanov. Observation of shock waves in a strongly interacting Fermi gas. *Phys. Rev. Lett.*, 106:150401, 2001.

[141] R. Meppelink, R. van Rooij, J. M. Vogels, and P. van der Straten. Enhanced heat flow in the hydrodynamic collisionless regime. *Phys. Rev. Lett.*, 103:095301, 2009.

[142] R. Meppelink, S. B. Koller, J. M. Vogels, H. T. C. Stoof, and P. van der Straten. Damping of superfluid flow by a thermal cloud. *Phys. Rev. Lett.*, 103:265301, 2009.

Appendix A

Implementation of FSM

Algorithm 1: calculation of the collision operator by the zero-padding technique

step 1. $\hat{f} = \mathrm{FFTSHIFT}\{\mathrm{IFFT}[\mathrm{FFTSHIFT}(f)]\}$

step 2. $\hat{Q}^{+} = 0$

For $\theta_p = (1, 2, \cdots, M-1)\pi/M$ and $\varphi_q = (1, 2, \cdots, M)\pi/M$

$t_1 = \hat{f} \cdot \phi_{\alpha+\gamma}(\xi_l, \theta_p, \varphi_q)$; $t_2 = \hat{f} \cdot \psi_{\gamma}(\xi_m, \theta_p, \varphi_q)$

zero-padding t_1, t_2 to the dimension $\geq \frac{3N_1}{2} \times \frac{3N_2}{2} \times \frac{3N_3}{2}$

$\hat{Q}^{+} = \hat{Q}^{+} + \mathrm{FFT}(t_1) \cdot \mathrm{FFT}(t_2) \cdot \sin\theta_p$

End

step 3. $t_1 = \hat{f}$; $t_2 = \hat{f} \cdot \phi_{loss}$

zero-padding t_1, t_2 to the dimension $\geq \frac{3N_1}{2} \times \frac{3N_2}{2} \times \frac{3N_3}{2}$

$\hat{Q}^{-} = \mathrm{FFT}(t_1) \cdot \mathrm{FFT}(t_2)$

step 4. $\hat{Q} = \mathrm{IFFT}(\hat{Q}^{+} - \hat{Q}^{-})$; delete the redundant data in $\hat{Q}$

step 5. $Q = (4\pi^2/\mathrm{Kn}'\, M^2)\, \mathrm{FFTSHIFT}\{\Re[\mathrm{FFT}[\mathrm{FFTSHIFT}(\hat{Q})]]\}$

Algorithm 2: simpler and faster calculation of the collision operator

step 1. $\hat{f} = \mathrm{FFTSHIFT}\{\mathrm{IFFT}[\mathrm{FFTSHIFT}(f)]\}$

step 2. $Q^+ = 0$

For $\theta_p = (1, 2, \cdots, M-1)\pi/M$ and $\varphi_q = (1, 2, \cdots, M)\pi/M$

$Q^+ = Q^+ + \mathrm{FFT}[\hat{f} \cdot \phi_{\alpha+\gamma}(\xi_l, \theta_p, \varphi_q)] \cdot \mathrm{FFT}[\hat{f} \cdot \psi_\gamma(\xi_m, \theta_p, \varphi_q)] \cdot \sin\theta_p$

End

$Q^+ = (4\pi^2/\mathrm{Kn}' M^2)\,\mathrm{FFTSHIFT}[\Re(Q^+)]$

step 3. $\nu = (4\pi^2/\mathrm{Kn}' M^2)\,\mathrm{FFTSHIFT}\{\Re[\mathrm{FFT}[\mathrm{FFTSHIFT}(\hat{\mathrm{f}} \cdot \phi_{\mathrm{loss}})]]\}$

$Q^- = \nu f$

step 4. $Q = Q^+ - Q^-$

Algorithm 3: accurate calculation of the collision frequency technique

step 1. get ϕ_{loss}^{ex} from Eq. (2.36) with $L^{ex} = 2L$ and $R^{ex} = \sqrt{2}L$

step 2. create a zero-value array f^{ex} of size $2N_1 \times 2N_2 \times 2N_3$

step 3. copy the value of f to the middle of f^{ex}

step 4. $\hat{f}^{ex} = \mathrm{FFTSHIFT}\{\mathrm{FFT}[\mathrm{FFTSHIFT}(f^{ex})]\}$

step 5. $\nu^{ex} = (4\pi^2/\mathrm{Kn}' M^2)\,\mathrm{FFTSHIFT}\{\Re[\mathrm{IFFT}[\mathrm{FFTSHIFT}(\hat{\mathrm{f}}^{\mathrm{ex}} \cdot \phi_{\mathrm{loss}}^{\mathrm{ex}})]]\}$

step 6. copy the middle region value of ν^{ex} to ν.

Note: FFTSHIFT represents the Matlab function that shifts the zero-frequency component to the center of spectrum, IFFT is the inverse FFT, and the function $\Re$ gets the real parts of complex numbers.